Dynamics of Field Domains in Semiconductor Superlattices

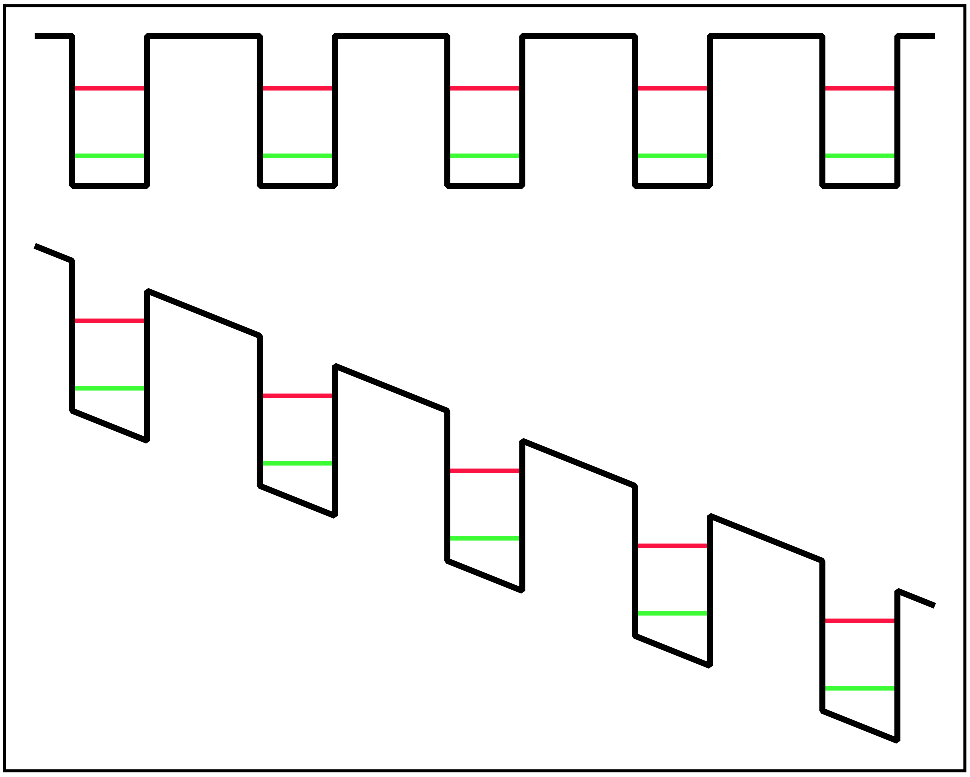

Michael Patra

Dynamics of Field Domains in Semiconductor Superlattices

(Domänendynamik in Halbleiter-Übergittern)

Master's Thesis (Diplomarbeit)

Michael Patra

written at
Institut für Theoretische Physik,
Technische Universität Berlin, Germany
in the group of Prof. Dr. E. Schöll

March 1996

Michael Patra
Institut für Theoretische Physik
Technische Universität Berlin
Sekretariat P-N 7-1
10623 Berlin
Germany

Michael Patra
Sprosserweg 11 B
12351 Berlin
Germany

eMail: patra@physik.tu-berlin.de
WWW: http://itp1.physik.tu-berlin.de/~patra/

Set using the EC-fonts by Norbert Schwarz,
additional symbols by $\mathcal{AMS}$-TEX.
Two-dimensional figures by PICTEX,
three-dimensional figure by gnuplot 3.6.

Contents

Chapter 1

Introduction

The concept of semiconductor superlattices was developed more than 25 years ago [Esa70]. Shortly after they were first proposed, regions of negative differential conductivity (NDC) in the current-voltage characteristic were predicted [Kaz72] and the corresponding current jumps were found experimentally [Esa74].

Due to improvements in epitaxy technology, a number of new results were obtained like the proof that the current-voltage characteristic consists of a number of separated branches [Kas94]. Furthermore, more insight into the relevant transport processes was gained [Kaw86, Cho87, Zha94, Kwo94, Kwo95a, Kwo95b, Kea95, Mer95, Kla95].

After first models describing the formation of field domains [Lai93, Kor93], models that could also describe superlattices in the absence of field domains were developed. These models are based either on simple microscopic models for the relevant transport processes [Pre94a, Pre94b] or on phenomenological quantities [Kor93, Bon94, Mil94]. Recent developments included the introduction of phenomenological quantities into microscopic models at points where no sufficient experimental data about microscopic phenomena is available [Pre95, Kas96].

First, these models were able to describe the branch structure of the current-voltage characteristic. Later, oscillations were predicted [Pre94a, Bon95, Wac95a, Wac] which were afterwards confirmed experimentally [Kas95b, Gra95b].

The further investigation of superlattices then split into two directions. The first direction started with the observation that current-voltage characteristics of experimentally investigated are far more irregular than the ones calculated from the models mentioned above [Gra95a]. The results for the model of PRENGEL et. al. could be improved substantially by allowing for microscopic disorder [Sch94, Sch95b].

The other direction involves the investigation of the different models with methods of nonlinear dynamics. For the relatively simple model of BONILLA et. al., rules describing the creation of branches [Bon94] and later the appearance of oscillations [Wac] could be derived. Parallel to this, similar investigations were started for the model of PRENGEL et. al. [Pat95, Sch96a].

This thesis deals with the dynamics as described by the model of PRENGEL et. al., especially when the effects of disorder are included. Thus, this thesis involves two different subjects, namely nonlinear dynamics and the physics of semiconductors. Of course, this has to manifest itself in the structure of this thesis: It starts with two chapters describing the necessary fundamentals of these two subjects.

Note that there is an index at the end of this thesis. Most readers of this thesis will have experience in at least one of the subjects necessary for understanding it so they do not need to study the respective introductory chapter. If there are problems with, e. g., the definition of a particular term, the index may be used to find the corresponding place in one of the introductory chapters.

On the last page of this thesis, you can find the legend for all figures in this thesis. Usually, not all parameters (U, N_D, α, …) are explicitly given in the caption of a particular figure as these are often not important in understanding the fundamental features presented in it. However, since these parameters are important, e. g., when making comparisons with experimental data, they are summarised in appendix H (page 125).

Chapter 2

Foundations of Nonlinear Dynamics

This chapter is intended to be a short introduction to the concepts of "nonlinear dynamics" necessary for understanding this thesis. Of course, it cannot replace a textbook on this subject. There are a number of books dealing with the foundations of nonlinear dynamics, e. g. [Abr83, Dra92] to name just two of them, or with applications to semiconductors like [Pei92, Sch87]. For more "exotic" bifurcations, please refer to [Guc83, Guc86].

2.1 Introduction

The dynamics of a specific system are given by an ordinary differential equation (ODE):

$$\dot{x} = f(x).$$

Usually x will not be simply a real number but a vector. A *fixed point* or *stationary point* is a point with $f(x) = 0$. The system cannot (at least in principle) leave such a point. If this is true even if x is perturbed slightly, the fixed point is called *stable*. If even a infinitesimal perturbation makes the system move away from the fixed point, it is called *unstable*. The stability of a fixed point can be inferred from the eigenvalues of the linearisation of f at the fixed point: If the real parts of all eigenvalues are negative, the fixed point will be stable. If at least one eigenvalue possesses a positive real part, the fixed point is unstable. If at least one eigenvalue of an unstable fixed points possesses a negative real part, the fixed point is also called a *saddle point*.

The ODE may also allow closed periodic solutions. These are called *limit cycles* if nearby trajectories are either pulled into or pushed away from the limit cycle. This is the main difference to closed solution curves of Hamiltonian systems (for example the movement of the planets around the sun) where there exists a solution for every value of the total energy (at least for energies in a certain interval). Limit cycle oscillations are thus associated with discrete values of oscillation amplitude and oscillation frequency. Similar to fixed points, limit cycles may be stable or unstable. Their stability can be determined from the Floquet-exponents [Par89, Dra92].

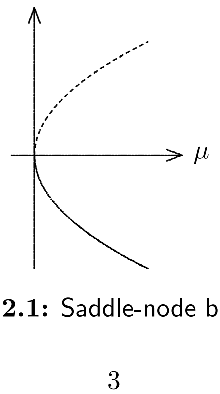

Figure 2.1: Saddle-node bifurcation

2.2 Saddle-Node Bifurcation

The *saddle-node bifurcation* may be described by the equation

$$\dot{x} = f(x) \qquad \text{with} \quad f(x) = x^2 - \mu.$$

The solutions $x_0(\mu)$ of the stationary equation $\dot{x} = 0$ are given by

$$x_0^{(1)}(\mu) = \sqrt{\mu} \quad \text{and} \quad x_0^{(2)}(\mu) = -\sqrt{\mu}.$$

The solutions are thus limited to the parameter interval $\mu \geq \mu_0 = 0$, i. e., one side of the bifurcation point μ_0. The derivative of f is given by

$$\frac{\partial f}{\partial x} = 2x.$$

$x_0^{(1)}$ is unstable due to $\frac{\partial f}{\partial x}|_{x_0^{(1)}(\mu)} = 2\sqrt{\mu} > 0$ (if it is said that a certain branch is stable or unstable, the bifurcation point – here $\mu = \mu_0$ – is not included) and, correspondingly, $x_0^{(2)}$ stable. This is depicted in Fig. 2.1. The solution changes its stability in the bifurcation point, the fixed points is thus changed from a node to a saddle point which leads to the name *saddle-node bifurcation.* Also used are the names *turning point*, *fold* and *limit point*.

2.3 Transcritical Bifurcation

The *transcritical bifurcation* may be described[1] by the equation

$$\dot{x} = f(x) \qquad \text{with} \quad f(x) = \mu x - x^2.$$

The solutions $x_0(\mu)$ of the stationary equation $\dot{x} = 0$ are

$$x_0^{(1)}(\mu) = 0 \quad \forall\mu \quad \text{and} \quad x_0^{(2)}(\mu) = \mu,$$

which intersect in the bifurcation point $\mu_0 = 0$. The derivative of f is

$$\frac{\partial f}{\partial x} = \mu - 2x,$$

yielding $\frac{\partial f}{\partial x}|_{x_0^{(1)}(\mu)} = \mu$ and $\frac{\partial f}{\partial x}|_{x_0^{(2)}(\mu)} = -\mu$. $x_0^{(1)}$ is stable for $\mu < 0$ and unstable for $\mu > 0$, with $x_0^{(2)}$ displaying the opposite behaviour. The two solution curves thus exchange their stability in the bifurcation point as is depicted in Fig. 2.2(b).

In order to verify a bifurcation experimentally (or just to be able to see it in a numerical simulation), it is necessary for the bifurcation be *structurally stable*, which means, that the same bifurcation can be found if f is replaced by a slightly modified function $\tilde{f}$ – an adaptation of the parameter $\tilde{\mu}_0$ may be necessary and is allowed.

As an example, we will choose $\tilde{f}$ as

$$\tilde{f}(\mu) = f(\mu) - \epsilon = \mu x - x^2 - \epsilon.$$

For $\epsilon > 0$, the stationary solutions $\tilde{x}_0$ are given by

$$\tilde{x}_0^{(1)/(2)} = \frac{\mu}{2} \pm \sqrt{\frac{\mu^2}{4} - \epsilon}.$$

One can see at once that there are no solutions for $-2\sqrt{\epsilon} < \mu < 2\sqrt{\epsilon}$.

By substituting $\frac{\mu}{2} - x \to x$ and $\epsilon - \frac{\mu^2}{4} \to \mu$ and comparing with section 2.2, it is possible to verify that two saddle-node bifurcation points $4\sqrt{\epsilon}$ apart are created. This is depicted in Fig. 2.2(c).

The other possibility is $\epsilon < 0$. The solutions are then given by

$$\tilde{x}_0^{(1)/(2)} = \frac{\mu}{2} \pm \sqrt{\frac{\mu^2}{4} + |\epsilon|}.$$

Regardless of μ, the square root will be positive. Thus, there are two solutions defined for any μ and not intersecting each other. Using $\frac{\partial \tilde{f}}{\partial x} = \frac{\partial f}{\partial x} = \mu - 2x = \mp 2\sqrt{\cdots}$ yields $\frac{\partial \tilde{f}}{\partial x}|_{\tilde{x}_0^{(1)}(\mu)} < 0$ and $\frac{\partial \tilde{f}}{\partial x}|_{\tilde{x}_0^{(2)}(\mu)} > 0$. Therefore, the stability of the two solution curves is not changed by the (former) bifurcation. This is depicted in Fig. 2.2(a).

It can be proven that a different choice for $\tilde{f}$ will not lead to any bifurcation scenarios qualitatively different from those depicted in Fig. 2.2. The variation of a single imperfection parameter, named ϵ in this section, is thus sufficient. This bifurcation is therefore said to posses codimension 1. In this sense, the transcritical bifurcation is the most simple of all bifurcations[2] and is thus also referred to as *simple bifurcation* or even shorter just as *bifurcation.*

---

[1] An other possibility is $f(x) = x^2 - \mu^2$. This offers the advantage of higher symmetry; in addition, it is easy to see that it results from the unfolding of the cuspoid x^2, $x^2 + b$. On the other hand, at least in my opinion, the graphical illustrations for this choice are more difficult to understand.

[2] The saddle-node bifurcation is often not referred to as a “real” bifurcation. Many authors, e. g. [Ioo90], define a singular point not only to have $\frac{\partial f}{\partial x} = 0$, but also $\frac{\partial f}{\partial \mu} = 0$. A saddle-node bifurcation point is thus no singular point. In addition, if x and μ are exchanged, such a point is no longer a bifurcation point. In this sense, it is a big difference whether one examines a function $f : \mathbb{R} \to \mathbb{R}$ with a dependence on an additional parameter, or a function $f : \mathbb{R} \times \mathbb{R} \to \mathbb{R}$.

2.4 Conjugated Point

We consider the equation

$$\dot{x} = f(x) \qquad \text{with} \quad f(x) = -x^2 - \mu^2.$$

The corresponding stationary equation $\dot{x} = 0$ possesses just a single solution, namely $x_0 = 0$ for $\mu_0 = 0$ (see Fig. 2.3(b)). This is changed if f is replaced by a slightly modified function

$$\tilde{f}(x) = f(x) + \epsilon = -x^2 - \mu^2 + \epsilon.$$

The solutions x_0 are then given by

$$x_0^{(1)/(2)} = \pm\sqrt{\epsilon - \mu^2},$$

which do not exist for $\epsilon < 0$ and are for $\epsilon > 0$ defined in the parameter interval $-\sqrt{\epsilon} \leq \mu \leq \sqrt{\epsilon}$. These two cases are depicted in Figs. 2.3(a) and 2.3(c) respectively.

The closed solution curve for $\epsilon > 0$ is called an *isola*, the bifurcation at $\epsilon_0 = 0$ thus an *isola centre*. A different choice for $\tilde{f}$ will lead to no new bifurcation scenarios which means that a conjugated point also has codimension 1.

2.5 Isola Bifurcation

It has been shown in Fig. 2.3 that the perturbation of a transcritical bifurcation may lead to a change in how solution branches are connected (see Figs. 2.2(a) to 2.2(c)). If the imperfection parameter ϵ is considered to be just another "normal" control parameter, the result is a bifurcation in which for $\epsilon < 0$ the two solution branches with $\mu < 0$ and the two with $\mu > 0$ are connected (Fig. 2.2(c)) whereas for $\epsilon > 0$ the two branches with $x > 0$ and the two with $x < 0$ are connected (Fig. 2.2(a)).

In section 2.4 it was demonstrated that there may be closed solution curves ("isolas") and that these isolas may disappear if a parameter is changed. It is now possible that an isola merges via a perturbed transcritical bifurcation with another solution curve (or splits off from another solution curve). After [Dra92] this shall be referred to as *isola bifurcation*[3].

There are two types of such a bifurcation differing in which two of the four branches of a perturbed transcritical bifurcation belong to an isola. Consequently, these two types differ in whether two saddle-node bifurcation points are created or destroyed in the bifurcation. Both types are depicted in 2.4. For type I, there exist two saddle-node bifurcation points near the designated bifurcation point while the isola is still separated from the other solution curve.

2.6 Cusp Point

In anticipation of section 2.6.4, we will start with the equation with the imperfection parameters already included. In order to yield all qualitatively different bifurcation scenarios, two imperfection parameters are necessary. The equa-

---

[3] Strictly speaking, [Dra92] (also) calls the splitting-off and following disappearing of a closed solution curve an isola bifurcation. One example of such a function is $f(x) = \frac{1}{2}x^2 + \frac{1}{3}\mu^3 - \mu - \frac{2}{3} + \epsilon$.

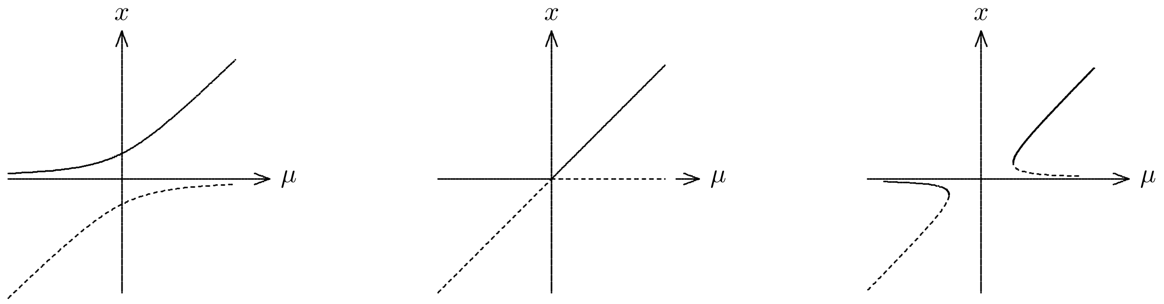

(a) $\epsilon < 0$ (b) $\epsilon = 0$ (c) $\epsilon > 0$

Figure 2.2: Perturbed transcritical bifurcation. Depicted are the solutions of the equation $\mu x - x^2 - \epsilon = 0$ for different values of ϵ.

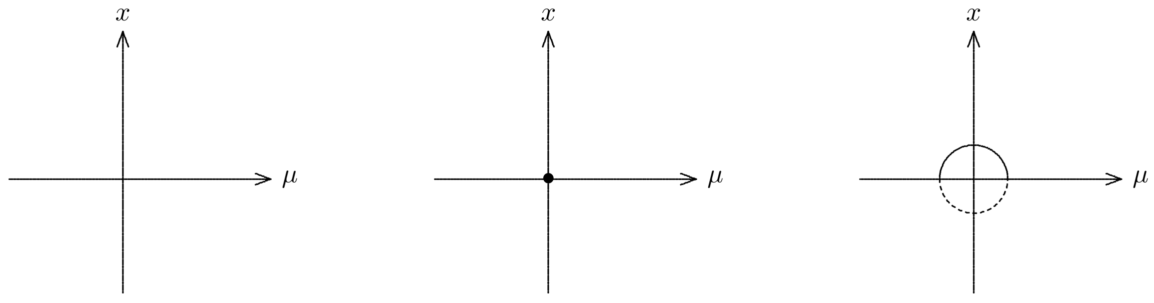

(a) $\epsilon < 0$ (b) $\epsilon = 0$ (c) $\epsilon > 0$

Figure 2.3: Conjugated point. Depicted are the solutions of the equation $0 = -x^2 - \mu^2 + \epsilon$ for different values of ϵ.

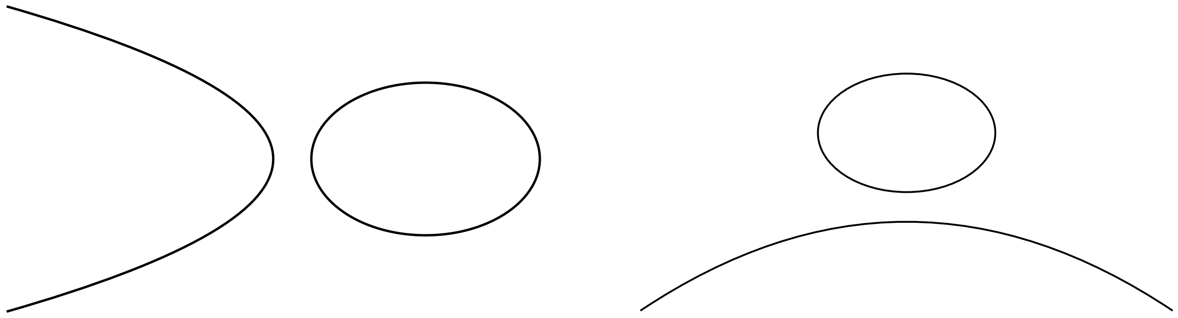

(a) Type I, before merging (b) Type II, before merging

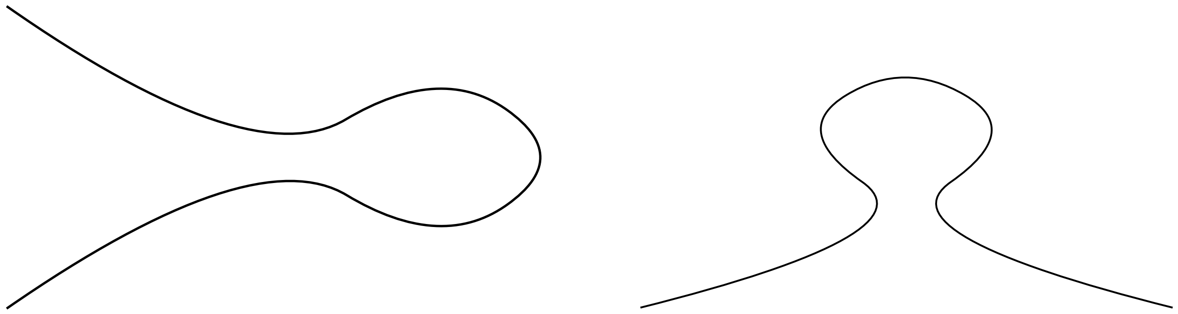

(c) Type I, after merging (d) Type II, after merging

Figure 2.4: Merging of two solution curves in an isola bifurcation (horizontally: parameter axis). Before merging, there is one open and one close solution curve. Afterwards there is just a single open solution curve. The stability of the different branches has not been marked in the figure.

tion reads then

$$\dot{x} = f(x) \qquad \text{with} \quad f(x) = -x^3 + \mu x - \lambda$$

The cusp point is $(x, \mu, \lambda) = (0, 0, 0)$. All solutions of the stationary equation $\dot{x} = 0$ are depicted in Fig. 2.5 in dependence on λ and μ.

Let us start with a number of special cases to demonstrate a few of the possible scenarios near a cusp point. If $\lambda = 0$ or $\mu = 0$ is assumed, this represents cross-sections through the cusp point. The bifurcations along there will be structurally unstable[4], as almost any perturbation will move the cusp point in such a way as that it moves out of the examined plane.

For the first case, $\lambda = 0$, the equation transforms into

$$0 = g(x) \qquad \text{with} \quad g(x) = -x^3 + \mu x$$

It possesses three solutions:

$$x_0^{(1)} = 0 \quad \forall \mu \quad \text{and} \quad x_0^{(2)/(3)}(\mu) = \pm\sqrt{\mu}$$

with the last one only existing for $\mu \geq 0$. Using

$$\frac{\partial g}{\partial x} = -3x^2 + \mu$$

yields $\frac{\partial g}{\partial x}|_{x_0^{(2)/(3)}(\mu)} = -2\mu < 0$; thus these two solutions are stable everywhere they are defined. Examining $x_0^{(1)}$ yields $\frac{\partial g}{\partial x}|_{x_0^{(1)}(\mu)} = \mu$. It is thus stable for $\mu < 0$ and unstable for $\mu > 0$. This scenario is depicted in Fig. 2.6(e) and is known as *pitchfork bifurcation*.

The other special case, $\mu = 0$, yields the equation

$$0 = h(x) \qquad \text{with} \quad h(x) = -x^3 - \lambda$$

Its only solution is $x_0(\lambda) = -\lambda^{1/3}$. It possesses a vertical tangent at $\lambda = 0$. Such a point[5] is called a *hysteresis point* and is depicted in Fig. 2.6(b).

2.6.1 Perturbed Hysteresis Point

One has to determine the solutions of the equation $-x^3 + \mu x - \lambda = 0$ in dependence on λ for μ fixed at $\mu \neq 0$. It is easier to solve for $\lambda_0(x)$ which reads

$$\lambda_0(x) = -x^3 + \mu x.$$

There is a single solution curve $x_0(\lambda)$ iff $\lambda_0(x)$ is invertible. The derivative of $\lambda_0(x)$ is

$$\frac{\partial \lambda_0}{\partial x} = -3x^2 + \mu,$$

$\lambda_0(x)$ is thus invertible iff $\mu < 0$. As

$$\frac{\partial f}{\partial x} = \frac{\partial \lambda_0}{\partial x} = -3x^2 + \mu < 0,$$

the solution is stable for $\mu < 0$. If on the other hand $\mu > 0$, $\lambda_0(x)$ is increasing for $-\sqrt{\frac{\mu}{3}} < x < \sqrt{\frac{\mu}{3}}$ and decreasing outside this interval. This means that there are three solutions for $x_0(\lambda)$ for λ in a certain interval and just one solution for λ outside. The middle branch ($\frac{\partial \lambda_0}{\partial x} > 0$) is unstable, the other two branches are stable. The unstable branch is connected to the two stable branches via saddle-node bifurcations. This scenario is depicted in Fig. 2.6(c).

---

[4] Due to additional constraints, especially symmetries, one may still observe these bifurcations in experiments. If, for example, $\tilde{f}(-x) = -\tilde{f}(x)$ has to be fulfilled, $\lambda \neq 0$ is not allowed.

[5] This point is no bifurcation point as the number of solutions does not change. In addition, it is no singular point as $\frac{\partial h}{\partial \lambda} \neq 0$.

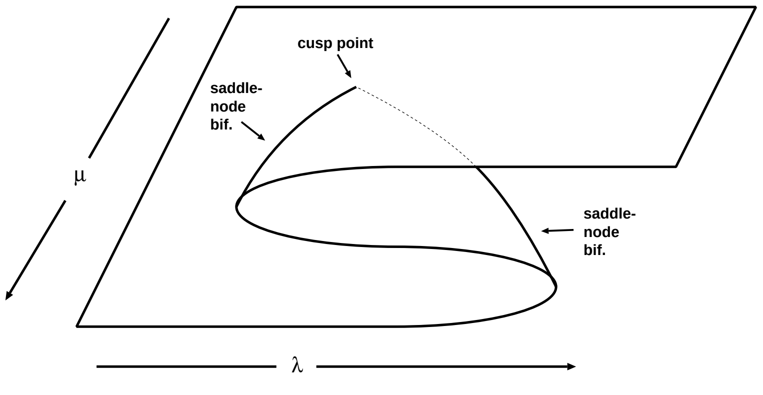

Figure 2.5: Cusp point. Depicted are the solutions of the equation $0 = -x^3 + \mu x - \lambda$ as a function λ and μ. The cusp point has the coordinates $(x, \lambda, \mu) = (0, 0, 0)$.

2.6.2 Perturbed Pitchfork Bifurcation

We examine $-x^3 + \mu x = \lambda$ in dependence on μ for fixed $\lambda \neq 0$. Calculating once again the inverse solution function $\mu_0(x)$ yields

$$\mu_0(x) = \frac{\lambda + x^3}{x}.$$

Once clearly sees that for finite μ there cannot be a solution with $x_0 = 0$ but rather $x = 0$ is a pole with a change of sign. This implies that there have to be at least to unconnected solution branches $x_0^{(1)}(\mu)$ and $x_0^{(2)}$ with $x_0^{(1)}(\mu) > 0$ and $x_0^{(2)}(\mu) < 0$. Depending on the sign of λ, either $\lim_{x\downarrow 0} \mu_0(x) = +\infty$ (for $\lambda > 0$) or $\lim_{x\downarrow 0} \mu_0(x) = -\infty$ (for $\lambda < 0$) is fulfilled. Independent of the sign of λ, one has

$$\lim_{x\to+\infty} \mu_0(x) = +\infty \quad \text{and} \quad \lim_{x\to-\infty} \mu_0(x) = -\infty.$$

$\mu_0(x)$ has exactly one extremum which due to

$$\frac{\partial \mu_0}{\partial x} = \frac{2x^3 - \lambda}{x^2}$$

lies at $x > 0$ for $\lambda > 0$ and vice versa. This means that there have to be two solution branches: One defined for all μ, which lies in the region $x < 0$ for $\lambda > 0$ and vice versa, and two other which merge in a saddle-node bifurcation. The two outer branches have to be stable due to $\frac{\partial f}{\partial x} = -x^2 + \mu < 0$ for high enough $|x|$. This is depicted in Figs. 2.6(d) and 2.6(f).

By choosing other perturbations, it is possible to derive additional bifurcation scenarios. A few remarks on this can be found in section 2.6.4, a possible scenario is depicted in Fig. 2.8(a).

2.6.3 Cusp Curve

As derived above, the solution curve for fixed $\mu > 0$ is given by $\lambda_0(x) = -x^3 + \mu x$. There are two saddle-node bifurcation points at $x = \pm\sqrt{\frac{\mu}{3}}$. Using these two equations yields a relationship for the values of λ and μ for which there are saddle-node bifurcations:

$$27\lambda^2 = 8\mu^3.$$

These curve is the *cusp curve* and can be interpreted as projection of all bifurcation points from Fig. 2.5 onto the λ-μ-plane.[6] It is depicted in Fig. 2.7(a). The equation $\dot{x} = 0$ possesses three solutions for parameter values inside the

---

[6] With the exception of the cusp point itself, all points on the cusp curve are saddle-node bifurcations.

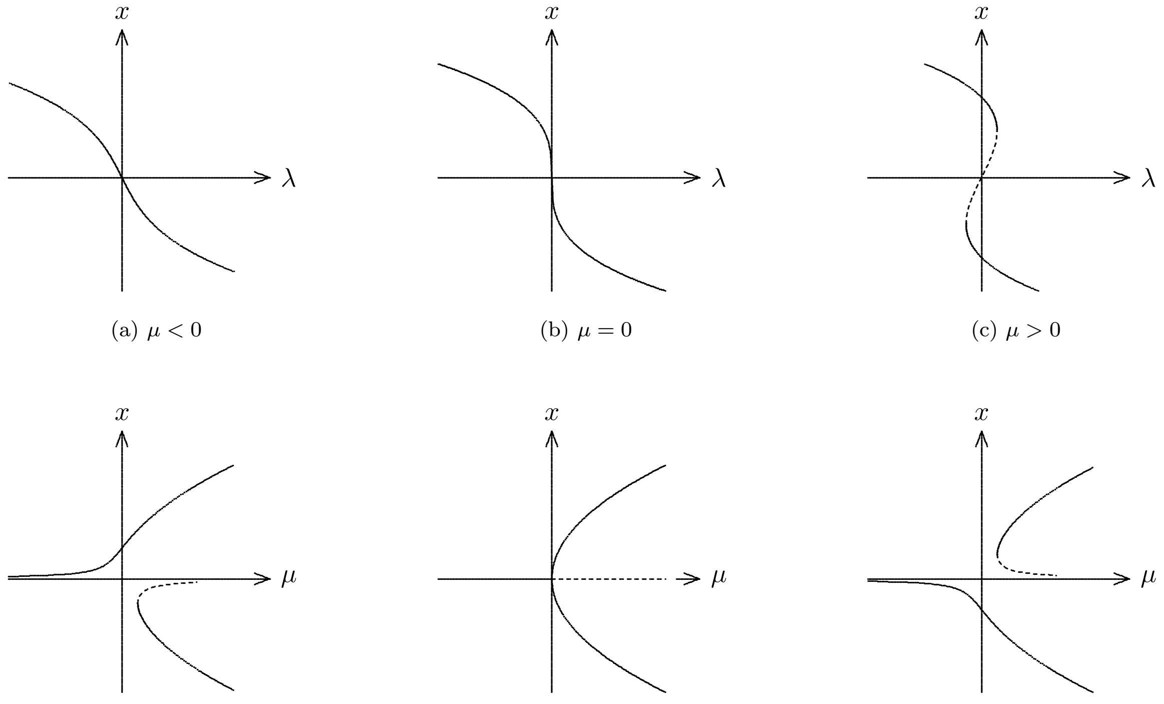

(a) $\mu < 0$ (b) $\mu = 0$ (c) $\mu > 0$

(d) $\lambda < 0$ (e) $\lambda = 0$ (f) $\lambda > 0$

Figure 2.6: Cross-section through a cusp point. Depicted are the solutions of the equation $0 = -x^3 + \mu x - \lambda$. In each subfigure, either μ or λ is fixed at a constant value.

cusp curve and one solution for parameter values outside. Its derivative reads

$$\frac{\partial\mu}{\partial\lambda} = \frac{8}{27}\lambda^{-\frac{1}{3}}.$$

It is infinite in the origin, i. e., the cusp point, the two branches for $\lambda < 0$ and $\lambda > 0$ thus do not touch but have a point of second order contact there. This allows the following interpretation of a cusp point: Two branches of saddle-node bifurcation points merge if a second parameter is varied. This can also be seen from Fig. 2.6(c): If μ is decreased down to zero, the distance between the two saddle-node bifurcation points decreases also until the two points merge and disappear at $\mu = 0$.

2.6.4 Codimension

Apart from the scenarios discussed above, there may be additional ones if the λ-μ is crossed on more complex paths (see for example [Gol85]). In the equation

$$\dot{x} = f(x) \qquad \text{with} \quad f(x) = -x^3 + \mu x - \lambda$$

given at the start of this section, there are two parameters μ and μ, of which one had been fixed at a constant value in the preceding calculations. More general is the parametrisation of a general curve in the μ-λ-plain by an additional parameter τ, which can be thought of as being a kind of "arc length":

$$\mu = \mu(\tau) \qquad \text{and} \qquad \lambda = \lambda(\tau)$$

The particular choice for the functions $\mu(\tau)$ and $\lambda(\tau)$ determines the bifurcation scenario which will be described by the system. $\mu(\tau) = \tau$ and $\lambda(\tau) = 0\,\forall\tau$ will, for example, describe the pitchfork bifurcation. The situation becomes more complicated when small perturbations p_μ and p_λ are introduced which shall depend on imperfection parameters α_1, α_2 etc. One then has to examine the functions

$$\begin{aligned} \mu(\tau;\alpha_1,\alpha_2,\ldots) &:= \mu(\tau) + p_\mu(\alpha_1,\alpha_2,\ldots) \\ \lambda(\tau;\alpha_1,\alpha_2,\ldots) &:= \lambda(\tau) + p_\lambda(\alpha_1,\alpha_2,\ldots). \end{aligned}$$

The imperfection parameters α_i shall be chosen in such a way that $p(0,0,\ldots) = 0$.

The bifurcation scenario one gets for $(\alpha_1,\alpha_2,\ldots) \neq (0,0,\ldots)$ will usually be different from that for $(\alpha_1,\alpha_2,\ldots) = (0,0,\ldots)$. These differences will usually be small and unimportant: The bifurcation point will be shifted a bit, some branches will be a litter longer, others slightly shorter. However, some differences might be of a qualitative nature when, for example, a bifurcation cannot be observed any more. The exact definition of what a "qualitative difference" exactly is, is rather difficult and is thus not handled consistently in the available literature. Such a exact definition is, however, not needed here as it is always clear for the problems discussed in this thesis when there is a qualitative difference so one example should suffice: Fig. 2.6(d) depicts a solution curve for $\mu < 0$. The precise value of μ is unimportant as there are no qualitative differences as long as μ does not cross the λ-axis. Qualitative changes occur if $\mu > 0$ is changed to $\mu = 0$ or even $\mu < 0$.

After these remarks it is possible to introduce the concept of codimension. There are two different questions one might want to answer:

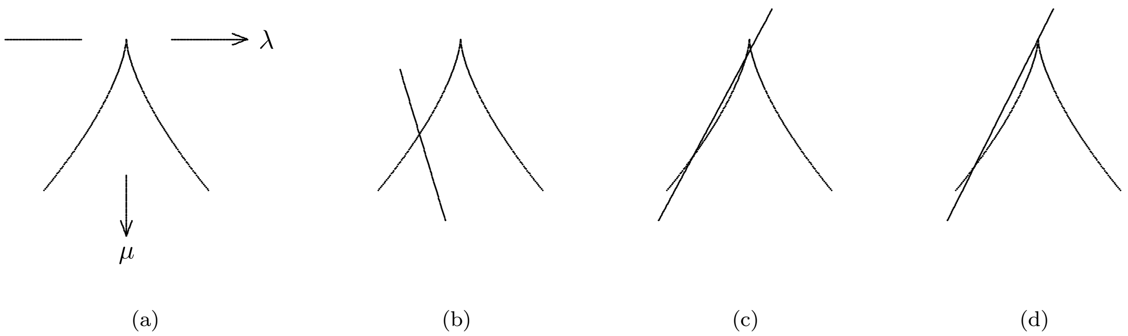

Figure 2.7: Cusp curve and different cross-sections in the λ-μ-plane. The corresponding bifurcation scenarios are depicted in Fig. 2.8. **(a)** Cusp curve. **(b)** One intersection with the cusp curve. **(c)** Three intersections with the cusp curve. **(d)** Cross-section through the cusp point. Please note that it is not possible to have exactly two intersections with the cusp curve unless the line is exactly horizontal or runs through the cusp point.

- At least how many different imperfection parameters α_i do the functions $p_{\mu/\lambda}(\alpha_1, \alpha_2, \ldots)$ have to possess so that every qualitatively different bifurcation scenario, which can be reached by an infinitesimal variation of $p_{\mu/\lambda}(\alpha_1, \alpha_2, \ldots)$, can be reached? To put it in an other way: When will the introduction of further imperfection parameters lead to no new bifurcation scenarios? This is the "mathematical view" taken in this thesis.

- If due to some unknown reason the functions $\lambda(\tau)$ and $\mu(\tau)$ are changed, how many parameters do there have to be that by changing them we are able to get back to the original bifurcation scenario. This is the "experimental view".[7]

- It is quite common to define the codimension as the number of parameters one has to vary in order to see the bifurcation in question. The main difference to the definition used in this thesis is that there is no parameter τ. This affects bifurcations of codimension 0 (saddle-node bifurcation and Hopf bifurcation) which will become codimension 1 bifurcation under this definition (as there has to be at least one parameter to see any bifurcation).

The minimum number of parameters defined above is the *codimension* of the bifurcation.

Pitchfork bifurcation and hysteresis point both can be considered as cross-sections through the cuspoid of order two[8]. Possible bifurcation scenarios of the perturbed bifurcation have already been investigated in sections 2.6.1 and 2.6.2 by considering cross-section through the cuspoid which did not run exactly through the cusp point. Comparing with table 2.1 one can see that the hysteresis point has been covered completely while there are additional bifurcation scenarios for the perturbed pitchfork bifurcation.

The different bifurcation scenarios could be understood as different cross-sections through Fig. 2.7(a). Until now all those cross-sections have been either vertically or horizontally. In order to determine the "missing" bifurcation scenarios of the perturbed pitchfork bifurcation, oblique cross-sections have to be allowed. The three possibilities are summarised in Figs. 2.7(b) to 2.7(d). They are a combination of the effects discussed in sections 2.6.1 and 2.6.2.

2.7 Hopf Bifurcation

In a *Hopf bifurcation*, a branch of limit cycles bifurcates from a branch of stationary solutions.

The Hopf bifurcation may be *supercritical* in

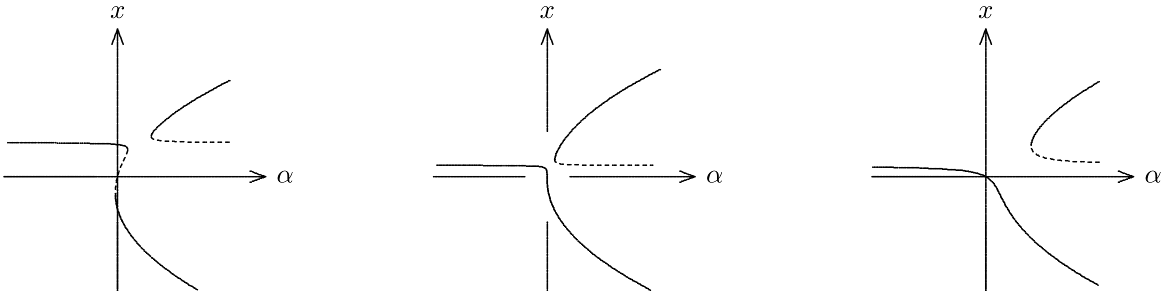

(a) (b) (c)

Figure 2.8: Oblique cross-sections through a cusp point. Depicted are the bifurcation scenarios corresponding to the cross-sections shown in Fig. 2.7. **(a)** This scenario contains three saddle-node bifurcation points and thus corresponds to Fig. 2.7(c). It can be obtained by perturbing a pitchfork bifurcation. **(b)** This scenario consists of a saddle-node bifurcation and a hysteresis point. The corresponding cross-section thus has to run through the cusp point and intersect the cusp curve an additional time (Fig. 2.7(d)). **(c)** This scenario consists of a single saddle-node bifurcation; it corresponds to Fig. 2.7(b).

---

[7] If a model of a dynamical system (or some circuit we want to do measurements on) does not posses this number of parameters (or knobs in the case of some circuit) and there no symmetries to reduce the effective codimension, one should be very careful with calculations yielding a bifurcation scenario with that codimension.

[8] The cuspoid of order m is given by x^{m+1}, its unfolding is $x^{m+1} + a_{m-1}x^{m-1} + a_{m-2}x^{m-2} + \cdots + a_1 x + a_0$.

Bifurcation	$f(x)$	codim.	unfolding
saddle-node	$x^2+\mu$	0	$x^2+\mu$
transcritical	$x^2-\mu^2$	1	$x^2-\mu^2+\alpha_1$
conjugated pnt.	$x^2+\mu^2$	1	$x^2+\mu^2+\alpha_1$
hysteresis pnt.	$x^3+\mu$	1	$x^3+\alpha_1 x+\mu$
pitchfork	$x^3+\mu x$	2	$x^3+\mu x+\alpha_1+\alpha_2\mu$

Table 2.1: Table of all bifurcation examined in this thesis (from [Gol85]).

which case a branch of stable limit cycles bifurcates from a stable fixed point which looses its stability in the bifurcation. If it is *subcritical*, a branch of unstable limit cycles bifurcates from a branch of unstable fixed points which will become stable in the bifurcation.

Necessary condition for the appearance of a Hopf bifurcation is that a pair of complex conjugate eigenvalues cross the imaginary axis when a parameter is varied. To distinguish between the supercritical and the subcritical case it is necessary to calculate higher derivatives (see [Khi92] which also deals with sufficient conditions for Hopf bifurcations). The crossing of the imaginary axis is no sufficient condition for the creation of a limit cycle [Gol85] but is usually takens as such because special cases are extremely rare.

Special feature of the Hopf bifurcation is the quadratic increase of the oscillatory amplitude in dependence of the distance (in parameter space) from the bifurcation point. The frequency of the oscillation is in the neighbourhood of the bifurcation given by the imaginary part of the pair of eigenvalues and is thus unaffected by the bifurcation. As the Hopf bifurcation is – especially in subjects outside "nonlinear dynamics" – the most widely known bifurcation type, I will not discuss the Hopf bifurcation in greater detail.

2.8 Unstable Manifold

The stability of fixed points is determined by the eigenvalues of the dynamical matrix at the fixed point. To every eigenvalues belongs an corresponding eigenvector[9] and thus one mode whose dynamics near the fixed point are determined by the corresponding eigenvalue. The manifold belonging to an eigenvector is given by the trajectory starting from the fixed point in the direction of the eigenvector (unstable manifold) or runs into the fixed point in the direction of the eigenvector (stable manifold).[10] For a more formal definition refer to [Par89]. One example of a saddle point is depicted in Fig. 2.9 including both stable and unstable manifold.

If a eigenvalue is not real but belongs to a pair of complex conjugated eigenvalue it is not possible to use single trajectories. In its place, the dynamics of planes has to be considered [Abr83].

---

[9] It is possible that there are fewer eigenvectors in bifurcation points. As is known from linear algebra, this can only happen if multiple eigenvalues have the same value. Thus, this does not apply to "standard" bifurcations but, for example, to Takens-Bogdanov points.

[10] For each eigenvector, there are two manifolds as the eigenvector may be multiplied by -1.

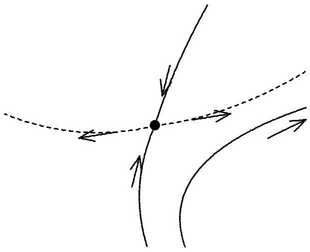

Figure 2.9: Stable (solid line) and unstable (dashed line) manifold of a fixed (saddle) point. The arrows indicate the direction of the dynamics along the manifold. The stable manifold is the only trajectory which is able to reach the fixed point. All other trajectories, of which one is included in the figure, will be repelled once they get near the fixed point. The fixed point may only be left along the unstable manifold.

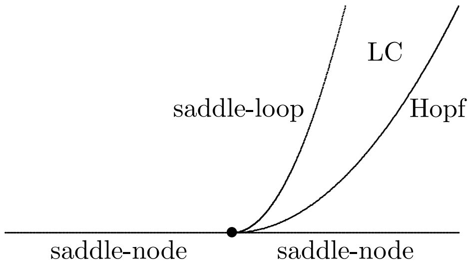

Figure 2.10: Depicted is the location of the bifurcation points ("phase diagram") in the neighbourhood of a Takens-Bogdanov point. Two branches of saddle-node bifurcation points merge with one branch of Hopf bifurcation points. The limit cycles created by the Hopf bifurcations exist only in the region marked with "LC" as an additional branch of saddle-loop bifurcation points is also created.

2.9 Homoclinic Orbits

If a trajectory starting in a fixed point returns to that fixed point, it is called a *homoclinic orbit* or *saddle loop*. This implies that the fixed point has to be a saddle point and that the saddle loop lies in both one stable and one unstable manifold. Please remember that the system needs infinite time to complete such a trip.

If both involved manifolds are one-dimensional (i. e. if both eigenvalues are real) the homoclinic orbit has to be structurally unstable.[11] Even very small perturbations destroy the saddle loop as the stable and the unstable manifold "miss" each other. If at least of the two manifolds is a plane the saddle loop might be structurally stable. The most important example for this is the Rössler-attractor.

2.10 Saddle-Loop Bifurcation

The homoclinic orbit described in section 2.9 is similar to a limit cycle in that it returns to its start position (the fixed point). However, it takes in infinite amount of time to complete one trip so a homoclinic orbit is kind of a limit cycle with zero frequency.[12] It is thus possible that a homoclinic orbit merges with a limit cycle when a control parameter is varied. During this process, the frequency of the limit cycle decreases down to zero at which point the limit cycle then disappears. Together with the fact that the amplitude is not affected by the *saddle-loop bifurcation* this can be used to detect this bifurcation.

2.11 Takens-Bogdanov Point

If the position of a Hopf bifurcation point is determined as a function of a second parameter there are two sensible possibilities if this branch of Hopf bifurcation points stays in a finite region (in parameter space): Either this branch forms a closed curve or it has two endpoints. The most common bifurcation at such a endpoint is a Takens-Bogdanov point.

In a Takens-Bogdanov point, the branch of Hopf bifurcation points merges with a continuous branch of saddle-node bifurcation points. In the Takens-Bogdanov point, the tangents of both curves are parallel (Fig. 2.10). In such a point, the eigenvalue conditions for both bifurcation types have to be fulfilled simultaneously. The condition for a Takens-Bogdanov point is that there two eigenvalues 0 with only one corresponding eigenvector. It may be found by continuing a branch of Hopf bifurcation points or a branch of saddle-node bifurcation points.[13]

Limit cycles are created along the Hopf bifurcation branch but have to be restricted to a finite area in parameter space. Thus, there has to be an additional branch of bifurcation points

---

[11] This is not true for maps.

[12] On the other hand, trajectories near a limit cycle are either pulled into or pushed away from the limit cycle. There is no such condition for homoclinic orbits.

[13] The corresponding bifurcation function along the Hopf branch changes its sign in the TB while the bifurcation function along the saddle-node branch has just a root without a change of sign. Thus it is not garantied that every TB is detected in the latter case [Khi90].

which can be shown to be saddle-loop bifurcations [Guc83]. The saddle-loop bifurcation point is a global bifurcation whereas the other bifurcations involved – including the Takens-Bogdanov point – are just local bifurcation. The Takens-Bogdanov point is an example of a local bifurcation which enforces the existence of global bifurcations. Of course, it is not possible to calculate the exact position of these global bifurcation points from a local analysis.

Further information about the Takens-Bogdanov point, including the occurrence of imaginary Hopf bifurcation points,[14] can be found in [Wer91, Roo87, Die90, Guc86].

2.12 Continuation

Let us consider solutions of the nonlinear equation

$$0 = f(\mathbf{x}, \lambda)$$

with $f : \mathbb{R}^n \times \mathbb{R} \to \mathbb{R}^n$. As f is equal to zero for all "allowed" values of $\mathbf{x}$ and λ, the same has to be true for its differential:

$$0 = \mathrm{d}\, f_j = \sum_{i=1}^{n} \underbrace{\frac{\partial f_j}{\partial x_i}}_{A_{ji}} \mathrm{d}\, x_i + \frac{\partial f_j}{\partial \lambda} \mathrm{d}\, \lambda \qquad j = 1, \ldots, n$$

"Dividing" by $\mathrm{d}\,\lambda$ yields:

$$\sum_{i=1}^{n} A_{ji} \frac{\mathrm{d}\, x_i}{\mathrm{d}\, \lambda} = -\frac{\partial f_j}{\partial \lambda}$$

This is a linear equation for the unknowns $\left\{\frac{\mathrm{d}\, x_i}{\mathrm{d}\, \lambda}\right\}$. It has a unique solution iff all eigenvalues of the matrix A are nonzero. This unique solutions leads to an ordinary differential equation:

$$\frac{\mathrm{d}\, x_i}{\mathrm{d}\, \lambda} = c_i(\mathbf{x}, \lambda)$$

By integrating this ODE, it is possible to determine the zeros of f in dependence on λ. Solving this ODE is especially easy as $|f|$ supplies a criterion about how large the error in x is. If it becomes too large, the value of x can be improved by application of a standard root-finding algorithm to f.

As this short introduction has shown, it is easy to continue a branch of fixed points of a dynamical system as long as there are no bifurcation points on that branch.[15] Continuation involves, in addition to that, finding bifurcation points along the branch and determining new branches of fixed point bifurcating in computed points. Please refer to [Khi90, Par89, All90] for more information on this subject.

---

[14] A "real" Hopf bifurcation has two imaginary eigenvalue x and $-x$, a "imaginary" Hopf has two real eigenvalues x and $-x$.

[15] Apart from the Hopf bifurcation, which is a bit more difficult to handle in this context, all bifurcations have at least one eigenvalue 0.

Chapter 3

Model

This thesis investigates the vertical transport of electrons in semiconductor superlattices. It continues on earlier work done at this institute. The model used in this thesis was developed by F. Prengel and is published in [Pre94a, Pre94b].

3.1 Introduction

Semiconductor superlattices are heterostructures consisting of two different semiconductor materials, for example $GaAs$ and $AlAs$. Layers of these two materials are alternately deposited on a wafer (Fig. 3.1). Contacts are applied to both ends (which are due to technical reasons usally different [Gra92, Sch96c, Gra95a]). All layers of a particular material (are intended to) have the same thickness. The growth direction is usually referred to as z-direction.

The two semiconductor materials, here $AlAs$ and $GaAs$, have a different band gap. This leads to discontinueties in the conduction and the valence band. The distribution of the difference of the band gaps among conduction and valence band is difficult to compute and it is thus determined from experimental data. In the model developed by Prengel, holes and thus the valence band are not considered as the holes are much heavier than the electrons and, as the superlattices in question are n-doped, of far smaller number. The situation is then the one depicted in Fig. 3.2:

The conduction band energy in $AlAs$ is higher than the one in $GaAs$ by V_0. If the electron energies are not too high, electrons cannot move freely in $AsAs$ but can in $GaAs$. The electron wavefunctions in the $AlAs$-layers (of width b) are thus damped exponentially which leads to the term *barrier* for the $AlAs$-layers. The electrons are able to move freely perpendicular to the growth axis in the $GaAs$-layers of width l (“two-dimensional quasi-free electron gas”).

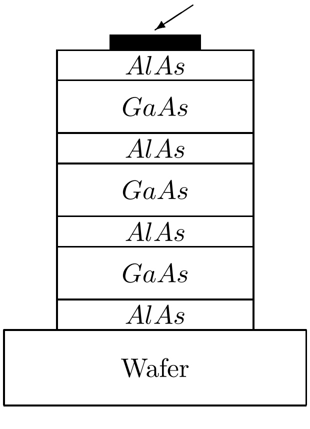

Figure 3.1: Schematic structure of a semiconductor superlattice. It consists of two different semiconductor materials, in this case $AlAs$ and $GaAs$, which are alternately deposited on a wafer. All layers of a particular material have (or rather, should have) the some thickness.

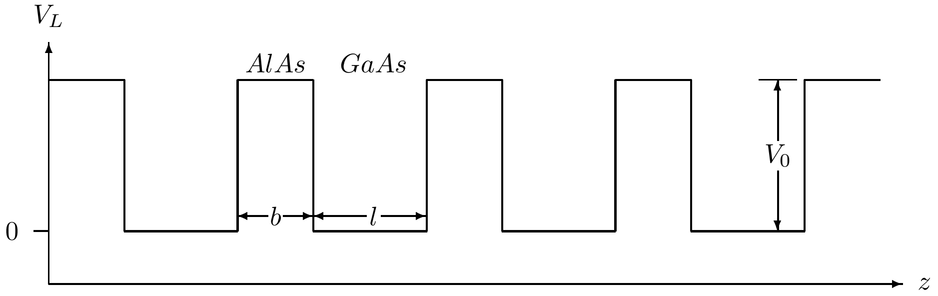

Figure 3.2: Structure of the conduction band in a semiconductor superlattice. The conduction band is higher in $AlAs$ than in $GaAs$ so that electrons with certain energies can move freely in the $GaAs$-layers but not in the $AlAs$-layers. The $AlAs$-layers thus act as barriers whereas there are bound states (in z-direction) in the $GaAs$-"quantum wells".

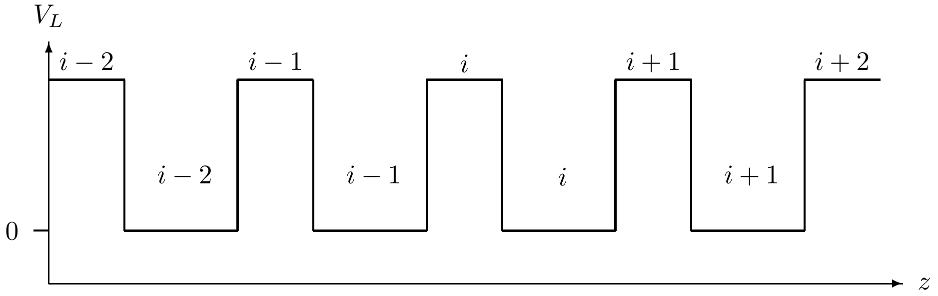

Figure 3.3: Numbering scheme for the quantum wells and the barriers. The barrier with index i lies between the $(i-1)$-th and the i-th quantum well.

This movement is of no further interest in a model describing only vertical transport.[1] The movement of electrons in the z-direction is confined by the barriers to a small region called *quantum wells* after the shape of the conduction band.

Let us assume that the barriers were infinitely high. Then we would have the standard textbook problem of a confined particle. As long as we restrict ourselves to one dimension, i. e. the z-direction, only discrete values of the energy are allowed. The number of possible solutions of the corresponding Schrödinger-equation depends on the well depth, V_0, and its width; typically, it is between 2 and 6. Of course, the actual barriers are only of finite thickness. Still, it makes sense to think of bound or at least localised states[2].

The entire superlattice consists of N quantum wells. The wells are numbered starting with 1; thus, their indices go from 1 to N. The barriers lying between the quantum wells are numbered corresponding to the following scheme: The i-th barrier lies between the $(i-1)$-th and the i-th quantum well. Thus, there are barriers with indices 1 to $N+1$ if the barriers at the boundaries of the superlattice are included (see Fig. 3.3).

3.2 Transition rates

As has already been mentioned in the preceding section, it makes sense to think of electrons as being localised in a particular quantum well. The basic idea behind the model of PRENGEL is that each electron is located in a particular energy level (subband) of a particular quantum well. Transport is then described by electrons leaving one state and entering another one. The

---

[1] To do this, the Hamiltonian has to be split into two parts: one involving only vertical effects and one involving only parallel effects. Strictly, this is only allowed if there is no scattering between these two operators. We have to be a bit more practical as we cannot proceed without this approximation.

[2] This seems to contradict the existence of minibands. However, one has to remember that it takes very long for a wave function, which was prepared to be localised in a particular quantum well, to smear out over the entire superlattice.

transition rates can then be calculated, for example, by perturbation theory. Thus, it is sufficient to know the number of electrons in each energy level of each quantum well to completely describe the state, in which the system is.[3]

In the model of PRENGEL, only the two lowest energy levels are included,[4] as higher energy levels are not occupied significantly. One energy level alone does not suffice as it cannot explain the necessary region of negative differential conductivity in the homogeneous current-voltage characteristic. $n_1^{(i)}$ is the electron density in the lower energy level of the i-th quantum well, $n_2^{(i)}$ the density in the upper level.

By applying an external voltage, U, to the sample and/or by formation of charge accumulation regions, an electric field forms in the superlattice. The value of the electric field over the i-th barrier is labelled $F^{(i)}$. As there are no (free) electrons in the barriers, the electric field cannot change in the barriers but only in the quantum wells.

Since there is frequent scattering, only transport between adjacent quantum wells has to be considered. The different transport processes are summarised in Fig. 3.4.

When calculating the transition rates, we assume that the conduction band is not degenerate.[5] Thus, each transition rate may be written as product of a *transport coefficient* and the electron density in the initial state. The transport coefficients depend – apart from the hetero-parameters (geometry and semiconductor properties) – only on the electric field over the particular barrier. We will use the same symbol for the transport coefficient and the transport process, that is, $R_2^{(i)}$ represents the transport coefficient as well as the transport process. The transport processes R_1 and R_2 (between "equivalent" subbands) are modelled by miniband conduction, the processes X and Y (between "different" subbands) by (explicit) resonant tunnelling.

As non-degeneracy is assumed, the transport process $R_2^{(i+1)}$ will result in the following terms in the differential equations that described the dynamics of the $\left\{n_1^{(i)}\right\}$ and $\left\{n_2^{(i)}\right\}$ (correspondingly for R_1):

$$\begin{aligned} \dot{n}_2^{(i)} &= \cdots - R_2^{(i+1)} n_2^{(i)} \\ \dot{n}_2^{(i+1)} &= \cdots + R_2^{(i+1)} n_2^{(i)} \end{aligned}$$

The i-dependence of the transport coefficients $R_2^{(i)}$ is just determined by the values of the electric field $F^{(i)}$ over the different barriers i. Thus, we can define $R_2^{(i)} := R_2\left(F^{(i)}\right)$ with $R_2(F)$ describing the effectiveness of miniband conduction as a function of the electric field.

We still have to take into account that miniband conduction happens only in field-direction. The formulas given are thus valid only if the electric field is positive (pointing towards the "right"). If the field is inverse, the transport coefficient has to be multiplied with $n_2^{(i+1)}$ instead of $n_2^{(i)}$ as the roles of initial and final state are exchanged. Since there is no preferred direction in the superlattice, the value of $R_2(F)$ must not change if the sign of F is inverted. For convenience, we allow only positive arguments for $R_2(F)$ so $-F$ has to be used in the latter case. Using the Θ-function, which is 1 for positive argument and 0 otherwise, we can write the equations "more correctly" as:

$$\begin{aligned} \dot{n}_2^{(i)} &= \cdots - R_2\left(F^{(i+1)}\right) n_2^{(i)} \Theta\left(F^{(i+1)}\right) + R_2\left(-F^{(i+1)}\right) n_2^{(i+1)} \Theta\left(-F^{(i+1)}\right) \\ \dot{n}_2^{(i+1)} &= \cdots + R_2\left(F^{(i+1)}\right) n_2^{(i)} \Theta\left(F^{(i+1)}\right) - R_2\left(-F^{(i+1)}\right) n_2^{(i+1)} \Theta\left(-F^{(i+1)}\right) \end{aligned}$$

---

[3] The opposite ansatz is to calculate electron wavefunctions extending through the entire superlattice (This is used, for example, to describe the double barrier resonant tunnelling device). There are two reasons why this is not advisable/necessary for superlattices: We are only interested in weakly coupled superlattices, that is, superlattices with wide barriers. Furthermore, heavy doping leads to frequent scattering at the doping atoms. Even if a particular scattering mechanism conserves the energy of the scattered electrons, their phase correlation is still destroyed.

[4] There are a few problems if additional energy levels are to be included in this model [Sch95b, appendix F]: For high voltage, the calculated current density may become negative. The reason for this might be that same of the assumptions made in this model are (even) less valid for higher energy levels. In addition, this model includes no mechanism to explain a background that increases with increasing voltage.

[5] This assumptions is only poorly fulfilled. However, the error caused by it is much smaller than that caused by some of the other assumptions made in this model.

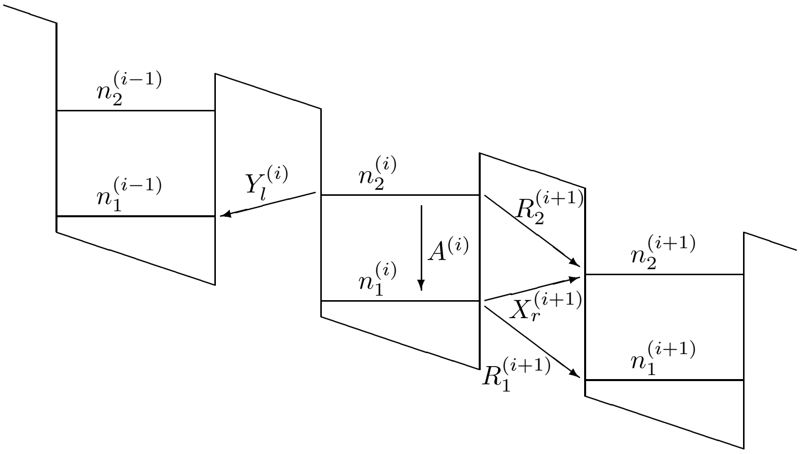

Figure 3.4: The transport coefficients R_1 and R_2 for transport between equivalent energy levels are modelled by miniband conduction [Ign91] whereas the coefficients X and Y are calculated from perturbation theory. A is assumed to be constant. The transition rates are simply the product of the transport coefficient and the electron density in the initial state as non-degeneracy is assumed. Through each barrier, there are two X- and two Y-transport processes. Only one of these four is indicated in each barrier.

Next, we have to deal with transport between different subbands. These transport processes have been marked with X and Y. X corresponds to a transport from a lower to an upper energy level, Y to a transport from an upper to a lower level. Resonant tunnelling is allowed also opposite the direction of the electric field; furthermore, this model assumes that electrons might even tunnel into a state whose energy is higher than that of the initial state.[6]

Thus, there are four transport processes modelled by resonant tunnelling through each barrier, of which only one is depicted in each barrier in Fig. 3.4. Through the $(i+1)$-th barrier, there are the transport processes $X_r^{(i+1)}$ ("r" for "to the right") from $n_1^{(i)}$ to $n_2^{(i+1)}$, $X_l^{(i+1)}$ from $n_1^{(i+1)}$ to $n_2^{(i)}$, $Y_r^{(i+1)}$ from $n_2^{(i)}$ to $n_1^{(i+1)}$ and $Y_l^{(i+1)}$ from $n_2^{(i+1)}$ to $n_1^{(i)}$. As has been the case for miniband conduction, it is sufficient to consider only two functions $X(F)$ and $Y(F)$. The corresponding transport coefficients for transport to the left and to the right differ in the sign of their argument, which may now be positive as well as negative. We will use the convention adapted in [Pre94a], which is a bit asymmetrical in that $X_r^{(i)} := X\left(F^{(i)}\right)$ but $Y_l^{(i)} := Y\left(F^{(i)}\right)$. The terms involving, for example, the transport from or to $n_2^{(i)}$ then read:

$$\begin{aligned}
\dot{n}_1^{(i-1)} &= \cdots + Y\left(F^{(i)}\right) n_2^{(i)} - X\left(F^{(i)}\right) n_1^{(i-1)} \\
\dot{n}_2^{(i)} &= \cdots - Y\left(F^{(i)}\right) n_2^{(i)} + X\left(F^{(i)}\right) n_1^{(i-1)} + X\left(-F^{(i+1)}\right) n_1^{(i+1)} - Y\left(-F^{(i+1)}\right) n_2^{(i+1)} \\
\dot{n}_1^{(i+1)} &= \cdots - X\left(-F^{(i+1)}\right) n_1^{(i+1)} + Y\left(-F^{(i+1)}\right) n_2^{(i+1)}
\end{aligned}$$

The functions $R_1(F)$, $R_2(F)$, $X(F)$ and $Y(F)$, that is, the physics behind the transport processes, are given in appendix G. The transport coefficient $A^{(i)}$, representing inter-subband relaxation, is modelled by a constant relaxation time τ. Combining all terms yields the complete dynamical equations for the electron densities:

$$\dot{n}_1^{(i)} = \frac{1}{\tau} n_2^{(i)}$$

---

[6] If we would use resonant tunnelling to also model transport between equivalent energy levels, no "directed" transport would be possible as the transport coefficients for both directions would be the same.

$$
\begin{aligned}
&-X\left(-F^{(i)}\right)n_1^{(i)}+Y\left(-F^{(i)}\right)n_2^{(i-1)}+Y\left(F^{(i+1)}\right)n_2^{(i+1)}-X\left(F^{(i+1)}\right)n_1^{(i+1)}\\
&-R_1\left(F^{(i+1)}\right)n_1^{(i)}\Theta\left(F^{(i+1)}\right)+R_1\left(-F^{(i+1)}\right)n_1^{(i+1)}\Theta\left(-F^{(i+1)}\right)\\
&+R_1\left(F^{(i)}\right)n_1^{(i-1)}\Theta\left(F^{(i)}\right)-R_1\left(-F^{(i)}\right)n_1^{(i)}\Theta\left(-F^{(i)}\right)\\
\dot{n}_2^{(i)} = {}&-\frac{1}{\tau}n_2^{(i)}\\
&-Y\left(F^{(i)}\right)n_2^{(i)}+X\left(F^{(i)}\right)n_1^{(i-1)}+X\left(-F^{(i+1)}\right)n_1^{(i+1)}-Y\left(-F^{(i+1)}\right)n_2^{(i+1)}\\
&-R_2\left(F^{(i+1)}\right)n_2^{(i)}\Theta\left(F^{(i+1)}\right)+R_2\left(-F^{(i+1)}\right)n_2^{(i+1)}\Theta\left(-F^{(i+1)}\right)\\
&+R_2\left(F^{(i)}\right)n_2^{(i-1)}\Theta\left(F^{(i)}\right)-R_2\left(-F^{(i)}\right)n_2^{(i)}\Theta\left(-F^{(i)}\right)
\end{aligned}
$$

In the following chapters, we will sometimes combine the electron densities $\left\{n_1^{(i)}\right\}$ and $\left\{n_2^{(i)}\right\}$ into a single vector $\mathbf{n}$. The rate equation above can then be written in the form of a multiplication of $\mathbf{n}$ with a matrix f:

$$\dot{\mathbf{n}} = f(\mathbf{n}) \cdot \mathbf{n}$$

$f(\mathbf{n})$ is a function of only the electric fields $\mathbf{F}$, and thus depends on $\mathbf{n}$ only via Poisson's equation. We can thus also write $f(\mathbf{F})$ with $\mathbf{F} = \mathbf{F}(\mathbf{n})$ where the dependence on the applied external voltage has been neglected.

Sometimes, the distinction between transition coefficients and electron densities might not be necessary. We can then write even shorter $\mathbf{n} = f(\mathbf{n})$ with a function $f : \mathbb{R}^N \rightarrow \mathbb{R}^N$ (in contrast to the preceding paragraph where $f : \mathbb{R}^N \rightarrow \mathbb{R}^{2N}$).

3.3 Field Distribution

By doping the superlattice, there are immobile donor atoms in the quantum wells as well as free electrons. We assume that the donor atoms and all (free) electrons are located in the centre of a quantum well;[7] we therefore have to consider the charge per unit area, σ, instead of the charge per unit volume, ρ (the conversion is $\sigma = l\rho$). Due to this assumptions, the electric field may jump only at the centres of the quantum wells and has to be constant otherwise, especially in the barriers.

The electric field $\left\{F^{(i)}\right\}$ can be calculated from the discrete version of Poisson's equation:

$$\epsilon\left(F^{(i+1)} - F^{(i)}\right) = \sigma_i = l\rho_i$$

Charge accumulations in the superlattice cause changes in the electric field and thus cause an internal potential which has to be equal to the *applied external voltage*, U:[8]

$$\sum_{i=1}^{N+1} F^{(i)}(N+1-i)l = U \tag{3.1}$$

The charge density ρ_i is the difference between the density of electrons in that particular quantum well and the density of donor atoms:

$$\rho_i = n_1^{(i)} + n_2^{(i)} - N_D$$

with the *doping density* N_D. This is the only formula that includes N_D even though the doping density is the most important parameter of the system. This demonstrates how important the global coupling due to equation (3.1) really is.

---

[7] Quite often, only a small part of the superlattice is doped ("δ-doping") in superlattices grown experimentally [Gra92]. The values of the doping densities given in this thesis are 3D-concentrations averaged over the entire quantum well. For electrons, this assumptions is rather crude. On the other hand, we are not interested in the distribution of electrons along each quantum well. This might be necessary if we were to include the effects at the boundary between two different semiconductor materials. These are not (too) important as – in contrast to, for example, a single *p*-*n*-junction – there is no intrinsic potential between both sides of the superlattice. Side effect of this assumption is that the Fermi-level is not affected by an applied external voltage (apart from the explicit shift by the applied external voltage).

[8] The question, whether we have to include the barriers at the boundary of the superlattice, is hard to answer. However, the results do not depend on the choice made.

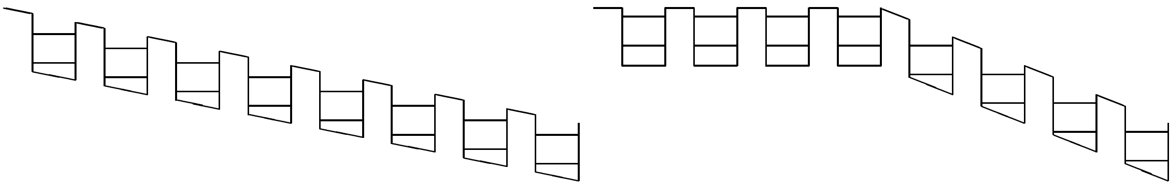

(a) Homogeneous state

(b) Field domains

Figure 3.5: Field distribution in the superlattice. The difference in "height" between the left and the right side of the superlattice is determined by the applied external voltage. There are two possibilities how this difference may be distributed along the superlattice: **(a)** If the field distribution is homogeneous, the electric field strength has the same value everywhere in the superlattice. Resonant tunnelling between adjacent quantum wells is not possible. **(b)** If there are field domains, the value of the electric field in one part of the superlattice is so high that resonant tunnelling between different energy levels is possible while in the other part resonant tunnelling between equivalent energy levels may happen.

3.4 Current Density

With the equations given so far, the dynamics of the system are completely described. For comparison with experimental data, however, the most important quantity is not the electron density profile or the field profile but rather the current flowing through this superlattice. Of course, with a one-dimensional model, it is only possible to determine the *current density* j (per unit area). If, for example, the i-th barrier is considered, the current $j^{(i)}$ through this barrier is given by:

$$\begin{aligned}
\frac{1}{e}j^{(i)} \quad = \quad & + \left[R_1\left(F^{(i)}\right)n_1^{(i-1)} + R_2\left(F^{(i)}\right)n_2^{(i-1)}\right]\Theta\left(F^{(i)}\right) \\
& - \left[R_1\left(-F^{(i)}\right)n_1^{(i)} + R_2\left(-F^{(i)}\right)n_2^{(i)}\right]\Theta\left(-F^{(i)}\right) \\
& + \left[X\left(F^{(i)}\right)n_1^{(i-1)} + Y\left(-F^{(i)}\right)n_2^{(i-1)}\right] - \left[X\left(-F^{(i)}\right)n_1^{(i)} + Y\left(F^{(i)}\right)n_2^{(i)}\right]
\end{aligned}$$

The four square brackets have the following meaning: The first two describe the (particle) current density due to miniband conduction. If the field is positive, electrons are transported from the "left" to the "right", and the current density is positive by definition. The other two brackets describe the (particle) current density due to resonant tunnelling between different energy levels. Electrons transported from "left" to "right" result in a positive current, electrons transported in the "wrong" direction in a negative current.

The current densities through different barriers may be different for instationary processes as charge carriers may accumulate in some part of the superlattice and thus lead to a current through only some barriers. If the displacement current is included, the total current is the same through all barriers even in the instationary case [Wac93, Sch95a].

3.5 Field Domains

Finally, we want to discuss what behaviour we might expect from a superlattice:

It is obvious that electrons are transported more efficiently from one quantum well into the adjacent well if there are many free states in the "target" well at the "right" energy, that is, if there is another energy level/subband. This is the case for very small electric field; correspondingly, miniband conduction is very good. Furthermore, it is the case when the electric field is equal to the *resonance field strength* F_{res}, at which the lower energy level in a particular quantum well is aligned with the upper one in the adjacent well.

One could say that the superlattice "wants" to reach a state in which all transition rates are as large as possible. The result of this shall be discussed with the help of Fig. 3.5. Depicted are two different configurations of the field profile for the same superlattice. The shift between both ends of the superlattice is determined by the applied voltage and is the same in both subfigures. In Fig. 3.5(b), the electric field is uniform throughout the superlattice. There are no resonances of the type described in the preceding paragraph. The other possibility, the formation[9] of *field domains* like in Fig. 3.5(b) allows such resonances. In one part of the superlattice, the electric field is approximately given by the resonance field F_{res} (*high-field domain*) whereas the field in the other part is almost zero (*low-field domain*). For the homogeneous case, the electric field throughout the superlattice is directly proportional to the applied voltage. For field domains, the electric field in the two domains does not change much when the applied voltage is changed but the sizes of the two domains do.

3.6 Boundary Conditions

Until now we have not discussed the proper choice of boundary conditions. For most problems dealing with modelling semiconductor devices, it is a good assumption that a plane wave enters the device at one end. This is not possible in our model as we are considering electron densities and not wave functions. We thus need to know how the dynamical equations for the first and the N-th quantum well have to be altered.

The modelling of contacts is often more difficult than to describe what happens in the device itself. Even experimentally, the making of contacts is still some kind of “alchemy” – at least, it is less understood than growing the superlattice itself. Thus, we do not even try to give a physical justifications for the choice of boundary conditions. “Good” contacts are contacts that lead to the desired (expected) results. Of course, this can only be decided if the results from the following chapter on unperturbed superlattices are already known.

We model contacts as follows: At each boundary of the superlattice, we affix an additional “virtual” quantum well (their indices are 0 and $N+1$). The transition rates through the first and the $(N+1)$-th barrier respectively are calculated using the formulas derived above. However, the electron densities in the virtual wells are not changed by the transport processes but are determined by some other formula.

We assume that the electron densities in the virtual quantum wells depend only on the electron densities in the adjacent “real” wells. As we have no physical description, we just assume that this dependence is linear. Then, we can write the electron densities in the virtual wells as:

$$
\begin{aligned}
n_1^{(0)} &= c_1 \cdot n_1^{(1)} + c_2 \cdot N_D &\qquad n_1^{(N+1)} &= c_1 \cdot n_1^{(N)} + c_2 \cdot N_D \\
n_2^{(0)} &= c_1 \cdot n_2^{(1)} + c_3 \cdot N_D &\qquad n_2^{(N+1)} &= c_1 \cdot n_2^{(N+1)} + c_3 \cdot N_D
\end{aligned}
$$

By varying the three constants c_1, c_2 and c_3, we are able to describe all possibilities (or rather, all possibilities symmetrical with respect to both contact layers[10]) that are compatible with our assumptions. Furthermore, we may neglect c_3 as electrons starting in the upper energy level will soon have relaxated into the lower level. Thus, we could have put them in the lower energy level in the first place.

The choice of a suitable boundary condition is thus reduced to the problem of choosing two constants, c_1 and c_2. We then have to decide in simulations or other numerical computations[11] which boundary conditions are “the best”. This

---

[9] We will not discuss at this point whether the high-field domain should be on the right or the left side. Our arguments apply to both cases.

[10] One could try to use different choices for each boundary layer. This would correspond to superlattices investigated experimentally. Their contacts are usually quite different [Gra92, Sch96c, Gra95a]. However, this is making the problem more complicated than it is. Electrons move mainly in field direction. Therefore, the boundary condition on the “exit-side” is of minor importance.

[11] *Simulations* are computer experiments, that is, we see (or rather, should see) precisely the same things as in an equivalent experiment – it is just easier to “measure” quantities like the electric field on a computer. *Numerical computations* include all kinds of algorithms giving us insight into the problem we want to examine. This includes, among others, the calculation of unstable branches and bifurcation points.

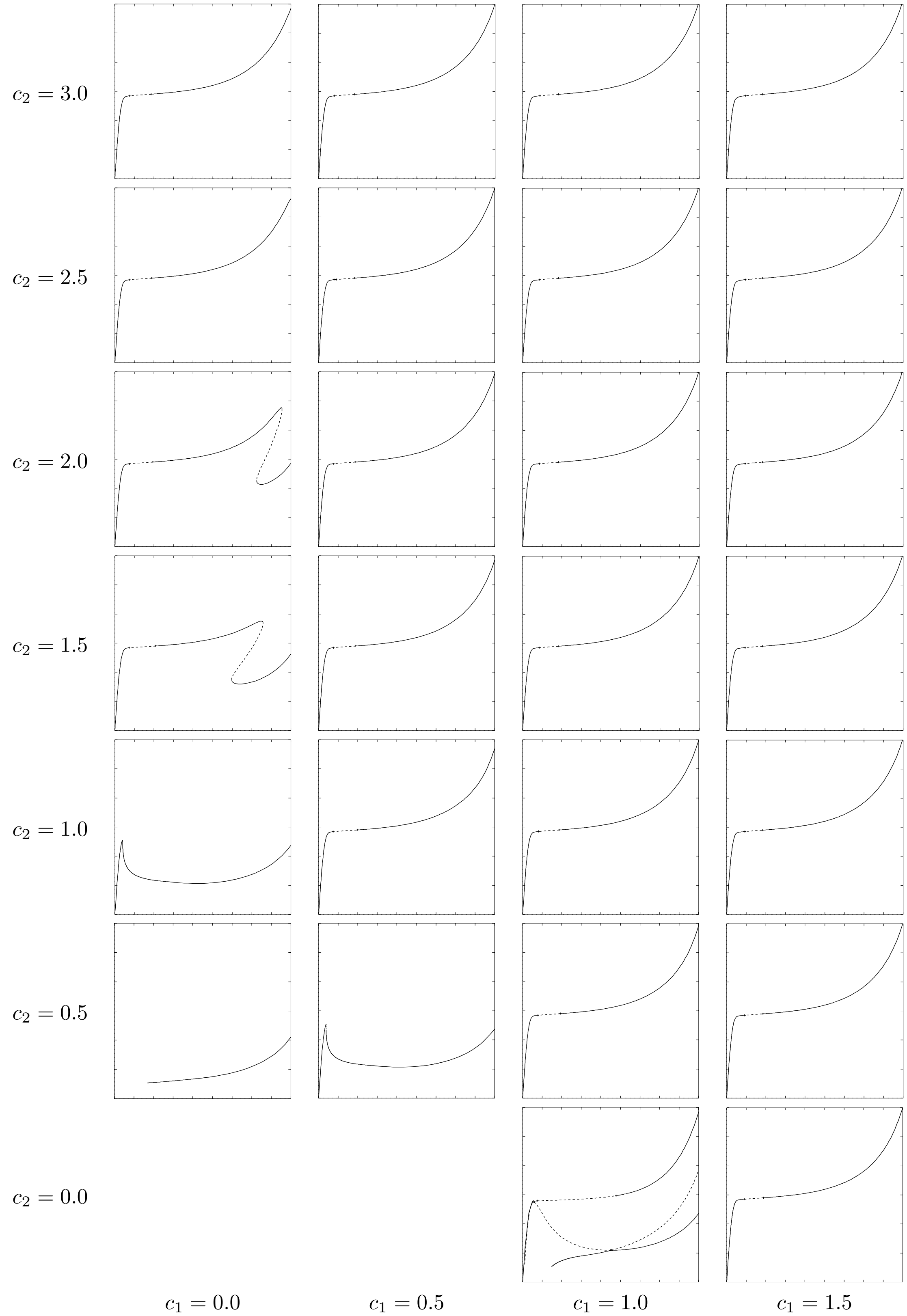

Figure 3.6: Current-voltage characteristics for different boundary conditions at a doping density of $N_D = 3 \cdot 10^{17}\ \mathrm{cm}^{-3}$. c_1 and c_2 are explained in the text. x-axis: U [V], one tic corresponds to 0.5 V; y-axis: j [kA/cm^2], one tic corresponds to $0.05\ \mathrm{kA/cm}^2$.

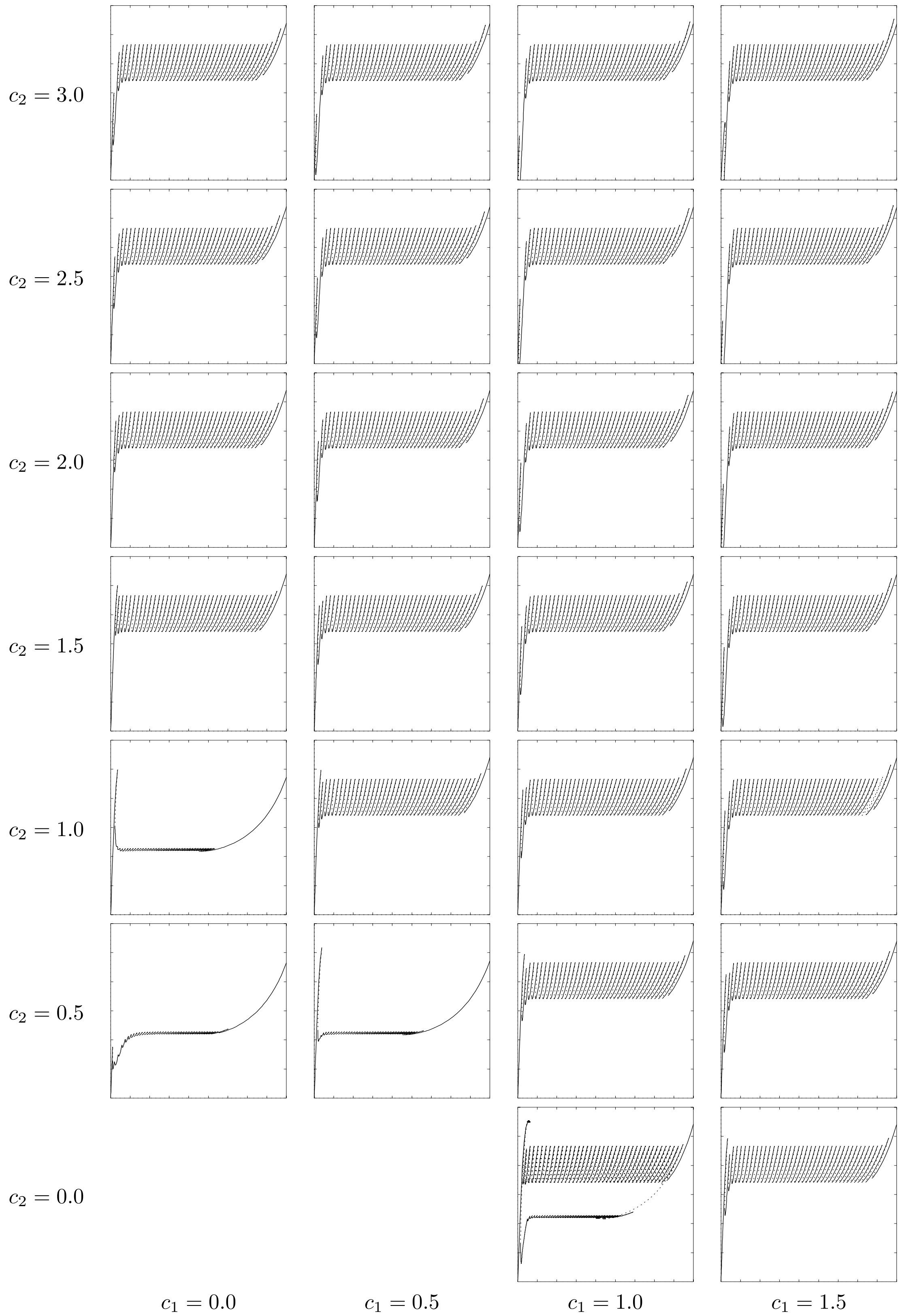

Figure 3.7: Current-voltage characteristics for different boundary conditions at a doping density of $N_D = 6 \cdot 10^{17}$ cm^{-3}. c_1 and c_2 are explained in the text. x-axis: U $[\mathrm{V}]$, one tic corresponds to 0.5 V; y-axis: j $[\mathrm{kA/cm^2}]$, one tic corresponds to 1 $\mathrm{kA/cm^2}$.

has been done for two values of the doping density. In Fig. 3.7, the results are depicted for a doping density high enough for branches to form whereas the doping density in Fig. 3.6 allows oscillations (for most of the values of c_1 and c_2 tested). The oscillations itself are not depicted, however, the unstable branch they bifurcate from is.

The results for the different choices of c_1 and c_2 can be divided into four groups: If c_1 and c_2 are too small, no sensible stationary state is possible as all electrons in the superlattice have a tendency to flow out of the superlattice into the contact layers. Thus, no figure can be shown. If the constants are a bit higher, a stationary state exists. However, it is not possible for a charge accumulation to form (remember that the charge accumulation has to start at one contact); thus, there are no (or only very small) branches in the current-voltage characteristic. There is one additional special case, $c_1 = 1$ and $c_2 = 0$, which is discussed in chapter 7. These boundary conditions have been used, for example, in [Pre94a, Pre94b].

The characteristics for most other values of c_1 and c_2 look almost the same. Some have an additional branch; however, this is no physical effect: All current-voltage characteristic have been calculated up to a voltage of 4.5 V. If this additional branch starts at a voltage higher than 4.5 V it is not depicted, even if part of it extends down to U smaller than 4.5 V. The exact choice of c_1 and c_2 is not important; I used $c_1 = 0$ and $c_2 = 2$ as in [Pat95]. Choosing a high value for c_2 can be interpreted as modelling the contacts as carrier reservoirs made by heavily doping the contact layers.

The two boundary conditions mentioned explicitly are the discrete versions of Dirichlet and Neumann boundary conditions. For some aspects, this “mathematical” point of view is helpful for Neumann boundary conditions (for example, to discuss the possibility of a truly homogeneous field profile). The Dirichlet boundary conditions should better be called “rigid” boundary conditions. Choosing $c_1 = 1$ and $c_2 = 2$ leads to the same results as $c_1 = 0$ and $c_2 = 2$ even though the former is no Dirichlet boundary condition.

Throughout most of this thesis, the “rigid” boundary conditions $c_1 = 0$ and $c_2 = 2$ are used; exceptions are marked in the text.

Chapter 4

Superlattices without Doping Fluctuations

The current-voltage characteristic of semiconductor superlattice differs quite substantially from the transmission characteristic of one single barrier (given, for example, by the $v(F)$-characteristic). The reason for this is the possibility that – as has already been discussed in section 3.5 – electrons may accumulate in particular quantum wells and thus form a spatial structure. The electrons necessary for this to occur are only available if the doping density N_D is sufficiently high.

For high doping density (a few times 10^{17} cm^{-3}), one gets the "typical current-voltage characteristic" (Fig. 4.2 on page 27). For a superlattice consisting of N quantum wells, the current-voltage characteristic is made up of approximately N stable branches connected by branches of unstable stationary states. The points at which a stable and a unstable branch join are saddle-node bifurcation points.

Current-voltage characteristics for different doping densities are depicted in Fig. 4.1. We will come back to these later in section 4.3. First, we want to discuss the two self-organised spatio-temporal structures that can be seen in these characteristics: First, there is the formation of branches[1] for high doping density; second, there are self-generated oscillations for medium doping.

4.1 Fully Developed Branches

As has already been mentioned, the current-voltage characteristic of a superlattice consists of approximately as many branches as there are quantum wells in the superlattice.[2] The stable branches, which can be reached in a simulation or an experiment, are connected by unstable stationary states ("unstable branches") thus making the entire current-voltage characteristic a single connected curve. The loss of stability at the end-points of each stable branch is caused by saddle-node bifurcation points. We will not discuss this bifurcation here as this has already been done in section 2.2.

Since the branches "turn" in the bifurcation points, the current-voltage characteristic exhibits multistability. Therefore, it is not sufficient to give only the voltage of a stable state if it is to be determined fully. Furthermore, if the applied voltage is increased monotonly, most quantities will show a discontinuity when the system jumps to a different branch at the end of the branch, on which the system is cur-

---

[1] Throughout this thesis, "branches" refers to the saw-blade pattern in the current-voltage characteristic. It can only be observed for sufficiently heavy doping. If we start with light doping and increase the doping density, these branches will form once the doping density becomes high enough. This process, *formation of branches* or *development of branches*, does not imply that there is threshold and once that threshold is reached, all branches will appear at once. As we will see later, the different branches appear at slightly different values of N_D.

Formation of branches is different from formation of domains. For the latter, it is only necessary to have a N-shaped $v(F)$-characteristic (see, for example, [Sch87, Sha92]), while branches additionally depend on the discrete structure of the superlattice. Domain formation is necessary for the formation of branches. However, no matter the small a charge accumulation might be, we already have field domains (at least from a mathematical point of view). For branches to develop, the field domains have to be multistable, which is only possible if all transport processes are discrete, and if the charge accumulations are large enough.

[2] The question is whether to include the "large branch" (at high voltage) as the mechanism causing this branch is different from that responsible for the other branches.

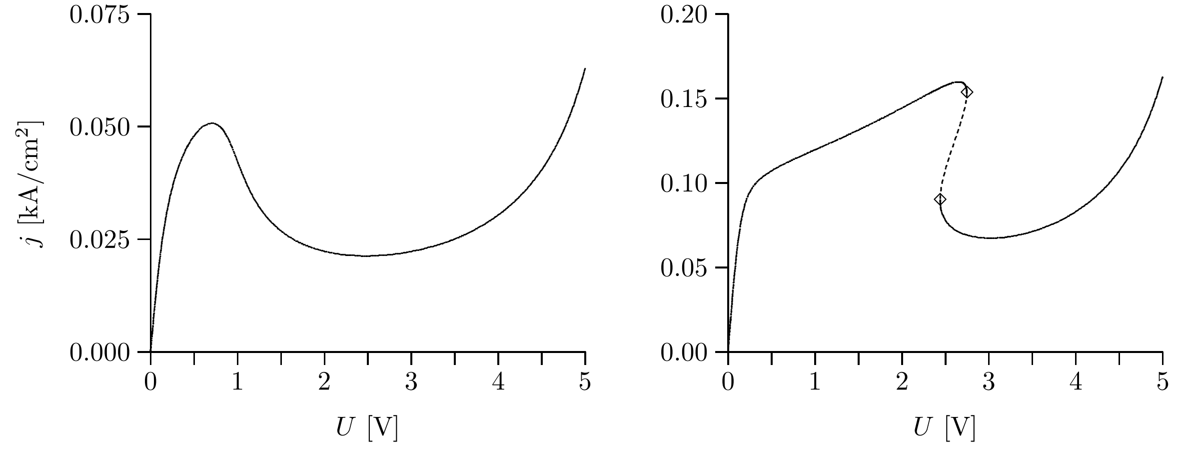

(a) $N_D \approx 3 \cdot 10^{15}$ cm^{-3} (b) $N_D \approx 10^{16}$ cm^{-3}

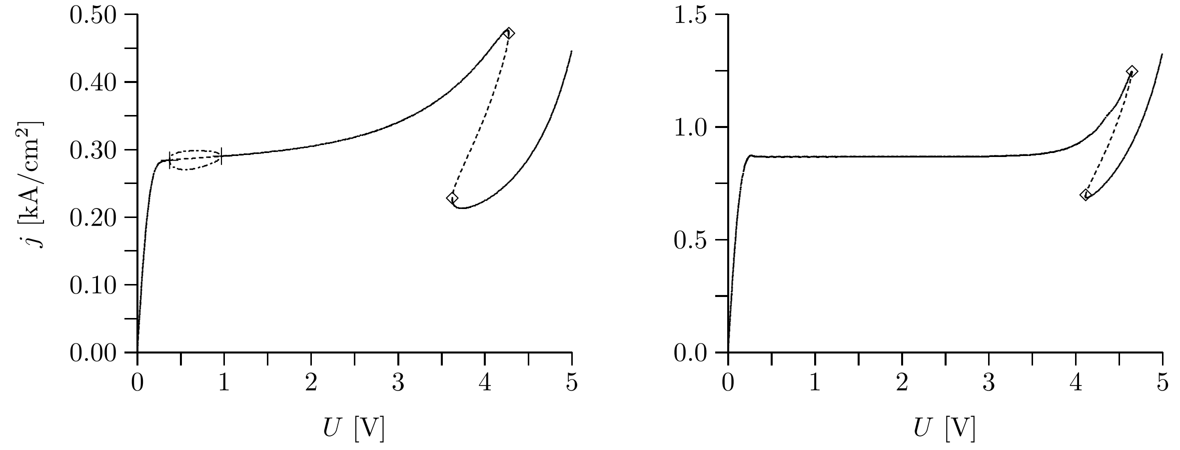

(c) $N_D \approx 3 \cdot 10^{16}$ cm^{-3} (d) $N_D \approx 10^{17}$ cm^{-3}

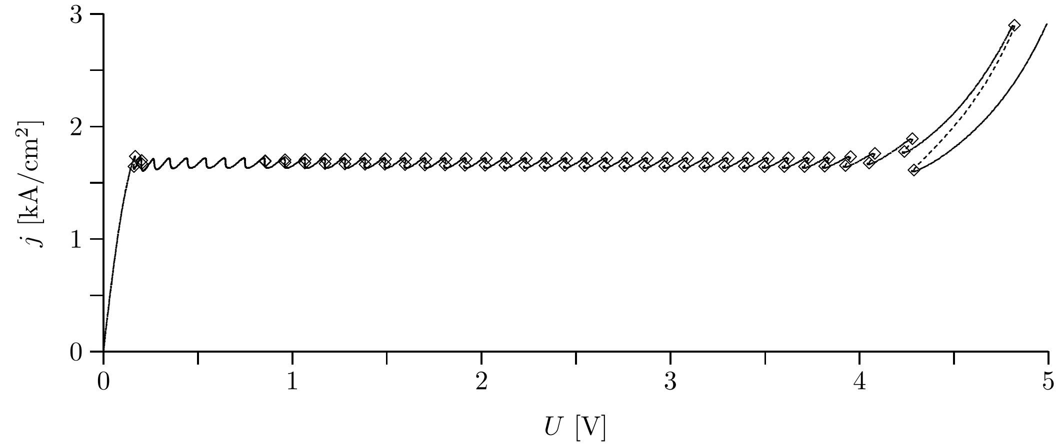

(e) $N_D \approx 2 \cdot 10^{17}$ cm^{-3}

Figure 4.1: Current voltage-characteristics for different doping density N_D. A characteristic with fully developed branches (=higher doping density) is depicted in Fig. 4.2.

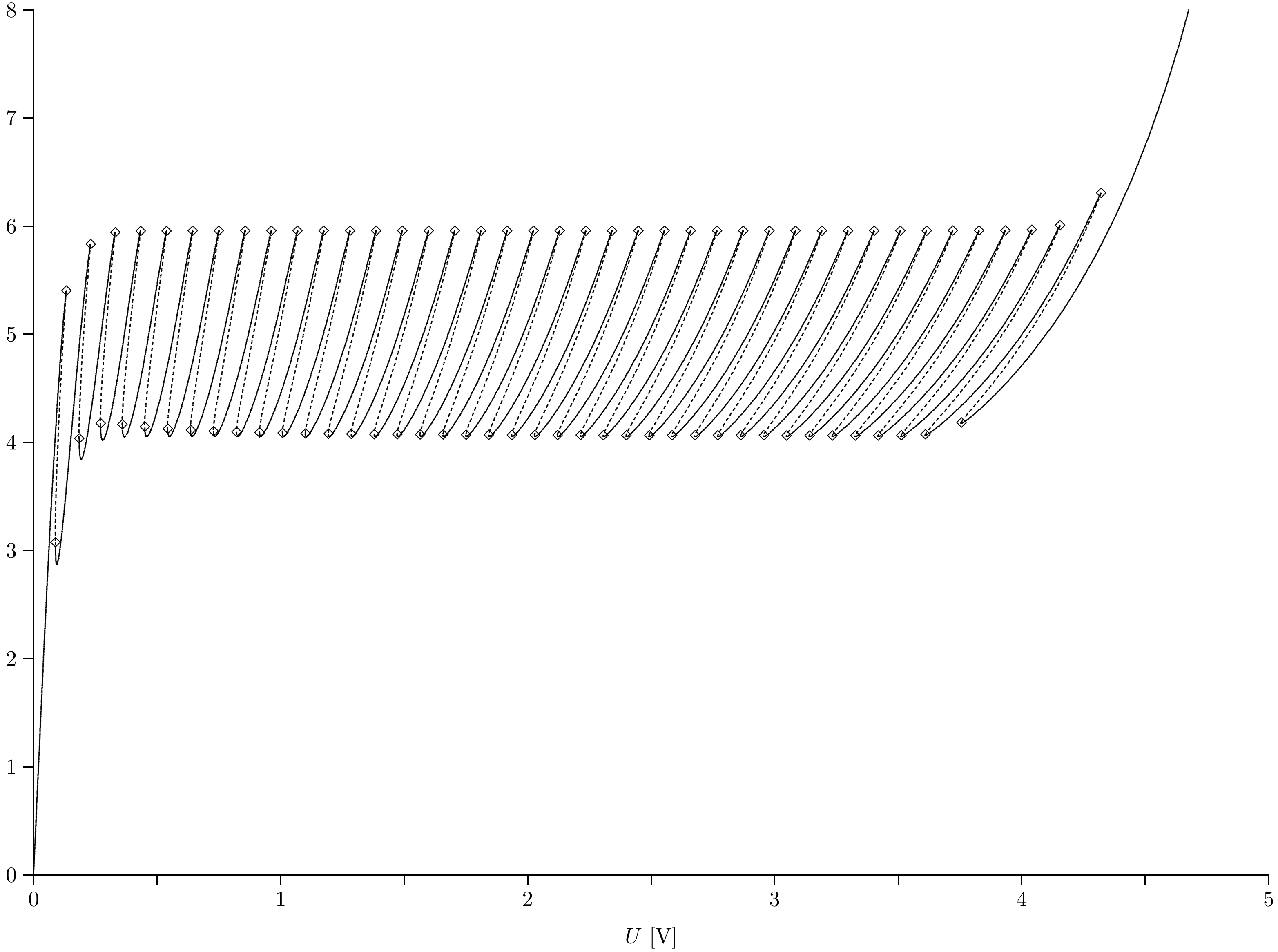

Figure 4.2: Full connected current-voltage characteristic for heavy doping.

rently. This problem can be solved by not using the voltage but the arc length as a parameter. This will be done throughout this thesis so the definition of "arc length" shall be given first:

The *arc length* used in this thesis is the one as seen in a j-U-diagram (that is, as seen in a current-voltage characteristic). The units chosen are kA/cm^2 and V. Comparing with Fig. 4.2, one can see that this definition of arc length corresponds approximately to the impression one gets from just seeing the current-voltage characteristic "on paper".

As has been known for some time now, the electric field in the superlattice is no longer uniform for sufficient doping. In its place, a low-field and a high-field domain form (see section 3.5): The value of the electric field is approximately zero in the low-field domain,[3] and a bit lower than the 1-2-resonance (that is, the value of the electric field for which the first (=lower) energy level in a particular quantum well is aligned with the second (=upper) in the adjacent well) in the high-field domain [Pre94a].

The field profile is depicted in Fig. 4.3(a) as a function of the arc length. One can clearly see that the high-field domain grows to occupy a higher portion of the superlattice when the voltage is increased. The small irregularities, for example the small "spikes" in the electron density profile (Fig. 4.3(b)), are a side effect of the method used for displaying the data: Sample points are taken equidistantly (as a function of arc length) along the current-voltage characteristic. The distance between two sample points is not correlated with the length of a particular branch. Therefore, the sample points taken on different branches are at different positions relative to that branch. This leads to small variations of the shape of the field profile and the electron density profile.

---

[3] Actually, its value is a bit larger than zero, and determined by the maximum of miniband conduction.

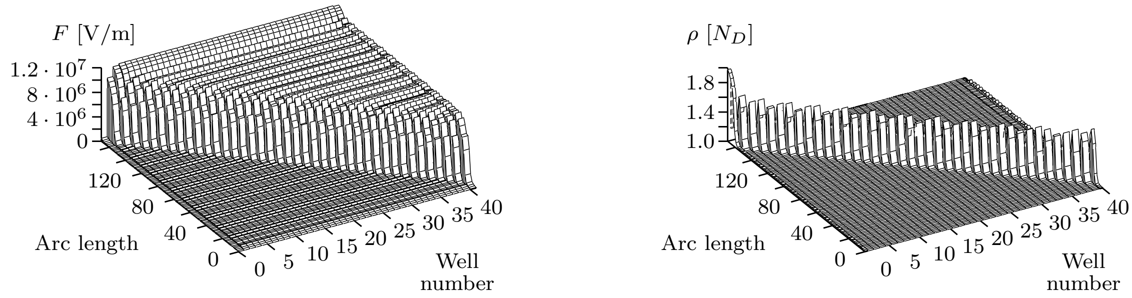

(a) Field profile

(b) Electron density profile

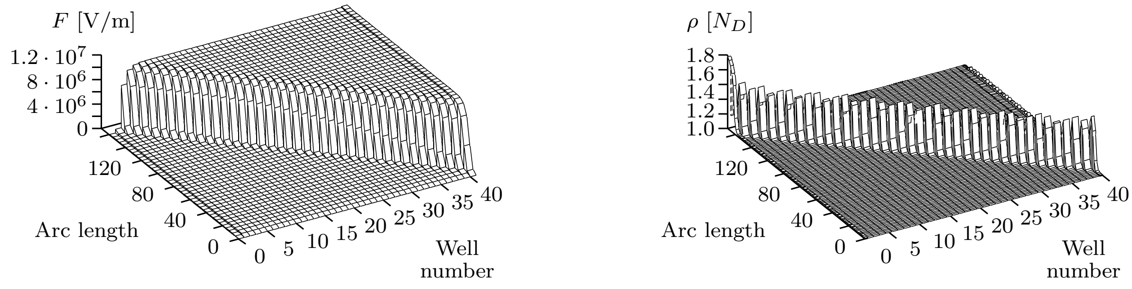

(c) Field profile (only upper bifurcation points)

(d) Electron densities (only upper bifurcation points)

Figure 4.3: Field profile and electron density profile along the current-voltage characteristic from Fig. 4.2 as a function of arc length. **(a)**, **(b)** The sample points used for the figure are distributed equidistantly along the characteristic. As the length of one branch is no integer multiple of this distance – this is impossible as the branches become longer for higher voltage – the sample points correspond to different points relative to each branch. As a result, artefacts can be seen in the figures. **(c)**, **(d)** These artefacts can be removed if only the upper saddle-node bifurcation points are considered.

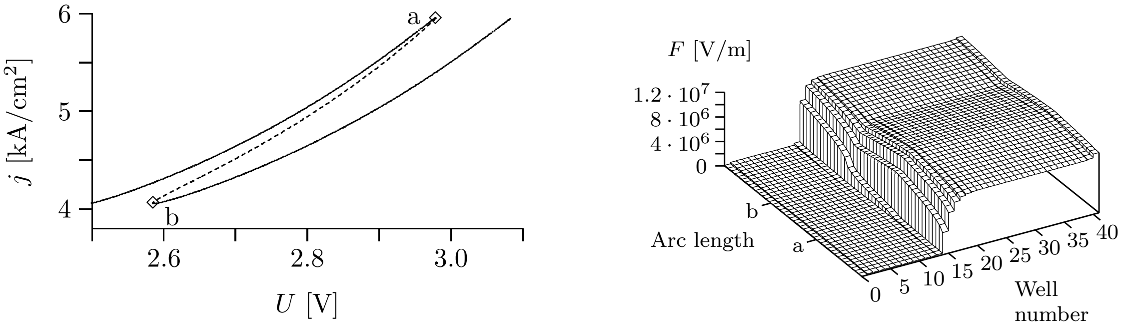

(a) Enlarged section of the characteristic

(b) Field profile

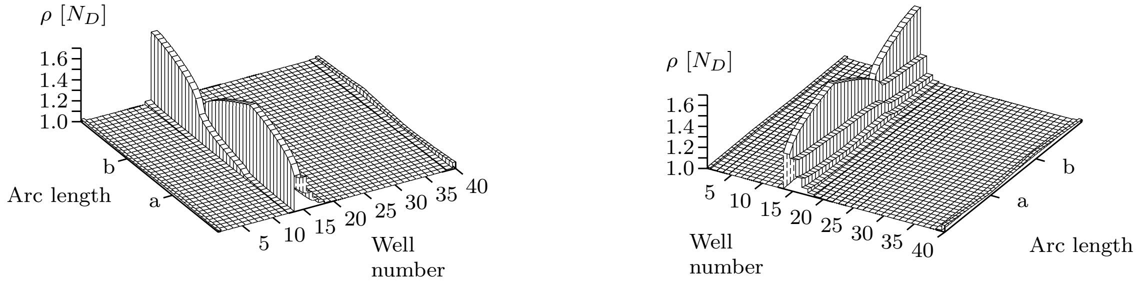

(c) Electron densities

(d) Electron densities

Figure 4.4: Changes in the electron configuration when a new branch is reached. **(a)** Enlarged section from Fig. 4.2. The two saddle-node bifurcation points important here are marked "a" and "b". **(b)** Field profile along the current-voltage characteristic depicted in subfigure a. The positions of the saddle-node bifurcation points have been indicated by "a" and "b". **(c), (d)** Electron density profile along the current-voltage characteristic. The same data is depicted in both subfigures.

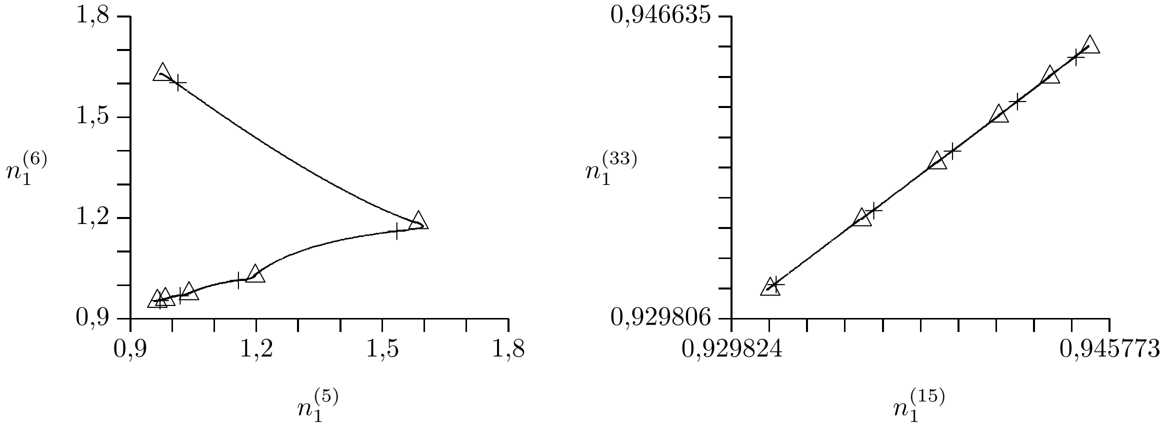

(a)

(b)

Figure 4.5: Unstable manifolds for $U = 3.8$ V. Depicted are the projections of the unstable manifolds of all fixed points onto the plane spanned by the electron densities in two different quantum wells.

If one wants to have a “better” figure, the following procedure has to be applied: One has to select one sample point for each branch which has to be at the same position relative to the branch in question. A drawback might be that there are only $N = 40$ sample points available now, and one has to interpolate. The choice of position relative to the branch is of rather small importance. For Figs. 4.3(c) and 4.3(d), the upper saddle-node bifurcation points have been used. The profiles are smoother now; in addition, it is easier to see how the value of the electric field increases once the high-field domain fills the entire superlattice.

As has been said before, the high-field domain has to extend with increasing voltage so as to make the interval voltage equal to the applied external voltage. The necessary movement of charge carriers can be no continuous process as the dynamics in a superlattice are discrete by nature. If electrons move into a new quantum well, a new branch is “reached”. An enlarged view of this process is shown in Fig. 4.4.

The figure depicts the transition from one (stable) branch to the next (stable) one. The saddle-node bifurcation points involved are marked “a” and “b”. The characteristic is unstable between these two points and stable otherwise. The positions of these two bifurcation points have also been indicated on the arc-length-axis of the three other subfigures. Along the stable branches, the field profiles are very “sharp”, that is, the domain boundary is confined to a single quantum well. In the centre of the unstable branch, the field profile and the electron density profile smear out a bit.[4]

The transition from one branch to the next is best seen in figures 4.4(c) and 4.4(d). In both figures, the same data is depicted; the viewing angles, however, are different. It can clearly be seen that the centre of the charge accumulation is shifted by one superlattice period.

The loss of stability at the end-points of a particular branch is caused by “standard” saddle-node bifurcations. This means that exactly one eigenvalue is greater than zero along the unstable branch, and that there is one unstable eigenvector along which the system leaves the neighbourhood of the unstable fixed point. This can be described more formally using unstable manifolds. For Fig. 4.5, a voltage of $U = 3.8$ V has been chosen as the slope of the branches is less steep for higher voltage and the number of branches is thus larger.

The unstable manifolds starting at a particular unstable fixed point run towards the two “neighbouring” stable fixed points. This means that for every initial condition in the “neighbourhood of the current-voltage characteristic”, the system will end up on one of the stable branches of the characteristic. The positions of the fixed points depicted in Fig. 4.5(a) might seem to be a bit strange at first; of course, they are not. Every stable branch corresponds to a particular position of the charge accumulation forming the domain boundary. If only a plane spanned by two coordinates (that is, we are only considering the electron densities in two quantum wells) is used, there will be “peaks” only if the charge accumulation forming the domain boundary is located in one these two quantum wells. All other branches will be at approximately the same position in the plane. If we want all fixed points to lie on some kind of straight line, we have to chose two quantum wells that are far away from the position of the domain boundary. This has be done in Fig. 4.5(b). The disadvantage of this method is that the electron densities in these quantum wells are of no direct physical relevance – in contrast to the quantum wells near the domain boundary.

The observation that the unstable manifolds run towards the neighbouring stable branch is what had to be expected: Neighbouring branches differ in that the position of the domain boundary (and thus the charge accumulation) is shifted by one superlattice period. If the system would, starting at a particular unstable branch, move to a “distant” stable branch, electrons would have to be transported over a distance of more than one quantum well. During this process, the electrons would have to move through the adjacent quantum well and thus a state on the neighbouring stable branch.

The “jumps”, when a particular stable branch becomes unstable when the voltage is increased, can be seen in a simulated current-voltage characteristic (Fig. 4.6). If the applied voltage is increased monotonly (“sweep-up”, Fig. 4.6(a)) or decreased monotonly (“sweep-down”, Fig. 4.6(b)), only a small part of each stable branch is reached. The current (for fixed voltage) during a sweep-up is always higher than (or at least equal to) that during a sweep-down.

---

[4] When using arc length parametrisation, all quantities are continuous even when a bifurcation point is passed. It thus might be possible to conclude from a field profile that it belongs to an unstable state (if it lies near the centre of an unstable branch); however, it is not possible to conclude from a field profile that it belongs to a stable state.

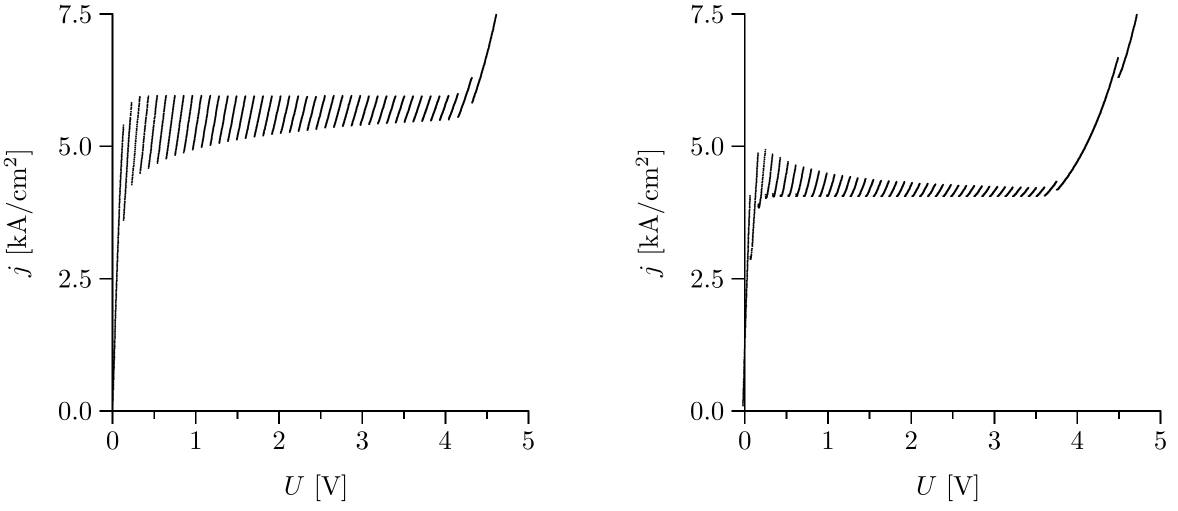

(a) Voltage sweep-up

(b) Voltage sweep-down

Figure 4.6: If there are multiple stable states for a given voltage, only one of them is reached in a simulation or an experiment; which state is reached depends on the "history" of the system. The result for a monotone increasing voltage (sweep-up) U is depicted in subfigure **(a)**, the one for a monotone decreasing voltage in subfigure **(b)**.

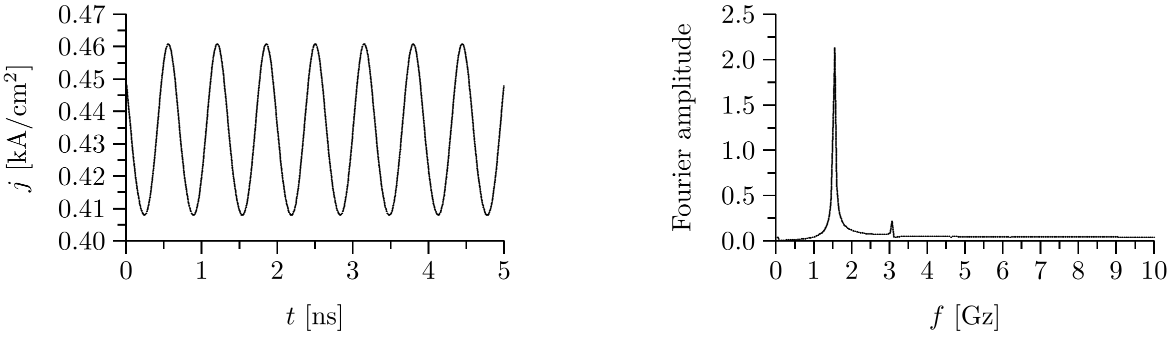

(a) Current oscillations

(b) Fourier spectrum

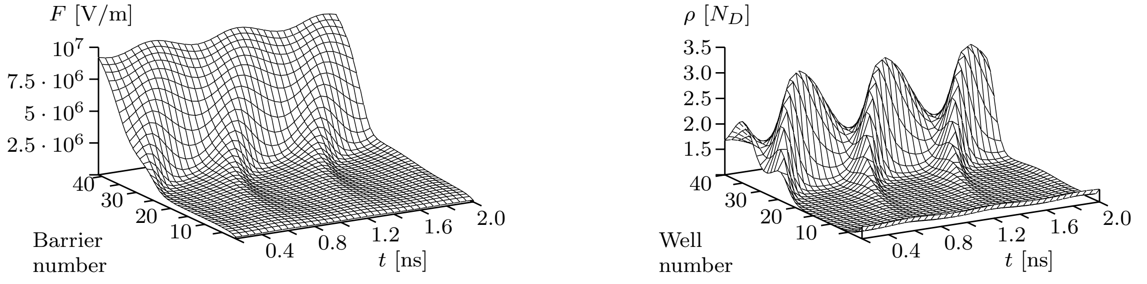

(c) Field distribution

(d) Electron densities

Figure 4.7: Current oscillation. **(b)** Absolute value of the complex Fourier amplitude.

4.2 Oscillations

Apart from the formation of field domains, one other form of pattern formation is also possible, namely the formation of limit cycle oscillations. A typical current oscillation is depicted in Fig. 4.7(a). It is almost sinusoidal, its frequency is of the order of Gigahertz.[5] The Fourier spectrum depicted in Fig. 4.7(b) also demonstrates that the oscillation is almost perfectly sinusoidal.

Oscillations are caused by the movement of electrons through the superlattice. This can be seen in the field profile (Fig. 4.7(c)) but even better in the electron density profile (Fig. 4.7(d)). The charge accumulation leads to an increase of the electric field, starting at the position of the charge accumulation. If its value reaches the NDC-region of the $v(F)$-characteristic, electron can move faster into this region that they can leave it at the other end. Thus, the charge accumulation will grow while moving slowly towards the anode. Once the value of the electric field grows beyond the NDC-region, the charge accumulation disappears and a new one is formed.

The undamped oscillations are in fact limit cycle oscillations. Fig. 4.8 depicts the projection of such a limit cycle onto the plane spanned by the electron densities in two different quantum wells. Apart from the limit cycle, a few additional trajectories are also shown. Trajectories starting “outside” the limit cycle are pulled into the limit cycle quite quickly. To demonstrate additional effects, two “special” trajectories are also depicted. The trajectory marked “b” starts in (actually, just very near) the unstable fixed point. Only a portion of this trajectory is shown; especially the part near the fixed point is not shown as it takes many “revolutions” to leave the immediate vicinity of the fixed point. This trajectory thus lies in the plane, in which the limit cycle as well as the unstable fixed point lie (approximately), i. e., the centre manifold. In contrast, the trajectory “a” starts “above” this plane. It is thus pulled quickly into the centre manifold; after that, it moves slowly towards the limit cycle (similar to trajectory “b”).

The limit cycles are created via supercritical Hopf bifurcations. This can already be demonstrated by presenting the results from simulations. The oscillation amplitude near the bifurcation point is depicted in Fig. 4.9(a). The sample points determined from simulations are marked with small crosses. The solid line is a square-root function “fitted” to the first ten or so data points to demonstrate that the amplitudes increase in the way expected for a supercritical Hopf bifurcation. Fig. 4.9(b) demonstrates that the oscillation frequency (solid line) is, to first order, not affected by the bifurcation. The frequency at the onset of the oscillations is finite and determined by the imaginary part of the corresponding eigenvalue.

The “usual” way to detect Hopf bifurcation points uses the eigenvalues of the dynamical matrix. The real part of the largest eigenvalue is therefore depicted in Fig. 4.10 as a function of voltage U and doping density N_D. For doping densities high enough for multistability, the state reached during a voltage sweep-up has been chosen. Fig. 4.10(c) depicts this data for the entire parameter region examined whereas the other two subfigures depict only the region relevant for the description of oscillations.

It can be seen that for small and medium doping the eigenvalues are usually smaller than for higher doping. Therefore, all eigenvalues smaller than -1 have been clipped. The “peaks”, which can be seen for high doping, correspond to states near bifurcation points. As these bifurcation points are saddle-node bifurcation points, one eigenvalue has to be zero. The states near the centre of a stable branch are “too stable”; so their eigenvalues are clipped off. The number of sample points depicted in the figure is too small for the individual branches to be recognisable. Thus, the peaks are located at seemingly random positions but this is nothing more than a sampling effect.

The section of the parameter space of interest to us is depicted in Figs. 4.10(a) and 4.10(b). In Fig. 4.10(b), contour lines are included; the outermost represents the value 0. The same data is also depicted in Fig. 4.10(a) with that exception that eigenvalues smaller than zero, that is, belonging to stable states, have been clipped. Considering both figures, we can say that the real part of the largest eigenvalue varies smoothly as a function of voltage and doping density; oscillations occur if it is larger then zero. This gives rise to the following comparison: The system (with damped or undamped oscillations) is just like an iceberg; only a small portion of it lies above the water line and can thus be seen (by oscillation). This also allows the prediction that, if the system is changed slightly (for example, by the introduction of dis-

---

[5] The frequencies observed with this model are far higher than the ones seen in experiments. Other models like [Bon94] therefore use the experimentally measured frequencies to adjust parameters of the model. This has not been done for the model used in this thesis as it depends only on microscopic quantities.

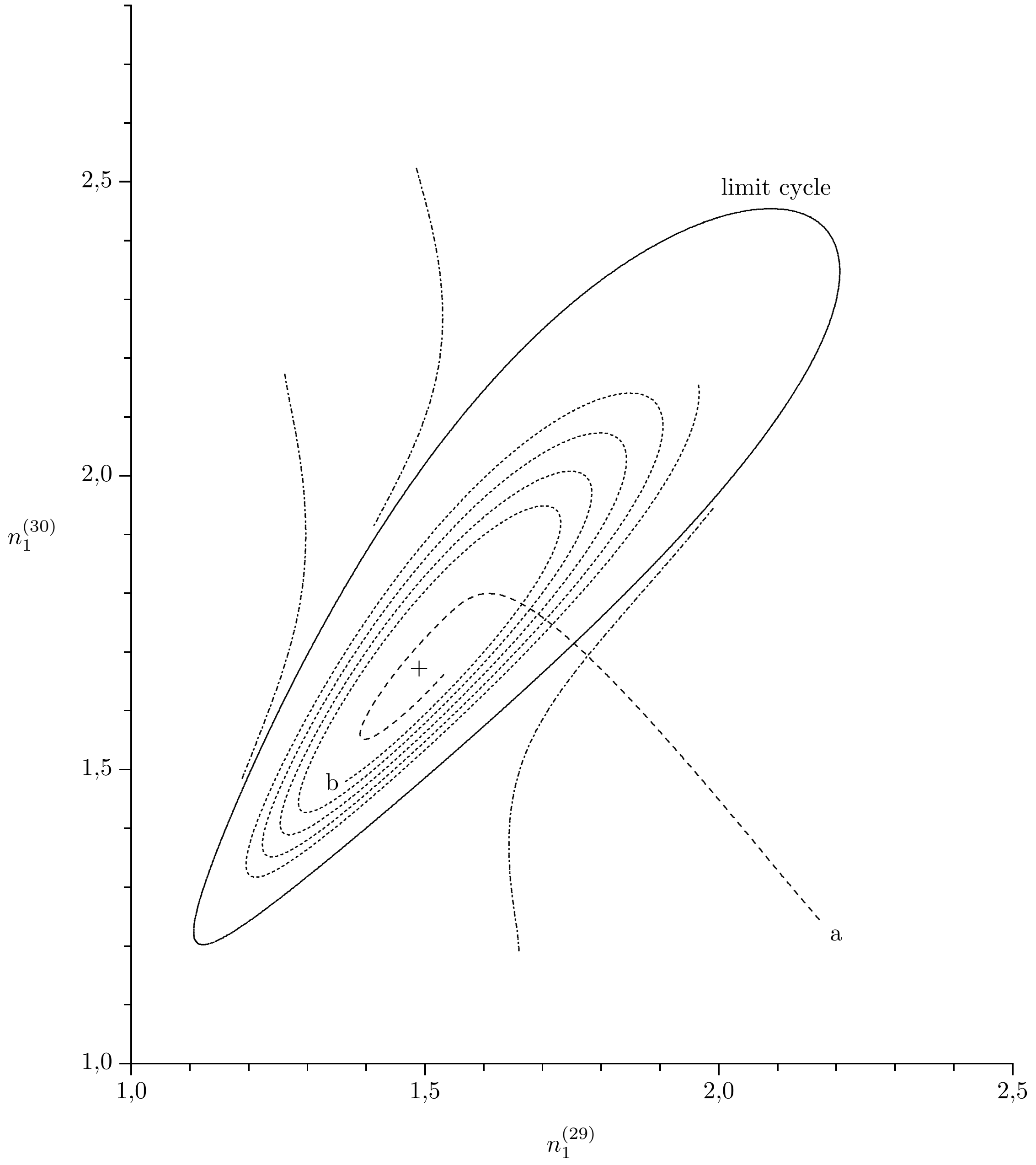

Figure 4.8: Limit cycle oscillation around an unstable fixed point. The trajectories without a label start near the limit cycle and are attracted by it. "a" is a trajectory starting above the plane, in which the limit cycle lies, and "b" is part of a trajectory which started near the unstable fixed point.

order), the region in which there are oscillations will change smoothly.

The imaginary part of the largest eigenvalue is depicted in Fig. 4.11. There is only a slight dependence on voltage and doping density. The "real" oscillation frequency as determined by a simulation is depicted in Fig. 4.9(b). Furthermore, the imaginary part of the eigenvalue, divided by 2π to convert angular velocity to frequency, is also shown.

The Hopf bifurcation is indeed supercritical as can be demonstrated by different methods: First, the oscillation amplitude increases like a square-root function (Fig. 4.9(a)). Second, there is no hysteresis between oscillatory and stationary behaviour. Third, the limit cycle was calculated directly, and finally, it is possible to decide this by calculating higher derivates [Khi92]. All Hopf bifurcation points found are supercritical regardless of at which point (i. e., at which parameter values) the oscillatory regime is entered.

If we divide the behaviour of the system just into "oscillating" and "stationary", this might be too harsh a division. Rather, it is advisable to group the "stationary" states by how

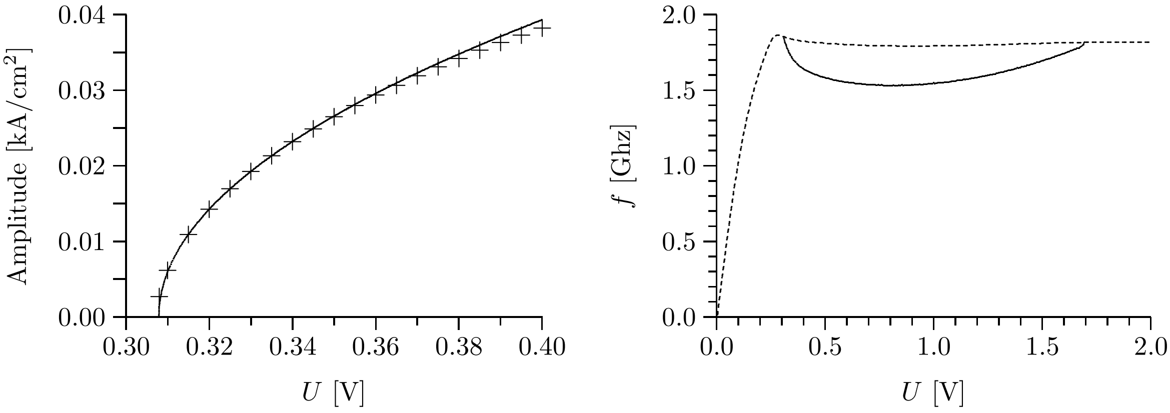

(a) Amplitude

(b) Frequency

Figure 4.9: Oscillation near a Hopf bifurcation point. **(a)** The oscillation amplitude as determined from a simulation is marked by small crosses (+). The solid line is a square-root function fitted to the first ten simulated data points. **(b)** Oscillation frequency as determined from a simulation (solid line) as well as the one calculated by dividing the imaginary part of the corresponding eigenvalue by 2π (dashed line).

the fixed point is reached. The first possibility is that the stationary state is reached in a damped oscillation (Fig. 4.12(b)). On the other hand, the distance between the current state and the fixed point may decay exponentially (Fig. 4.12(a)).[6] The oscillating case is depicted in Fig. 4.12(c).

These three cases can be characterised by the configuration of their eigenvalues.[7] The three configurations and the corresponding transitions are depicted schematically in Fig. 4.13. Undamped oscillations are associated with a pair of complex conjugate eigenvalues whose real part is greater than zero (right), and damped oscillations with a pair whose real part is smaller than zero (centre). The transition between these two regimes happens in a Hopf bifurcation. Exponential decay means that there are two real eigenvalues (left). The transition to damped oscillations happens at the point where both eigenvalues are equal.

The distinction between the cases depicted in Figs. 4.12(a) and 4.12(b) might not have a direct influence on the current-voltage characteristic. However, it is essential in understanding the phase diagram. For parameter values for which the current-voltage characteristic has fully developed branches the largest eigenvalue has to be real as otherwise there could not be any saddle-node bifurcations. Furthermore, the unstable manifolds in figure 4.5 do not show any tendency to oscillate when they approach the stable fixed points.[8] On the other hand, oscillations (that means, Hopf bifurcations) are only possible if we have a pair of complex conjugate eigenvalues.

As result, we can divide the parameter space of our system into different regimes: a “branch dominated” part (exponential decay) and an “oscillation dominated” part (damped or undamped oscillations). The system is “branch dominated” if the largest eigenvalue is real; it is “oscillation dominated” if it has a pair of complex conjugate eigenvalues. The boundary between these two regimes can be determined by plotting all points where the two largest eigenvalues are equal.

This leads to a very important conclusion: Unless there are bifurcations of higher codimension, branch formation and oscillations have to be separated (in the phase diagram). This can only change if a saddle-node bifurcation and a Hopf bifurcation happen at the same place, that is, we have a Takens-Bogdanov point. For the unperturbed superlattice, we have only “plain” saddle-node bifurcations and Hopf bifurcations. The locations of the Hopf bifurcation points are marked with dashes in Fig. 4.14; the positions of all points, where the two largest eigenvalues

---

[6] This is similar to a damped, harmonic oscillator. The cases “exponential decay” and “damped oscillations” are usually called “overdamped” and “underdamped” when dealing with oscillators.

[7] In the following, we assume that the self-generated oscillations start at a supercritical Hopf bifurcation, and that there are no additional bifurcation points.

[8] Fig. 4.17 depicts the case that the “upper” stable fixed point shows a tendency to oscillate – note the curvature inside the triangle which is not just a numerical artefact. However, since a saddle-node bifurcation is nearby, the tendency to oscillate is rather small.

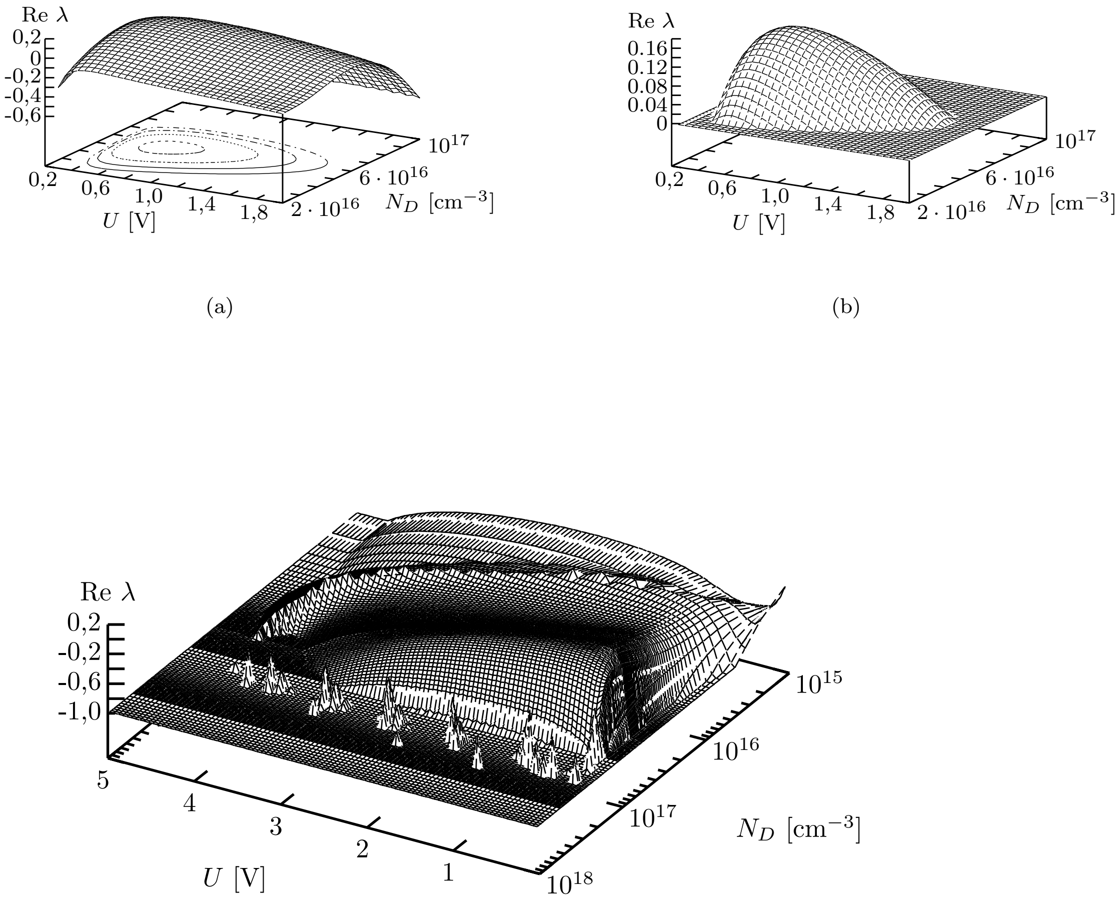

(a)

(b)

(c)

Figure 4.10: Real part of the largest eigenvalue as a function of voltage U and doping density N_D. **(a)** Neighbourhood of the region in which there are oscillations. The outermost contour line corresponds to the value 0, the innermost to 0.25. **(b)** Like subfigure (a) with the exception that eigenvalues smaller than zero are clipped. **(c)** Figure of the entire parameter region examined. For parameter values with multistability, the data obtained by a voltage sweep-up was taken. Eigenvalues smaller than -1 are clipped.

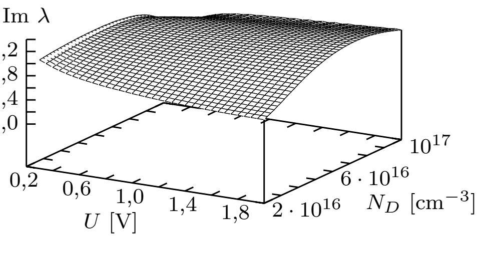

Figure 4.11: Imaginary part of the largest eigenvalue as a function of doping density and applied voltage. The region depicted is the same as in Figs. 4.10(a) and 4.10(b).

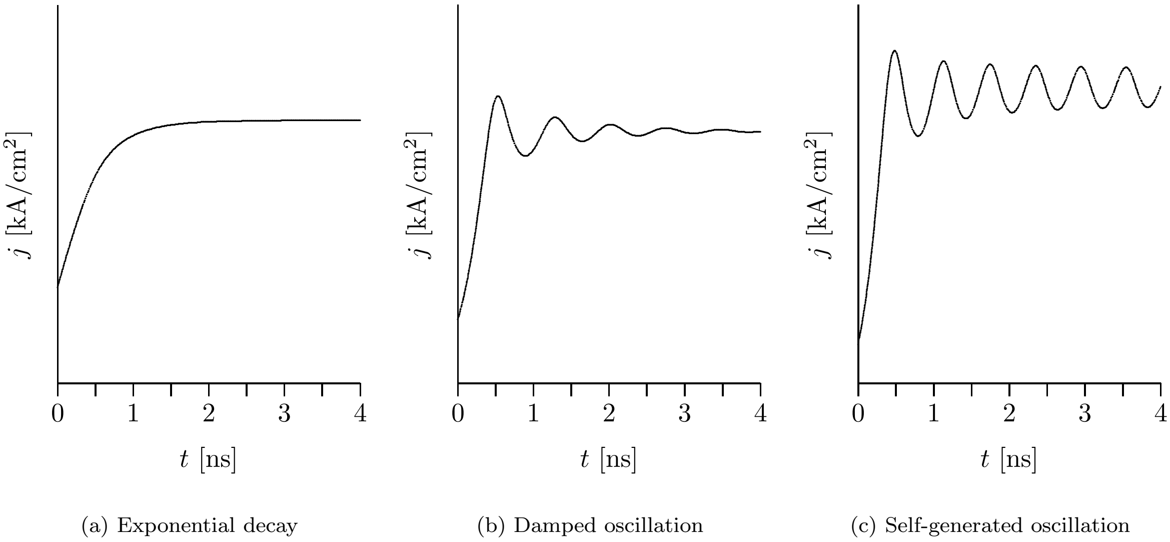

(a) Exponential decay (b) Damped oscillation (c) Self-generated oscillation

Figure 4.12: There are three distinct cases for the dynamics near a fixed point if the initial conditions are not too far away from the attractor. The subfigures have been calculated for different doping density so that the current densities had to be scaled appropriately. **(a)** The distance to the fixed point decays exponentially. **(b)** The fixed point is reached via damped oscillations. **(c)** The system does not end up on the fixed point but on a nearby limit cycle.

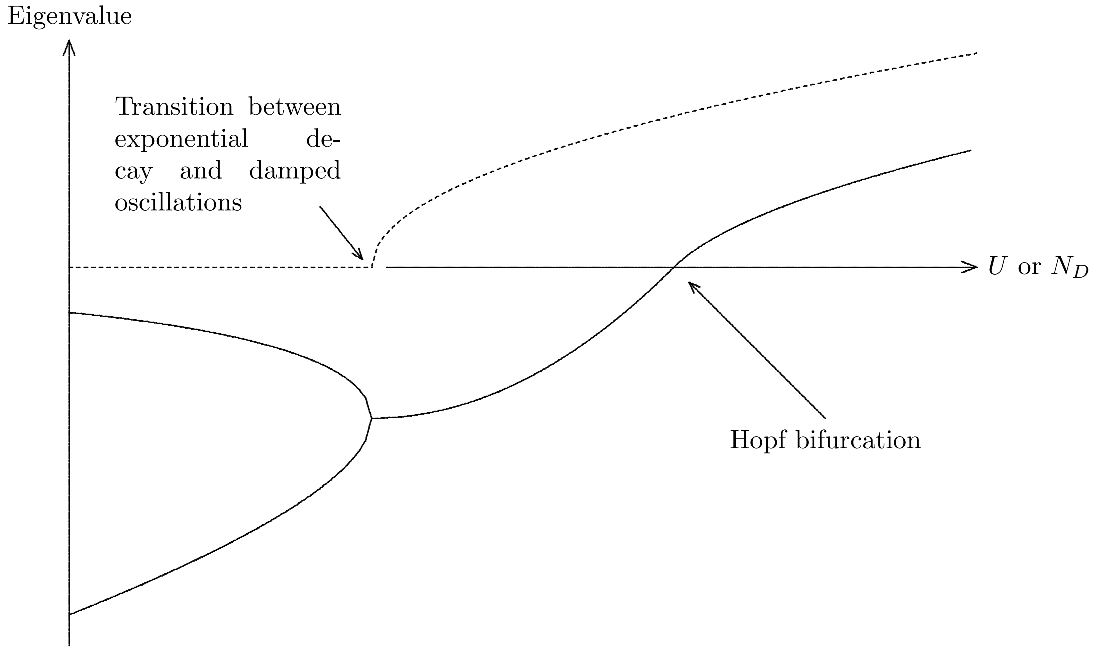

Figure 4.13: Schematic structure of the eigenvalues near a region with oscillations. The real part is marked as solid line, the imaginary part as dashed line. In the left part of the figure, there are two distinct, real eigenvalues; the system moves directly into the fixed point. In the middle, the two real eigenvalues have merged and formed a pair of complex conjugated eigenvalues (only the positive imaginary part is included in the figure); the system shows damped oscillations. To the right, the real parts of the eigenvalues have become positive in a (supercritical) Hopf bifurcation; self-generated, undamped oscillations can now be observed.

are equal, are marked with a line of alternating dashes and dots.

As has been mentioned before, all Hopf bifurcation points are of supercritical type. Thus, we have oscillations only inside the region limited by Hopf bifurcation points. This region is surrounded by a region of damped oscillations. Its boundary between has not been calculated

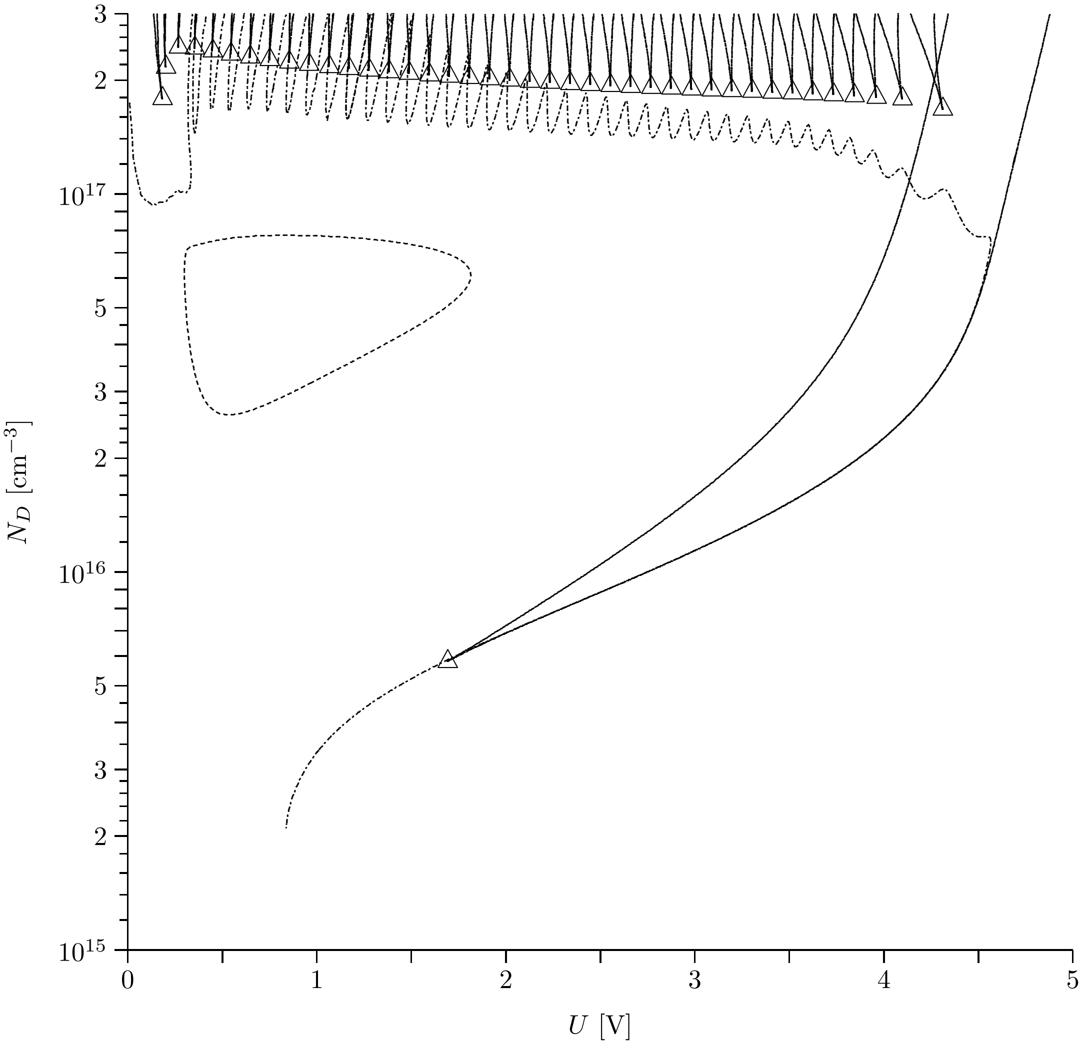

Figure 4.14: Position of the region in which there are oscillations in parameter space. The transition between exponential decay and damped oscillations is marked by a line of alternating dashes and dots. Besides the positions of the Hopf bifurcation points, the positions of the saddle-node bifurcation points are also included. The existence of branches implies multistability so it is not possible to see in the figure, on which branch the transition between exponential decay and damped oscillations happens.

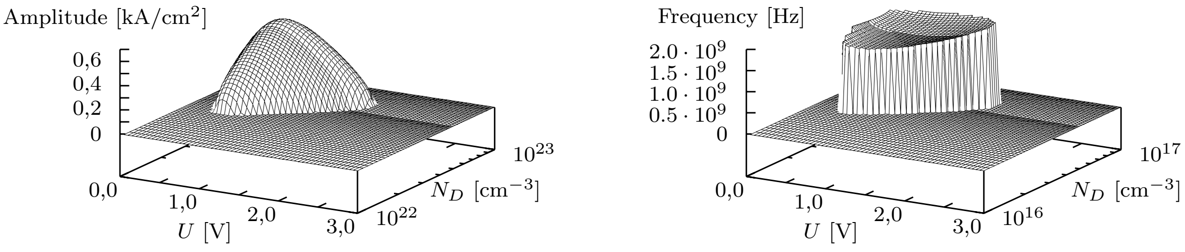

(a) Amplitude

(b) Frequency

Figure 4.15: Oscillation amplitude and frequency as a function of doping density and applied voltage.

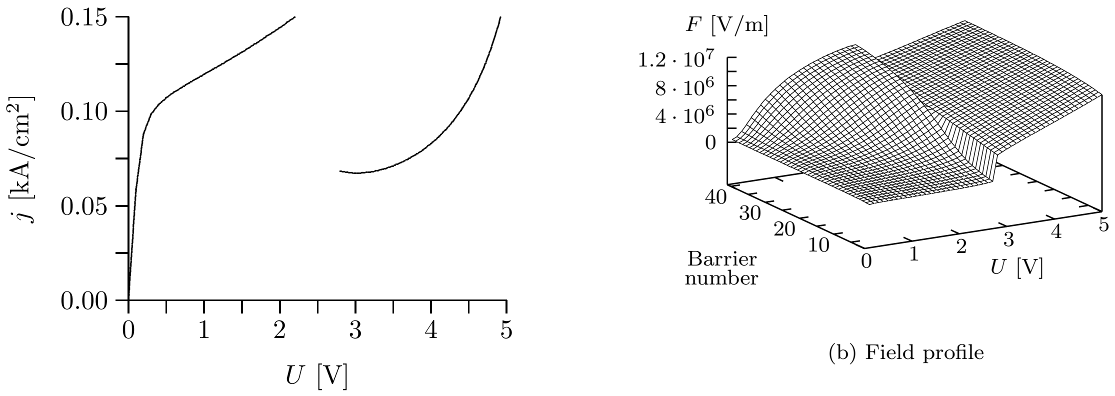

(a) Current-voltage characteristic

(b) Field profile

Figure 4.16: Simulated current-voltage with a single branch and corresponding field profile. The jump and thus the branch itself are caused by the transition from a washed-out domain to a nearly homogeneous field profile.

for very small doping densities due to numerical problems.[9]

Finally, the oscillation amplitude and frequency are depicted in Fig. 4.15 as a function of voltage and doping density. It can be seen that both parameters have similar effects, and that the results presented for a particular, fixed doping density are indeed typical.

4.3 Superlattices with Different Doping Density

Now we can return to the current-voltage characteristics in Figs. 4.1 and 4.2 (pages 26 and 27). For small doping (Fig. 4.1(a)), the shape of the current-voltage characteristic is almost the same as the one of the $v(F)$-characteristic. There are not enough charge carriers available for spatial pattern-formation; the field profile is almost homogeneous (more about this in the next section).

Already for doping densities as low as $N_D \approx 10^{16}$ cm^{-3}, a single branch has formed. The mechanism responsible for the formation of this is different from that responsible for the other branches existing only for heavy doping.[10] Fig. 4.16(a) once again depicts the corresponding current-voltage characteristic, however, only the voltage sweep-up is included. Fig. 4.16(b) depicts the corresponding field profile. It can clearly be seen from the latter figure that the jump from one branch onto the other one is accompanied by a qualitative change in the field profile: Up to a certain voltage, the field profile corresponds to that of a washed-out domain; above that value, the field distribution is nearly homogeneous.

This branch differs also in an additional aspect: As Fig. 4.17 demonstrates, the dynamics near the upper stable branch shows damped oscillations (see also the preceding section). The unstable manifold, which indicates the direction of fastest leaving the neighbourhood of the unstable fixed point and the slowest direction of moving into the stable fixed point,[11] does not run straight into the fixed point, but has the form of a spiral. This can best be seen inside the small triangle.

Fig. 4.1(c) depicts a current-voltage characteristic showing oscillations of the type discussed in section 4.2. The minimum and maximum current reached during one period of the oscillation is marked in the figure. If the doping density is increased, the oscillatory region becomes smaller again until it is disappears (Fig. 4.1(d)).

If the doping density is increased further, branches start to form. Fig. 4.1(e) depicts a

---

[9] A random matrix consisting of n by n elements, n being even, will usually have no real eigenvalues. Numerical errors can be considered as random effects (if we knew how large they were, we could compensate them). Thus, numerical errors have the tendency to convert two real eigenvalues into a pair of complex conjugate eigenvalues with a small imaginary part. This is what is seen for small doping.

[10] This "special" branch exists also for heavy doping. It is the larger, rightmost branch of the current-voltage characteristic.

[11] For stable states, not the fastest direction but the slowest direction is of importance. The fast degrees of freedom adapt adiabatically to the slowest ones thus making the latter the dominating ones.

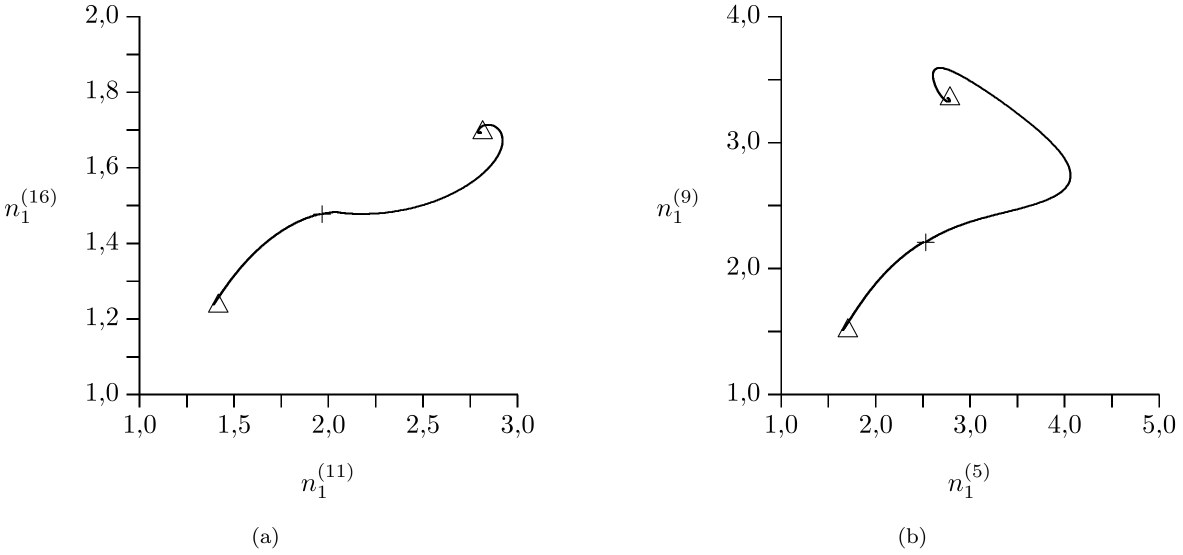

Figure 4.17: Dynamics (phase portrait with unstable manifolds) in the neighbourhood of the branch described in the text ($U = 3.8$ V).

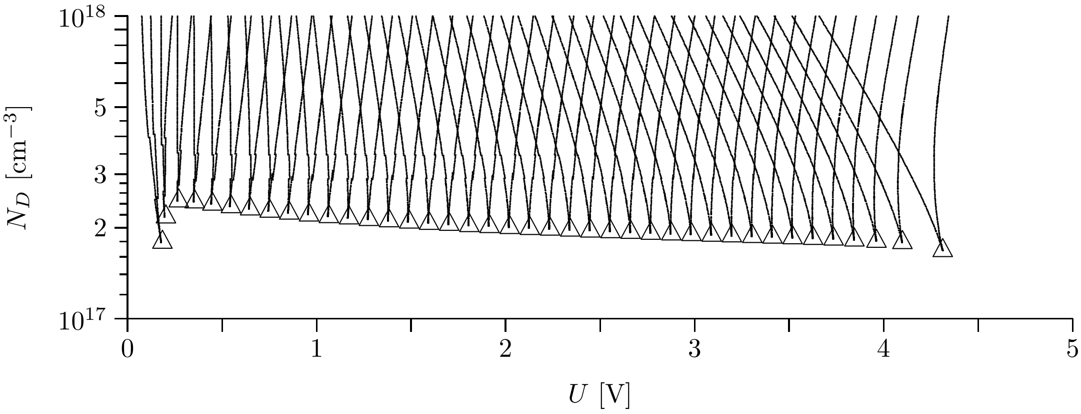

Figure 4.18: Locations of all saddle-node bifurcation points connected with the development of branches at heavy doping. Two branches of saddle-node bifurcation points merge in a cusp point.

current-voltage characteristic for a doping density chosen so that only some branches have actually started to develop (mainly at high voltage) whereas for smaller voltage the current-voltage characteristic shows just a kind of "oscillation".

This process already leads – using the general results from section 2.6 – to the assumption that all branches are formed in cusp points. This can be verified by plotting the location (parameters voltage U and doping density N_D) of all saddle-node bifurcation points. This has been done in Fig. 4.18. The particular branches do not all start at the same doping density. Rather, the cusp points lie – except for boundary effects – roughly on a straight line in the U-N_D-plane.

4.4 Dependence on Doping

In the preceding sections, current-voltages characteristic for different values of N_D were presented, that is, U was varied for fixed N_D. Of course, the opposite procedure is also possible. Fig. 4.19 depicts the "current-doping characteristic" for fixed $U = 1$ V. To first order, j is proportional to the number of available charge carriers and thus to the doping density N_D. Therefore, the structure of the "characteristic" can only be examined when j/N_D is plotted instead.

In Fig. 4.19, we can see multiple, unconnected branches for sufficient doping. These are just

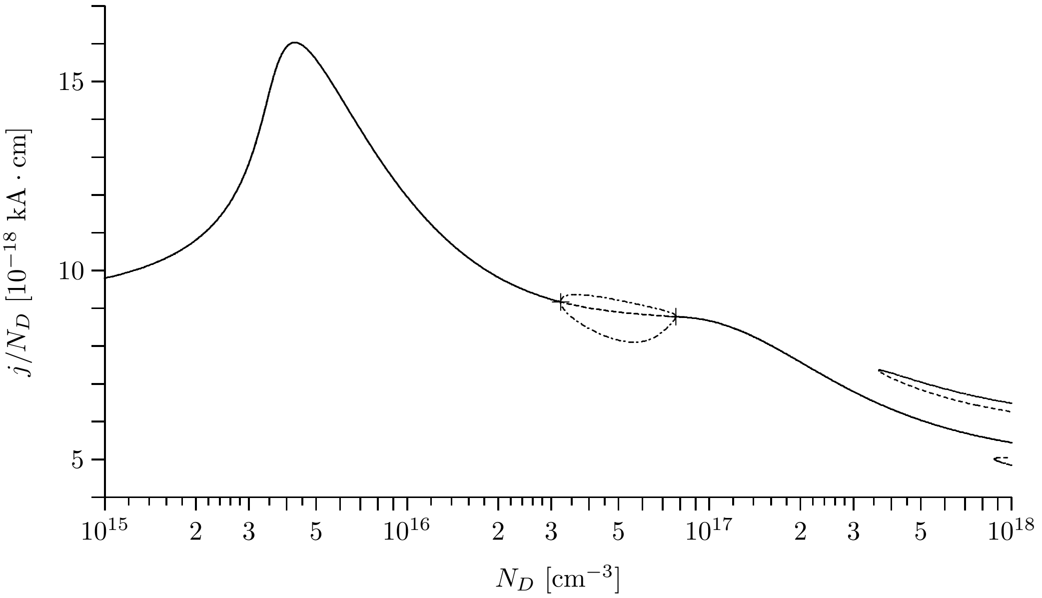

Figure 4.19: Current density as a function of doping density. As j is, to first order, proportional to N_D, j/N_D is depicted instead. For high doping, there are multiple states as has already been discussed in section 2.6.

the "side view" of the branches known from the "conventional" current-voltage characteristic. As has already been mentioned, branches form in cusp points, which were discussed in section 2.6. Fig. 2.6 on page 8 presented different cross-sections through the parameter plane near a cusp point. Subfigure 2.6(c) depicts (in principle) the conventional current-voltage characteristic for heavy doping whereas the case of variable doping density and fixed voltage corresponds to subfigures 2.6(d) and 2.6(f).

Furthermore, we can see that the "peaks" in the scaled current density are higher for light doping. This is due to the fact that charge accumulations for smaller doping densities are smaller absolutely but larger when compared with N_D. For heavy doping, there cannot be a charge accumulation of more than about $0.5 \cdot N_D$ as such a accumulation is already sufficient to cause a jump in the electric field from zero to the resonance field strength. Comparing the subfigures in Fig. 4.1, it is also the current-voltage characteristic for the smallest doping density that has the largest "mountain/valley-ratio". This claim is also supported by Fig. 4.20, in which the scaled current density j/N_D is depicted as a function of voltage and doping. For small doping, a "mountain" moves from left to right whereas the branches for heavy doping are hardly noticeable.

Finally, we want to discuss the dependence of the field profile on the doping density using Fig. 4.21. The problem of multistability has been solved by using the states on the continuous branch of Fig. 4.19; this way, it is guaranteed that the field profile varies smoothly as N_D is changed.

As can be seen in the figure, the field profiles becomes more "sharp" when the doping density is increased, that is, the width of the domain boundary shrinks and the division of the superlattice into a high-field domain and a low-field domain becomes more distinct. For light doping, there is hardly any domain structure. This becomes apparent by the fact that the electric field in the "low-field domain" rises. The data in the voltage was calculated for a voltage of 1 V; the resonance condition is – for a homogeneous field profile – fulfilled for a voltage of approximately 4 V. Thus, for very small doping (and therefore an almost homogeneous field profile), the electric field throughout the superlattice has to be approximately one quarter of the resonance field for this choice of voltage.

4.5 Phase Diagram

In the first few sections of this chapter, some specific values of the doping density N_D were considered, and U was varied for fixed N_D ("current-voltage characteristic"). In the preceding section, the same has been done except that the role of U and N_D had been exchanged

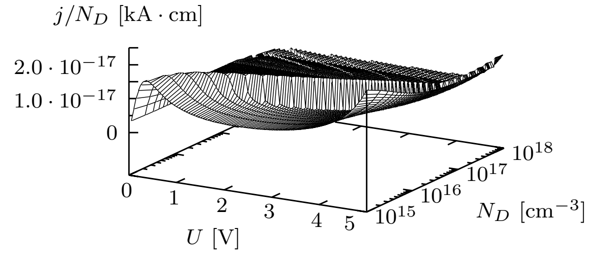

Figure 4.20: Scaled current density j/N_D as a function of voltage U and doping density N_D. For parameter values with multistability, the states reached during a voltage sweep-up are taken.

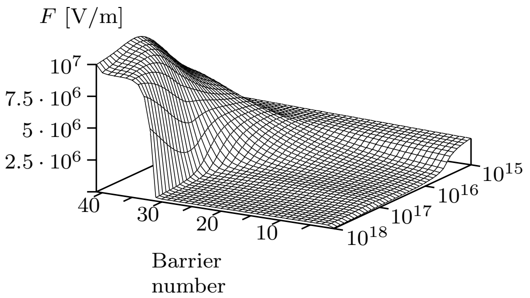

Figure 4.21: Field profile as a function of doping density. Depicted is the field profile along the continuous branch from Fig. 4.19.

("current-doping characteristic"). If one is not interested in the precise values of the current or similar quantities but only in the qualitative shape of the current-voltage characteristic, it is sufficient to consider only the positions (the two parameters applied voltage *and* doping density) of all "important points", that is, bifurcation points. In this thesis, such a diagram is usually only referred to as *phase diagram*. Actually, this name is not completely correct as we do not label the different phases but only the transitions between them.

These diagrams have already been used to examine individual aspects like the formation of branches or limit cycle oscillations. Thus, we just have to combine these to yield Fig. 4.22. This figure gives a complete summary of what behaviour we may expected for an unperturbed ("perfect") superlattice at given parameter values.

First, we will deal once again with the Hopf bifurcation points. Since all Hopf bifurcations are supercritical, there are oscillation everywhere in the region limited by the Hopf bifurcations, and nowhere outside. There are no additional bifurcation points inside this region.

In the upper part of the phase diagram, there are the saddle-node bifurcation points connected with the formation of branches in the current-voltage characteristic. The phase diagram is useful in this region as it allows the construct the qualitative shape of the current-voltage characteristics:

For $U = 0$ V, there is only one stable state. Thus, we have to start at the left border of the figure in the desired height, that is, doping density. Now, we move right until we "hit" a saddle-node bifurcation that is the *right* saddle-node bifurcation of a pair of saddle-node bifurcations emerging in a particular cusp point. Thus, at this voltage, there is a saddle-node bifurcation, the stable branch becomes unstable, and the direction of voltage variation is inverted. Therefore, we move back until we reach the other (left) saddle-node bifurcation that started at this cusp point. Thus, at this voltage, the unstable branch becomes stable, and the voltage variation is towards higher voltage once again. Now, we move right to the next *right* saddle-node bifurcation point that we have not used yet. . .

This way, we can construct the entire current-voltage characteristic as long as only the positions of the bifurcation points and thus the positions of the stable and unstable branches are of interest. Of course, it is not possible to determine the current from the phase diagram. All other features of the current-voltage character-

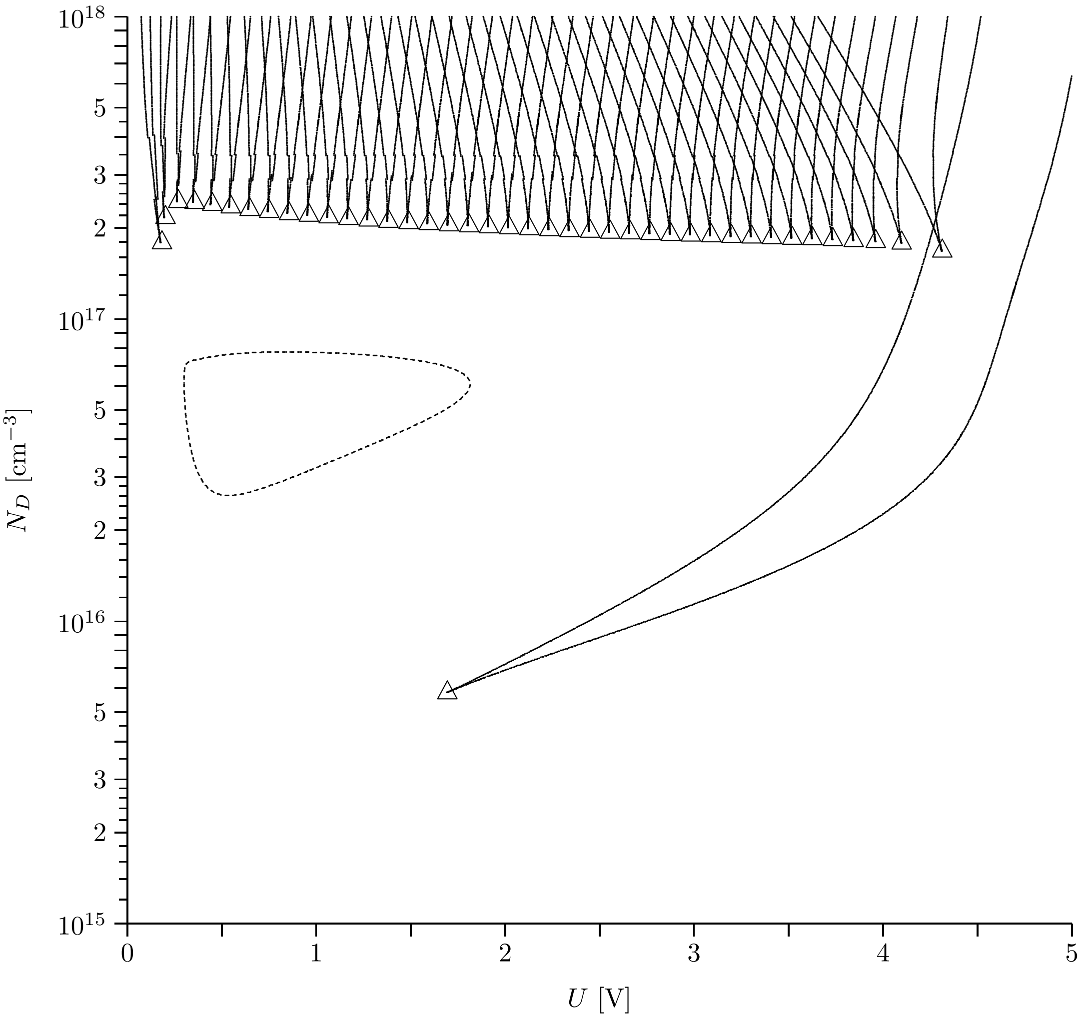

Figure 4.22: Location of all bifurcation points (in parameter space).

istic constructed this way are the same as the ones of the "real" current-voltage characteristic. For example, if there are additional lines of saddle-node bifurcation points between the two lines starting from a particular cusp point, this means that for this voltage and doping density there are not just two but even more stable states. It is thus easy to see that the number of multistable states has a tendency to increase as the doping density (and/or voltage) increases.

Summarising: An unperturbed ("perfect") superlattice may – at least with the model used in this thesis – display two types of self-organised structures, namely branches (multistable field domains) and limit cycle oscillations. Both structures are independent of each other. There even is a "buffer zone" between branch formation and oscillations (see Figs. 4.22 and 4.14).

4.6 Superlattices with Different Number of Quantum Wells

Fig. 4.23 depicts the location of all bifurcation points in dependence on the number of quantum wells, N, in the superlattice. The cusp points and the branches of saddle-node bifurcation points connected with the formation of branches due to domain formation change their number if the number of quantum wells is changed. Apart from that, the overall structure does not change which makes sense as branches exist only for doping densities high enough so that the charge accumulation forming the domain boundary is at most a few quantum wells wide. It thus "makes no difference" to a branch whether it is near the boundary of the superlattice. If one is only interested in fully developed branches it is thus possible to reduce the number of quantum wells to speed up the simulation (or the growth process).

The situation is different if oscillations are considered. As could already been seen in

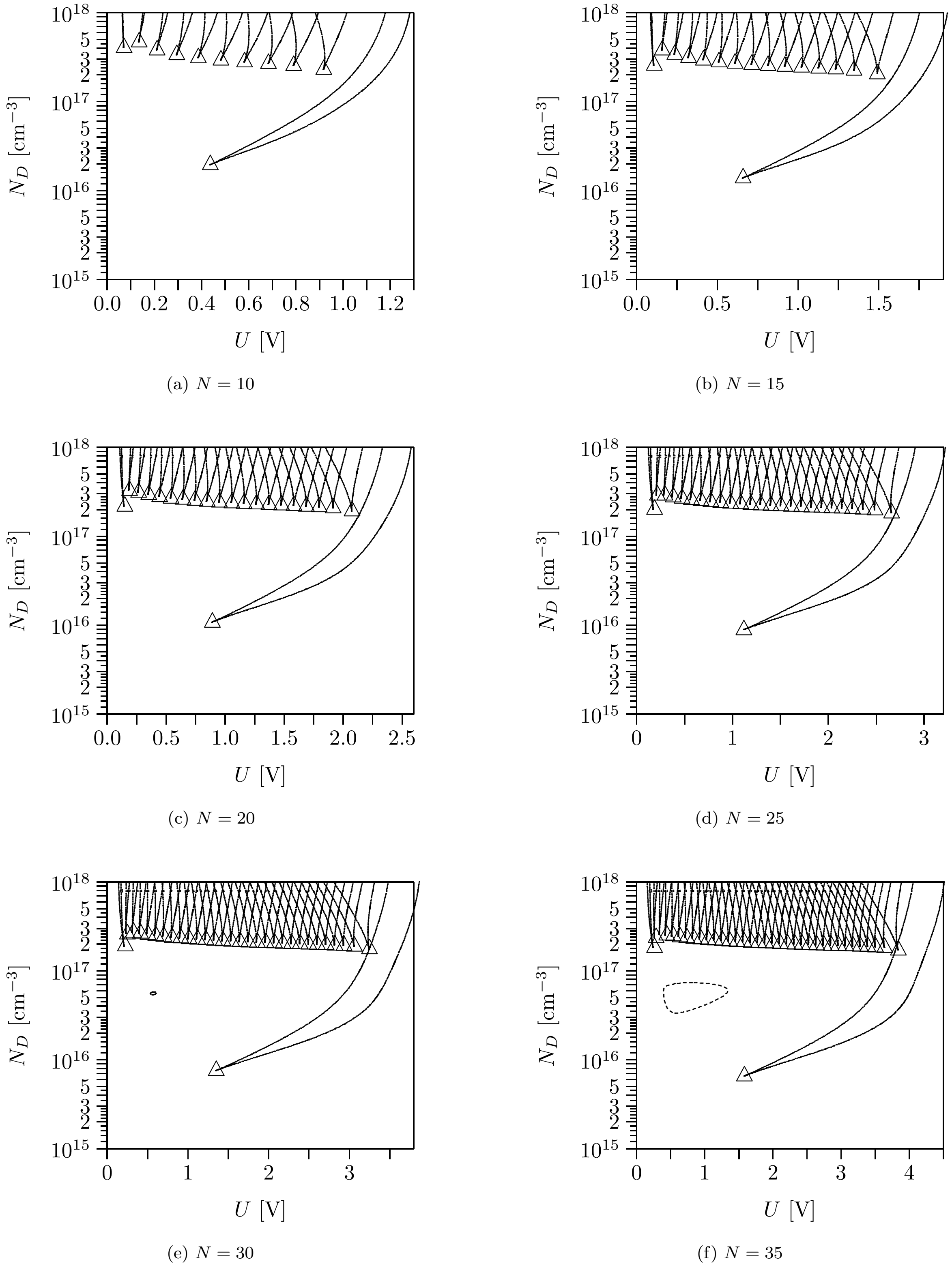

(a) $N = 10$

(b) $N = 15$

(c) $N = 20$

(d) $N = 25$

(e) $N = 30$

(f) $N = 35$

Figure 4.23: Locations of all bifurcation points ("phase diagram") for superlattices with a different numbers of quantum wells. It can clearly be seen in this figure that the formation of branches is possible even for superlattices with very few wells whereas there has to be a minimum number of wells for oscillations to be possible.

Fig. 4.7(c) (page 31), the oscillation involves a large part of the superlattice. The superlattice thus has to have a minimum number of quantum wells for the oscillation mode to fit into it (this number is $N = 27$ for the parameters used in this thesis). This minimum length can be divided into two parts: The oscillation mode itself has a certain length, and the boundary conditions might inhibit oscillations near the boundary. The second effect can be investigated by changing the choice of boundary conditions. This has been done in chapter 7 where Neumann boundary conditions are used which allow the system more "freedom" than the Dirichlet boundary conditions used in the main part of this thesis.

4.7 "Strange States"

So far only the "standard" current-voltage characteristic has been investigated, that is, one fixed point is determined by simulating the dynamical equations first, and the entire current-voltage characteristic is calculated by continuation techniques. Regardless of the precise choice of initial conditions, this process results in the same current-voltage characteristic. In this section we will investigate what additional zeros the dynamical equations posses, that is, we are looking for unstable fixed points or stable fixed points with a very small basin of attraction.

To find additional fixed points, some root-finding algorithm, here Newton-Raphson is used, has to be applied to the dynamical equations. Finding zeros in more than one dimension is an "almost impossible" task [Pre92, chapter 9.6] which can only be fulfilled if additional assumptions are made. This means especially that "suitable" initial condition have to be supplied. Unfortunately, there is not better definition for "suitable" than that the algorithm will converge with them. For high-dimensional problems like the one examined in this thesis, the choice of initial conditions becomes a very complex problem.

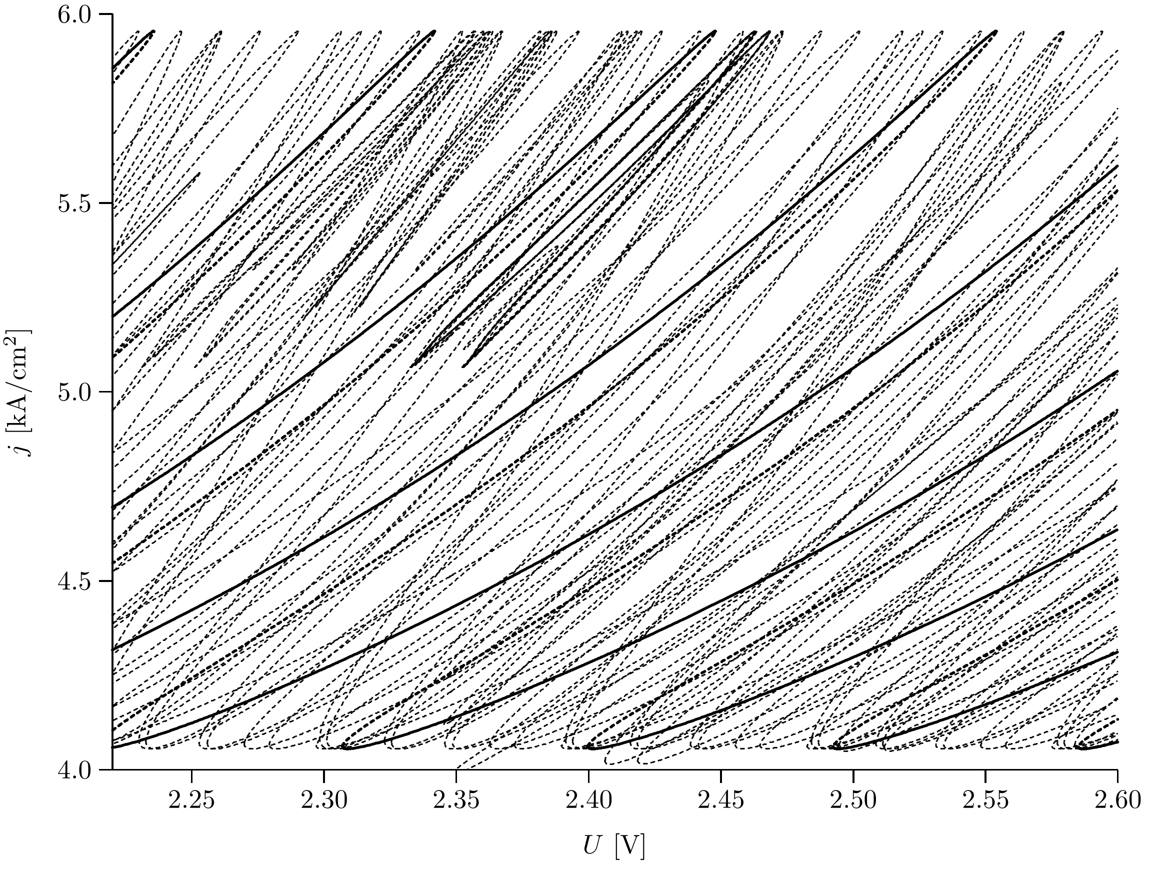

Figure 4.24: "Strange states", starting at the voltage $U = 2.348$ V. The meaning of the numerous curves in this figure is explained in the text. The "standard" current-voltage characteristic (bold line) contains just a small part of all stationary states.

Let us think about what conditions the initial states have to fulfil: They should be similar to the states on the "standard" current-voltage characteristic. The only feasible way to get such states is to take states from the "standard" current-voltage characteristic. Next, we want to find some other state than the one that was inserted into the algorithm as initial condition. The first idea may be simply to alter the initial state a bit. The problem is that the algorithm will then either converge back to the old state or not converge at all. There is just one way to solve this problem: The chosen initial state is an upper saddle-node bifurcation point. If the voltage is decreased a bit, there are two fixed points; if it is increased a bit, there are no fixed points (at least in the neighbourhood of the bifurcation point in question). By increasing the voltage a bit, one has an initial condition being very similar to a "valid" state; on the other hand, the original state no longer exists so the algorithm cannot converge back to it.

Of course, we are not interested in just a single new state but want to have as many as possible. This can be done be randomly altering the initial conditions a bit. It is not advisable to alter the electron densities in each quantum well on its own but to use a more "global" approach: One determines randomly how many quantum wells should be affected, selects a corresponding number of quantum wells and alters the electron densities in each of these quantum wells the same way. This process should be repeated a couple of times.

The states found by application of this procedure are depicted in Fig. 4.24. There is a large number of stationary, mostly unstable states; the "standard" current-voltage characteristic is also depicted for comparison. The unstable states can be grouped into two classes: First, there are *continuous* states which exist – like the "standard" current-voltage characteristic – for a large (or even infinite) range of voltages. Second, there are *closed* curves which are approximately as wide as one branch of the "standard" characteristic. On the other hand, the different states may also be grouped by their field profile. There are six different types of field profiles which are summarised in Fig. 4.25.

The field distribution depicted in Fig. 4.25a is the one which is found along the "standard" current-voltage characteristic (at least for

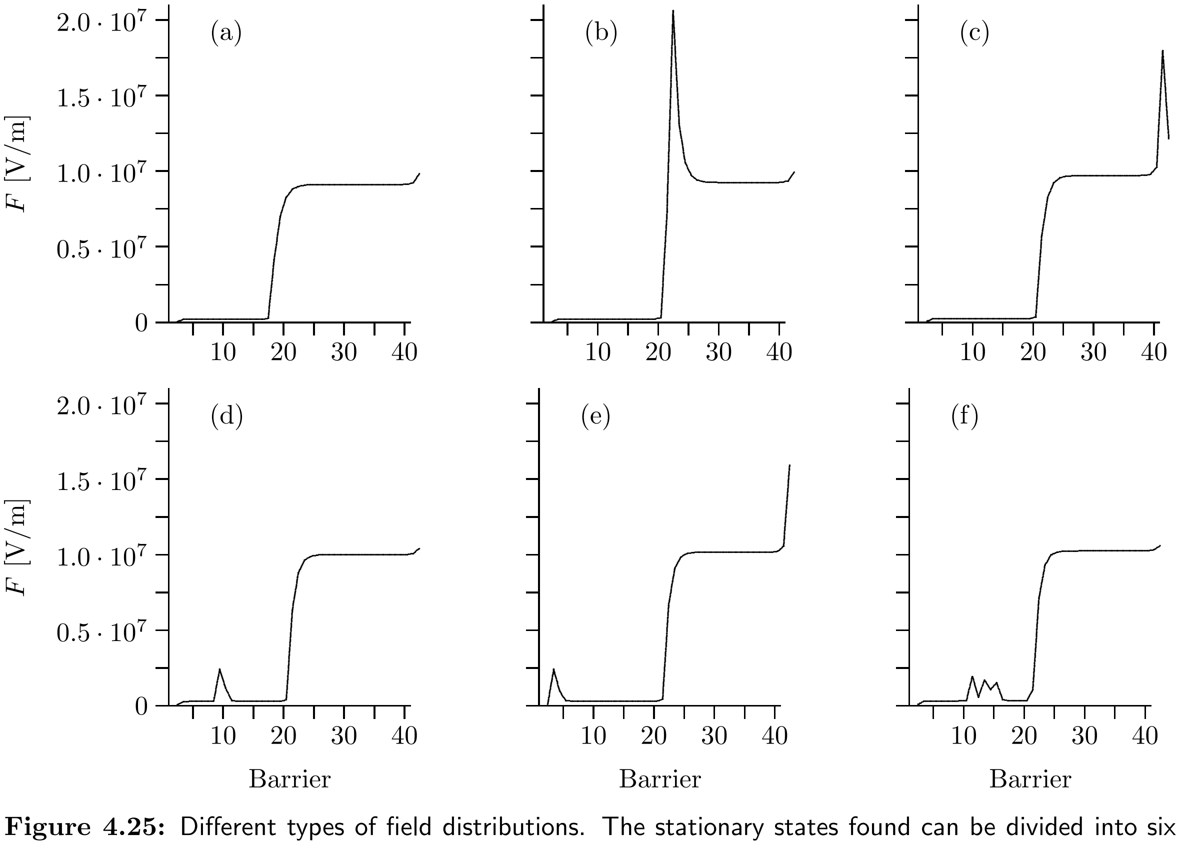

Figure 4.25: Different types of field distributions. The stationary states found can be divided into six classes. Type **(a)** can only be observed along the "standard" current-voltage characteristic. Types **(b)**, **(c)** and **(e)** exhibit peaks with field strength above the resonance condition (approximately 10^7 V/m) and are thus of questionable physical relevance. Types **(d)** and **(f)** have a "normal" high-field domain and an additional smaller peak of one or a few wells width in the low-field domain.

voltages for which there are branches; thus, this excludes very small or very large voltage). The electric field in the high-field domain is given approximately by the resonance condition which allows resonant tunnelling between adjacent quantum wells. This transport mechanism is so effective that a further increase in the electric field "makes no sense for the system". This condition is violated in subfigures (b), (c) and (e) of Fig. 4.25. Therefore the physical relevance of these states is questionable[12].[13] The field distributions depicted in subfigures (d) and (f) have a high-field domain similar to the "standard" current-voltage. However, there is an additional smaller peak in the low-field domain. The difference between types (d) and (f) lies in whether this peak extends over just a single barrier – meaning that the electron density is increased in a specific quantum well and decreased in the adjacent one – or several barriers. The necessity for this distinction will become clear later.

These two classifications – by type of field distribution and by whether the states form a closed curve – are not independent of each other: States with a field distribution of types (b), (d), (e) and (f) belong (usually) to closed curves whereas types (a) and (c) imply continuous characteristics. The closed current-voltage characteristics are depicted in Fig. 4.26 along with the corresponding field profiles in Fig. 4.25. The field profile does not change much along the curve as its width is only that of a single branch of the "standard" current-voltage characteris-

---

[12] We will see in the following chapters that these states will be of no more interest while we will come back to unstable states of the other types.

[13] One could come up with the following idea to decide whether a given (unstable) state is of physical relevance. We postulate that all (stable) states of the "standard" current-voltage characteristic are of physical relevance, and that all states which result in a negative current are forbidden. One then takes the unstable state in question and starts a simulation with that state as initial condition. We see then that these two postulates are sufficient, that is, the result of the simulation is either a state on the "standard" current-voltage characteristic or a state with negative current. Unfortunately, the state reached in the simulation does not depend on the type of field distribution of the initial state. Sometimes states on the same closed curve even reach stable states of different type.

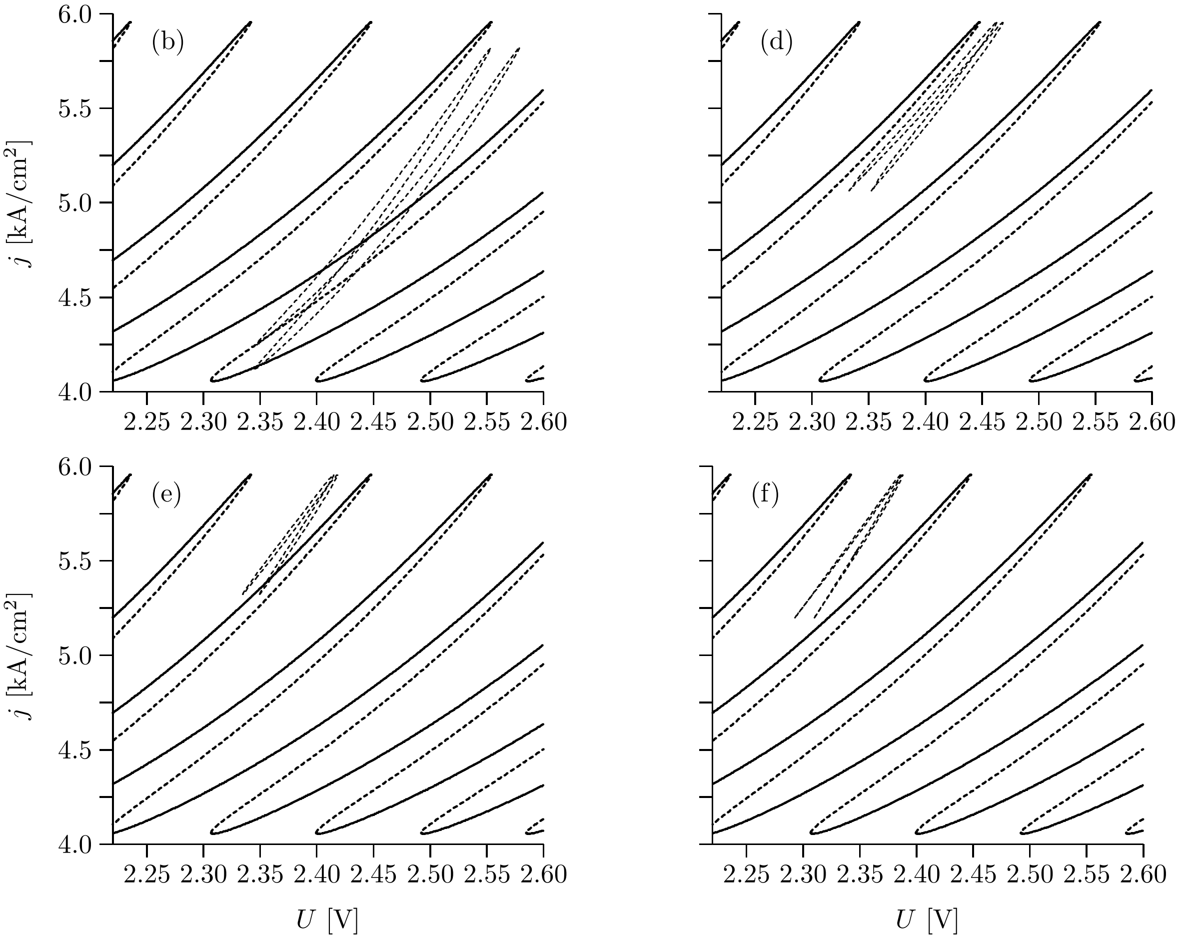

Figure 4.26: Closed current-voltage characteristics. Depicted are the characteristics corresponding to the field distributions in Fig. 4.25. The subfigures are marked with the same letter in both figures.

tic. The jumping of electrons from one quantum well to next when a new branch is reached must thus not be expected. Please note that the field distributions are depicted as a function of arc length. This means that both end-points of the field profiles in Fig. 4.27 refer to the same state.

Next, we want to take a closer look to continuous stationary states. One example of such a "current-voltage characteristic" is depicted in Fig. 4.28. The curve consists almost only of unstable starts. Starting from high voltage, the curve exists down to approximately $U = 0.5$ V – a small part of the curve is stable in that region – and turns back towards higher voltage. The corresponding field profile is depicted in Fig. 4.29 as a function of arc length. The end points correspond to the two states for $U = 5$ V.

Finally, we will come back to the distinction between field profiles of the types depicted in Figs. 4.25(d) and 4.25(g). If the doping density is increased a bit there are states like the ones depicted in Fig. 4.30. Subfigure (a) depicts the current-voltage characteristic, subfigure (b) the field profile as a function of arc length. The difference between this closed current-voltage characteristic and the closed characteristics presented before is that a part of it is stable. This part becomes larger when the doping density is increased. The creation of stable branches for higher doping happens only for this type of field profile.

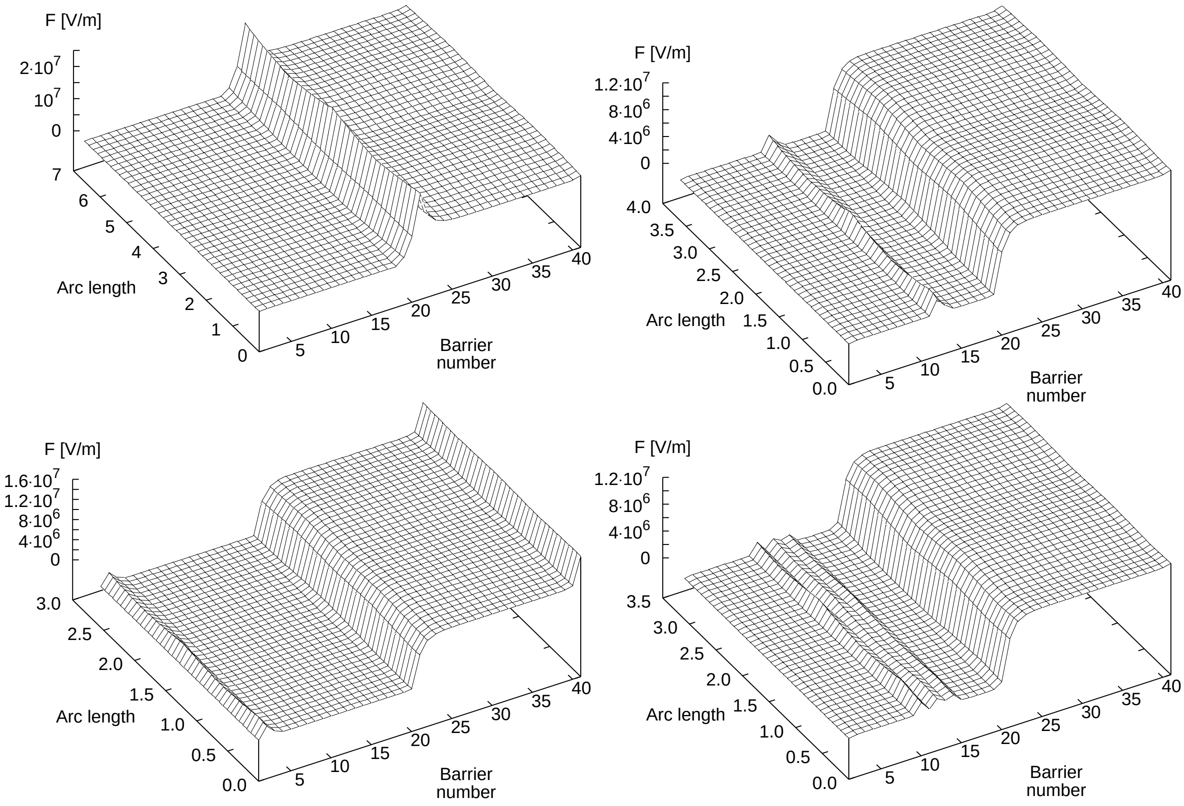

Figure 4.27: Field distributions corresponding to current-voltage characteristics in Fig. 4.26. The subfigures are marked with the same letter in both figures. For more information refer to the text.

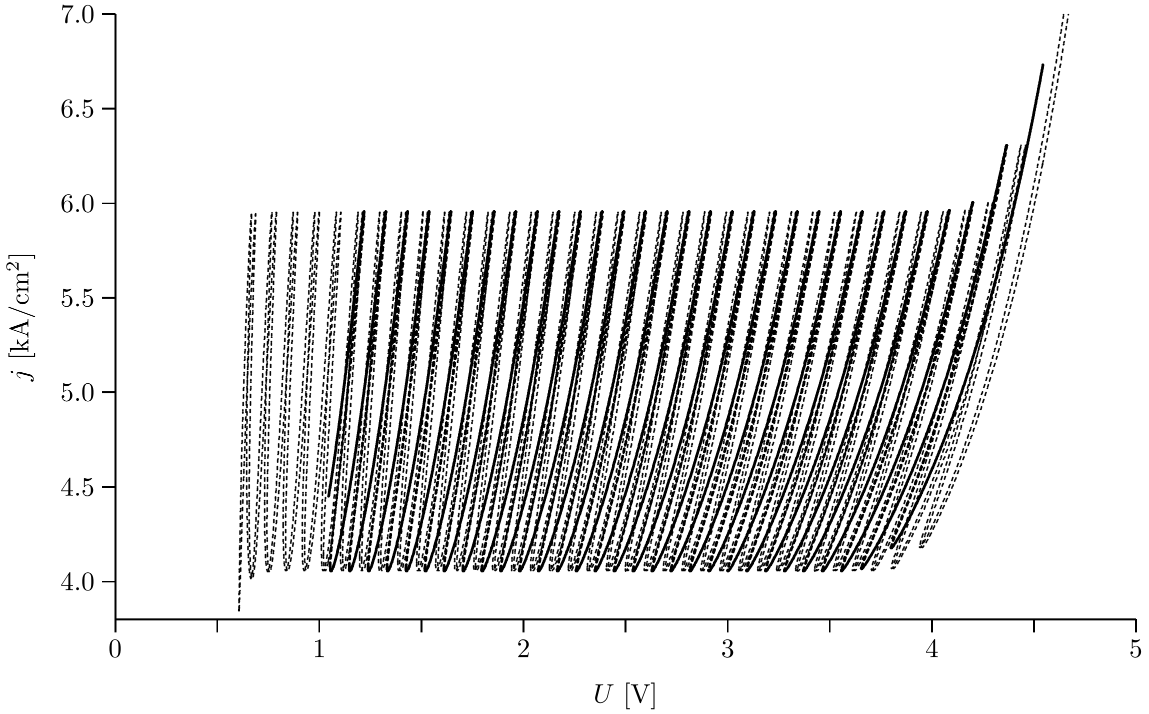

Figure 4.28: Example of an continuous “strange” current-voltage characteristic. The state depicted in Fig. 4.25(c) lies on this curve. The “standard” current-voltage characteristic has also been depicted.

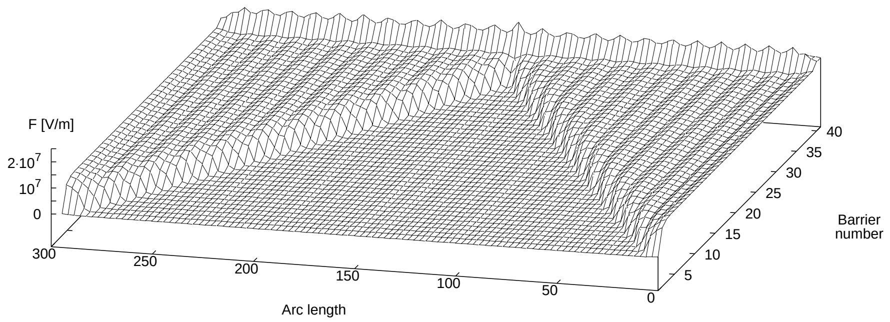

Figure 4.29: Field distribution along the “current-voltage characteristic” from Fig. 4.28.

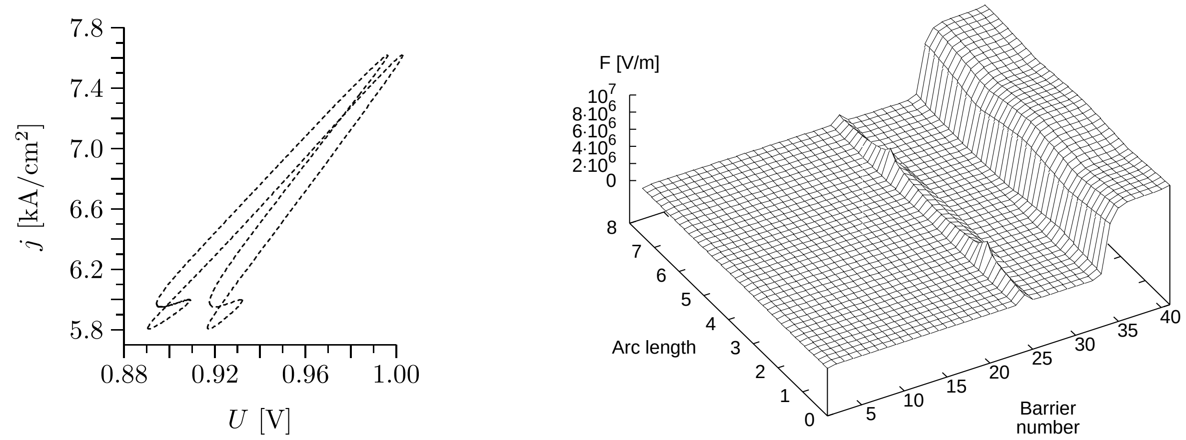

Figure 4.30: Isola of “strange” states with stable parts. **(a)** “Current-voltage characteristic”. **(b)** Field distribution as a function of arc length.

Chapter 5

Superlattices with Moderate Disorder

Until now, a superlattice has been described completely by the doping density N_D, the barrier width d and the quantum well width l. This means that the superlattice is strictly periodic, and there are thus no local fluctuations of these three parameters. Of course, these assumptions are not fulfilled for experimentally investigated superlattices. A better reproduction of measured current-voltage characteristics is therefore only possible if appropriate fluctuations are included in the model.

The model used throughout this thesis is only one-dimensional as it only describes the vertical transport of electrons along the growth direction (z-direction). It is therefore only possible to include fluctuations along the z-direction whereas fluctuations in the growth plane can not be dealt with. The question, whether the latter are relevant, can be answered be comparing the measured current-voltage characteristics from different samples taken from the same wafer [Hel90, Wac95b]. The result is that they show no important differences.[1] Considering only fluctuations along the z-direction is thus no important restriction.

The effects of fluctuations of the three hetero-parameters doping density N_D, quantum well width l and barrier width d have been compared in [Sch94, Sch95b]. One of the most important results is that increasing the width of a barrier by just a single mono layer results in a very strong and characteristic change in the current-voltage characteristic. More recently, this has been verified by growing a wafer with one intentionally widened barrier [Kas95a]. These characteristic features are found in just a few experimentally measured current-voltage characteristics. Since there should be no difference between growing barriers and growing quantum well, and since it should be equally likely for a layer to be thicker or thinner, this allows us to conclude that fluctuations of layer widths are very unlikely. It is thus sufficient to include only fluctuations of the doping density N_D such that it may differ slightly in each quantum well.

In this chapter We will thus discuss doping fluctuations. At first, We will analytically examine a simpler model than the one used otherwise in this thesis. The results from this simplified model will be checked on the "complete" model by numerical computations. After this has been done, computations for different amount of doping fluctuations will be presented.

The phenomena discussed in this chapter are independent of the amount of doping fluctuations. However, if the level is disorder is not to high, there are no additional effects. This is the reason why the chapter has been named "superlattices with moderate disorder".

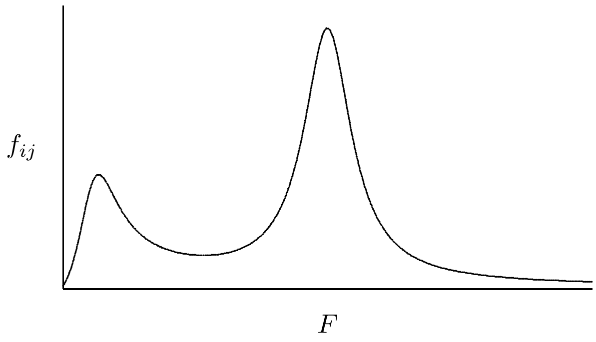

Figure 5.1: Qualitative shape of the $f_{ij}(F)$-characteristic. It has two maxima which determine the approximate values of the electric field in the high-field and in the low-field domain respectively. For doping densities at which the branches of the current-voltage characteristic are fully developed the necessary charge accumulation for a jump from low-field to high-field is approximately one half to one time the doping density.

5.1 Analytical Estimations

In this section, we will use a more simplified model, considering only one energy level in each quantum well. The temporal development of the electron densities n_k in the k-th well can then be written as

$$\dot{n}_i = \sum_j f_{ij} n_j. \tag{5.1}$$

The transport coefficient f_{ii} is smaller than zero as this term describes electrons leaving the i-th quantum well. All other transport coefficients are equal to or greater than zero. The number of nonzero coefficients is determined by whether only transport from one quantum well to the adjacent one is allowed.

The precise value of the coefficients f_{ij} depends only on the field profile in the superlattice. It, however, in turn depends on the effective charge density, that is, the difference between n_k and the doping density N_k in the k-th quantum well. It is obvious that there is no difference between an increase in n_k and an decrease in N_k as long as only the field profile is of interest. Thus, we can write:

$$\frac{\partial f_{ij}}{\partial n_k} = -\frac{\partial f_{ij}}{\partial N_k} \tag{5.2}$$

Now we consider a particular stationary state. Thus, we have:

$$0 \equiv \dot{n}_i = \sum_j f_{ij} n_j.$$

The rates $\dot{n}_i$ depend – directly and also indirectly via Poisson's equation – on the $\{n_k\}$ and the $\{N_k\}$. The equation above is thus an "invitation" to calculate all values of $\{n_k\}$ and $\{N_k\}$ so that the functional $\dot{n}_i[\{n_k, N_k\}]$ is zero. The same has then to be true for its differential:

$$0 = \mathrm{d}(\dot{n}_i) = \sum_k \frac{\partial \dot{n}_i}{\partial n_k} \mathrm{d}n_k + \sum_k \frac{\partial \dot{n}_i}{\partial N_k} \mathrm{d}N_k$$

Inserting (5.1) yields

$$0 = \sum_{k,j} \frac{\partial f_{ij}}{\partial n_k} n_j \mathrm{d}n_k + \sum_{k,j} f_{ij} \underbrace{\frac{\partial n_j}{\partial n_k}}_{\delta_{jk}} \mathrm{d}n_k + \sum_{k,j} \frac{\partial f_{ij}}{\partial N_k} n_j \mathrm{d}N_k + \sum_{k,j} f_{ij} \underbrace{\frac{\partial n_j}{\partial N_k}}_{0} \mathrm{d}N_k$$

---

[1] Actually, this is in agreement with what had to be expected: The diameter of the samples investigated is much larger than the thickness of each layer. Fluctuation with very short correlation length, commonly referred to as "interface roughness", average out and can only lead to measurable effects if the amount of interface roughness changes during the growth process [Dev86, Gra92, Ete93, Sch96c]. Effects on larger length scales are not likely as the thickness of the individual layers seldom fluctuates (see text).

Using 5.2, we can simplify to get:

$$\boxed{0 = \sum_{k,j} \frac{\partial f_{ij}}{\partial n_k} n_j (\mathrm{d}n_k - \mathrm{d}N_k) + \sum_k f_{ik} \mathrm{d}n_k} \tag{5.3}$$

This is an – unfortunately implicit – equation which allows to calculate the infinitesimal variations $\{\mathrm{d}n_k\}$ of the electron densities necessary so that the system will stay stationary when infinitesimal variations $\{\mathrm{d}N_k\}$ of the doping density are introduced. By integration this equation, it is possible to calculate the variations of the electron densities for finite variations for the doping densities. During this process, the field profiles and thus the transport coefficients f_{ij} and $\frac{\partial f_{ij}}{\partial n_k}$ have to be adapted by application of Poisson's equation.

We have to make additional assumptions if we want to derive some important predictions. We will only discuss the current-voltage characteristic of heavily doped superlattices, that is, current-voltage characteristics with fully developed branches in the characteristic. This implies that there are a high-field domain, a low-field domain and a sharp domain boundary. The values of the electric fields in the domains are a bit smaller than the positions of the maxima of the transport coefficients f_{ij} [Pre94a] whose qualitative shape is depicted in Fig. 5.1.

As has been demonstrated in the preceding chapter, the necessary charge accumulation for the formation of a domain boundary is about one half to one time the doping density. A small variation of an electron concentration n_i will thus change the transport coefficients quite strongly.[2] Thus we get,[3] where we simplify by assuming "natural" units (doping density and resonance field):

$$|\frac{\partial f_{ij}}{\partial n_k}| \gg |f_{ik}|$$

The term f_{ij} is part of a sum over j in equation 5.3. The sum over k causes no problems as the $\mathrm{d}n_k$ are independent of each other. The transport coefficient f_{ii} is smaller than zero; its absolute value, however, has a similar dependence on the field profile as the coefficients f_{ij} for $i \neq j$. Thus, the sign of the derivative $\frac{\partial f_{ii}}{\partial n_k}$ is opposite to that of $\frac{\partial f_{ij}}{\partial n_k}$ for $i \neq j$. Therefore, it might be possible that these term cancel each other so that the following inequality might not be true:

$$|\sum_j \frac{\partial f_{ij}}{\partial n_k} n_j| \gg |f_{ik}|$$

It is not possible to solve this problem using a simple argument but we will still make this assumption here.[4] Thus, we simplify (5.3) to yield:

$$0 = \sum_{k,j} \frac{\partial f_{ij}}{\partial n_k} n_j (\mathrm{d}n_k - \mathrm{d}N_k) \tag{5.4}$$

This can be written with vectors as

$$0 = A(\mathrm{d}\mathbf{n} - \mathrm{d}\mathbf{N}), \tag{5.5}$$

where the matrix A is given by $A_{ik} = \sum_j \frac{\partial f_{ij}}{\partial n_k} n_j$. If A is regular, the linear equation (5.5) possesses only the trivial solution. This can be written in components once again:

$$\boxed{\mathrm{d}n_k = \mathrm{d}N_k}$$

As the field profile depends only on the difference between n_k and N_k, we get the following

---

[2] If we want to discuss the slope of the $f_{ij}(F)$-characteristic, it is best to use a normed quantity like $\frac{1}{f_{ij}}\frac{\partial f_{ij}}{\partial F}$. Its absolute value is greater than 1 almost everywhere as can be seen from Fig. 5.1. If the electric field is changed by only 5 %, the transport coefficient is twice as large or only half as large as before. The only exception is the region around the maxima. The values of the electric field in the field domains differ enough from the positions of the maxima not to make this a problem [Pre94a]. Thus, for the electron configurations of interest to us, $|\frac{1}{f_{ij}}\frac{\partial f_{ij}}{\partial F}| \gg 1$ may be assumed as is done in the text.

[3] Of course this is not valid if we choose one of the transport coefficients which vanishes.

[4] The question, whether the different terms may cancel each other, depends on the details of the transport model used. The results from the numerical verifications in section 5.2 clearly show that we may use this assumption for the model used in this thesis. The "side effects" caused by this assumption are dealt with in theorem 3 and will be calculated quantitatively in section 5.2. The result will be that they are vanishingly small.

Theorem 1 *The field profile is – in first order – not affected by variations of the doping density.*

Furthermore, $\mathrm{d}n_i$ and $\mathrm{d}n_j$ are independent of each other for $i \neq j$. Thus, $\mathrm{d}N_i$ will only affect $\mathrm{d}n_i$ and no other $\mathrm{d}n_k$, $k \neq i$.

Theorem 2 *The effect of variation in the doping density is – in first order – only of a local nature.*

Next, we have to estimate what influence dropping the term $\sum_k f_{ik}\mathrm{d}n_k$ (from equation (5.3) to (5.4)) has. The is very difficult to do by using only "formal" mathematics. In its place we will resort to common sense: When the doping density in a particular quantum well is increased, the field distribution was not changed in first order, so did the transport coefficients f_{ij}. On the other hand, the electron densities were changed which means that the system will no longer be stationary (equation (5.1)). The transport coefficients f_{ij} thus have to be changed a bit to compensate for the variations in the electron densities.

If this is not done, there will be "too many" electrons in the quantum wells with increased doping density. Some of these electrons will move into the adjacent quantum wells, mainly into the wells in field direction (from the i-th well into the $(i+1)$-th well, that is, they will move "right").

Theorem 3 *The electron densities in quantum wells with increased doping density will not increase by as much as the doping density was increased. In its place, the doping density in the adjacent quantum wells, mainly those in field direction, will increase slightly. The opposite happens for quantum wells with decreased doping density.*

This leads to a change in the field distributions: The electrons which were supposed to lead to an increase in the electric field starting from the i-th quantum well will now do this starting from the $(i+1)$-th well. The electric field over the barrier between the i-th and the $(i+1)$-th quantum well thus decreases. If the original value of electric field over this barrier is to be restored, the applied external voltages has be increased. This applies especially to the point at which the particular stable branch will become unstable.

Theorem 4 *An increase in the doping density of a quantum well results in an increase in the voltage at which that branch will loose stability and vice versa.*

If the branch is shifted, the part of it reached during a voltage sweep-up will become longer or shorter. As only a small part of each branch is reached during a sweep-up or sweep-down, this effect becomes more prominent in a simulated or measured current-voltage characteristic than in the full connected one.

Theorems 1 and 2 considered only the field profiles and the electron densities. Both quantities are difficult to investigate experimentally. We are therefore interested in what the effects on the current density are. For this problem it is sufficient to consider only the first approximation in which the field profile does not change. Consequently, all transport coefficients, which also determine the current, do not change either, and the variation of the current depends only on the variation of the electron densities.[5] This applies especially to the maximum current on each branch as well as to the bifurcation point nearby.

Theorem 5 *The current density reached along a stable branch is directly proportional to the doping density of the corresponding quantum well.*

5.2 Numerical Verification

In the preceding section, a few predictions were made by analysing a simplified model. For a few of the assumptions made there, no general proof could be given. One could certainly think of sit-

---

[5] The current density j may be written as linear combination of the transport coefficients f_{ij} and the electron densities n_k. How this has to be done exactly, depends on the details of the model in question. If only transport from one quantum well to the adjacent quantum well in field direction is allowed, the current density through the barrier between the i-th and the $(i+1)$-th quantum well is given by $|f_{i+1,i}n_i|$.

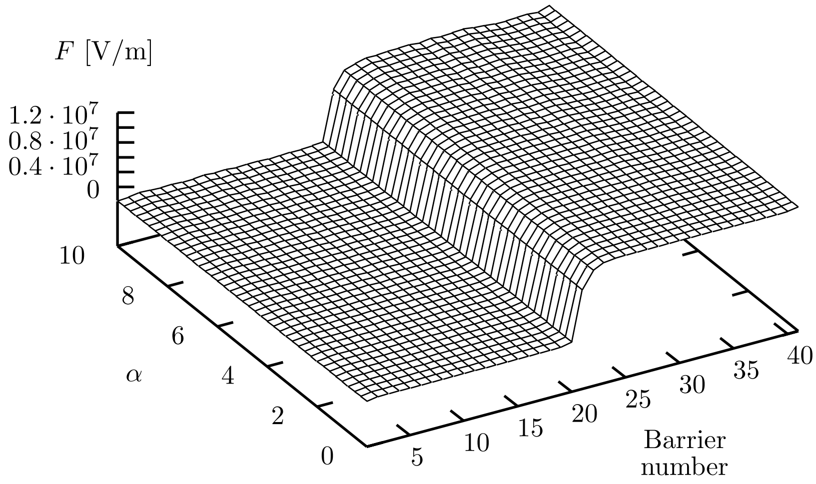

Figure 5.2: Dependence of the field profile on the level of disorder. Depicted is the field profile when the amount of fluctuations, α, is increased from $0\,\%$ to $10\,\%$. The data depicted is that of a saddle-node bifurcation point; the voltage U is adapted during the process so that the system stays on the bifurcation point (it moves by approximately 20 meV). As can clearly be seen in this figure, the field profile does almost not change at all.

uations where these assumptions are no longer valid. Thus, we will verify these predictions using the "complete" model.

In contrast to the analysis in the preceding sections, there is no sense in allowing independent fluctuations of the doping densities $\{N_k\}$. Especially for comparison with experimental data, we need some "global" indicator of the level of disorder. We thus introduce the *amount of doping fluctuations*, α. The fluctuation in a particular quantum well can then be determined by multiplying α with a "realisation" $\{e_i\}$. The doping densities $\{N_i\}$ are in this case given by:

$$N_i = N_D \cdot (1 + \alpha \cdot e_i)$$

The realisation consists of random numbers which are determined before the computation and are not changed after that. The realisations used throughout this thesis are listed in appendix H. With just a few exceptions, which are marked explicitly, the realisation from table H.2 was used. By reducing the variation of N doping densities $\{N_i\}$ to the variation of just a single quantity, namely α, it becomes possible to ask what is changed when the "level of disorder" is increased.

The first and probably the most important result from the preceding section has been that the field distribution is not changed when doping fluctuations are introduced (theorem 1). To verify this, the field distribution has been depicted in Fig. 5.2 in dependence on α. As has already been mentioned in theorem 4, the applied voltage has to be adjusted as the branch may move a bit. Since it is not easy to know in advance how much the voltage has to be increased or decreased, we resorted to the following procedure: The states depicted are those of a saddle-node bifurcation point. When α is increased, we have the additional constraint that the bifurcation condition still be fulfilled. This additional equation allows to adjust another parameter, for example the voltage U. This way, we can be certain that the same point relative to the entire branch is considered throughout the computation.[6] A change in the field distribution is hardly noticeable which means that this theorem has been verified.

Theorem 5 said that the current reached along a branch[7] is directly proportional to the doping

---

[6] Actually, this is not necessary if one is only interested in the field distribution. We assume heavy doping which means that we have a well-defined high-field domain and a well-defined low-field domain. The domains do not change much if the voltage is varied a bit. The problems really start if the branch is shifted (along the voltage axis) so much that the branch does not exist any longer for the voltage considered if α is increased above some threshold. At the very value of α for which the saddle-node bifurcation point lies at the considered voltage, one also sees a saddle-node bifurcation when α is varied. The direction of α is then inverted and one moves back along the unstable branch.

[7] It is not necessary to distinguish between the current at the highest point of the branch and the current at the bifurcation point nearby as the difference is extremely small.

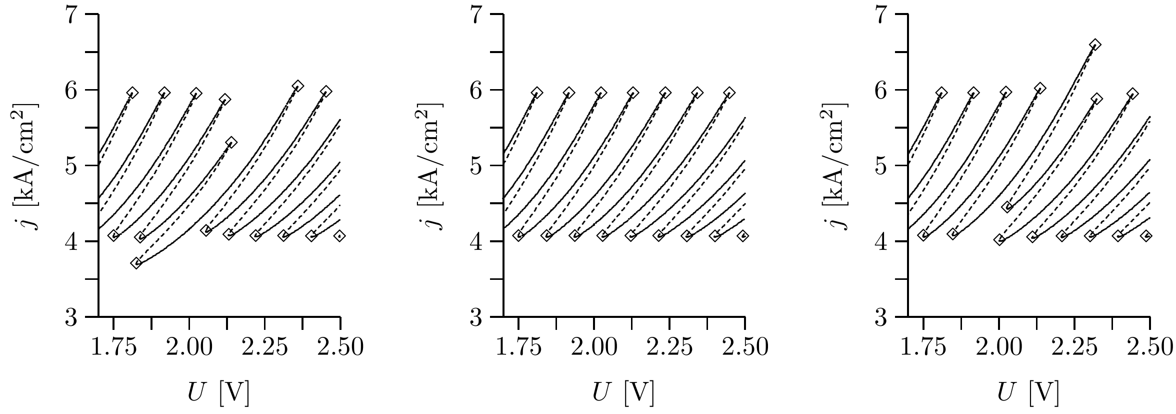

(a) 10 % smaller

(b) unchanged

(c) 10 % higher

Figure 5.3: Current-voltage characteristics of superlattices in which the doping density is changed by 10 % in just a single quantum well. The corresponding part of an unperturbed characteristic is also depicted.

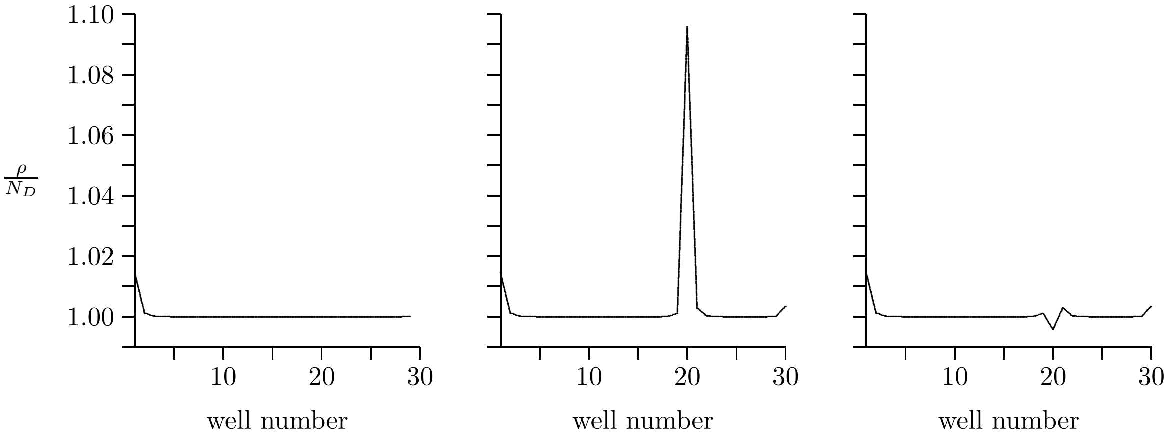

(a) $\alpha = 0\,\%$

(b) $\alpha = 10\,\%$

(c) $\alpha = 10\,\%$, after corrections

Figure 5.4: Dependence of the electron density on the amount of fluctuations. Depicted is the electron density in only the first 30 quantum wells. The charge accumulation is located in the 32-th well and would otherwise hide the relevant effects. **(a)** Unperturbed superlattice. **(b)** Perturbed Superlattice with $\alpha = 10\,\%$. **(c)** Like subfigure b with the exception that the doping fluctuations in the individual quantum wells have been subtracted. This allows the see the effects described by theorem 3.

density in the corresponding quantum well. To verify this, the current-voltage characteristic of two superlattices, in which the doping density in just a single quantum well is increased respectively decreased by 10 %, were calculated and are depicted in Fig. 5.3 along with an unperturbed characteristic. The maximum current is also increased respectively decreased by 10 % compared with the other branches or with the unperturbed superlattice. In addition, the voltage shift of the branches as predicted by theorem 4 can also be seen quite clearly. The effect of this single doping variation is local in that the other branches of the current-voltage characteristic are hardly affected.

The prediction that the field distribution is not changed by doping fluctuations was later corrected by theorem 3. Its effect, however, is so small that it can only be seen if the domain boundary is located far from the location of the imperfection. The electron density profile of a superlattice, in which the doping density is increased in a single quantum well (the 20-th) by α, is depicted in Fig. 5.4; Fig. 5.4(b) depicts the case $\alpha = 10\,\%$. In Fig. 5.4(c), the electron density in the 20-th well has been reduced by α to compensate for the effects of theorem 1. If this figure is compared with the unperturbed profile from Fig. 5.4(a), it can be seen that the electron density in the 20-th quantum well is indeed decreased slightly (compared with the predictions from theorem 1), and that the electron densities in the two adjacent wells – especially the one in field direction – are increased. However, this effect is too small to be of any importance.

The local correlation between the doping densities in the individual quantum wells and the current densities shall now be verified for a superlattice with "realistic" fluctuations. An enlarged part of the current-voltage characteristic is depicted in Fig. 5.5. The realisation used in this figure has also been used for most of the computations presented in this thesis. Each branch is marked with a number which indicates how much the doping density is increased or decreased in the quantum well, in which the domain boundary is located along that branch.[8] The two branches at each end of the current-voltage characteristic have not been marked as the currents reached on these branches differs from that on the other branches already for an unperturbed superlattice (see Fig. 4.2). The result is that even if there are fluctuations everywhere the entire superlattice, there still is a mostly good correlation between current density and doping density. Of course, there a few deviations where, for example, the doping density in a quantum well is a bit smaller than that in the adjacent well but the current density is a bit higher. Still, theorem 2 can be considered as being verified.

With this knowledge it is possible to "read" the amount of fluctuations, α, off the calculated (full connected) current-voltage characteristic: One just has to determine the minimum and the maximum current (density) at which branches become unstable. These values are $j_{max} = 3.95$ kA/cm^2 and $j_{min} = 3.39$ kA/cm^2 for the characteristic in Fig. 5.5; the current at the bifurcation points thus fluctuates by $\Delta j = 0.28$ kA/cm^2 around an average of $j_0 = 3.67$ kA/cm^2. This corresponds to 7.7 % which is in good agreement with the value $\alpha = 8\,\%$ used for computing the characteristic. This value can be improved to $\alpha = 8.06\,\%$ by a short calculation[9].

5.3 Different Levels of Disorder

Three current-voltage characteristics for different values of α are depicted in Fig. 5.6. As has been shown in the preceding sections, there is no qualitative difference as far as only the full, connected current-voltage characteristic (solid line in normal strength) is concerned. Furthermore, it is marked in the figure which parts of the characteristics are actually reached experimentally or by numerical simulations. Both the voltage sweep-up and the voltage sweep-down are marked with thicker lines; the sweep-down is dashed so it can be distinguished from the sweep-up.

Comparing the characteristic for $\alpha = 4\,\%$ (Fig. 5.6(b)) with the corresponding curve for a perfect superlattice (Fig. 5.6(a)), one can see that the length of the part of each branch reached during sweep-up or sweep-down changes quite substantially whereas the total length of each branch is changed only slightly. By combining voltage sweep-up and voltage sweep-down, every point on each stable part can nevertheless still be reached.

For $\alpha = 8\,\%$, the qualitative structure of the continuous current-voltage characteristic has not changed, either. However, certain stable branches are missed out by both a voltage sweep-up and a voltage sweep-down. These branches can thus no longer be found experimentally. It is also possible for a branch to be missed out only by either a voltage sweep-up or by a voltage sweep-down.

The condition for a branch to be missed out during a voltage sweep-up is that its right end-point (saddle-node bifurcation point) lies at a smaller voltage than the corresponding point of the branch left to it. Correspondingly, a branch is missed out during a voltage sweep-down if its left end-point lies at a higher voltage than the corresponding point of the branch right to it. It order to check whether branches are missed out for a given α it is thus not necessary to actu-

---

[8] Actually, the domain boundary is located in the quantum well right to the well whose doping density is "scanned". To decide whether it should be this way or the way it is stated in the text, one would have to know whether transport is more efficient in the high-field domain, in the low-field domain or in the domain boundary. The quantum well which is limiting the current the most is the one whose doping density will be seen in the current-voltage characteristic.

[9] If we say that a certain superlattice has a particular value of α we do not mean that there actually has to be one quantum well in which the doping density is higher by α, and one in which the doping density is smaller by α. As could already be seen in Fig. 5.5, the highest doping density is higher by just 0.936α, the smallest smaller by 0.958α. The value for α thus has to be multiplied by $2/(0.936 + 0.958)$. For experimental data, of course, there is no information about the realisation of the fluctuations available so statistical methods have to be used.

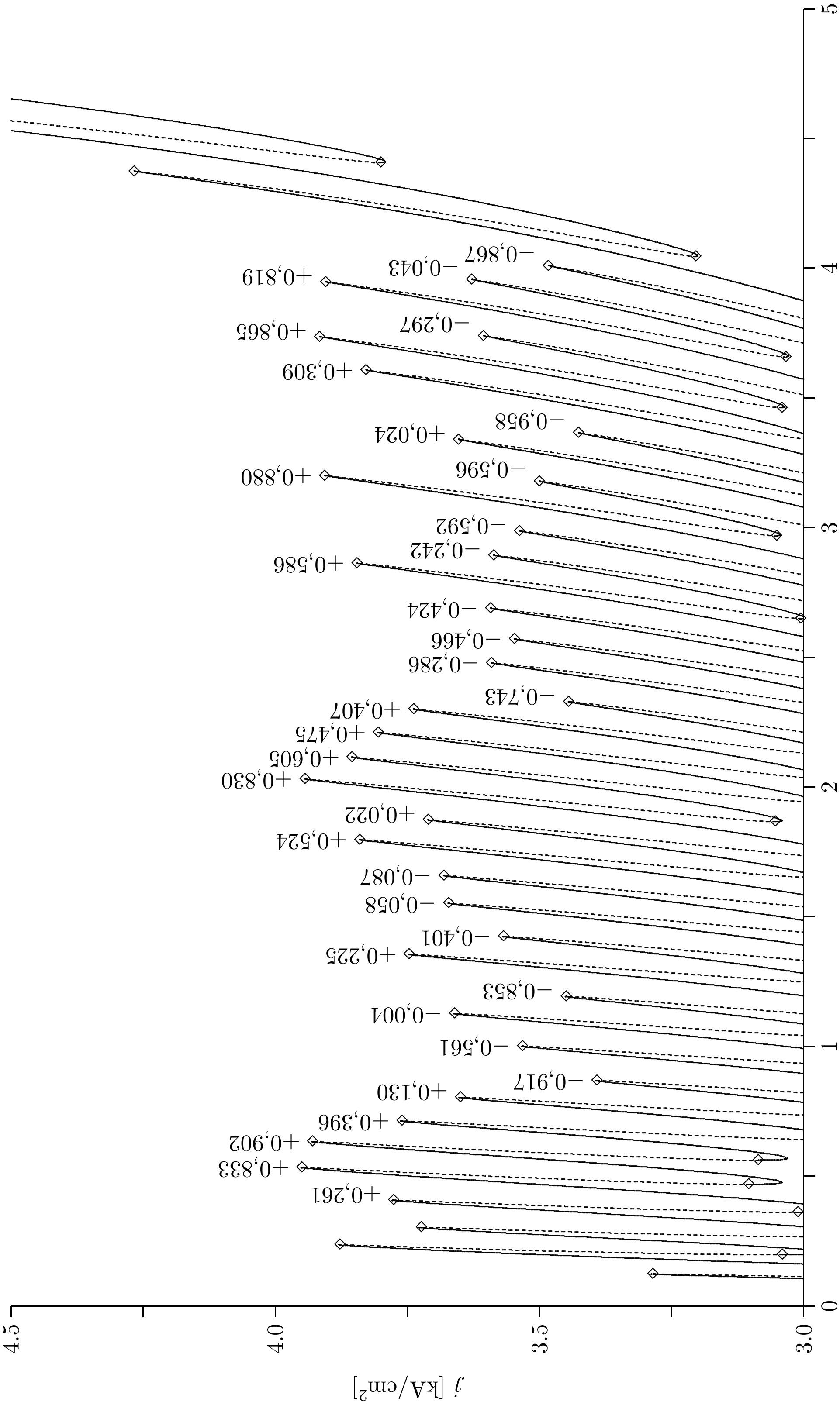

Figure 5.5: Current-voltage characteristic of a superlattice with doping fluctuations. For each branch it is indicated how the doping density in the corresponding quantum well differs from the "standard" doping density. This number has to multiplied with $\alpha = 8\,\%$ to determine the variation of the doping density.

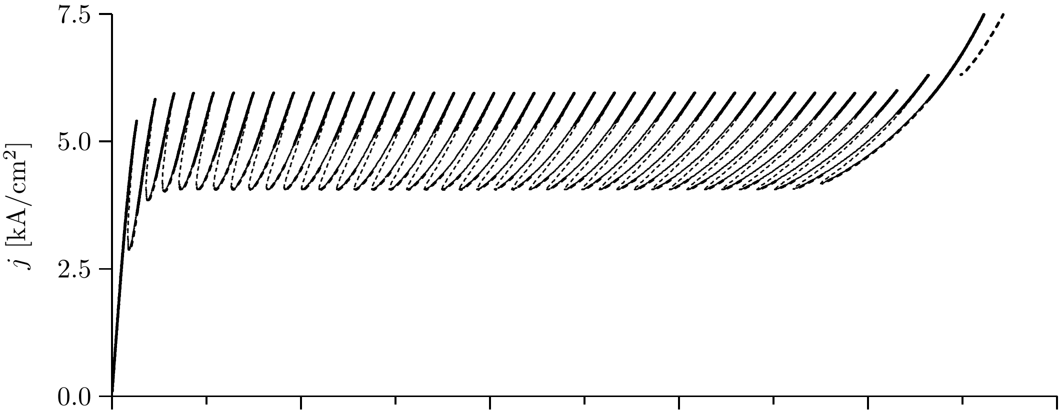

(a) $\alpha = 0\,\%$

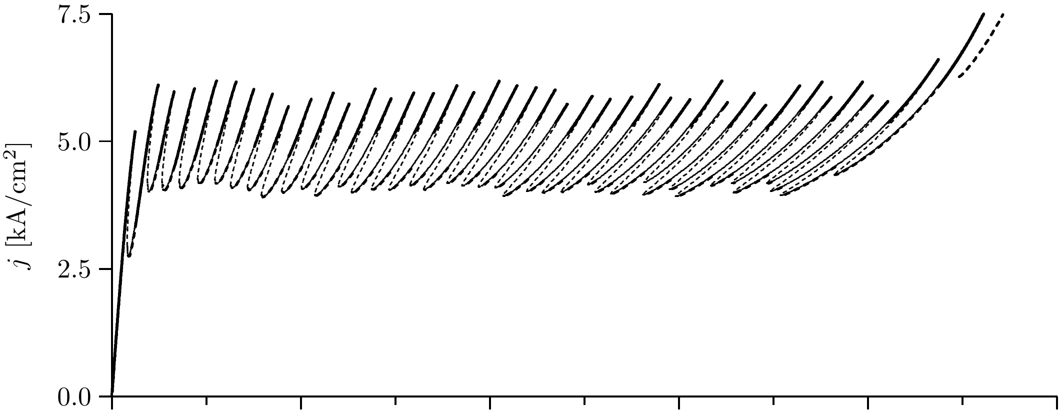

(b) $\alpha = 4\,\%$

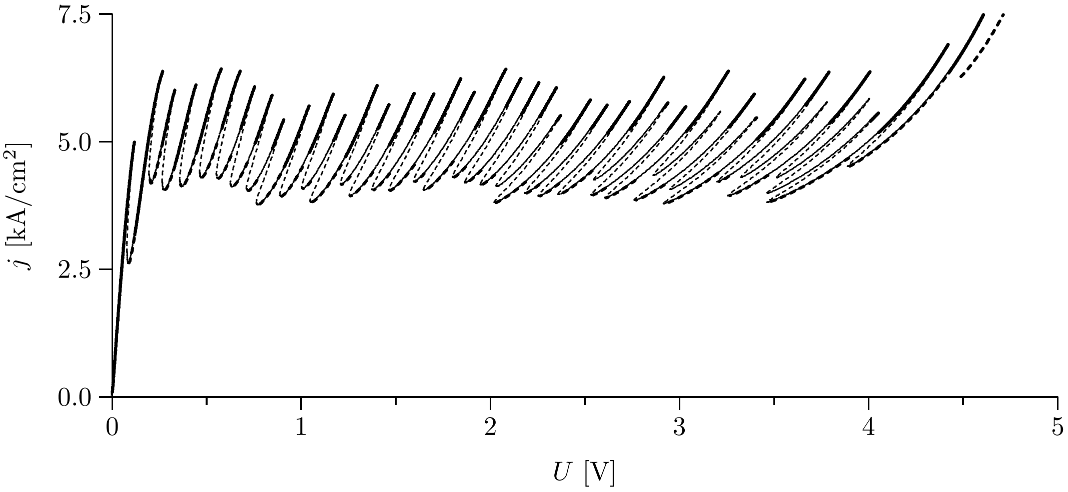

(c) $\alpha = 8\,\%$

Figure 5.6: Simulated voltage sweep-up and voltage sweep-down for superlattices with different amount of doping fluctuations, α. The sweep-up and sweep-down are marked with thick lines, the sweep-down is also dashed. In subfigure **(c)**, some branches are missed out altogether by both the sweep-up and the sweep-down.

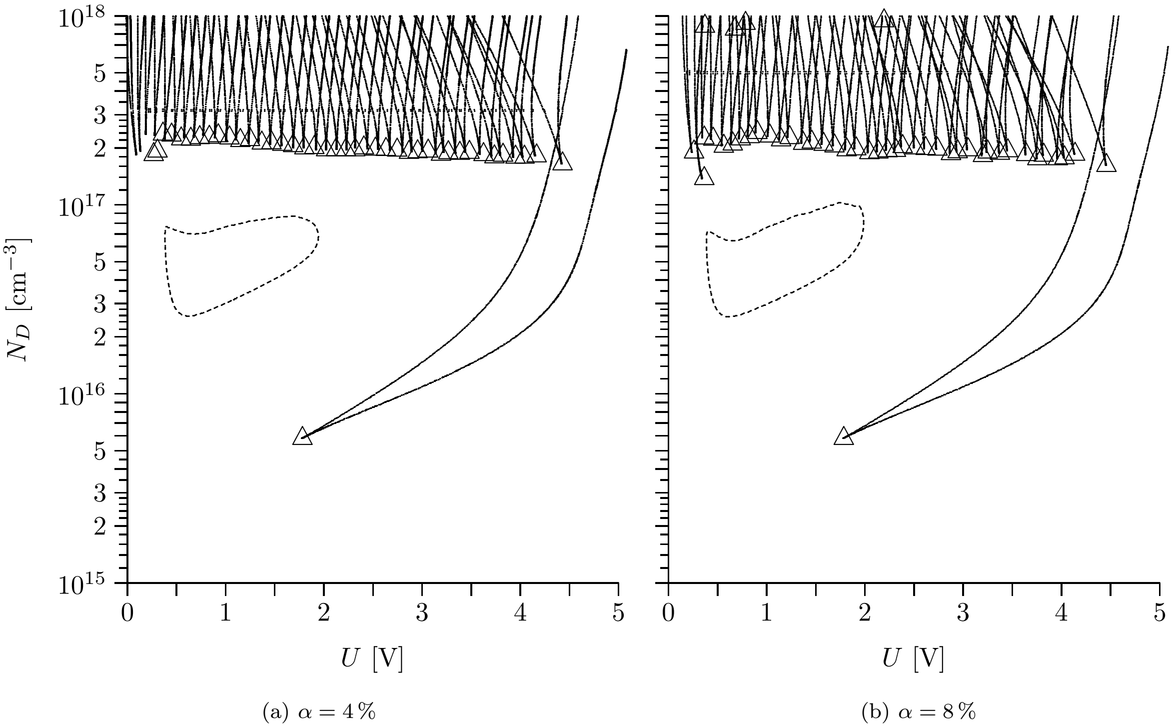

(a) $\alpha = 4\,\%$

(b) $\alpha = 8\,\%$

Figure 5.7: Positions of the bifurcation points ("phase diagram") for different values of α. The corresponding diagram for an unperturbed superlattice is depicted in Fig. 4.22 on page 42.

ally compute the current-voltage characteristic for the given α. Already sufficient is a diagram of the positions (voltage U) of all saddle-node bifurcation points in dependence on α. However, such a diagram is rather impractical as one has to know which two saddle-node bifurcation points started in the same cusp point. This knowledge is only available if the cusp points are also visible. This is no problem if the location of the bifurcation points is depicted in the U-N_D-plane for fixed α as all cusp points are included then. If, on the other hand, the positions are depicted in the U-α-plane for fixed N_D, then there will only be cusp points visible when N_D is just at the threshold for the formation of branches to start; in this case, α will decide whether and where there are branches.

As a result we have to resort to depicting the bifurcation points in the U-N_D-plane. Two diagrams for different α are displayed in Fig. 5.7. Using this diagrams it is possible to check whether any branches are missed out for given α and given doping density N_D. Usually, branches are missed out first for higher voltage; as the slope of the branches is less steep there, smaller variations in the length of each branch are sufficient.

The positions of the Hopf bifurcation points have been included in Fig. 5.7. Just as for the unperturbed case, the Hopf bifurcations are supercritical. This means that there are oscillations only inside the closed Hopf bifurcation curve. The oscillation amplitudes and frequencies have been determined in dependence on U and N_D and are depicted in Fig. 5.10. If the area enclosed by the Hopf bifurcation points is changed, so is the area in which amplitude and frequency are nonzero. Apart from that, the amplitudes and frequencies are not affected much by doping fluctuations (compare with Fig. 4.15 on page 37).

Finally, current-voltage characteristics for different doping densities and different amount of disorder are depicted in Figs. 5.9 and 5.8. Shown is the characteristic as seen during a voltage sweep-up as well the stable parts of the full continuous characteristic. The qualitative effects (the branches are shifted etc.) are the same regardless of how high the doping density is. However, other effects like the missing-out of branches happens for smaller values of α if the doping density is higher.[10].

---

[10] This is the reason why the "standard" doping density used in this thesis is higher than that used, for example, in [Sch95b]. As the main focus of this thesis was not to reproduce experimental data in detail, the doping density was chosen so as to "optimise" the effects of interest.

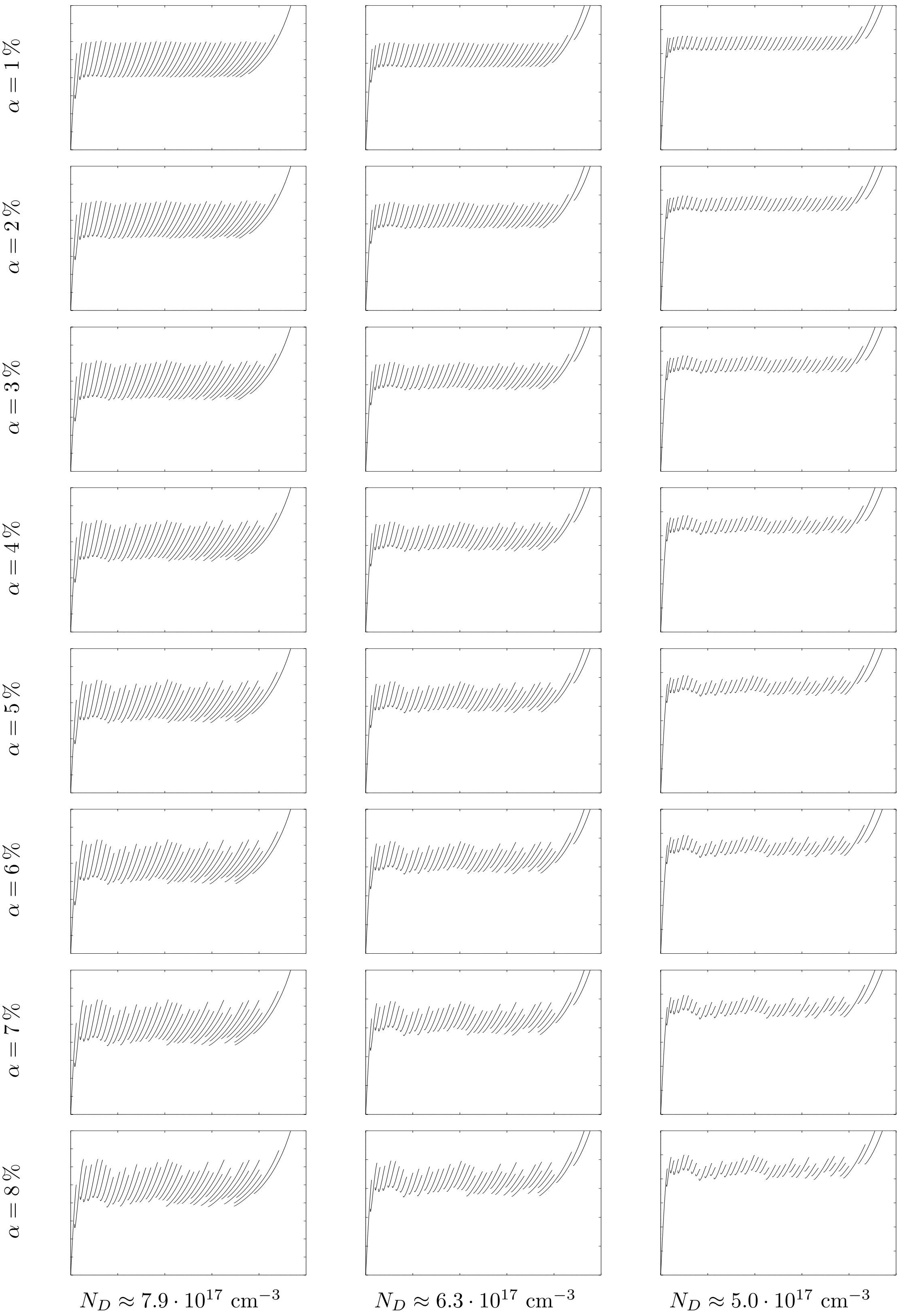

Figure 5.8: Stable parts of the full connect current-voltage characteristic for different values of α and N_D. x-axis: U [V] $(0-5)$, y-axis: j [kA/cm^2] $(0-8/0-5/0-3)$. The lengths of the branches change as the doping density does; the "pattern" of longer and shorter branches, however, does not.

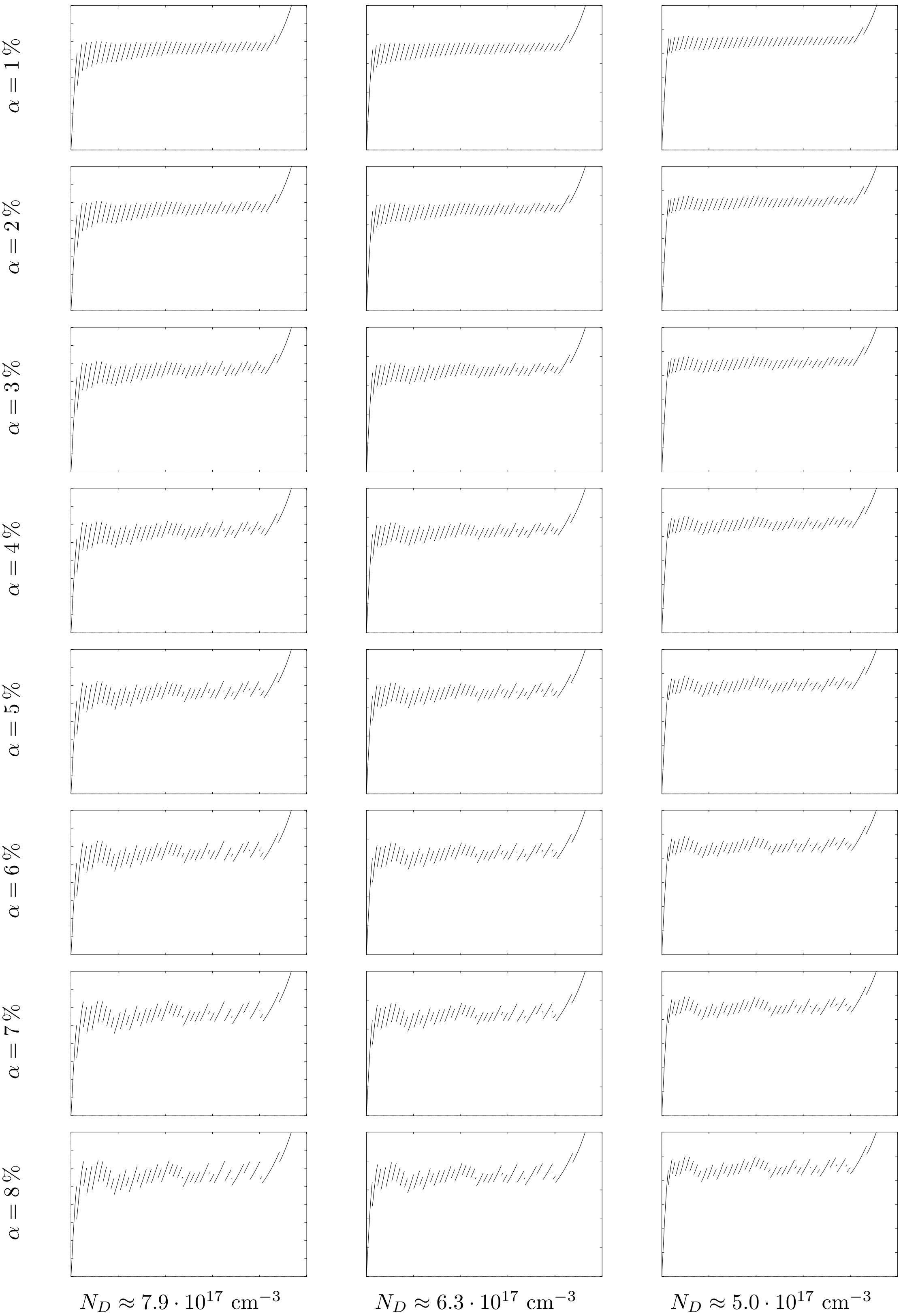

Figure 5.9: Simulated voltage sweep-up for different values of α and different doping density; otherwise this figure is identical to Fig. 5.8. In contrast to the full connected characteristic, the doping density is very import for whether branches are missed out.

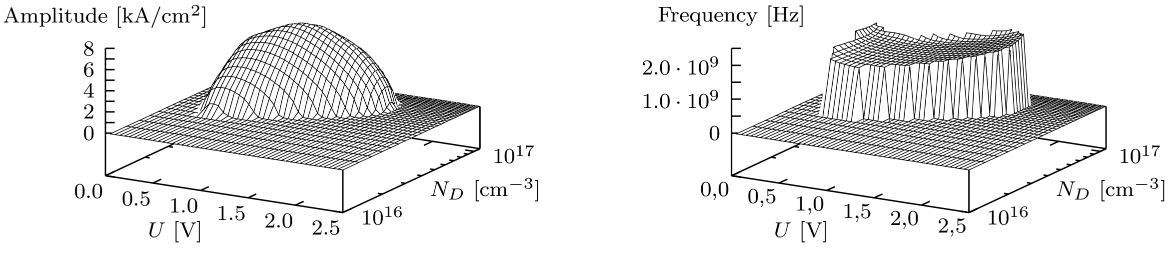

(a) Amplitudes for $\alpha = 4\,\%$ (b) Frequencies for $\alpha = 4\,\%$

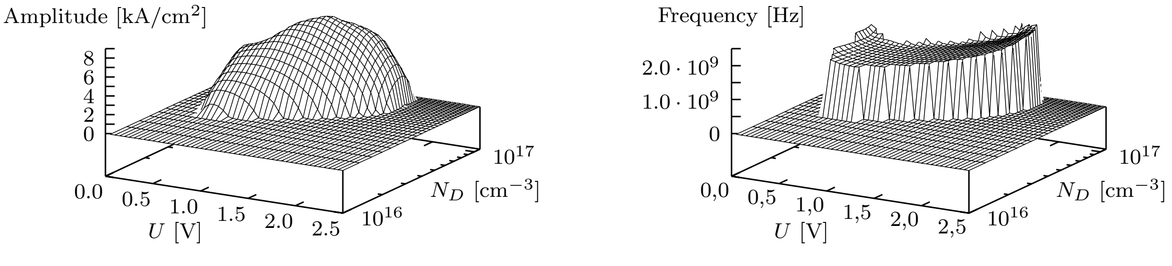

(c) Amplitudes for $\alpha = 8\,\%$ (d) Frequencies for $\alpha = 8\,\%$

Figure 5.10: Dependence of the oscillation frequency and amplitude on doping density N_D and voltage U for superlattices with different α.

5.4 Comparison of Different Realisations

In sections 5.1 and 5.2, it was demonstrated that there is a direct correlation between the local doping densities in the individual quantum wells and the branches of the current-voltage characteristic. Thus, for the case of high doping, it is trivial to compare the effects of different realisations. However, this question is very interesting as far as the existence of oscillations is concerned.

The result of the preceding section was that the oscillation frequencies do almost not change at all when fluctuations of the doping density are introduced. The oscillation amplitudes change but mainly due a shift and a deforming of the parameter region in which there are oscillations. The easiest way to investigate this problem is to directly compare the locations of the Hopf bifurcation points.

In order to have large effects, $\alpha = 12\,\%$ is chosen. At these value of α, the branch structure at high doping is no longer only “moderately perturbed”. However, for lower doping, the system is still moderately perturbed for most of the realisations examined, especially for the “standard” realisation used throughout most of this thesis.

Fig. 5.11 depicts the phase diagram for four different realisations of the fluctuations. The precise values of the doping densities in the individual quantum wells can be determined from appendix H. The dashed curve marks the corresponding curve for an unperturbed superlattice. The oscillatory regimes for the four realisations differ quite strongly, both in the precise shape and in the degree in which the curve is affected at all. For example, the curve in Fig. 5.11(c) does almost not change at all.

A correlation between the features of the Hopf bifurcation curve and the doping densities in the individual quantum wells cannot be determined, however. As has been states in section 4.6, the oscillation affects a region of approximately 15 quantum wells at the same time. Thus, most of the details of the realisation will be averaged out.

Nevertheless, at first we will investigate the effects of single perturbations, that is, the doping density is changed in just a single quantum

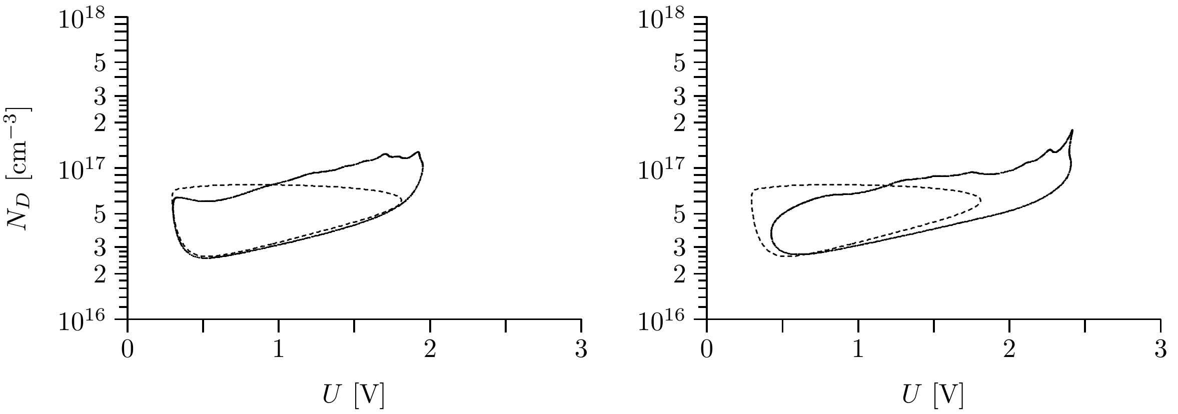

(a) "Standard" realisation

(b) Realisation 4

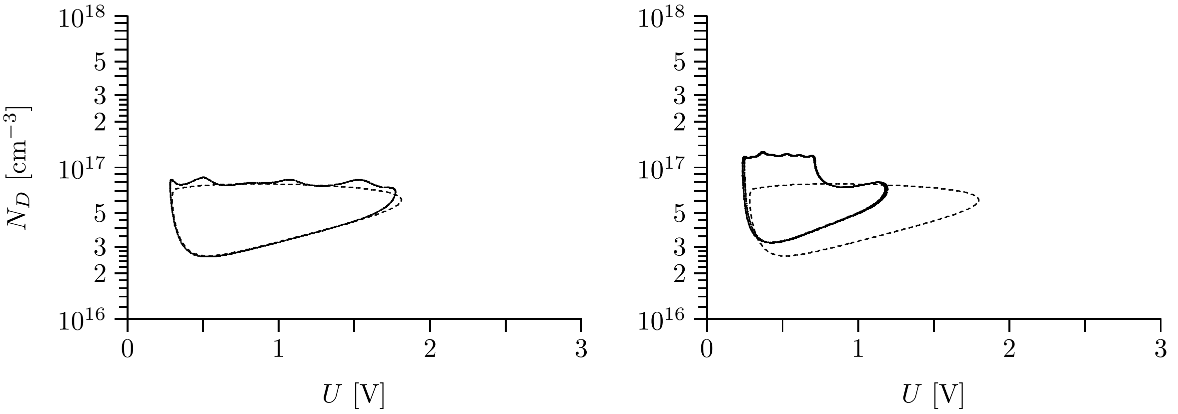

(c) Realisation 6

(d) Realisation 7

Figure 5.11: Comparison of the region, in which there are oscillations, for different realisations of the fluctuations for the same amount of disorder. The locations of the Hopf bifurcations for $\alpha = 12\,\%$ are marked as solid line; the dashed line marks the locations for an unperturbed superlattice. **(a)** "Standard" realisation used for most of the figures in this thesis. **(b)**-**(d)** Other realisations (see appendix H for details).

well. The effects of such variations are depicted in Fig. 5.12 for different quantum wells. With increasing voltage, the high-field domain (it is a washed-out domain for the doping densities considered here) expands, starting at the anode. Thus, we may expect that wells lying near the anode (large quantum well index) have mainly an effect for low voltage and vice versa. In principle, this is confirmed by the figure. However, there is an additional effect for quantum well indices smaller than about 15: As could be seen in Fig. 4.7(d) on page 31, oscillations appear when a small charge accumulation forms near the cathode, moves towards the anode and grows while doing so. Thus, perturbations near the anode (small quantum well index) will have a smaller effects as the charge accumulation is only very small when it is located in these quantum wells. Thus, there will be a specific quantum well in which an increase in the doping density will result in a oscillatory regime that extends the most towards high voltage. For smaller quantum well indices, there will also be an extension towards higher voltage but the effect will be smaller. The "optimum" quantum well index is about 17 or 18 (see Fig. 5.14).

The results are similar for a decrease of the doping density in a particular quantum well (Fig. 5.13). Considering a sequence starting at the 35-th well and ending at about the 20-th, one can see a monotone change in the shape of the oscillatory regime. However, the details of the shapes of the curves are even more difficult to explain than for the case of increased doping; there is a trend for the effects of increased and decreased doping to be inverse.

Fig. 5.14 depicts the result if the doping density is increased not in a single but in two quantum

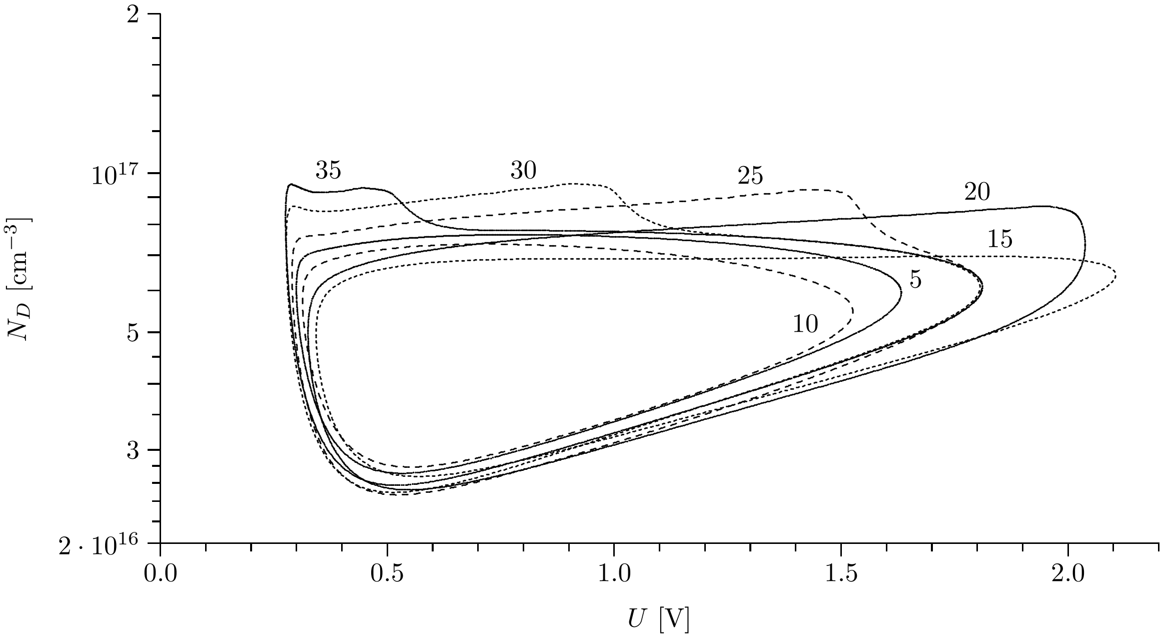

Figure 5.12: Locations of all Hopf bifurcation points ("phase diagram") for different superlattices in which the doping density is increased by $12\,\%$ in a single quantum well. The numbers on the curves are the indices of the quantum well in which the doping density is altered.

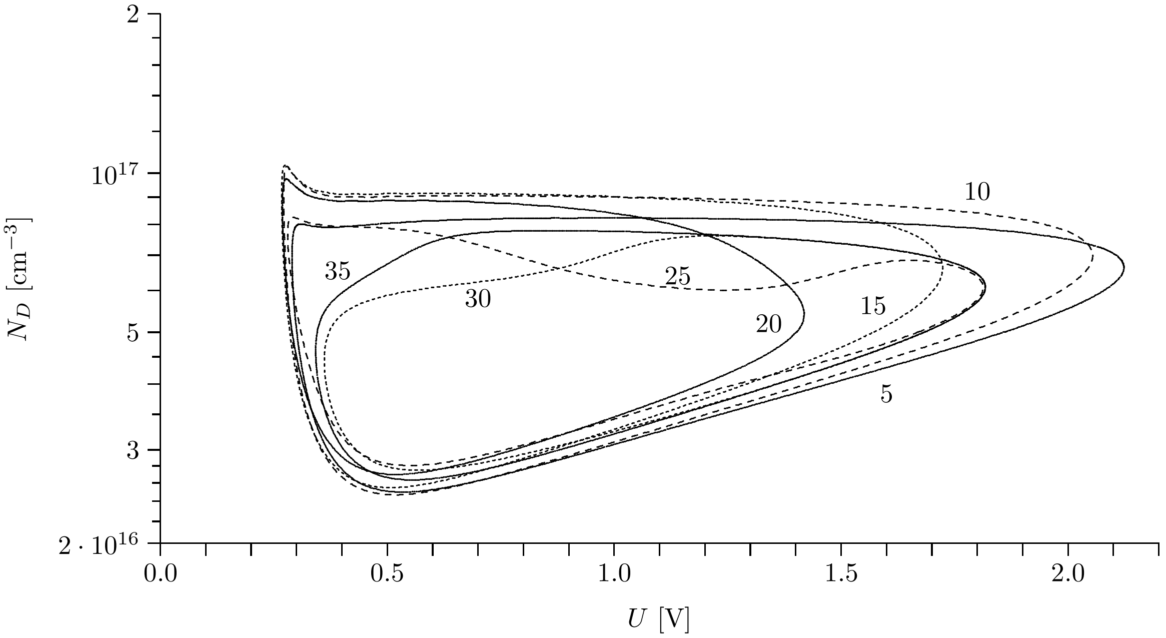

Figure 5.13: Locations of all Hopf bifurcation points ("phase diagram") for different superlattices in which the doping density is decreased by $12\,\%$ in a single quantum well. The numbers on the curves are the indices of the quantum well in which the doping density is altered.

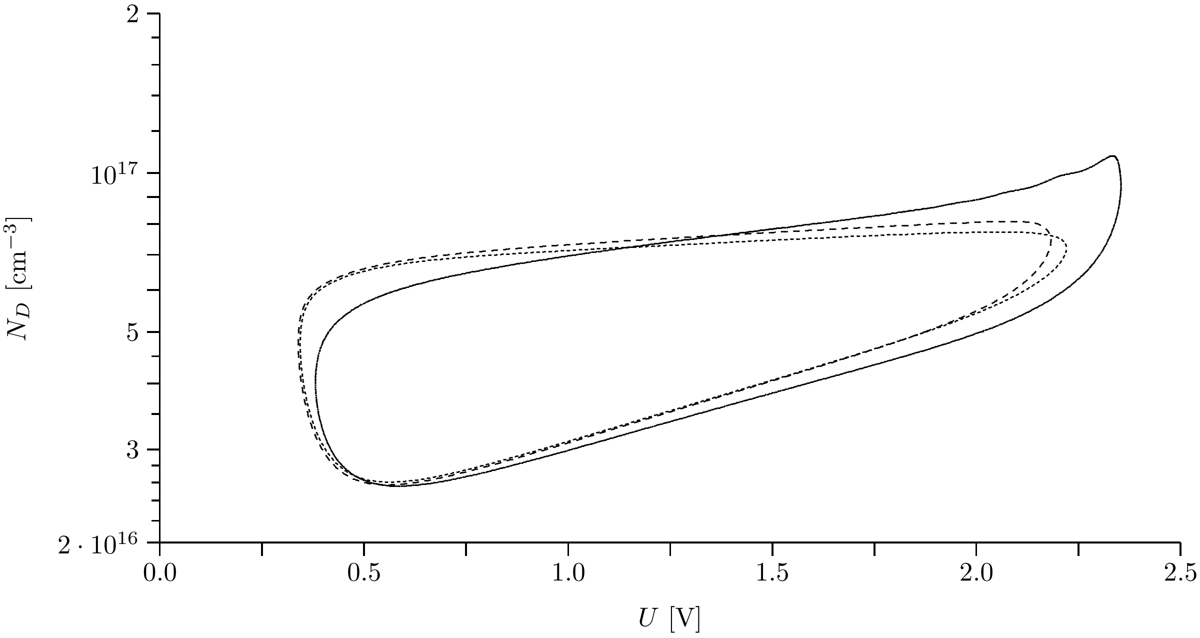

Figure 5.14: Locations of the Hopf bifurcation points ("phase diagram") for a superlattice, in which the doping density is increased in two quantum wells. The short respectively long dashes mark the locations for a superlattice in which the doping density in the 17-th respectively 18-th quantum well is increased by 12 %. The solid line marks the locations for a superlattice with both imperfections present.

wells at the same time. The quantum wells chosen were the 17-th and the 18-th as these are the quantum wells which show the largest effect for single perturbations. Comparing the curve for the double perturbation with the curves for single perturbations, the oscillatory regime extends to even higher voltages. Furthermore, the oscillatory regimes also extends towards higher doping which is difficult to explain from the effects of single perturbations.

By investigating the effects of single perturbations, some features of the curves in Fig. 5.11, for example the plateau from Fig. 5.11(d), can be explained. However, the curves are deformed by additional effects, and the effects of increased and decreased doping in different quantum wells can compensate each other. As Fig. 5.11(c) clearly demonstrates, one cannot determine the local properties of the realisation used, not even the "global" level of disorder, α. At the present, it does not help to investigate oscillations in order to learn something about the disorder of the superlattice in question.

This will not change even if a "perfect" model is found: Oscillations are not confined to one or two quantum wells but depend on the properties of a large number of quantum wells. Thus, it will always only be possible to determine same "averaged" quantities. Investigating the current-voltage characteristic at high doping does not have such problems.

Chapter 6

Superlattices with Strong Disorder

As has been hinted at in the preceding chapter dealing with “moderate disorder”, there are additional effects once the level of disorder, α, is increased above a certain threshold: The *qualitative* shape of the current-voltage characteristic will then change.

If we consider a particular perturbed current-voltage characteristic, we may ask how its different parts (stable branches, unstable branches and bifurcation points) are connected with the ones of the corresponding unperturbed characteristic. For moderate disorder, this question is easy to answer and is dealt with in section 5.1.

For strong disorder, not only the answer but even the question becomes more complex. The questions which “unperturbed parts” belong to same particular section of the perturbed characteristic, and which “perturbed” parts belong to same particular section of the unperturbed characteristic, are no longer equivalent and have to be answered individually.

6.1 Starting with the Unperturbed Characteristic

If one considers a particular state at a particular value of α and wants to determine, to which state for a different value of α it is connected, is usually not sensible to simply “increase” α. Due to this reason, only bifurcation points were considered in chapter 5 as it is then possible to also adapt U so that the bifurcation condition is still fulfilled. This is even more important for strong disorder.

Here we start with a section of an unperturbed current-voltage characteristic. The computed saddle-node bifurcation points are the numbered, i. e., the number corresponds to the sequence the bifurcation points form along the continuous current-voltage characteristic. For these bifurcation points, α is the increased from $0\,\%$ to $10\,\%$ while adapting the value of U.

Next, a current-voltage characteristic for $\alpha = 10\,\%$ is computed. Now, we can compare the bifurcation points along this characteristic with the bifurcation points described in the preceding paragraph. The result is depicted in Fig. 6.1, an enlarged section is displayed in Fig. 6.2.

The largest part of the perturbed characteristic resembles the ones presented in the chapter on superlattices with moderate disorder. Furthermore, for every bifurcation point on the unperturbed characteristic, there is a corresponding bifurcation point on the perturbed characteristic. However, there is a large number of additional states which cannot be explained from the unperturbed characteristic. Please remember that all branches form just a *single*, continuous curve. The “tangle” lies between the bifurcation points labelled “12” and “13”. Thus, if we start on the right, we move along states connected with parts of the unperturbed characteristic until we get to the point “13”, then we move through the “tangle” until, starting at the point “12”, we once again move along states connected to the unperturbed characteristic.

Especially in the enlarged section depicted in Fig. 6.2, there is a large number of additional branches – only a small part of which are stable – which cannot be explained by simply discussing the unperturbed characteristic. Thus, we have to investigate what happens with these “additional” states if α is decreased.

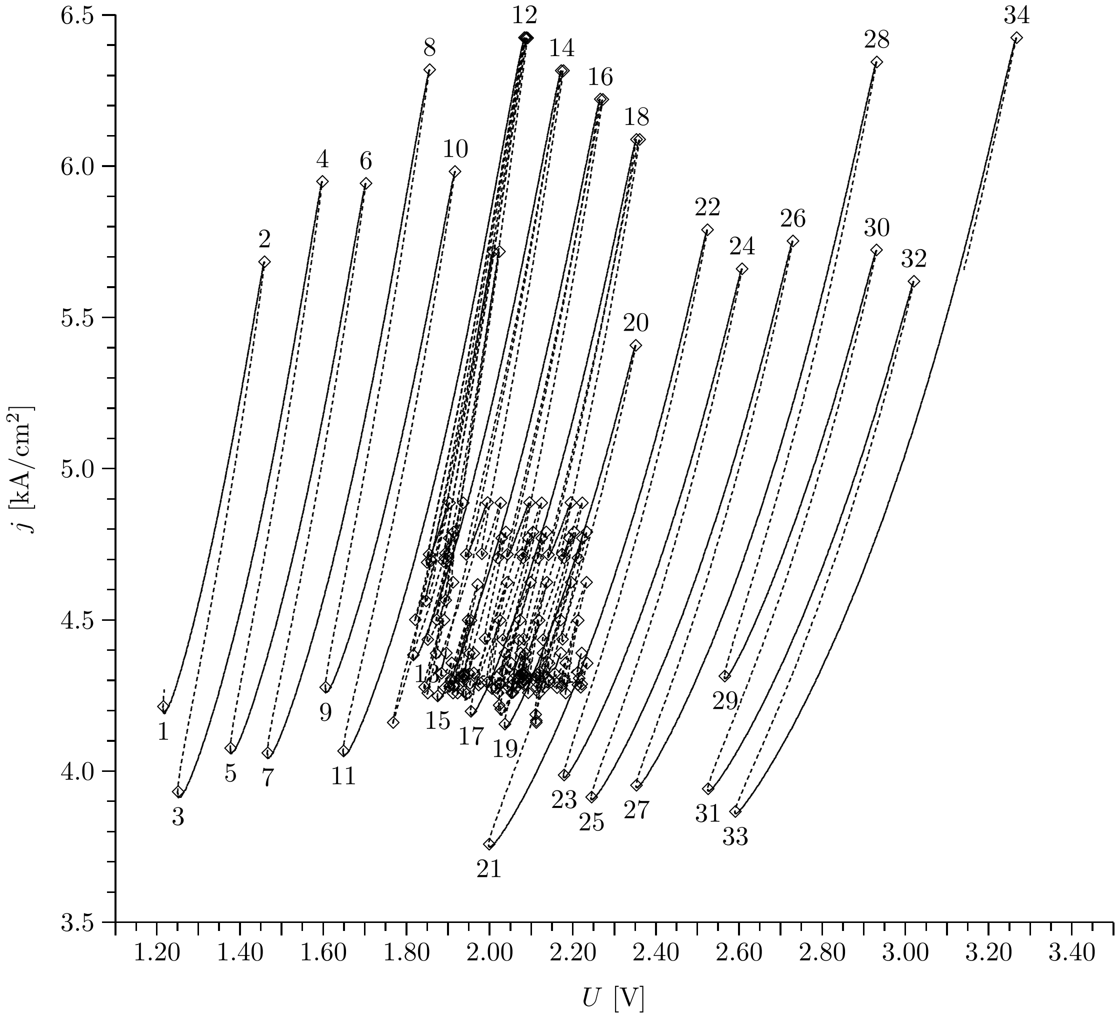

Figure 6.1: Perturbed current-voltage characteristic for $\alpha = 10\,\%$. The saddle-node bifurcation points on the corresponding part of the unperturbed current-voltage characteristic were numbered; these numbers were used to label the corresponding bifurcation points on the perturbed characteristic. The depicted section of the current-voltage characteristic consists of just a single curve; the "tangle" lies between the points numbered "12" and "13". The latter is also depicted in Fig. 6.2.

6.2 Starting with the Perturbed Characteristic

Until now, we have only compared the "shape" of the current-voltage characteristic. From a more "physical" point of view, we also have to consider the variation of the field profiles of the states in question when α is changed. We want to do this for two states: one connected with the "standard" current-voltage characteristic, and one which is not. As comparing "distant" states may cause unnecessary problems, two states near the start of the "tangle" should be picked, i. e., one of the points "12" or "13" should be chosen. However, these two branches do not "reach" their corresponding bifurcation points directly but make a "detour" via a cusp point. This does not cause any principal problems, it just makes it impossible to use α as parameter. Thus, the point "10" has been chosen. Similar problems occur also when choosing the other point; here, the point "c" is used (in the figure, this point is just above the "13"; it is the third point starting from the "boundary" between "strange" and "standard" states).

Fig. 6.3 depicts the results for both points. First, one can see that theorem 1 from section 5.1 is valid for both states investigated here: The variation of the electron densities is proportional to the level of disorder, α. The field distribution in Fig. 6.3(a) is – as expected – just a "plain" field domain whereas the field distribution in Fig. 6.3(b) is similar to the "strange" states from section 4.7.

Thus, this gives rise to the assumption that "strange" stationary (but mostly unstable) states of the unperturbed superlattice may be

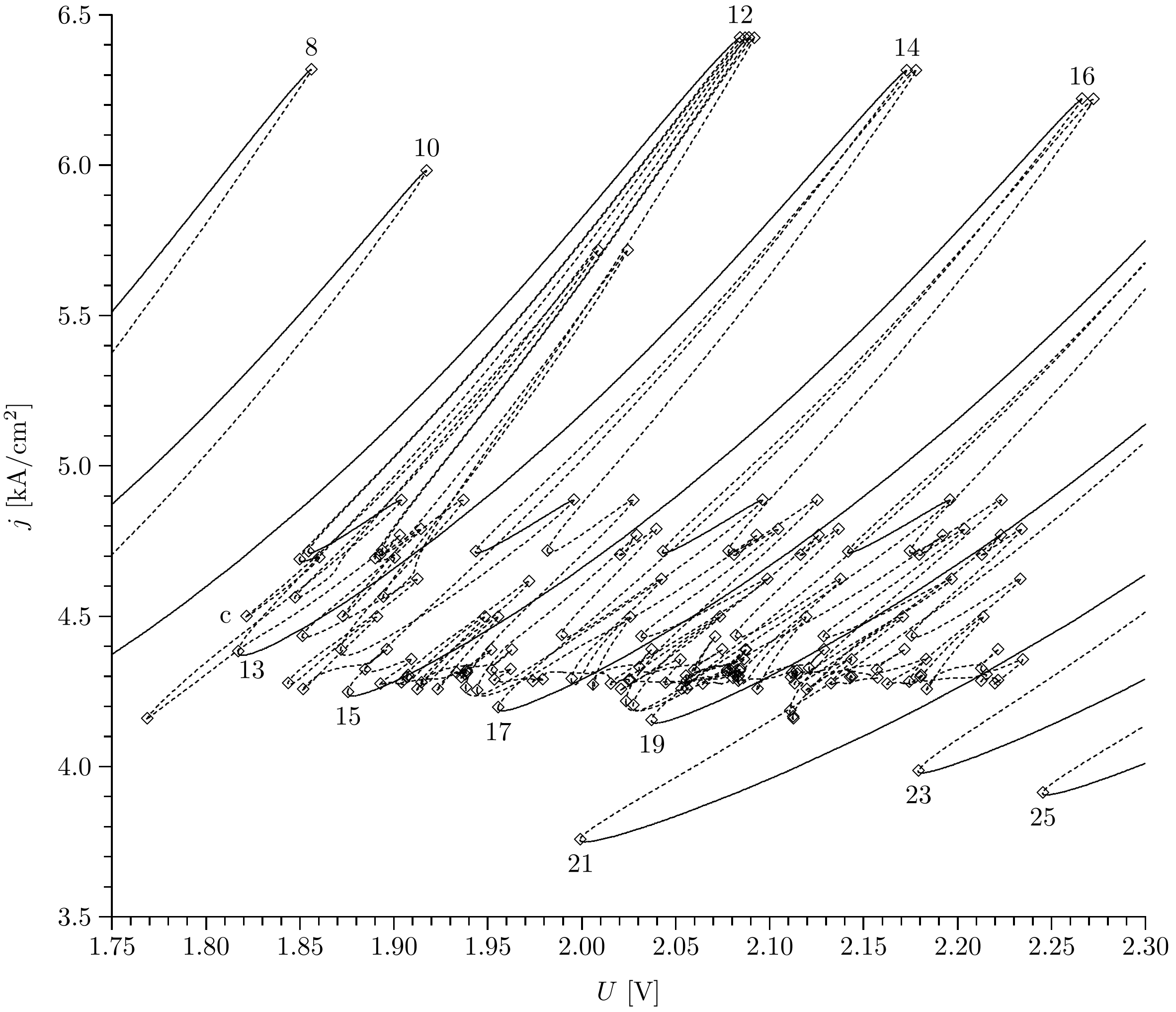

Figure 6.2: Perturbed current-voltage characteristic (enlarged section from Fig. 6.1).

important for the continuous current-voltage characteristics of perturbed superlattices. This can be proven as follows: Starting from the perturbed current-voltage characteristic, the corresponding point at $\alpha = 0\,\%$ for each bifurcation point is determined. Since the number of bifurcation points is comparably large, this has to be restricted to just a small portion of the current-voltage characteristic.

This portion is depicted in Fig. 6.4 for $\alpha = 10\,\%$. For each bifurcation point, α was decreased from $10\,\%$ to $0\,\%$, and the corresponding bifurcation point was thus determined. This was not possible for some bifurcation points as they merge with another bifurcation point in a cusp point. In this case, the two respective bifurcation points have been labelled with the same letter. For some other bifurcation points, no definite answer was possible due to numerical problems[1] (for example, the small branches between “C” and “D”). However, for most bifurcation points at $\alpha = 10\,\%$, there is a corresponding point for $\alpha = 0\,\%$. These points have been numbered; note that the numbers are not the same as the ones used in the preceding section. Now, we want to present the parts of the unperturbed current-voltage characteristic containing the computed bifurcation points for $\alpha = 0\,\%$; as in the preceding section, the corresponding bifurcation points are labelled with the same number as in Fig. 6.4.

Figs. 6.6 and 6.5 depict the states for $\alpha = 0\,\%$. The curve in Fig. 6.6 is – as expected – nothing else than the “standard” current-voltage characteristic. The “characteristics” in Fig. 6.5, on the other hand, definitely consist of “strange” states as described in section 4.7. The shape of the isolas as well as of the field distributions are

---

[1] A cusp point is not characterised by a simple condition for the eigenvalues (in contrast to, e. g., the Hopf or the saddle-node bifurcation) but certain higher terms also have to disappear (the cusp point shares the same eigenvalue condition as the saddle-node bifurcation). In high-dimensional problems, these more complex conditions are more sensitive to numerical problems.

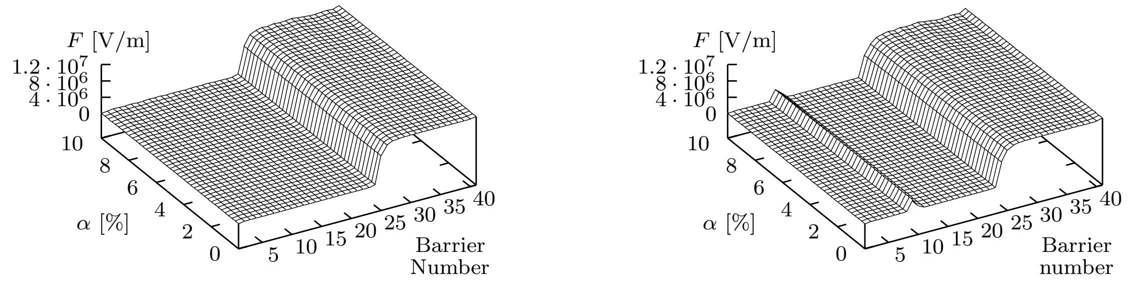

(a) Field distribution at “10”

(b) Field distribution at “c”

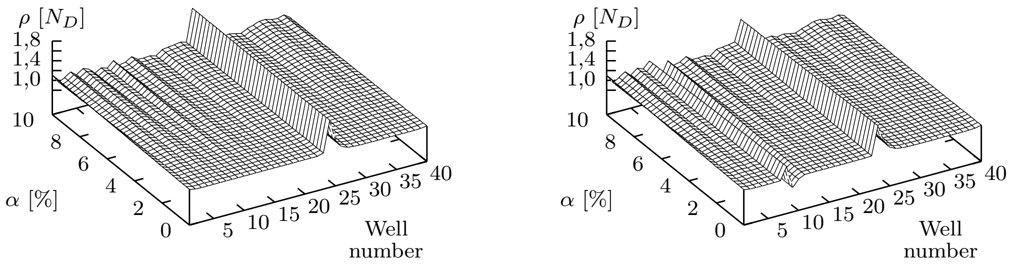

(c) Electron densities at “10”

(d) Electron densities at “c”

Figure 6.3: Variation of the field profiles (upper figures) and electron configurations (lower figures) with increasing disorder, α. The figures on the left depict a state on the “standard” current-voltage characteristic (labelled “10” in Fig. 6.2), the figures on the right a “strange” state (labelled “c” in Fig. 6.2).

of type (d) (Figs. 4.25 and 4.26 on page 45). The field distribution in Fig. 6.3(b) and the shape of the current-voltage characteristic for $\alpha = 0\,\%$ is typical of the states corresponding to states in the “tangle” for strong disorder. The procedure described here has been executed for more than 200 bifurcation points without a single deviating result.

6.3 “Strange” States

In the first section of this chapter, we started with the unperturbed “standard” current-voltage characteristic and computed the corresponding perturbed states. In the second section, we started with the perturbed characteristic and computed the corresponding unperturbed characteristic(s) resulting in both “standard” and “strange” states. Since “strange” states have so far only been discussed for unperturbed superlattices in section 4.7, we now have to investigate the effects on “strange” states when α is increased.

Fig. 6.7 demonstrates how the strange states from Fig. 6.5(d) change when α is increased: The curve becomes more complex as α becomes higher. Responsible for this are cusp points; when a cusp point is passed, two saddle-node bifurcation points and thus one additional branch are inserted into the characteristic. This is similar to the formation of branches in the “standard” current-voltage characteristic when the doping density N_D is increased. Since the sign of one eigenvalue along the new branch differs from the branch it has bifurcated from, the inserted branch may be stable even though the original branch or even the entire isola has been unstable for smaller α.

Due to the high number of branches, it is difficult to see important details in Fig. 6.7. Therefore, the same data is also depicted in Fig. 6.8; however, this time the unstable branches are hidden and only the stable branches and the bifurcation points are shown. Now it is possible to see that (small) parts of the isola are

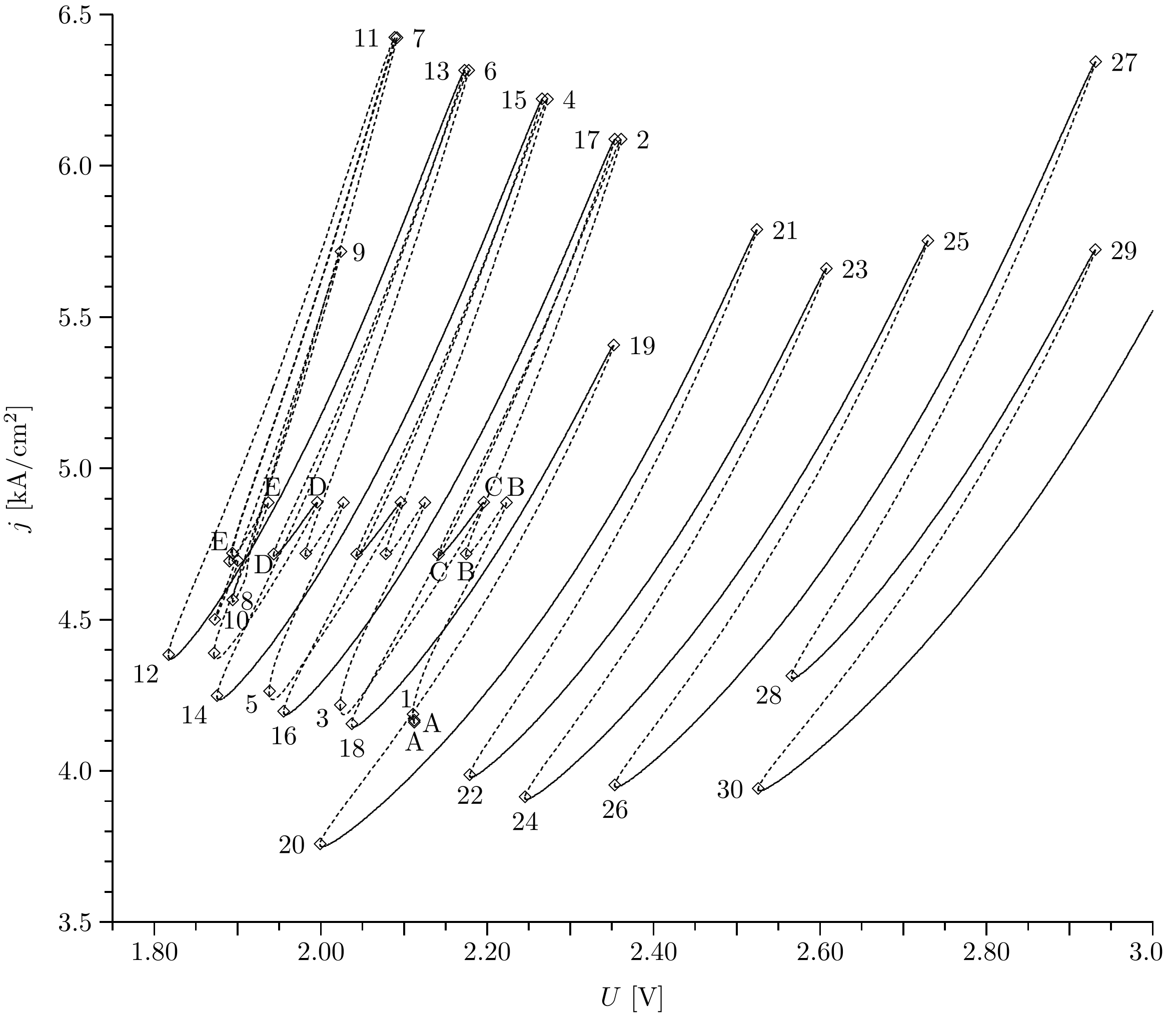

Figure 6.4: Perturbed current-voltage characteristic with labelled saddle-node bifurcation points. If a bifurcation point is labelled with a number, this means that it turns into the point with the same number in Figs. 6.6 respectively 6.5 for $\alpha = 0$. If it is labelled with a capital letter, it merges with the other bifurcation point with the same label in a cusp point. Due to numerical problems, some bifurcation points could not be labelled.

stable. In fact, the stable branch already exists for $\alpha = 2\,\%$ and just becomes longer when α is increased.

The parts of the current-voltage "characteristic" depicted in Figs. 6.7 and 6.8 were only computed for discrete values of α. A diagram showing current-voltage characteristics in dependence on an additional parameters is hardly possible if there is multistability in the characteristics. However, if the precise values of the current density are not of importance and the positions (voltage) of the bifurcation points are sufficient, it is possible to depict these in dependence on α. This is in principle the same as the phase diagrams (N_D-U-diagrams) already introduced.

Such a diagram is shown in Figs. 6.9(a) and 6.9(c). The latter diagram starts from the data presented in Fig. 6.5(d) as do most of the diagrams in this section; the former starts from Fig. 6.5(e) to demonstrate that the qualitative behaviour is the same for all strange states. However, there is an additional difference: For Fig. 6.9(a), the computation started with the unperturbed system ($\alpha = 0$) whereas the initial data for Fig. 6.9(a) was for $\alpha = 8\,\%$. If the computation is started at $\alpha = 0\,\%$, all pairs of saddle-node bifurcations created "later" in cusp points are not taken into account. This explains the different number of branches in the two figures.

Let us start with the "simpler" characteristic in Fig. 6.9(a). Note that they are not four saddle-node bifurcation points for each $\alpha = 0\,\%$ and $\alpha = 10\,\%$. Rather one of the curves – starting at $\alpha = 0$ – "turns back". Thus, there is now one bifurcation point "too much" for $\alpha = 0\,\%$. This bifurcation point is labelled "a". If the current-

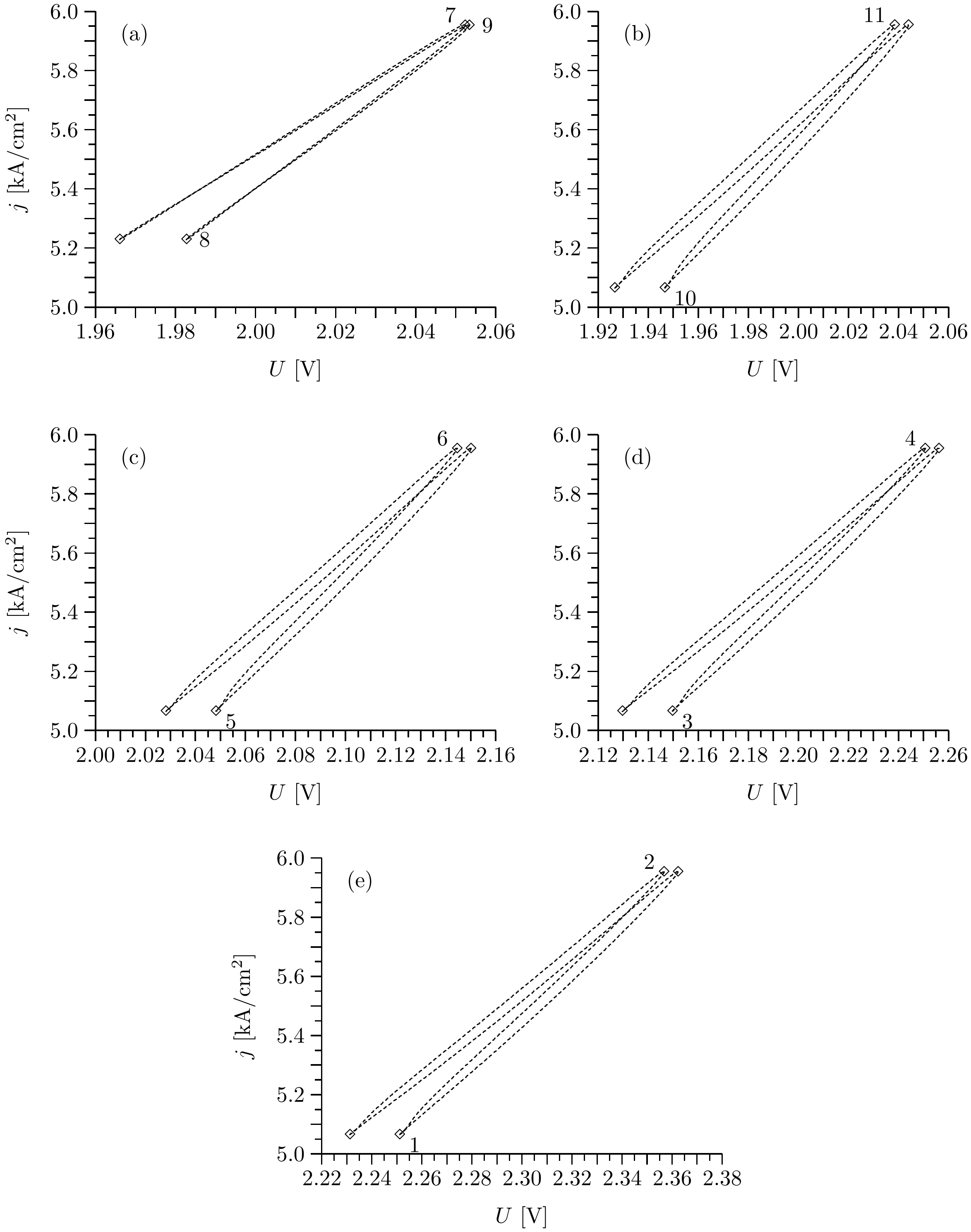

Figure 6.5: Unperturbed, unstable parts of the current-voltage characteristic. The bifurcation points corresponding to the points in Fig. 6.4 are labelled. If a points is not labelled, it just means that it is not connected with one of the points from Fig. 6.4; it is possible that the corresponding point simply lies outside the region depicted in 6.4.

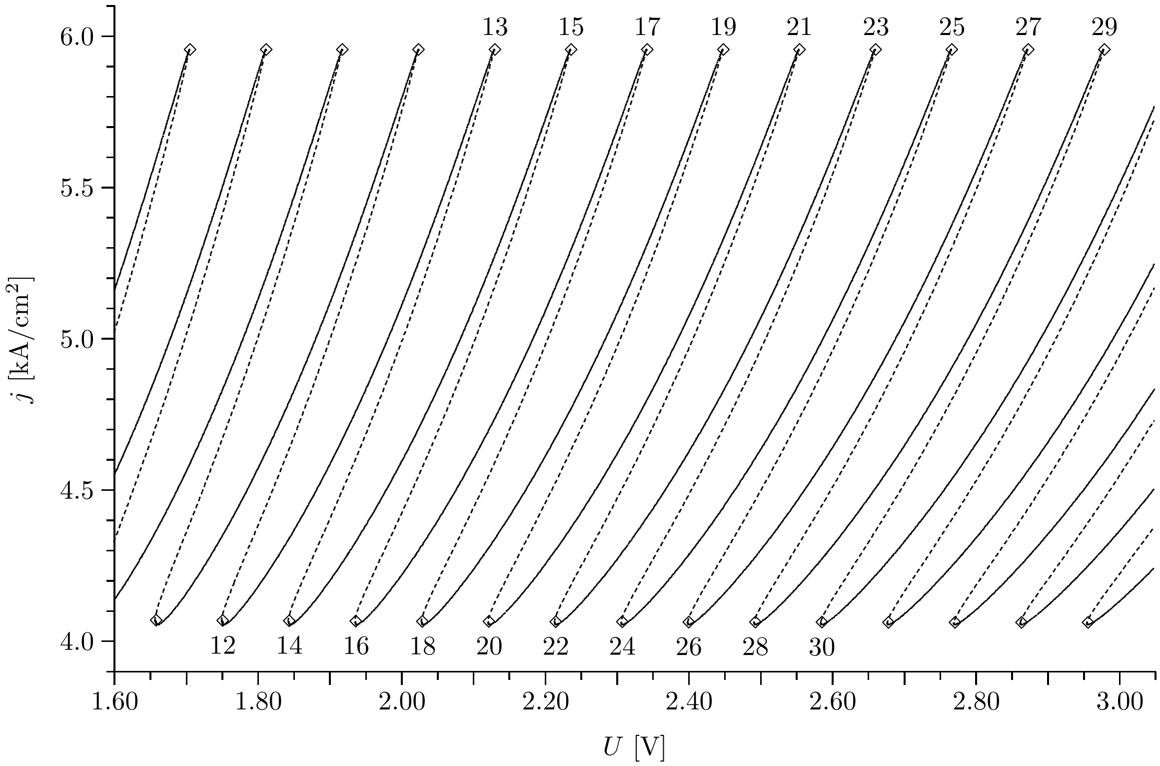

Figure 6.6: Unperturbed "standard" current-voltage characteristic. For more information, refer to Fig. 6.4.

voltage characteristic through this point is computed, one gets another isola (Fig. 6.9(b)). Similar can be done with the curve from Fig. 6.9(c). As the initial data is for $\alpha = 8\,\%$, a larger number of branches has to be examined. Even though many of these bifurcation points have been created only for high values of α, some of them are connected with bifurcation points for $\alpha = 0$. One ends up with a total of four "new" bifurcation points for $\alpha = 0$, which all lie on the isola depicted in Fig. 6.9(d). Thus, the explanation why we did only find one of the four bifurcation points in Fig. 6.9(b) is simply that the initial data was for $\alpha = 0\,\%$, and we therefore started with "too few" bifurcation points.

To compute these figures, not only α was varied. Using the bifurcation condition allows (and forces) to adapt a second parameter (e. g. U). Thus, there is no qualitative difference between the two parameters α and U. This implies that it is not always possible to parameterise the entire curve using only one of these two parameters; this includes the case that there may be local extrema relative to α. As will be demonstrated in the next section, this leads to a splitting-off of a part of the current-voltage characteristic which will then form a closed curve of its own.

We will not discuss this subject further as it is very difficult to get "usable" results. We have to conclude that it is not always possible to infer the structure of the total continuous current-voltage characteristic using only U-α-diagrams. One frequently ends up having to compute (parts of) the actual current-voltage characteristic for the values of α of interest.

6.3.1 Merging of Isolas

We already knew at the start of the preceding section that the perturbed current-voltage characteristic consists of multiple parts which are separated for $\alpha = 0\,\%$, namely the "standard" current-voltage characteristic and a number of isolas of "strange" states. These separated entities somehow have to "interact". The leads to the question whether the isolas interact while still being separated or whether they interact among each other before the resulting new structure interacts with the "standard" characteristic. The result will be that both scenarios are possible.

Fig. 6.10 depicts the development of three isolas for increasing α. These isolas are, from left to right, the ones presented in Figs. 6.5(b), 6.5(c)

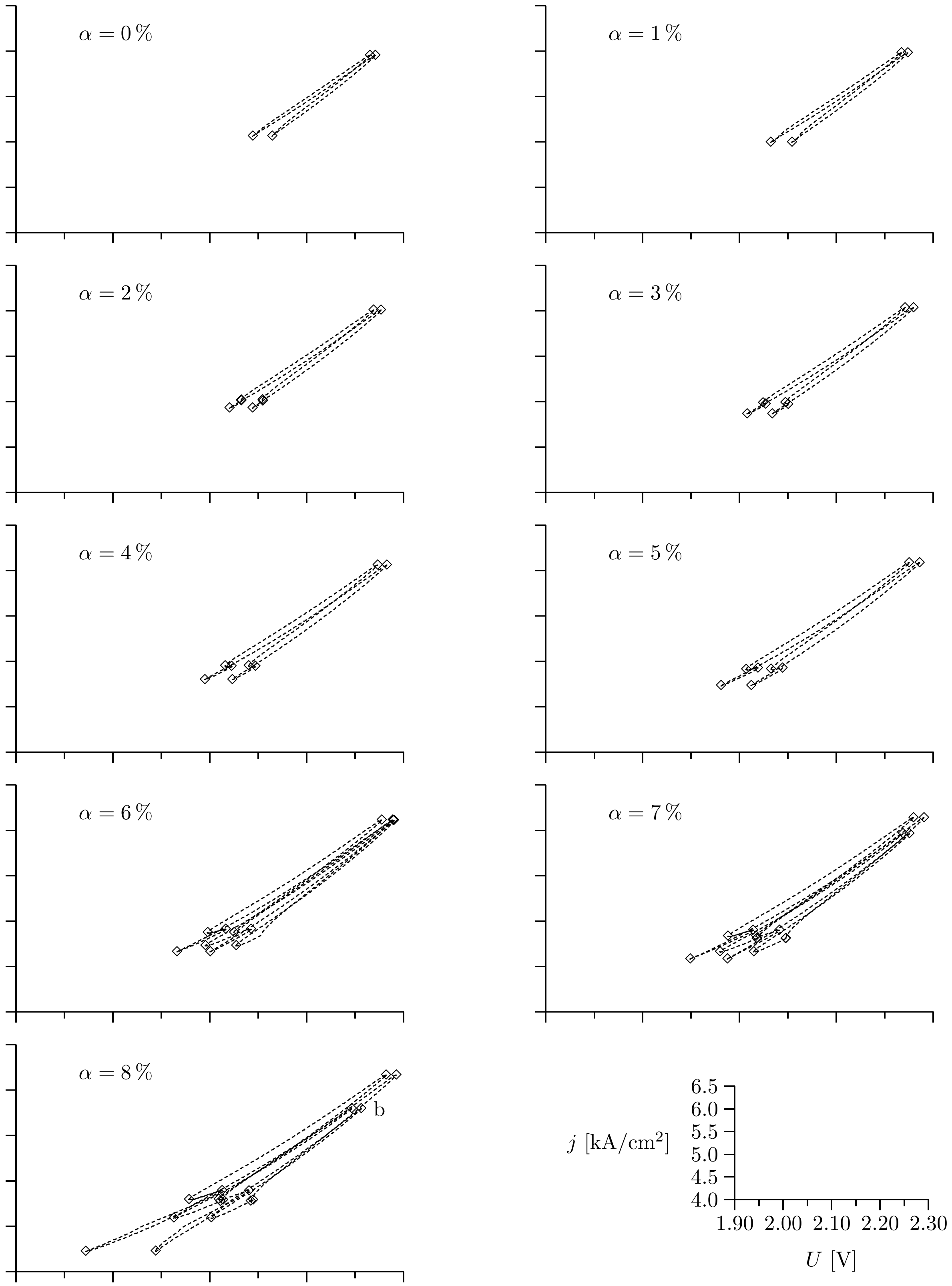

Figure 6.7: Strange states with increasing disorder. Depicted is the variation of the isola from Fig. 6.5(d) when the level of disorder is increased.

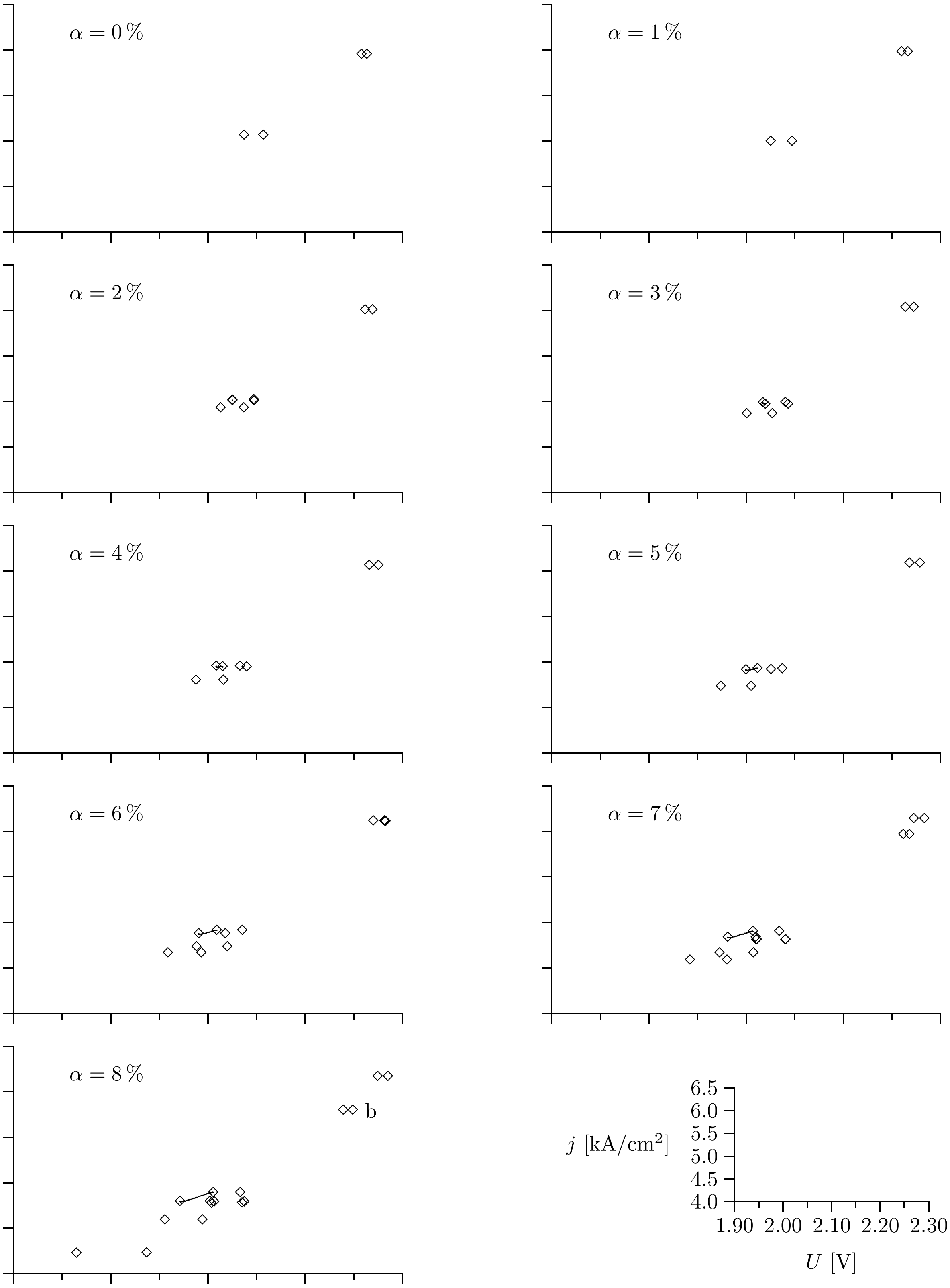

Figure 6.8: Strange states for increasing disorder. The same data is the same as in Fig. 6.7, however, all unstable have not been depicted, and only the stable branches and the saddle-node bifurcation points are shown.

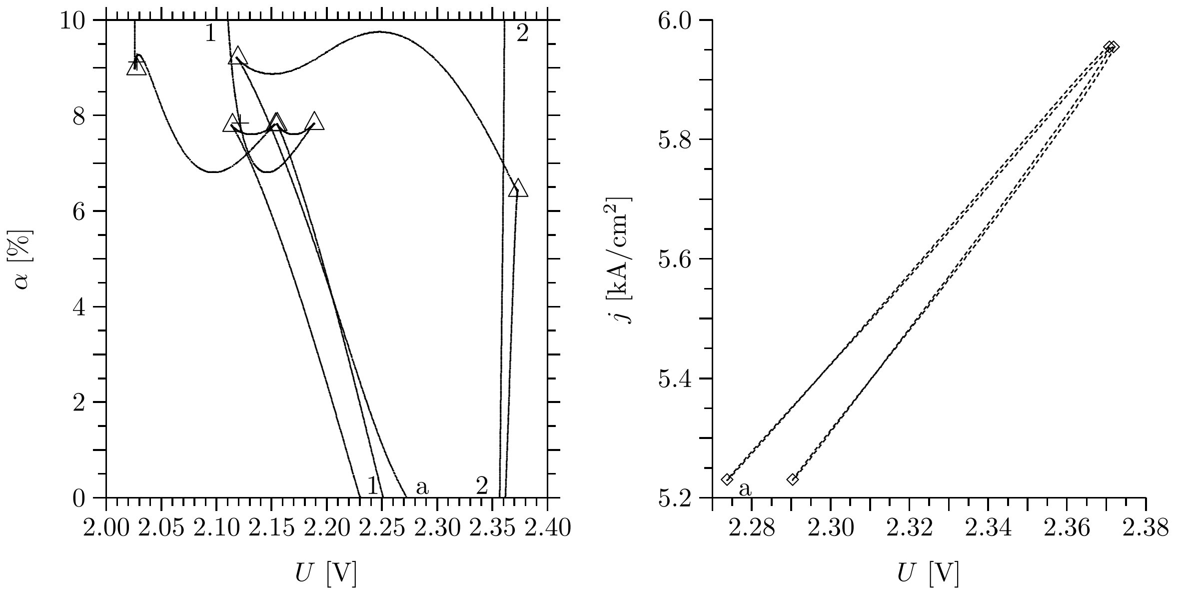

(a) Portrait corresponding to Fig. 6.5(e)

(b) Current-voltage characteristic for $\alpha = 0$ through "a"

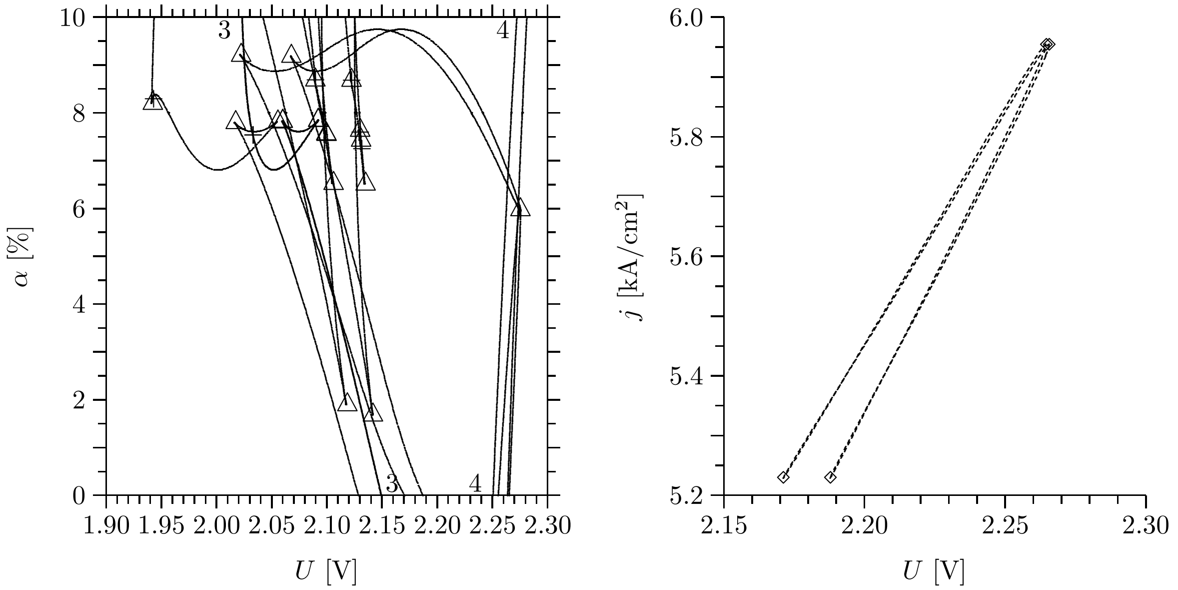

(c) Portrait corresponding to Fig. 6.5(d)

(d) Current-voltage characteristic for $\alpha = 0$ through additional states

Figure 6.9: Connection between perturbed and unperturbed states. **(a)** Positions of the saddle-node bifurcation points as a function of α starting with the bifurcation points from Fig. 6.5(e). The labels at the curves for $\alpha = 0\,\%$ respectively $\alpha = 10\,\%$ are the same as in Fig. 6.5 respectively Fig. 6.4. The state labelled "a" does not correspond to any of the bifurcation points in Figs. 6.5 and 6.6. The current-voltage characteristic, on which this point lies, is depicted in subfigure **(b)**. **(c)**, **(d)** Correspondingly but starting from Fig. 6.5(d). For more information, please refer to the text.

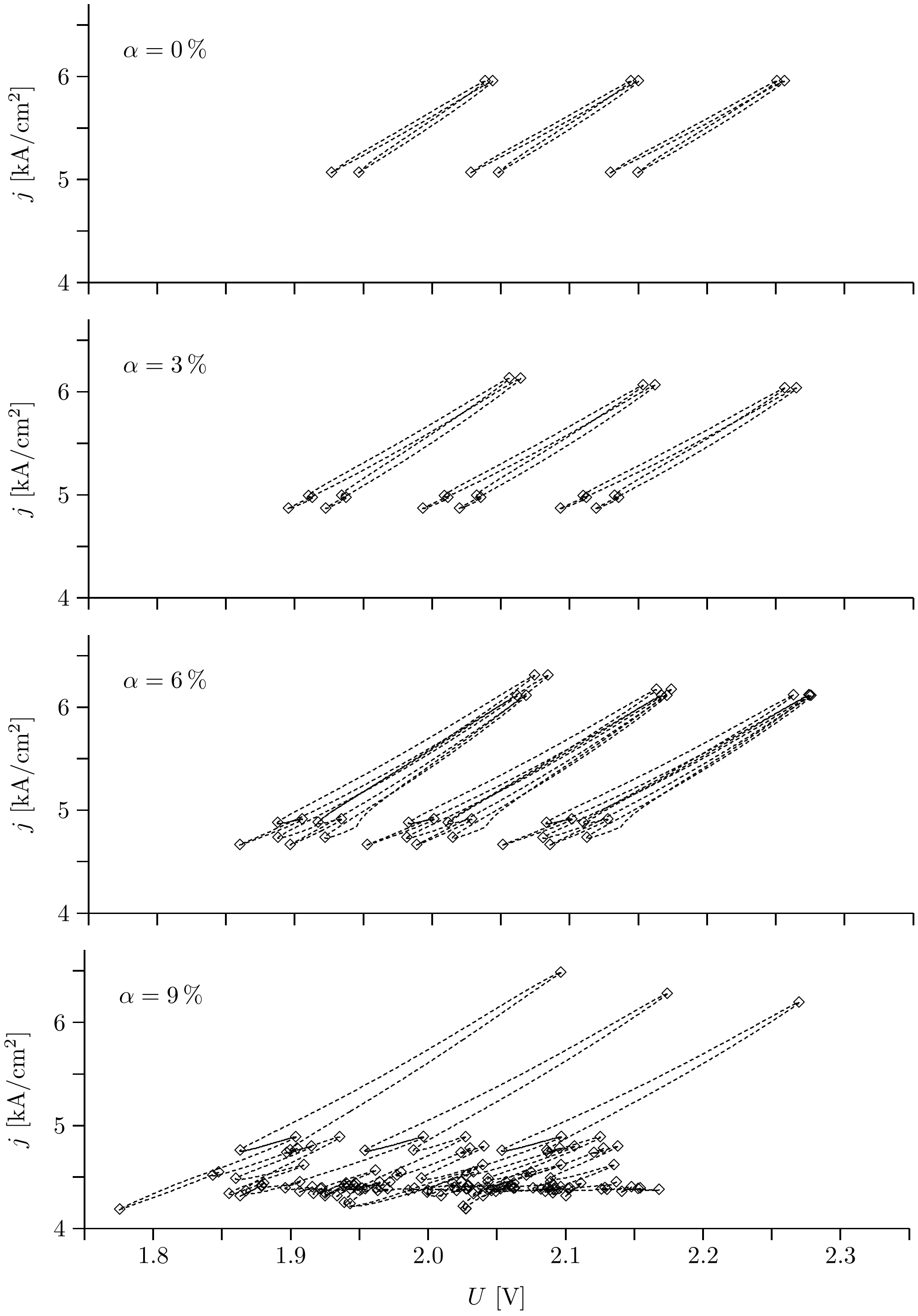

Figure 6.10: Merging of branches of "strange" states. Three small isolas merge into a single, larger isola. One of these three isolas is the one from in Fig. 6.7. Thus, the isola have to merge somewhere between $\alpha = 8\,\%$ and $\alpha = 9\,\%$.

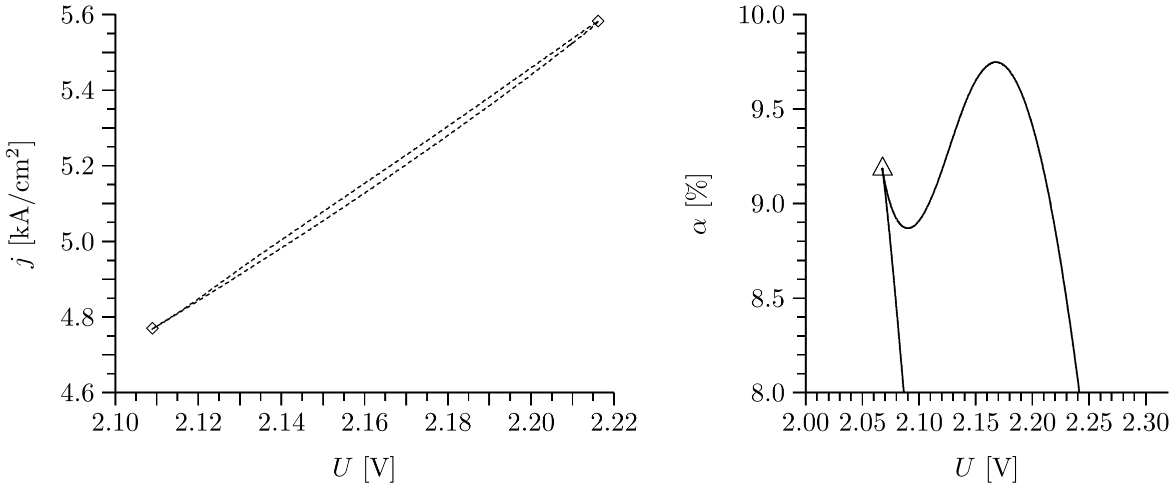

(a) Split-off part of the characteristic

(b) Positions of the saddle-node bifurcations

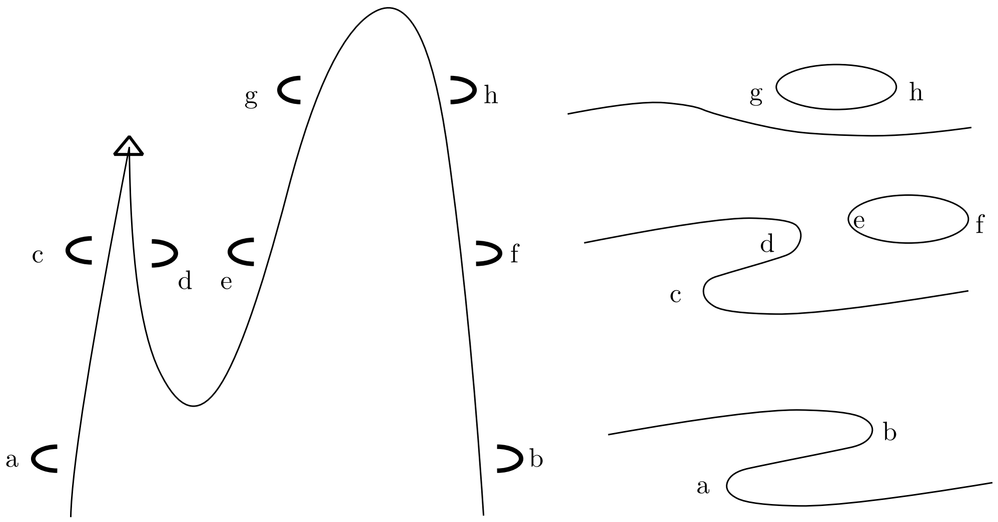

(c) Schematic of the current-voltage characteristics and the bifurcation points

Figure 6.11: An isola splitting off when the level of disorder is increased. The upper right bifurcation point in subfigure **(a)** corresponds to the bifurcation point labelled "b" ($\alpha = 8\,\%$) in Fig. 6.7. **(b)** Variation of the position of the bifurcation points when α is changed. The two states for $\alpha = 8\,\%$ are two consecutive bifurcation points from Fig. 6.7 for $\alpha = 8\,\%$. The two states on the left for $\alpha = 9\,\%$ are also consecutive bifurcation points but taken from Fig. 6.10. The two bifurcation points on the right are the same as in subfigure (a). **(c)** Schematic to explain how the current-voltage characteristic can be determined just from the positions of the bifurcation points.

and 6.5(d). With increasing α, the curves become more complex as could already be seen in Fig. 6.7. The latter figure also demonstrated that the isola does not combine with other curves for α up to $8\,\%$. As it has done so for $\alpha = 9\,\%$, this merging has to happen for some value of α between $8\,\%$ and $9\,\%$. The precise scenario has not been investigated but there is no reason to believe that it should be different from the one described in the following section.

If one compares the isolas for $\alpha = 8\,\%$ in Fig. 6.7 with the corresponding parts for $\alpha = 9\,\%$ in Fig. 6.10, one may find the following difference: In the right upper part of each isola, there is a pair of saddle-node bifurcation points for $\alpha = 8\,\%$ whereas there is just a single bifurcation for $\alpha = 9\,\%$. What has become of the second point?

If we start with one of the "missing" points and increase the level of disorder to $\alpha = 9\,\%$, we see that it now lies on a small isola like depicted in Fig. 6.11(a); thus, it has separated from the

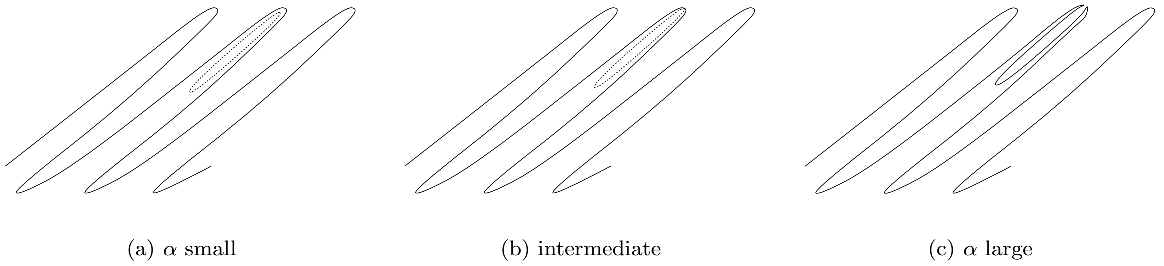
(a) α small (b) intermediate (c) α large

Figure 6.12: Schematic current-voltage characteristics for different levels of disorder. **(a)** For moderate disorder, the "standard" current-voltage characteristic remains qualitatively unchanged (solid line). Additionally, there are isolated, closed branches of stationary states (dashed). **(c)** For strong disorder, these two structures have merged into a single, more complex one. Thus, there has to be an intermediate state where the "standard" characteristic and the isola just touch (subfigure **(b)**).

main isola.

The position (voltage) of the two saddle-node bifurcation points is depicted in Fig. 6.11(b) as a function of α. This diagram might not seem to be very helpful. But in fact, it allows us to determine the qualitative shape of the different parts of the current-voltage characteristic for every value of α. This shall be explained with the help of the schematic diagram in Fig. 6.11(c).

In a saddle-node bifurcation point, the current-voltage characteristic "turns back" (hence the name turning point). Just knowing the position of the bifurcation point does not give us the information, on which side of it the two branches lie. However, there is a cusp point in the diagram. We know from section 2.6 that there are three solution branches "inside" and only one "outside". Thus, the current-voltage characteristic near the points "c" and "d" has to be like it is indicated by the small semicircles. When the direction of the bifurcation curves reverses, the opening of the semicircles also has to reverse. Thus, we can determine the local shape of the current-voltage characteristic near the bifurcation curves; it is indicated by the additional semicircles. If we choose a point in parameter space far away from the structures discussed here, the system cannot "feel" these bifurcations. Furthermore, there are no bifurcation points "above" the diagram (at least no bifurcation points important here) but there still has to be a solution. As result, a solution branches "comes" from the right and "goes" to the left regardless of the value of α.

Now, we are able to construct all current-voltage characteristics by just connecting the semicircles ("local" current-voltage characteristics). In the lower part of the diagram, the characteristic comes from the right, goes to the point "a" and on to the point "b" before leaving the depicted are at the other side. Thus, the current-voltage characteristic has to look like is depicted on the right.

Near the middle, the characteristic has to be as follows: It starts on the right and goes to the point "c". Now it has to turn back at the point "d" as otherwise it would be impossible to connected the two "free" exits of the point "d" so there would have to be two additional solution branches on the left. So far, we have not "used" the points "e" and "f", which have to form an isola as this is the only way to prevent solution branches from "escaping". Thus, this procedure yields the current-voltage characteristic as depicted on the right.

Finally, in the upper part of the diagram, the points "g" and "h" have to form an isola for similar reasons. If the current-voltage characteristic would be like in the neighbourhood of a cusp point there would have to be a cusp point nearby (which there is not). As there are no further bifurcation points, the continuous part of the current-voltage characteristic is not affected.

6.4 Merging of the Current-Voltage Characteristic

As has been demonstrated in the preceding sections, the overall structure for moderate disorder is like is depicted in Fig. 6.12(a): The "standard" current-voltage characteristic is qualitatively the same as in the unperturbed case; in addition, there isolas, i. e., closed curves of stationary states that are separated from the "continuous" characteristic. For strong disorder, the

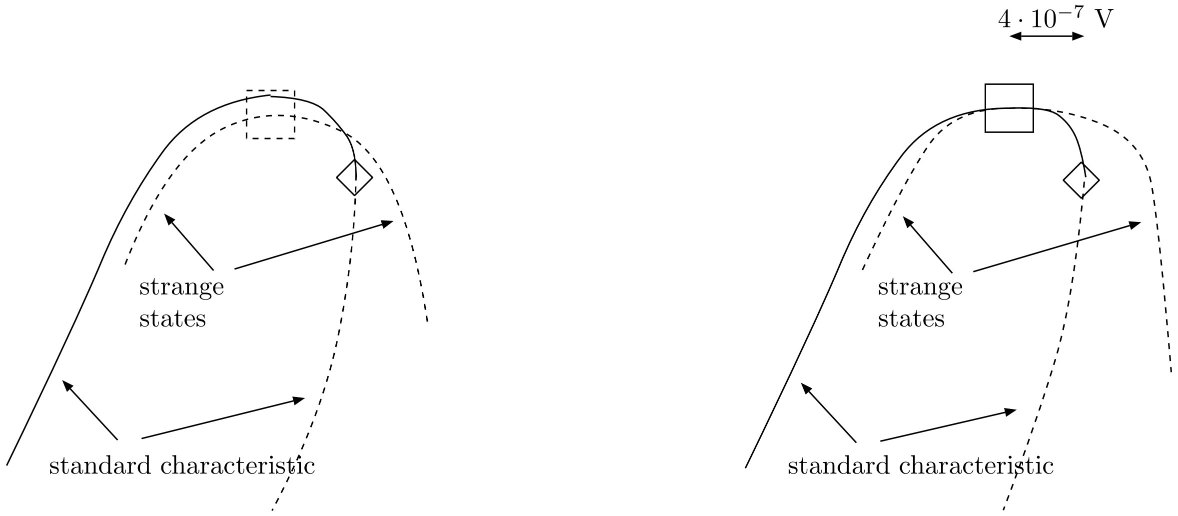

(a) before

(b) bifurcation point

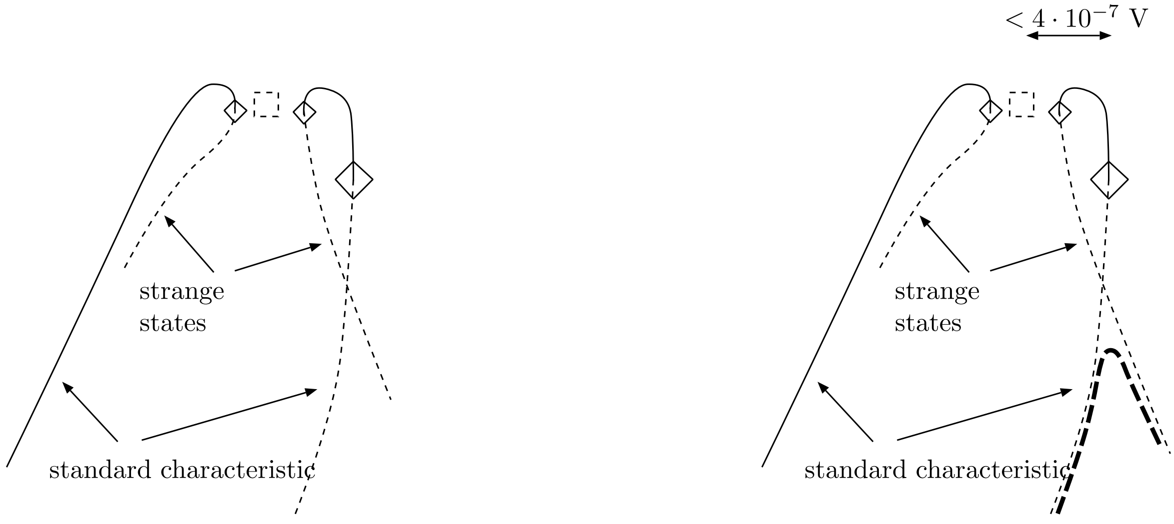

(c) after

(d) after, numerical

Figure 6.13: Merging of a branch of strange states with the standard current-voltage characteristic. Depicted is a schematic of these two structures before merging (subfigure **a**), at the very moment of merging (subfigure **(b)**) and after merging (subfigure **c**). The "potential" position of the "potential" transcritical bifurcation is marked with dashed lines in subfigures a und c. **(d)** The distance between the two saddle-node bifurcations point on the right is too small to be able to distinguish between them in a numerical computation; the computed branch will be similar to the bold curve.

situation is as depicted in Fig. 6.12(c): There is just a single continuous curve containing parts from both structures. Thus, there has to be a state as depicted in Fig. 6.12(b) in between: Both structures, the continuous current-voltage characteristic and the isola, touch at a single point.

This bifurcation itself has already been discussed in section 2.5 (page 5) where the isola-bifurcation was described. However, there is a small difference between the bifurcation described earlier and the situation encountered here: The "generic" case is that one has two solution branches whose slopes are not changed in the bifurcation point. Thus, it is easy to say which branches belong together.

Here, is is a bit more difficult as the bifurcation happens (almost) exactly at the point where the

---

[2] Note that there is almost no difference between this point and the bifurcation point nearby. This situation is different

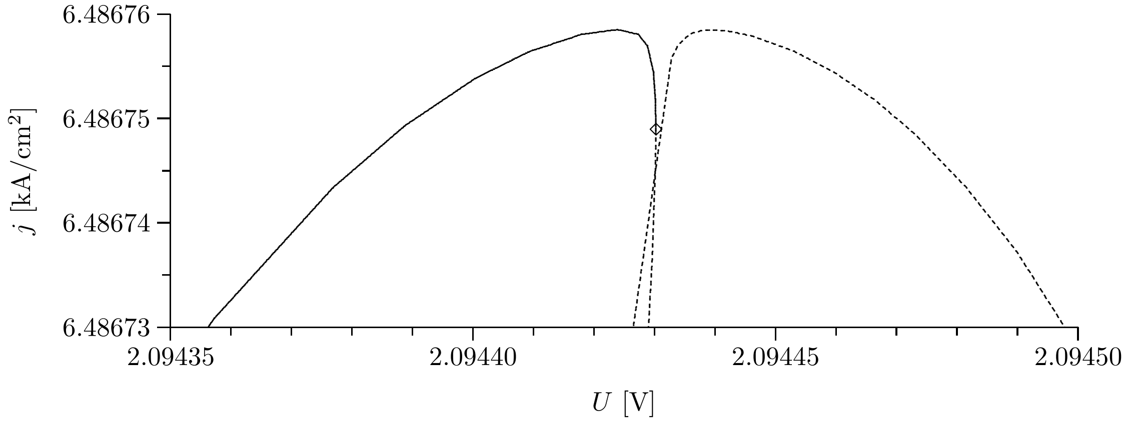

(a) before

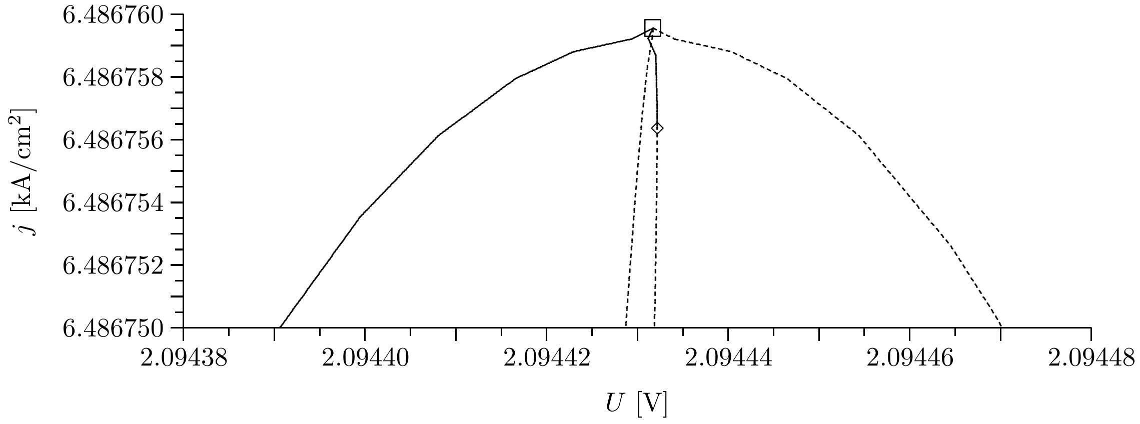

(b) bifurcation point

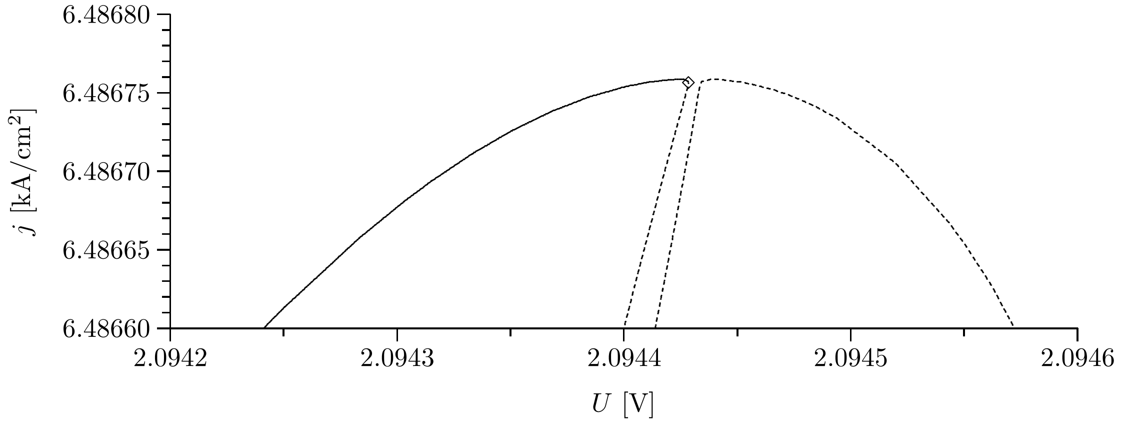

(c) after

Figure 6.14: Merging of a branch of strange states with the standard current-voltage characteristic. The data in this figure are the "real" curves corresponding to the schematics from Fig. 6.13. Note that the three subfigures are scaled differently.

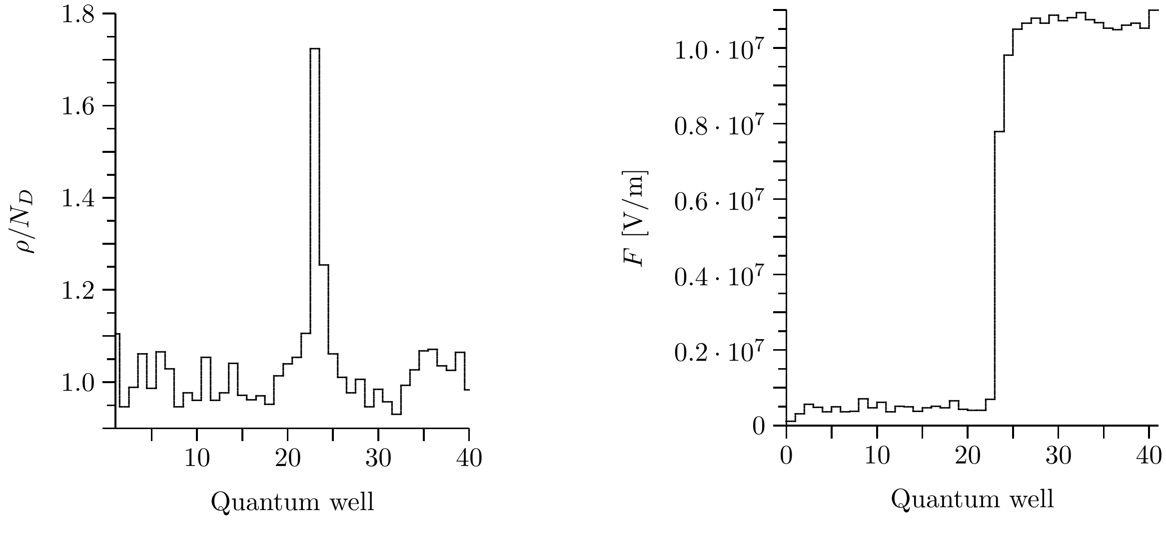

(a) Electron density

(b) Field distribution

Figure 6.15: Bifurcation point. **(a)** Electron densities at the point where the standard current-voltage characteristic first merges with an isola. **(b)** Corresponding field distribution.

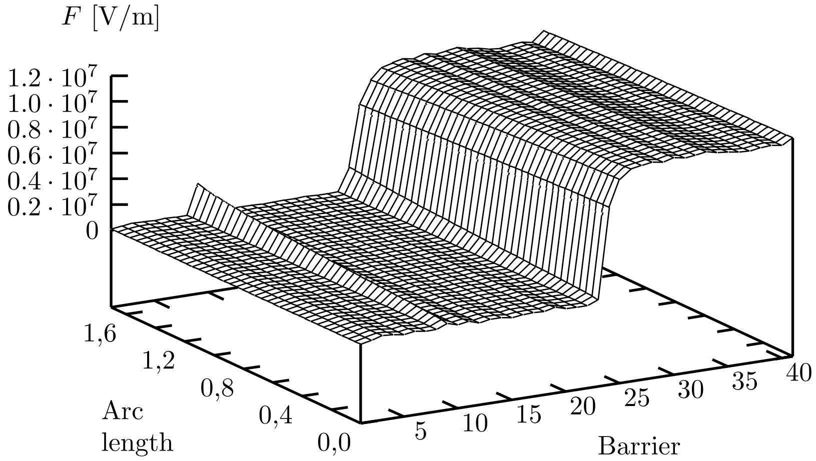

Figure 6.16: Field distribution along a branch of "strange" states near the bifurcation point. The data is displayed starting at the bifurcation point and going towards increasing voltage.

current density reaches its maximum[2]; the same applies to the isola involved in the bifurcation.

There is an additional problem: The distance between the maximum of the current-density and the upper saddle-node bifurcation point is very small; here, it is just $4 \cdot 10^{-7}$ V. This leads to numerical problems as the Jacobi-matrix has to be singular at a bifurcation point.[3] Most algorithms will then fail to converge, including the ones used by continuation. Thus, if one starts at a bifurcation point, one first has to make a large enough step before these algorithms may be "switched" on again. On the other hand, if one approaches a bifurcation point, one has to "see" it before one gets too near. Therefore,

---

for the point where the current reaches its minimum (see, for example, Fig. 4.2 on page 27). At or near the point of the current maximum, most of the electron densities also have an extremum. Thus, there would be no difference if we were to consider a particular electron density instead of the current density.

[3] Of course, this applies only to local bifurcations. In addition, the Hopf-bifurcation has to be excluded as the number of branches of stationary points does not change in it.

continuation algorithms have to be able to detect a bifurcation point a number of steps before they would otherwise enter the "forbidden" zone around the bifurcation point; the continuation algorithm will then use a special algorithm – there has to be one for every type of bifurcation supported – to converge directly onto the desired bifurcation point. This implies that two bifurcation points of different type may have a smaller distance than two of equal type. In the latter case, the continuation algorithm would either fail to detect the second bifurcation point or – if it did – would converge back to the first one when trying to converge onto the newly detected bifurcation point.

After this remarks, we are able to discuss the actual merging of the current-voltage characteristic. A schematic of the "standard" current-voltage characteristic and an isola of "strange" states is shown in Fig. 6.13(a). The position of the transcritical bifurcation at the moment of merging is marked with dashed lines as is also in subfigure c. The only bifurcation existing for this level of disorder is the saddle-node bifurcation separating the stable and the unstable branch of the standard current-voltage characteristic. The very moment of merging is depicted in Fig. 6.13(b). A new bifurcation point, the transcritical bifurcation, has appeared out of the blue sky. If the level of disorder is increased further, the transcritical bifurcation is perturbed into a pair of saddle-node bifurcation points as has been described in section 2.3 on page 4. The distance between the right of these two points and the bifurcation point in subfigure a is less than $4 \cdot 10^{-7}$ V. Thus, it is impossible to distinguish between them in a numerical computation. The only solution is to steer the continuation algorithm so as to give the path shown bold in Fig. 6.13(d). Of course, this has no relevance to the two branches left of the (destroyed) transcritical bifurcation.

Now we want to discuss the "real" curves. The first merging of the standard current-voltage characteristic with an isola[4] happens for $\alpha = (9.042462 \pm 0.000003)\,\%$. This "moment" is depicted in Fig. 6.14(b); the level of disorder varies only minimal for the other two subfigures of Fig. 6.14.

The important question now is about the bifurcation point itself, i. e., about its electron configuration and its field profile. Until now, the question whether a given state belongs to the "standard" current-voltage characteristic or is a "strange" could be answered just by examining its field profile. However, if branches of these two types are to join, their field profiles have to adapt to each other. The data of the bifurcation point is depicted in Fig. 6.15. The field distributions show a well defined domain structure without a region of increased field strength as would be characteristic for a strange state. Thus, the strange states adapt to the standard current-voltage characteristic and not vice versa.

Finally, this leads to the question how the field distribution evolves from the one at the bifurcation point towards the "typical" strange state farther away. The answer is given by Fig. 6.16 where the field distribution is depicted as a function of arc length, starting at the bifurcation point. One can see that it quickly changes into the "typical" one.

6.5 Further Increasing α

When the level of disorder, α, is increased further, the scenarios described so far may happen multiple times: Additional pairs of saddle-node bifurcation points may be created in cusp points, and additional isolas of "strange" states may merge with the continuous current-voltage characteristic. It does not make sense to discuss all bifurcations happening up to a certain α so just the number of bifurcation points as a function of α is depicted in Fig. 6.17. For the perfect superlattice and for moderate disorder, this number is equal to twice the number of (unstable) branches. This number rises sharply once isolas of strange states are inserted into the characteristic. Above a certain value of α, the number of bifurcation points starts to decreases again.

The explanation for this is given in Fig. 6.18. Just as it is possible for an isola to merge with the continuous current-voltage characteristic, it is also possible for it to separate again. In contrast to the process of merging where the isola consisted only of strange states, the separated isola may also contain one or multiple branches of the "standard" current-voltage characteristic. Since Fig. 6.18 does not include the unstable branches due to their vast number, the different parts of the current-voltage characteristic can only be distinguished by the different dashes of the corresponding lines.

---

[4] Actually, there is an "earlier" merging. However, this happens at a voltage of just a few tenth of one volt so boundary effects are too important there.

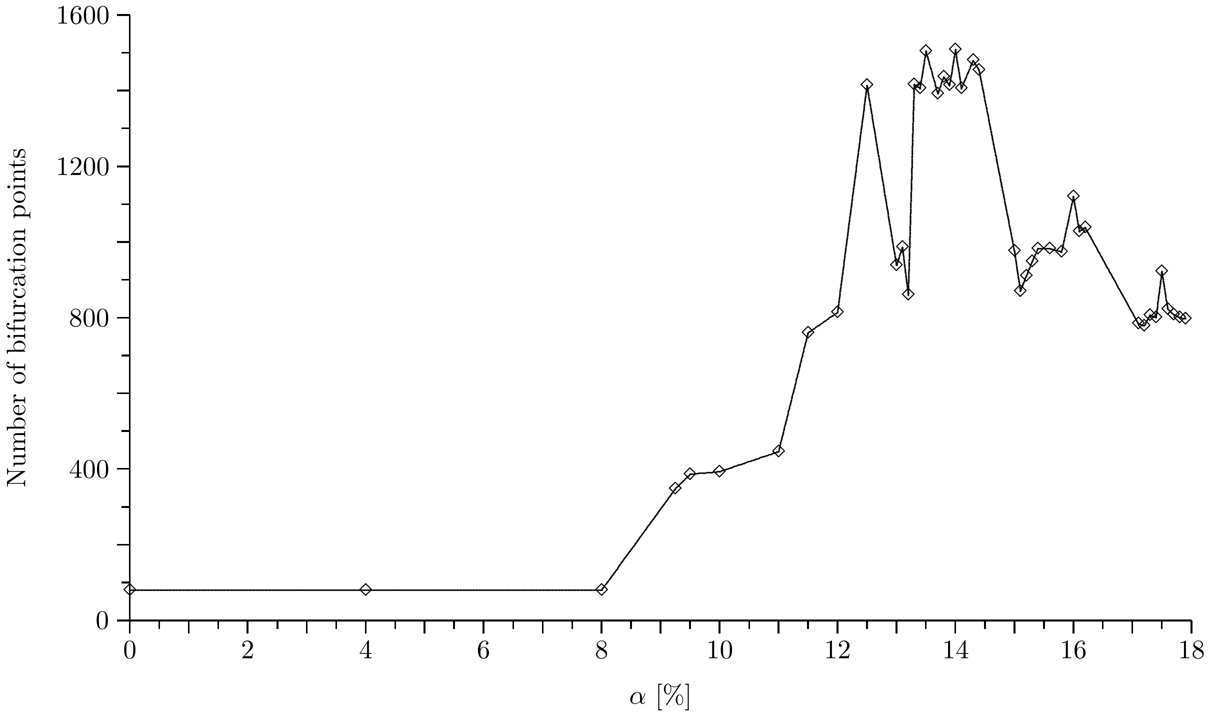

Figure 6.17: Number of saddle-node bifurcation points on the full connected current-voltage characteristic as a function of the level of disorder, α. The diamonds mark data-points determined by calculating characteristics for the respective value of α. The lines give the linear interpolation of these points. For $\alpha \leq 8\,\%$, there are exactly 80 bifurcation points, i. e., 40 (unstable) branches. For higher α, the number of branches increases sharply but there are also regions in which the number decreases again.

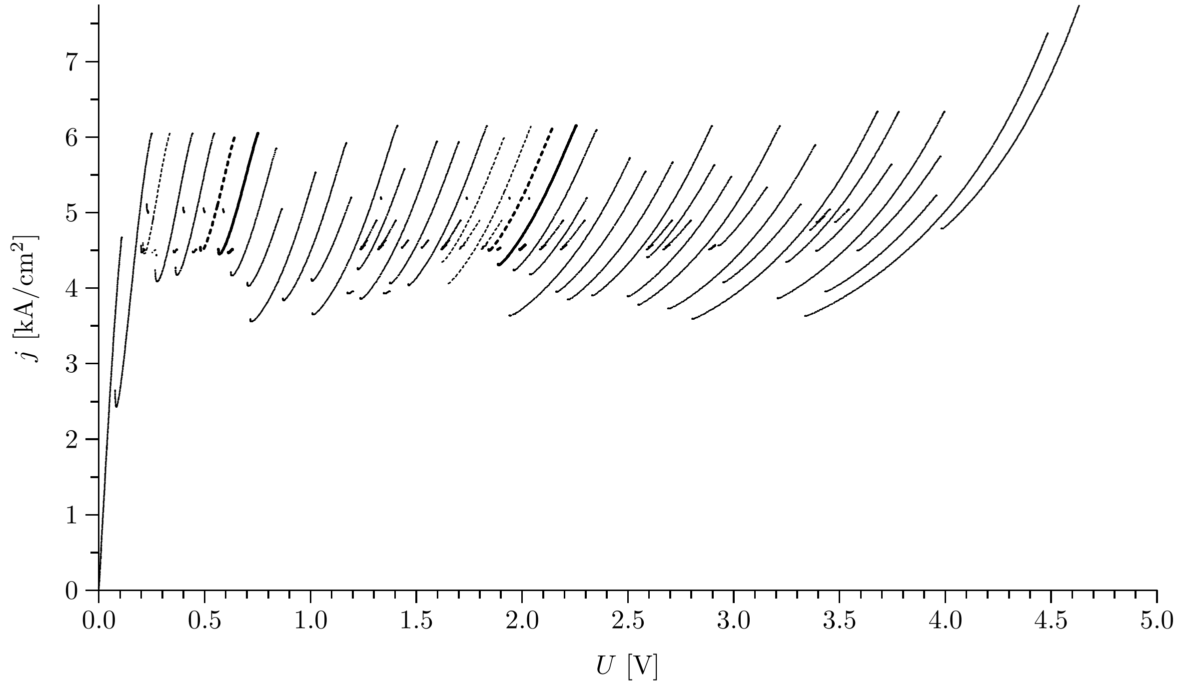

Figure 6.18: Splitting of the full connected current-voltage characteristic into different parts for very high α. The total data depicted consists of a continuous characteristic and six isolas; only their stable branches are shown. The branches belonging to different parts are dashed differently.

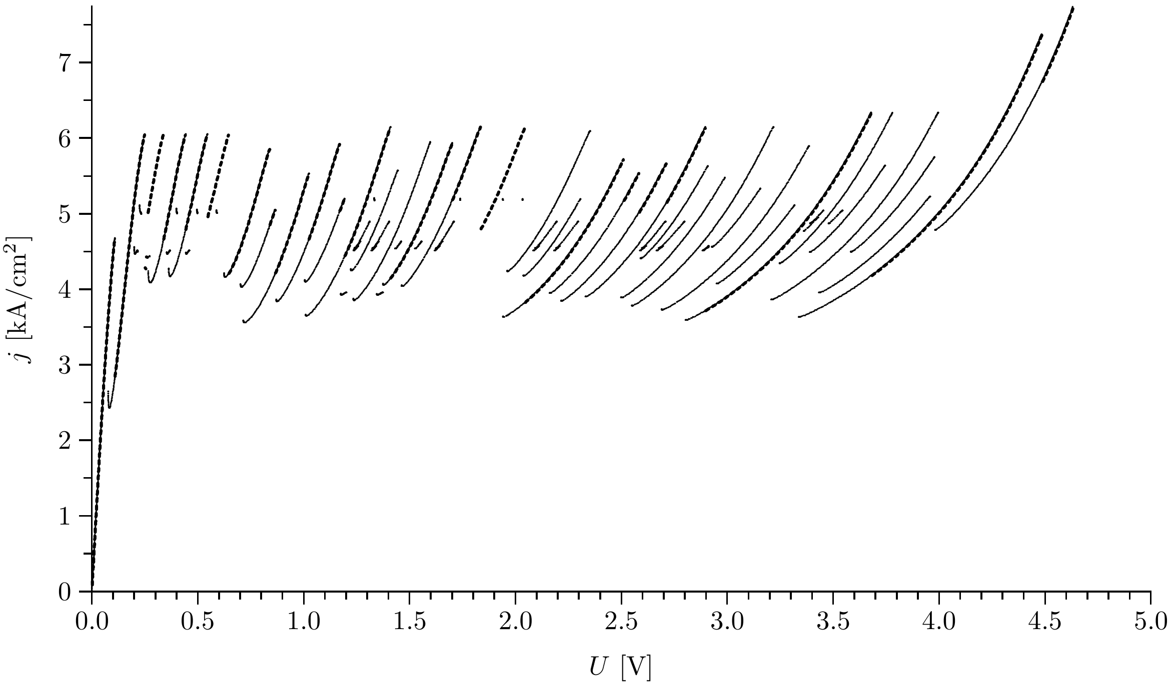

Figure 6.19: Comparison of the full connected current-voltage characteristic with the simulated characteristic. The stable branches of the full connected characteristic are marked with solid lines, its unstable branches are not depicted, and the simulated voltage sweep-up is marked with thicker but dashed lines.

6.6 Comparison of Simulation and Continuation

So far, we have only discussed the results of continuation algorithms. The question now is whether it is possible to find the additional stable branches also in a simulation and thus (in principle) also in experiments. This is similar to the problem whether all branches can still be reached in superlattices with moderate disorder.

The answer to this question is depicted in Fig. 6.19 where the full connected current-voltage characteristic and a simulated voltage sweep-up are displayed. First, branches that have separated from the continuous characteristic are – as expected – still reached in the simulation. Second, some of the additional branches are also reached. As these branches are usually very short and, furthermore, only a small part of a branch is actually reached during a voltage-sweep up, these branches are displayed just as dots. This primarily happens for small voltage as the branches are more steep there [Sch95b] and thus there is less "competition" from the "standard" branches.

The precise shape of the current-voltage characteristic changes at bit if time-dependent fluctuations (for example, to simulate thermal noise in experiments) of the electron configuration are taken into account. This can be done by a slight variation the initial electron configuration – usually one takes the result of the simulation for the preceding voltage step – before the simulation is started. This variation is necessary anyway as this is the only way to guarantee that an unstable stationary state is actually left. Thus, the electron density in a particular quantum well was increased by 2 % for all simulations presented in this thesis. Similar is done by other authors [Bon94, Sch95b] for similar reasons. This kind of variation leads to the current-voltage characteristic depicted in Fig. 6.20(a).

An other approach is to randomly variate the initial electron densities in all quantum wells. This has been done for the remaining subfigures of Fig. 6.20. If the variation is rather large (Fig. 6.20(d)), some branches that are missed out otherwise are reached as the "preceding" stable branch can then be left before the saddle-node bifurcation is actually reached. Furthermore, additional branches of "strange" states can be reached as can be seen near approximately $U = 3$ V.

When making experiments, such fluctuations of the electron densities are certainly important. Most probably, there are also effects amplifying the effects of these fluctuations. Thus, it may be easier to reach branches of "strange" states in experiments (if they actually exist) than it is in "plain" simulations. Unfortunately,

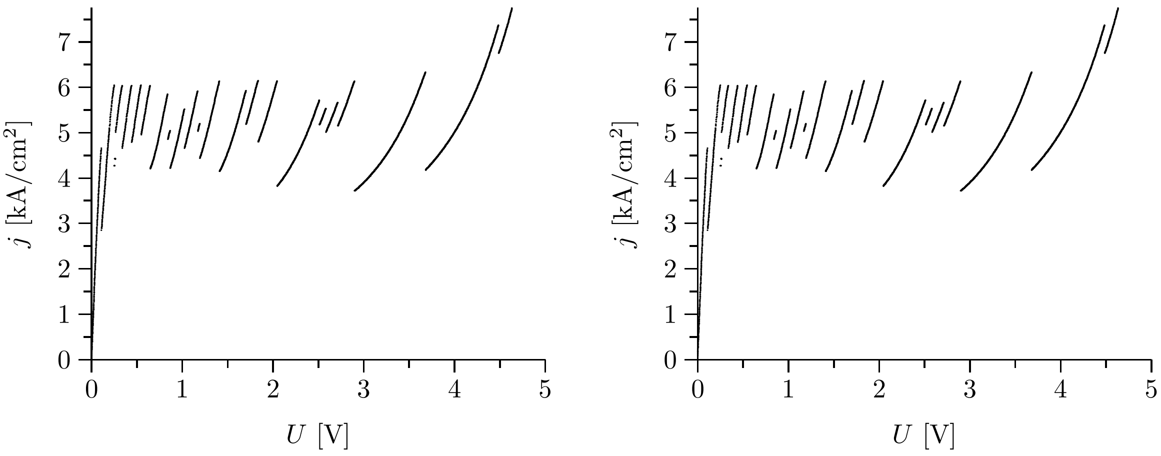

(a) "Standard" variation

(b) No variation

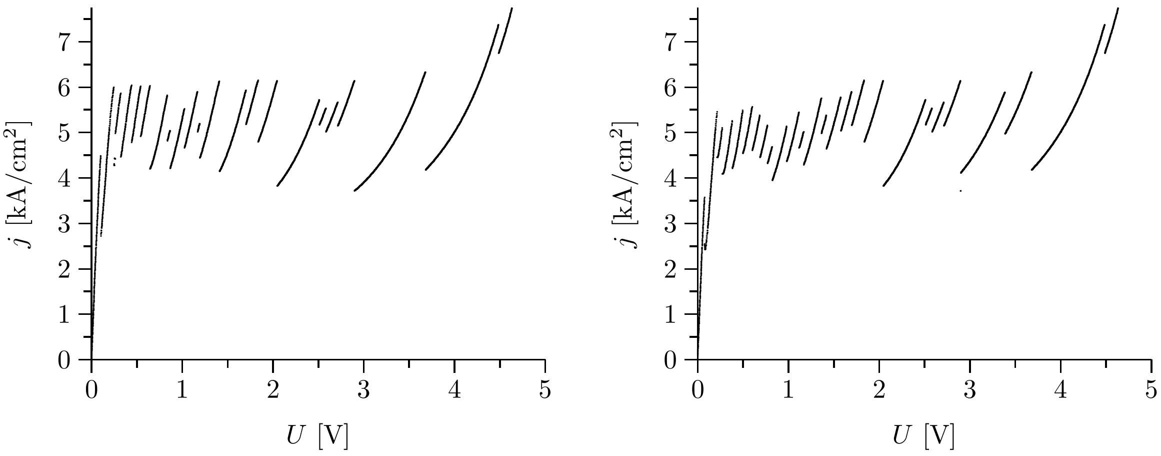

(c) Random variation up to 0.5 %

(d) Random variation up to 2.5 %

Figure 6.20: Effects of variations of the initial data after each voltage step on the resulting current-voltage characteristic. For more information, refer to the text.

the field profiles of strange states are not different "enough" from the ones on the "standard" current-voltage characteristic to be able to see the difference using experimental technologies like the measurement of photo luminescence. If one would reach strange states in an experiments, one probably would not notice.[5]

6.7 Oscillations

As has been demonstrated in chapter 5, the effects of doping fluctuations on the frequencies and amplitudes of oscillations is rather small. However, the effect on the oscillatory regime (the values of U and N_D, for which there are oscillations) is very strong. For $\alpha = 14\,\%$, the figure looks qualitatively the same as the corresponding figures for moderate disorder. However, if α is increased (Fig. 6.21(b)), a second branch of Hopf-bifurcation points is created. Both end points of this branch are Takens-Bogdanov points (see also section 2.11 on page 12). Thus, a second region with oscillations is created. The exact size or shape of

---

[5] The only solution would be to simply compare the number of the branches in the current-voltage characteristic with the number of quantum wells in the superlattice. On the other hand, many measured experimental characteristics contain very short branches; it is not clear whether these are just an artefact of the method used to measure the current-voltage characteristic. Furthermore, we do not know for sure whether there should be $N-1$, N or $N+1$ branches for a superlattice with N quantum wells as boundary effects might inhibit the domain boundary to be located in the quantum well next to the boundary layer. Thus, it does not help to simply count the number of branches.

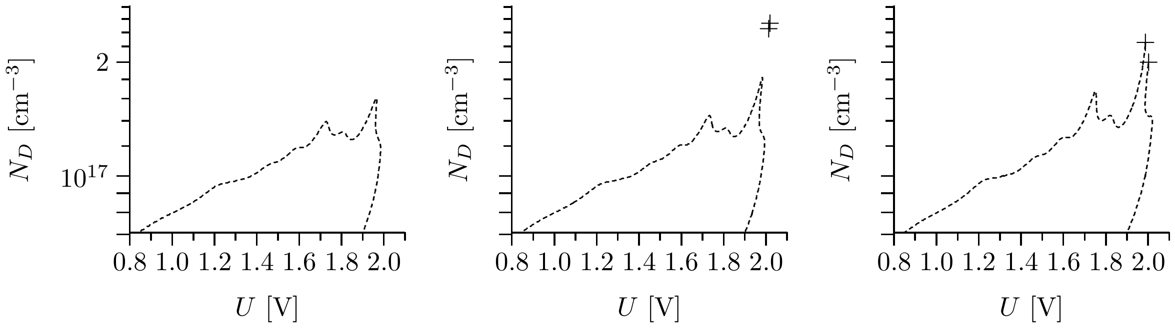

(a) $\alpha = 14\,\%$ (b) $\alpha = 14.5\,\%$ (c) $\alpha = 16\,\%$

Figure 6.21: Location of the Hopf-bifurcation points ("phase diagram") for superlattices with a different amount of doping fluctuations. **(a)** Like in the case of moderate disorder, the Hopf-bifurcation points form an isola, inside of which there are oscillations. **(b)** A new region with oscillations forms as two Takens-Bogdanov points emerge. The line of Hopf-bifurcation points between the two Takens-Bogdanov points is hard to see (see also Fig. 6.22). **(c)** The isola has merged with the oscillatory regime caused by the Takens-Bogdanov points.

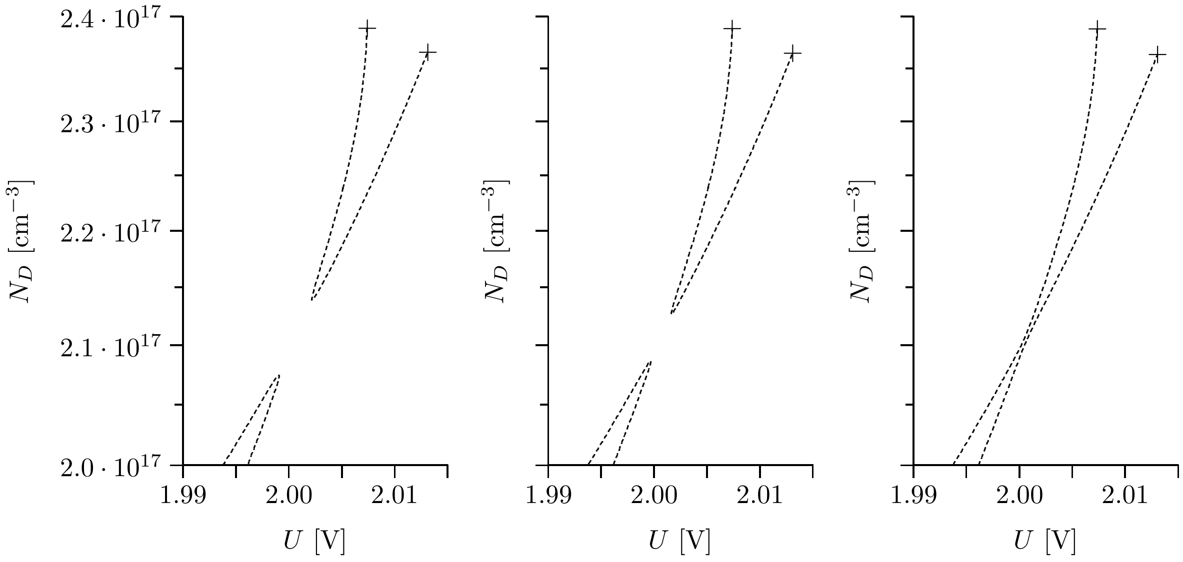

(a) $\alpha = 14.670\,\%$ (b) $\alpha = 14.671\,\%$ (c) $\alpha = 14.672\,\%$

Figure 6.22: Merging of the oscillatory regimes when α is increased. The lower of the two curves (Figs.**(a)** and **(b)**) belongs to the Hopf-isola existing also in the unperturbed case; only a very small part of this isola is depicted.

this region is not as easy to compute as for the oscillations "trapped" inside the Hopf-isola already existing for lower α. We will return to this subject a bit later. If α is increased further, this new oscillatory region merges with the Hopf-isola. The result is a single large oscillatory region with oscillations but this region is now "open".

The process of merging is examined a bit closer in Fig. 6.22. Please note that it is not a bifurcation. The positions of all Hopf-bifurcation points form a two-dimensional manifold in the U-N_D-α space. The phase diagrams depicted so far are sections perpendicular to the α-axis. This is similar to contour-lines on a map of a mountain: Around each summit, there are a number of closed contour-lines enclosing only that particular summit. However, contour-lines corresponding to smaller heights may enclose more than just a single summit. Thus, by changing the height at which we cut through the mountain, we may get a single or multiple

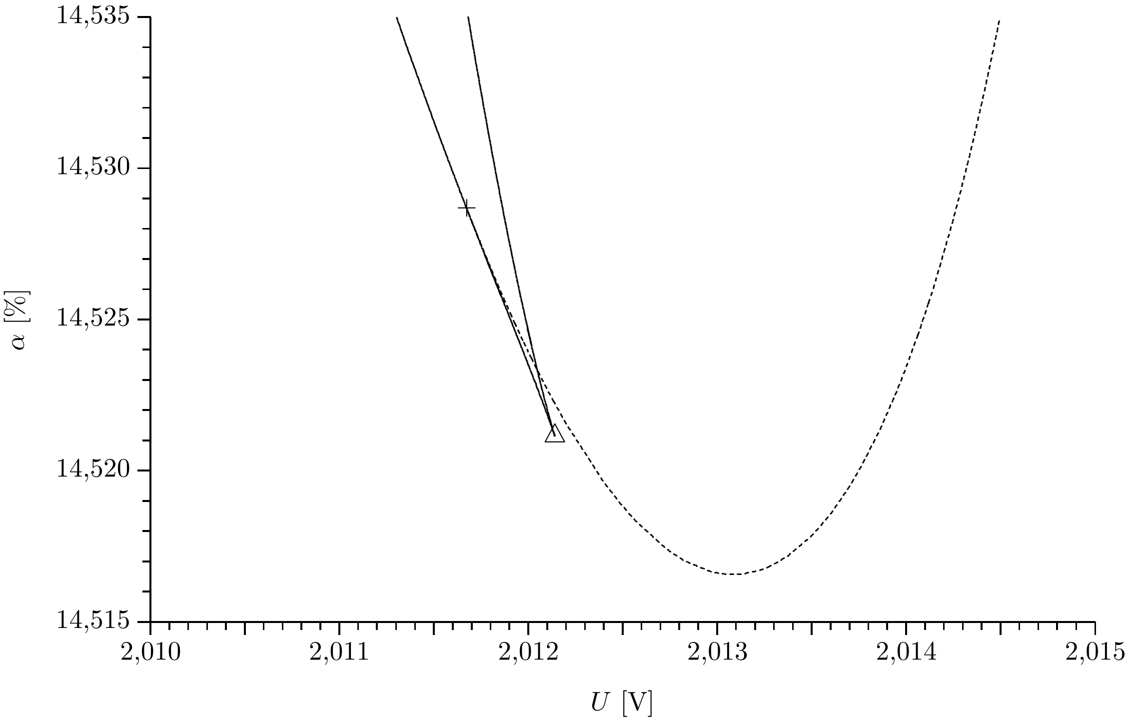

Figure 6.23: Neighbourhood of a Takens-Bogdanov point. The branch of Hopf-bifurcation points merges with a branch of saddle-node bifurcation points in a point of second-order contact. The latter curve goes into a cusp points and changes it direction there.

curves. The merging of different curves to a single one when a parameter is changed is therefore nothing “special”.

As has already been discussed in section 2.11, a Takens-Bogdanov points marks the intersection of a branch of Hopf-bifurcation points and a continuous branch of saddle-node bifurcation points. These are depicted in Fig. 6.23. Please note that U and α have been chosen instead of U and N_D. There is no principal difference between α and N_D but this choice allows to determine the qualitative shapes of the current-voltage characteristics for different amount of disorder.

As can be seen in Fig. 6.23, the branch of Hopf-bifurcation points extends towards lower α than the branch of saddle-node bifurcation points. Thus, the Takens-Bogdanov point can first be “seen” by an additional pair of Hopf-bifurcation points (Fig. 6.24(c)). When α is increased, two saddle-node bifurcation points are also inserted (Fig. 6.24(d)). When α is increased above the position of the Takens-Bogdanov point, one of the two Hopf-bifurcation points vanishes (Fig. 6.24(e)). In the current-voltage characteristics, a Takens-Bogdanov points may be recognised by the merging of a saddle-node bifurcation point and a Hopf-bifurcation point with latter being destroyed. Actually, it is not necessary to compute the current-voltage characteristics as these scenario can completely be derived just from Fig. 6.23.

When the Hopf-bifurcation point is destroyed, the regime of oscillations has to be restricted by saddle-loop bifurcation points. The effects of this bifurcation will now be examined in more detail. Fig. 6.25 depicts the location of the Hopf bifurcation point for the superlattice in question. We will now focus on the parameters along the drawn-out line in this figure. The right end-point of this line is a saddle-loop bifurcation point, the left end-point is a Hopf-bifurcation point.

Fig. 6.26 depicts the oscillation frequency and amplitude along this line. For small voltage, there is a Hopf-bifurcation points as is confirmed by the decrease of the oscillation amplitude. The simultaneous decrease of the oscillation frequency might seem to be atypical but can also be explained: A Takens-Bogdanov points has zero as a double eigenvalue. Thus, it is kind of a Hopf-bifurcation point with frequency zero. Along the branch of the Hopf-bifurcation points going towards the Takens-Bogdanov points, the frequency of the bifurcating limit cycle thus decreases continuously down to zero. With increasing distance to the Hopf-bifurcation point (and thus to the Takens-Bogdanov point) the frequency increases. Near the saddle-loop bifurcation, both oscillation am-

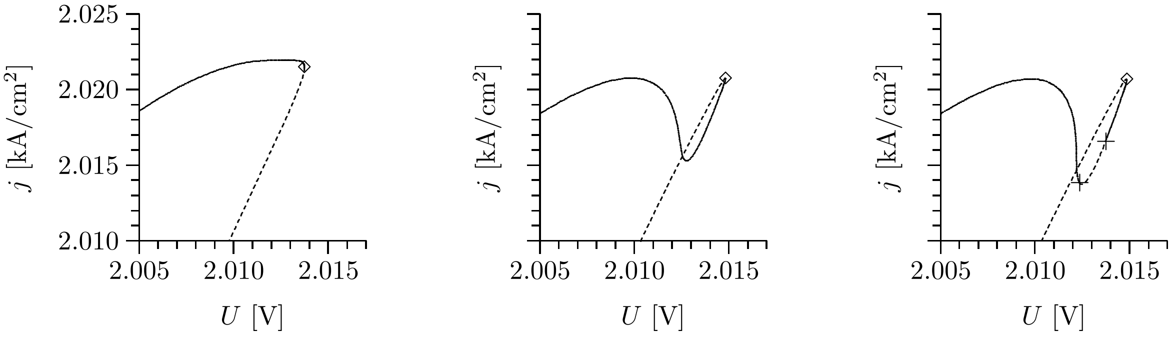

(a) $\alpha = 14.4\,\%$ (b) $\alpha = 14.515\,\%$ (c) $\alpha = 14.520\,\%$

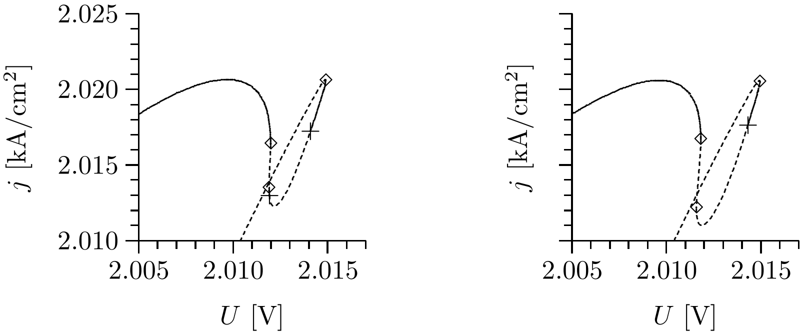

(d) $\alpha = 14.525\,\%$ (e) $\alpha = 14.530\,\%$

Figure 6.24: Current-voltage characteristics for different levels of doping fluctuations. It is possible to deduce the qualitative shapes of these characteristics from Fig. 6.23.

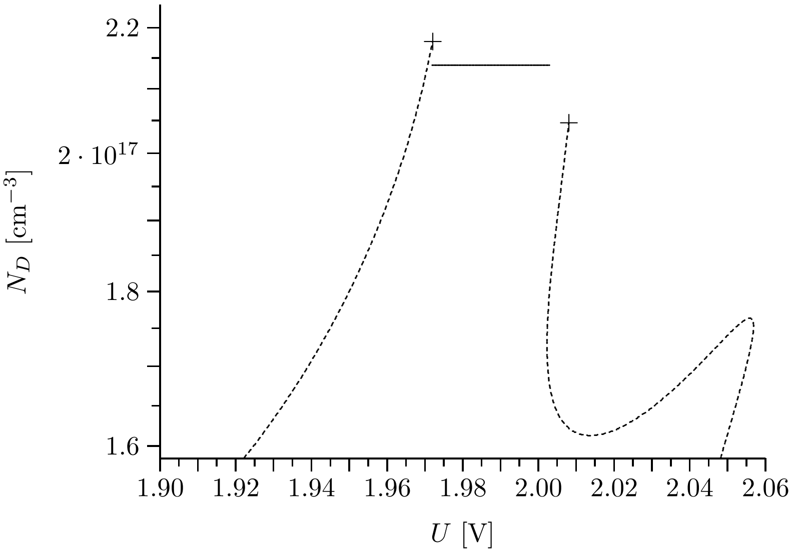

Figure 6.25: Location of the Hopf-bifurcation points near the Takens-Bogdanov points for $\alpha = 17.5\,\%$. The drawn-out line marks the parameters for which the oscillations will be examined in more detail later on. At the end-points of this line, the oscillations also end.

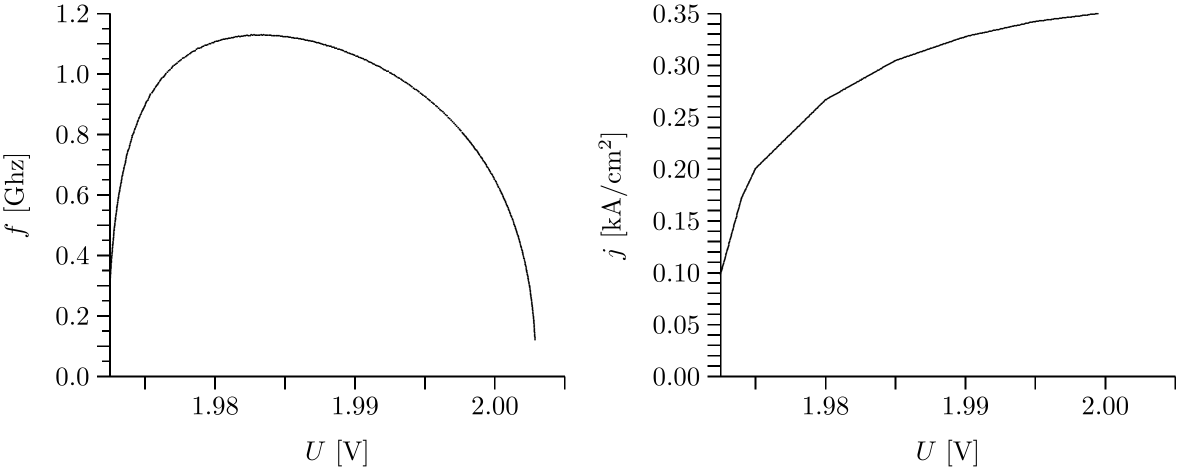

(a) Frequency (b) Amplitude

Figure 6.26: Oscillation amplitude and frequency along the drawn-out line from Fig. 6.25. For higher voltage, the saddle-loop bifurcation leads to a decrease of the frequency of the oscillation down to zero while the amplitude is not affected. The decrease in the frequency for small voltage is atypical for a Hopf-bifurcation point but can also be explained: A Takens-Bogdanov points is kind of a Hopf-bifurcation point where the bifurcating limit cycle has frequency zero. Thus, near a Takens-Bogdanov point the limit cycle bifurcating in a Hopf bifurcation will have a relatively small frequency.

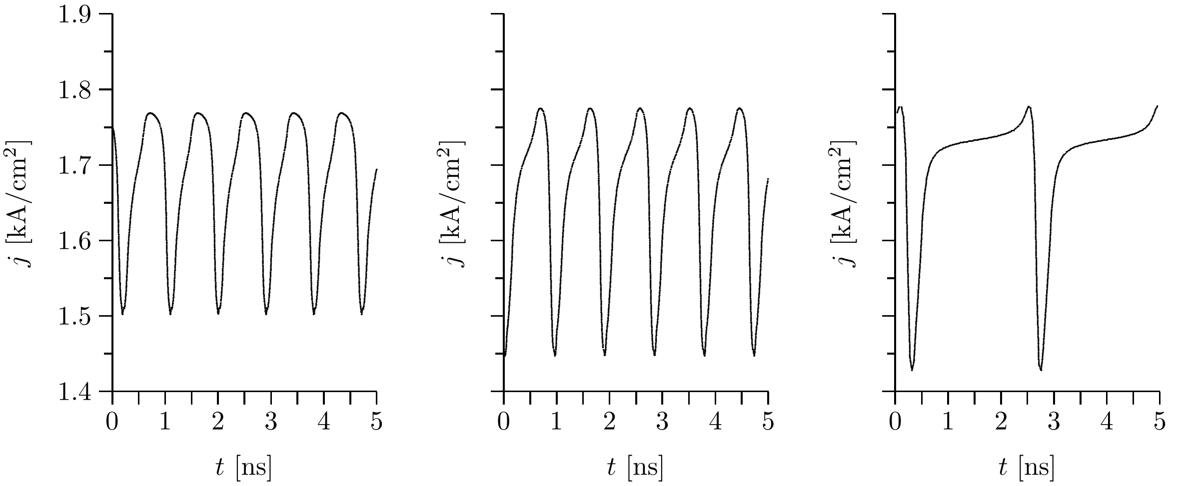

(a) $U = 1.98$ V (b) $U = 1.99$ V (c) $U = 2.002$ V

Figure 6.27: Oscillations near the saddle-loop bifurcation point (this bifurcation happens at approximately $U = 2.0029$ V). When the voltage is increased, the frequency decreases and there is an ever longer phase during which the current density changes only very slowly.

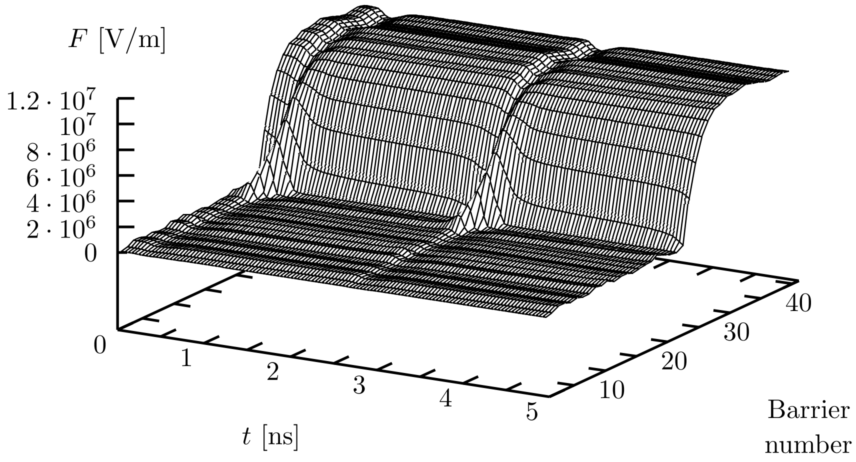

Figure 6.28: Field distributions corresponding to the current oscillations depicted in Fig. 6.27(c). The division into a clearly distinguishable high-field and low-field domain is due to the high doping density, the long "inactive" periods are caused by the nearby saddle-loop bifurcation.

plitude and frequency show the typical behaviour.

If we examine not only the frequency but also the shape of the oscillations, we see that the saddle-loop bifurcation leads to ever longer periods of almost inactivity (Fig. 6.27). This is what had to be expected as the limit cycle adapts more and more to the shape of the homoclinic orbit, with which it is about to merge in the saddle-loop bifurcation. Near the involved fixed point, the dynamics is slow with fast "outburst" when the system leaves the neighbourhood of the fixed point.[6] Such a oscillation is often referred to as "spiking".

The field distribution during such a oscillation is depicted in Fig. 6.28. Due to the high amount of doping fluctuations, oscillations are now possible for significantly higher doping density. At this doping density, there is already a clearly distinguishable high-field and a low-field domain whereas oscillations in an unperturbed superlattice always are connected with a washed-out domain structure. The "spike" during the oscillation leads to a short change in the shape of the domains such that the boundary between the two domains is not so steep any more. Thus, we observe "spiking" between two domain states and not between a domain state and the homogeneous state.

Finally, we want to discuss all three parameters simultaneously by investigating the locations of the Takens-Bogdanov points. They lie on a curve in U-N_D-α-space which makes it only possible to present a projection here. In Fig. 6.29, we have chosen N_D and α as it is possible to deduce from this figure how large N_D may be in order to still have oscillation, and how large the amount of disorder has to be for this. Besides the two Takens-Bogdanov points, the cusp point already depicted in Fig. 6.23 is also included. The simultaneous creation of two Takens-Bogdanov points and one cusp point is a scenario described before [Dum92].

---

[6] Similar effects are discussed in section 7.2. The homoclinic orbit investigated there has absolutely nothing to do with the one discussed here. However, the effects are the same.

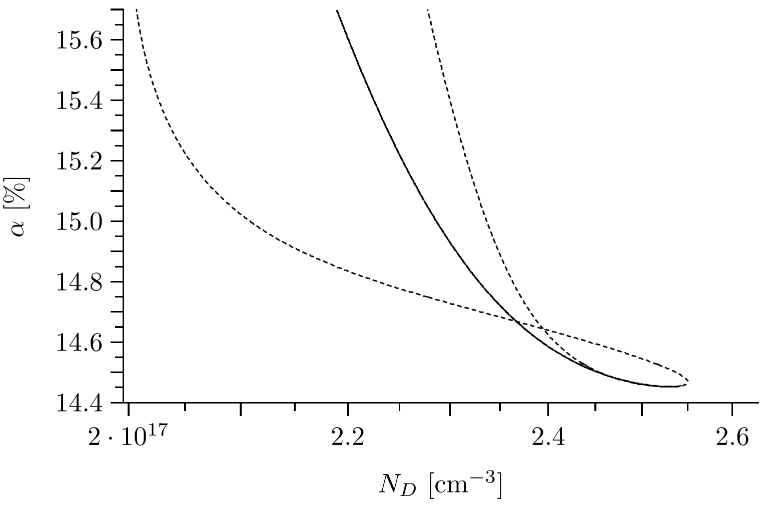

Figure 6.29: Locations of the Takens-Bogdanov points. These lie on a curve in U-N_D-α-space. Thus, it is only possible to depict a projection. The Takens-Bogdanov points are marked with dashed line, cusp points as drawn-out line.

Chapter 7

Neumann Boundary Conditions
or
“Boundary conditions that allow an exactly homogeneous field distribution”

It was already mentioned in section 3.6 that almost all boundary conditions will lead to similar results – with one exception which will be dealt with in this section. In the notation introduced earlier, these “special” boundary conditions are denoted by $c_1 = 1$ and $c_2 = 0$. This can best be understood as copying the electron densities from the last “real” quantum wells to the “virtual” ones. From a mathematical point of view, these boundary conditions are nothing but the discrete version of Neumann boundary conditions.

There are two reasons why the analysis of these boundary conditions may lead to interesting results: On the one hand, the system becomes degenerate and additional bifurcations are thus introduced. On the other hand, these boundary conditions have been used in earlier publications (for example [Pre94a] and [Pre94b]; [Sch96b] gives a short comparison with “rigid” boundary conditions), so the results in this chapter will be able to explain a few of the observations made in these references from the results of simulations.

7.1 Light and Medium Doping

In contrast to the boundary conditions considered in the preceding chapters, only Neumann boundary conditions allow a stationary state with an exactly homogenous field distribution. For such states, the effective charge in every quantum well, including the additional virtual ones, has to be zero which excludes any boundary conditions with fixed doping density in the virtual wells.[1] As an exactly homogeneous field distribution cannot explain the familiar features of a superlattice, further states have to exist.

Fig. 7.1 depicts the current-voltage characteristic of a superlattice with $N_D = 2 \cdot 10^{16}$ cm^{-3}. At this doping density, self-sustained oscillations occur which will be discussed a little later and are omitted in this figure. The total current-voltage characteristic consists of three branches labelled “a” to “c”; the homogenous branch is labelled “b”. It is unstable in the NDC region

---

[1] If only one energy level is considered, fixing the doping density in the virtual wells at one times the doping density N_D allows an homogenous state. If two energy levels are considered, not only the total number of electrons but also the distribution of these electrons among the two energy level has to be right – this ratio, however, depends on the applied voltage. Note that it is not important that the electron density in the virtual wells is equal to the doping density for every state but only for the homogeneous one. So one may also choose more complex boundary conditions like $n_2^{(0)} = n_2^{(1)}$, $n_1^{(0)} = 3n_1^{(1)} + 2n_2^{(1)} - 2N_D$, which also fulfil all these conditions without being Neumann boundary conditions.

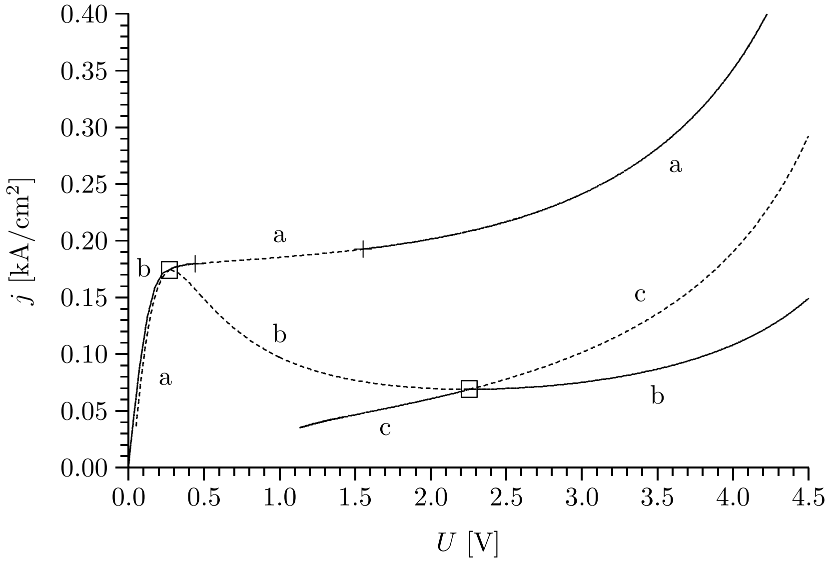

Figure 7.1: Current-voltage characteristic for $N_D = 2 \cdot 10^{16}\ \mathrm{cm}^{-3}$. The limit cycles bifurcating in the Hopf bifurcation points are not depicted in this figure. The characteristic consists of three branches labelled "a", "b" and "c".

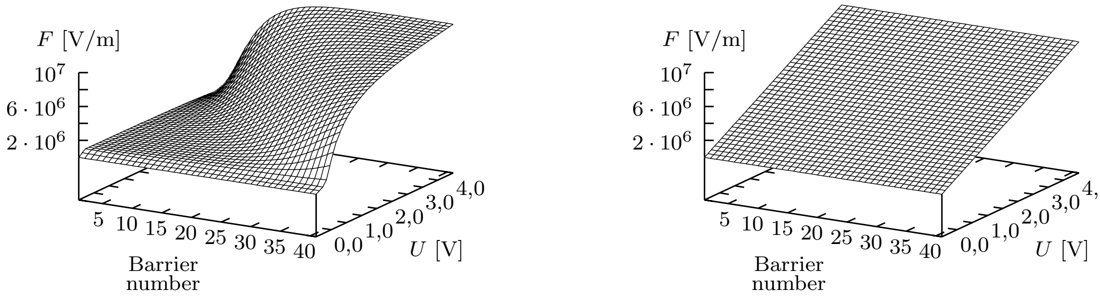

(a) "Domain branch"

(b) Homogeneous branch

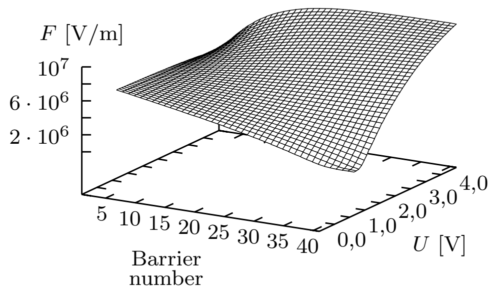

(c) "Wrong-domain branch"

Figure 7.2: Field profiles of the three branches of the current-voltage characteristic in Fig. 7.1. The labels of the corresponding subfigure are the same as the labels of the respective branch in Fig. 7.1.

and stable outside this region, precisely as expected due to general reasons. This branch is connected to the two other branches by transcritical bifurcations.

The branch "a" ends at about 0.1 V, branch "c" at 1 V. This is not supposed to mean that the branches do not exist for lower values of the applied external voltage. Rather, the electron densities decrease along this branches and tend asymptotically towards zero. From a physical point of view, it makes no sense to continue the calculations once the electron densities have fallen below a certain threshold.[2]

The field distributions along the three branches are depicted in Fig. 7.2. Due to graphical reasons the positions of the voltage- and the "quantum well"-axis have been exchanged compared with similar figures in the preceding chapters. As has already been mentioned, the field distribution along branch "b" is exactly homogeneous; the electric field is strictly proportional the applied external voltage. The field distribution along branch "a" is a washed-out domain similar to the ones for other boundary conditions at similar values of N_D (see, for example, Fig. 4.21). As the Hopf bifurcations in Fig. 7.1 clearly demonstrate, the limit cycle oscillations bifurcate from this branch; for higher doping, current branches develop on this branch.[3] Thus, this branch is the one corresponding to the single branch seen for other boundary conditions.

The field distribution along branch "c" exhibits a domain structure, too. The domain lies on the "wrong" side, however. The "standard" high-field domain lies on the anode side (where the electrons move to) and is caused by a charge accumulation. The "wrong" domain structure lies on the cathode side and is caused by a charge depletion. Thus, the current will be smaller along this branch as the current is proportional to the number of available electrons. Please refer also to appendix C (page 111) for a discussion about on which side the high-field domain should be.

In some earlier publications (for example [Pre94a] and [Sch95b]), it is suggested that the entire homogeneous branch should be stable if the doping density is small enough.[4] For this reason, the largest eigenvalue (this eigenvalue is real) is depicted in Fig. 7.3 as a function of the doping density. The result is that it is strictly proportional to N_D. This is in accordance with the results from [Sch95b, Appendix E] except that an additional offset is assumed there.[5] Thus, the two transcritical bifurcation points also exist regardless of the value of N_D. As the voltage region exhibiting NDC does not depend on the doping density, so do the parameter values of these two bifurcation points.

As result, we conclude that Fig. 7.1 is typical for every value of N_D as long as no current branches have developed. If Hopf bifurcation points exists, we just have to "make" the corresponding part of the "domain" branch unstable.

7.2 Oscillations

Fig. 7.4 once again depicts the current-voltage characteristic for $N_D = 2 \cdot 10^{16}$. However, this time the limit cycles are included. For every limit cycle, the minimum and the maximum value of the electric current during one oscillation period are marked in the figure. For every

---

[2] In addition, there are problems of a numerical nature. The electron densities cannot become negative as the rate of electrons leaving a certain quantum well is strictly proportional to the number of electrons in that quantum well. The integration algorithm uses error control to adapt the step size so that the error of each step stays below a given value. For very small values of the electron densities the necessary step size may become too small and the algorithm will fail. A sure sign of this is that the numerically calculated electron densities become negative.

[3] In this chapter, "branch" means a curve of fixed points. If I want to refer to the saw-blade shaped structure of the current-voltage characteristic for heavily doped superlattice, I will use the term "current branch"

[4] When doing simulations, one experiences the following problem: Along the homogeneous branch the total electron concentrations is constant (and equal to the doping density). When the applied external voltage is varied, only the distribution of the electrons among the two energy levels may change. However, the dependence of this ratio on the applied voltage is very small. Furthermore, the dynamics within a given quantum well are fast compared to transport between different quantum wells. If one wants to leave to homogenous branch and switch to one of the other two branches, one has to transfer electrons to (or from) the desired location of the domain boundary. If the homogenous branch becomes unstable when the applied voltage is changed to some value in the NDC-region, the fast intra-well dynamics will adapt the electron configuration so that the resulting state is "almost stationary". If one stops the integration at this point, one will think that the state is still stable. One has to integrate further (for small doping density up to one hundred times longer) to see that the homogeneous state is in fact left.

[5] This offset exists in fact for the other $2N-1$ eigenvalues. For high enough doping, not only a single eigenvalue but all eigenvalues will be positive. As the offsets for the $2N-1$ other eigenvalues are of similar value, the corresponding modes will become unstable at similar values of N_D, the precise value being approximately $2.3 \cdot 10^{16}$ cm^{-3}. This high degeneracy makes it numerically impossible to trace the homogeneous branch as a function of the doping density over this value of N_D. It is possible to calculate this branch for higher values of N_D as well as for lower values but it is not possible to determine all bifurcation points in between.

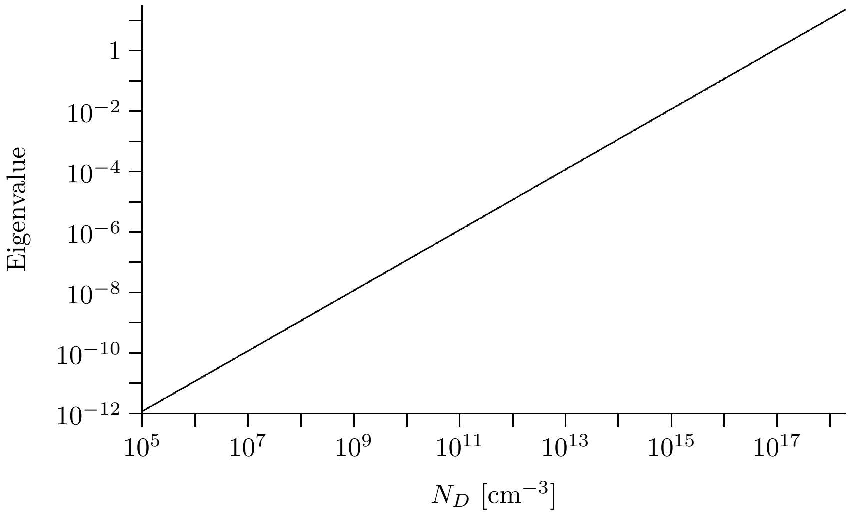

Figure 7.3: Largest eigenvalue of the homogeneous branch (NDC region) as a function of the doping density. Note that both axis are scaled logarithmically. The eigenvalue is exactly proportional to the doping density.

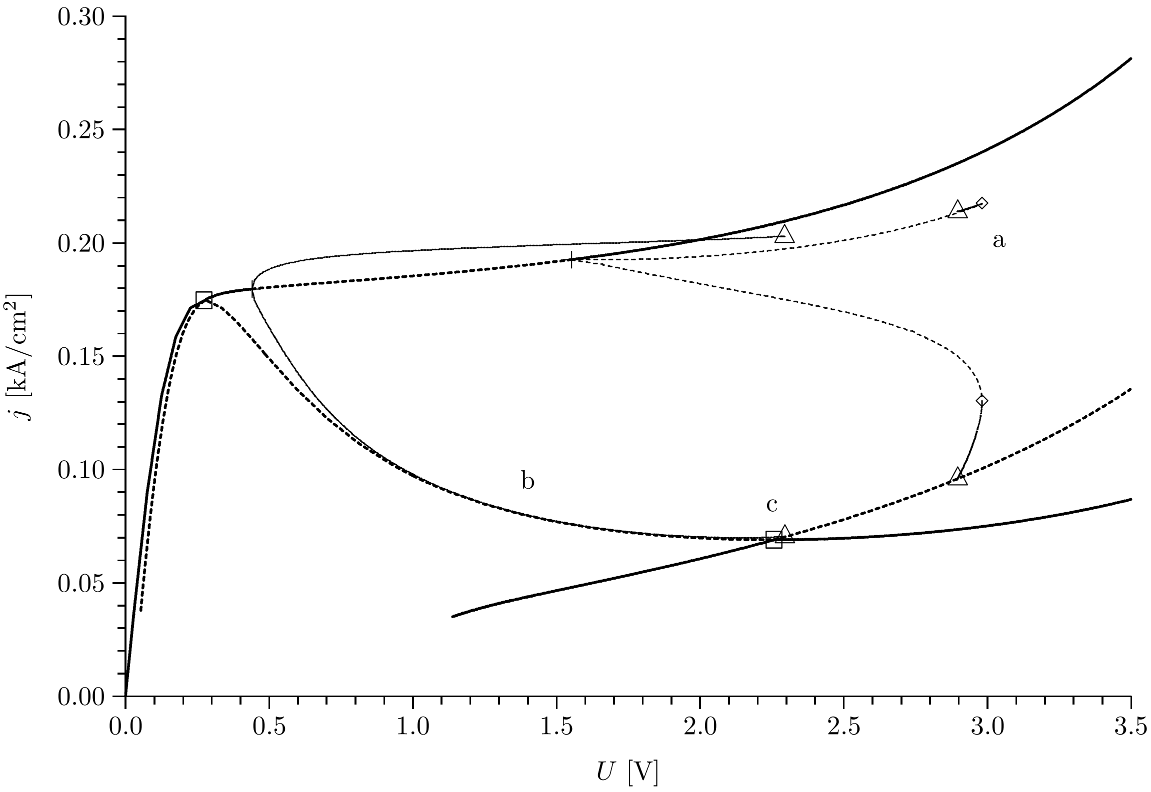

Figure 7.4: Bifurcation diagram with limit cycles. Stable "objects", fixed points as well as limit cycles, are drawn-out, unstable ones dashed. The lines corresponding to fixed points are a bit thicker than the ones corresponding to limit cycles. For limit cycles, the minimum and the maximum of the electric current during one oscillation period are depicted. Every bifurcation point on a limit cycle is thus depicted twice: once on the upper curve and once on the lower curve. The letters mark positions in the diagram which are discussed in more detail in the text.

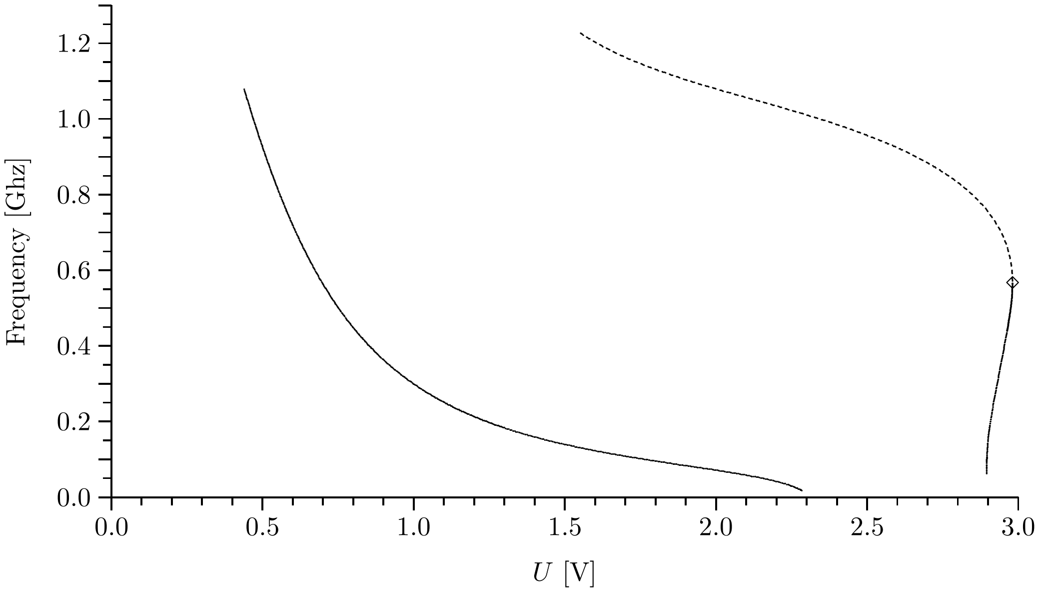

Figure 7.5: Dependence of the oscillation frequency on the applied external voltage for the limit cycle oscillations from Fig. 7.4. The frequencies along the stable limit cycle branches are depicted as solid lines, the ones along unstable branches are dashed. The decrease of the frequency down to zero while the amplitude stays finite is characteristic for a saddle-loop bifurcation.

limit cycle, there are thus two curves in the figure which will be called "upper" and "lower" curves in the following discussion.

The left Hopf bifurcation point is – just as the Hopf bifurcations investigated in the preceding chapters – supercritical whereas the right one is subcritical. The unstable limit cycle, which is bifurcating in the subcritical Hopf bifurcation point, exists for values of U up to approximately 3 V. There the limit cycle becomes stable in a saddle-node bifurcation. The now stable limit cycle turns back towards lower voltage. This can best be seen along the lower curves whereas the upper curves (in the figure near "a") are very close.

The amplitude along the other stable limit cycle (the one, which bifurcates in the supercritical Hopf bifurcation) grows as the distance to the bifurcation point increases until part of the limit cycle lies near the fixed point on the homogeneous branch (point "b"). It will be shown later on that this is in fact so and not just a consequence of only displaying the electric current j corresponding to each state.

The two stable limit cycles each end in a saddle-loop bifurcation. Characteristic for this bifurcation is the decrease of the oscillation frequency down to zero whereas the oscillation amplitude is not affected by the bifurcation. The dependence of the oscillation frequency on the applied voltage is depicted in Fig. 7.5. The first saddle-loop bifurcation lies near one of the transcritical bifurcations (point "c"). Therefore it seems plausible that these two bifurcations happen at the same position. On the other hand, one has to remember that the position of the transcritical bifurcation can be determined with great precision whereas the saddle-loop bifurcation is usually detected a bit too "soon" (a saddle-loop bifurcation is detected numerically at the very point where the oscillation period exceeds a certain threshold; in principal, this threshold should be infinity). If these effects are taken into account, the "real" distance between the saddle-loop bifurcation and the transcritical bifurcation should even be a bit higher than depicted in the figure.

As has been mentioned before, the homogeneous branch influences the limit cycle bifurcating in the supercritical Hopf bifurcation point and thus the shape of the oscillation. Fig. 7.6 depicts the corresponding phase portrait. The fixed point belonging to the homogeneous branch is origin of a homoclinic orbit. The other unstable manifold (not depicted here) runs towards the third fixed point ("wrong" domain, stable at this voltage). Even though the differences between the homoclinic orbit and the limit cycle are almost impossible to detect in the figure, the oscillation has a period of less than 10 ns. One can thus see that very small deviations have very large effects. The limit cycle is trapped inside the homoclinic orbit; this is possible even in very high dimensional systems when the dynamics is slow inside a certain plane in phase space but fast orthogonal to that plane.

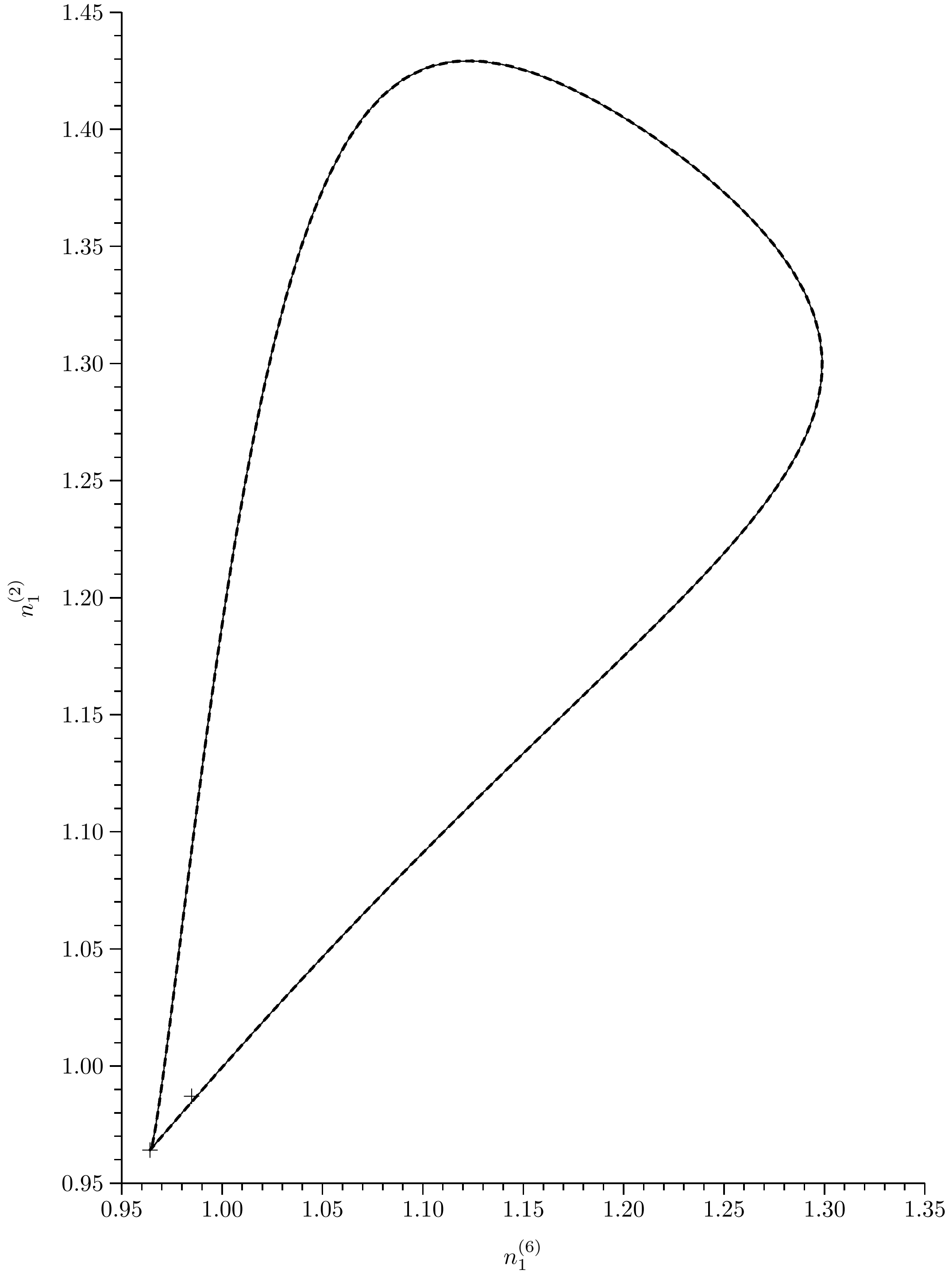

Figure 7.6: Homoclinic orbit and limit cycle. The homoclinic orbit is depicted as thin solid line, the limit cycle as thicker, dashed line. The fixed point near the origin belongs to the homogeneous branch, the one further away to the domain branch.

The homogeneous branch affects not only the shape of the limit cycle but is also responsible for its destruction in a saddle-loop bifurcation. The fact that these bifurcation points are on the homogeneous branch in Fig. 7.4 is not an effect of neglecting the high-dimensional phase space and considering just the current density.

This also explains the appearance of spiking oscillations (Figs. 7.7(e) and 7.7(f)), commonly associated with Neumann boundary conditions. Spiking oscillations can be characterised by two facts: They have a long phase with an almost homogeneous field distribution as well as a short phase of fast "out-breaks". This can also be explained by the limit cycle being trapped inside the homoclinic orbit. Since the responsible fixed point possesses a homogeneous field distribution, one can observe a long homogeneous phase during the oscillation. Once the system has moved sufficiently away from the fixed point, it describes a "normal" oscillation until it returns to the neighbourhood of the fixed point.

When the limit cycle bifurcates in the supercritical Hopf bifurcation, it cannot be under the in-

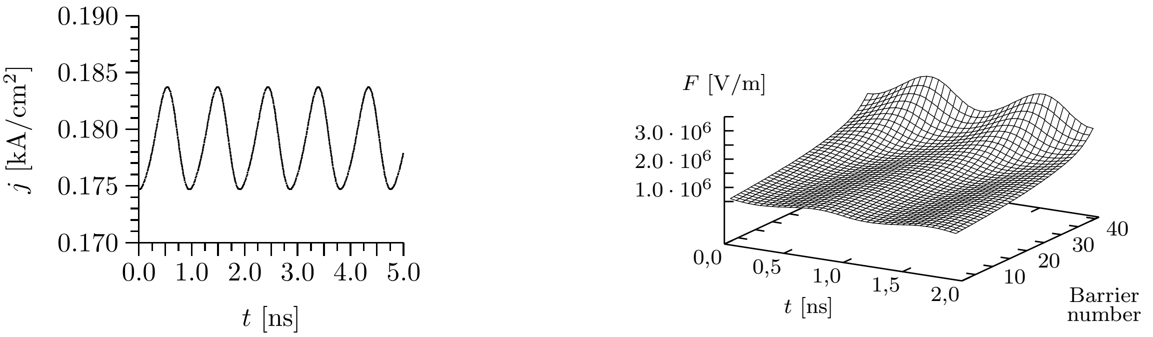

(a) Current density, $U = 0.45$ V

(b) Field distribution, $U = 0.45$ V

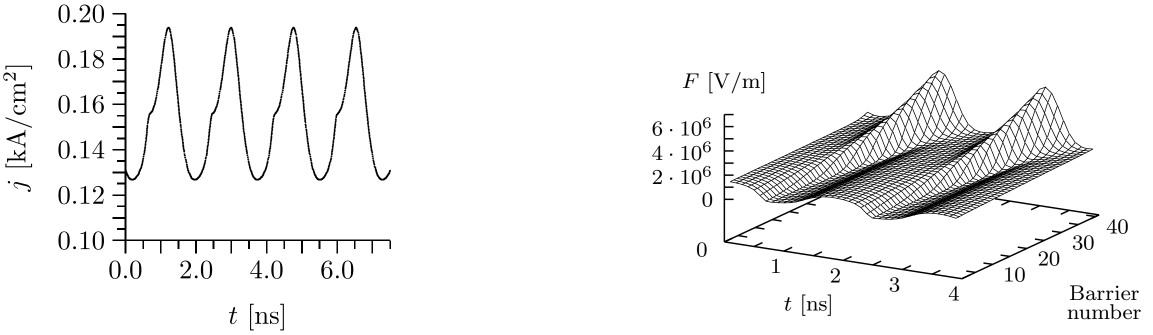

(c) Current density, $U = 0.7$ V

(d) Field distribution, $U = 0.7$ V

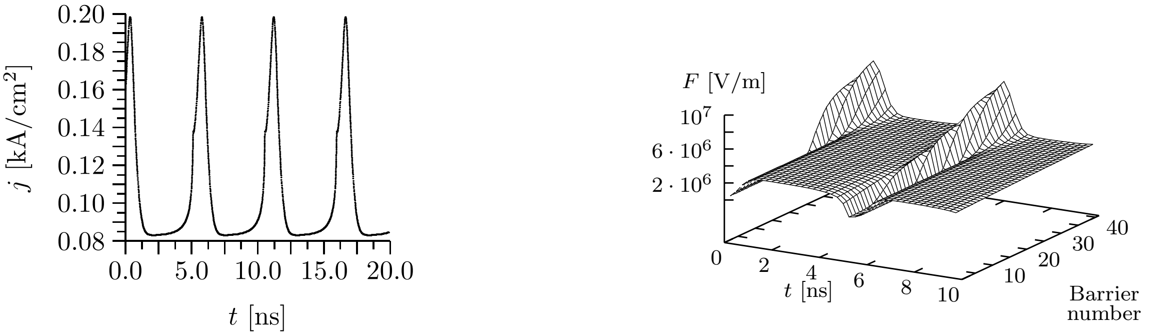

(e) Current density, $U = 1.3$ V

(f) Field distribution, $U = 1.3$ V

Figure 7.7: Oscillations for different values of the applied external voltage. With increasing distance to the bifurcation point, the sinusoidal oscillation deforms to a spiking oscillation.

fluence of the homogeneous branch right away. This is not possible as the system will remain near the domain branch when the distance to the bifurcation point is not too large. The homogeneous branch can thus only affect the oscillation when the oscillation amplitude has grown sufficiently. As Fig. 7.7 clearly demonstrates, sinusoidal oscillations are also possible for Neumann boundary conditions if the distance to the bifurcation point is not too large.

7.3 Heavily Doped Superlattices

In contrast to the current-voltage characteristics for small and medium doping, the characteristics for heavy doping are not fully understood yet. Fig. 7.8 depicts part of such a characteristic. Many branches could not be calculated due to numerical problems. In addition, the number of bifurcation points is very high. For test purposes, the current-voltage characteristic of a superlattice consisting of only four quantum wells has been investigated: The calculation was aborted when more than 1000 bifurcation points had been found. It is thus questionable whether the number of bifurcation points is finite.

Main reason for this is the homogeneous branch. As has been discussed in section 7.1, one eigenvalue is positive in the NDC region for medium doping but all eigenvalues become positive for high enough doping. Since the homogeneous branch has to be stable outside the NDC region, there have to be multiple bifurcation points, in each of which one eigenvalue changes its sign. These bifurcations can also be seen in Fig. 7.8. A few of these bifurcation points have been detected as Hopf bifurcation points – probably due to numerical problems.[6] The transcritical bifurcations are not less of a problem. It is clear from general considerations that there have to be some on the homogeneous branch. The two additional branches bifurcating in each transcritical bifurcation lead to a new transcritical bifurcation which in turn leads to a new transcritical bifurcation and so on. The distance between these bifurcation points is very small. One thus can determine a large number of branches and bifurcation points of doubtful physical relevance.

Apart from that, one can see in the figure – its reduced graphical quality is due to the large number of bifurcation points and branches – that there is a stable structure of current domains in the “domain” branch as well as in the “wrong domain” branch. The “wrong domains” are no effect which can only be found by continuation techniques. Actually, in simulations these states are often reached – usually undesired – if the initial conditions do not already have a small charge accumulation.

7.4 Superlattices with Different Numbers of Quantum Wells

The behaviour of a superlattice cannot be understood by simply considering a single quantum well or a single barrier. This is especially true for oscillations which are a collective effect of a large number of quantum wells. The location of all Hopf bifurcation points has thus been depicted in Fig. 7.9 for superlattice with a different number of quantum wells. The bifurcation points connected with the formation of current branches for heavy doping have been neglected as their relevance is questionable.

If one compares the location of the bifurcation points with the corresponding figure for Dirichlet (“rigid”) boundary conditions on page 43, one sees that the necessary number of quantum wells for oscillations to appear has decreased (to $N = 17$). Note that – as one of the two Hopf bifurcation points is subcritical – the oscillatory regime is larger than the area enclosed by the Hopf bifurcation points. However, for the question, whether there are oscillations at all, this is of no relevance.

Fixing the doping densities at the boundaries at certain values is a strong constraint to the system. Just copying the electron densities into the virtual quantum wells is much less of a constraint. The difference in the necessary number of quantum wells for oscillations to appear can thus be interpreted as (twice) the number of quantum wells near each boundary which are influenced so much by the boundary conditions that they cannot be part of a oscillatory mode.

---

[6] It has not been possible to find any of the limit cycles which should bifurcate from the homogeneous branch. On the other hand, this can also be explained by the other unstable eigenmodes.

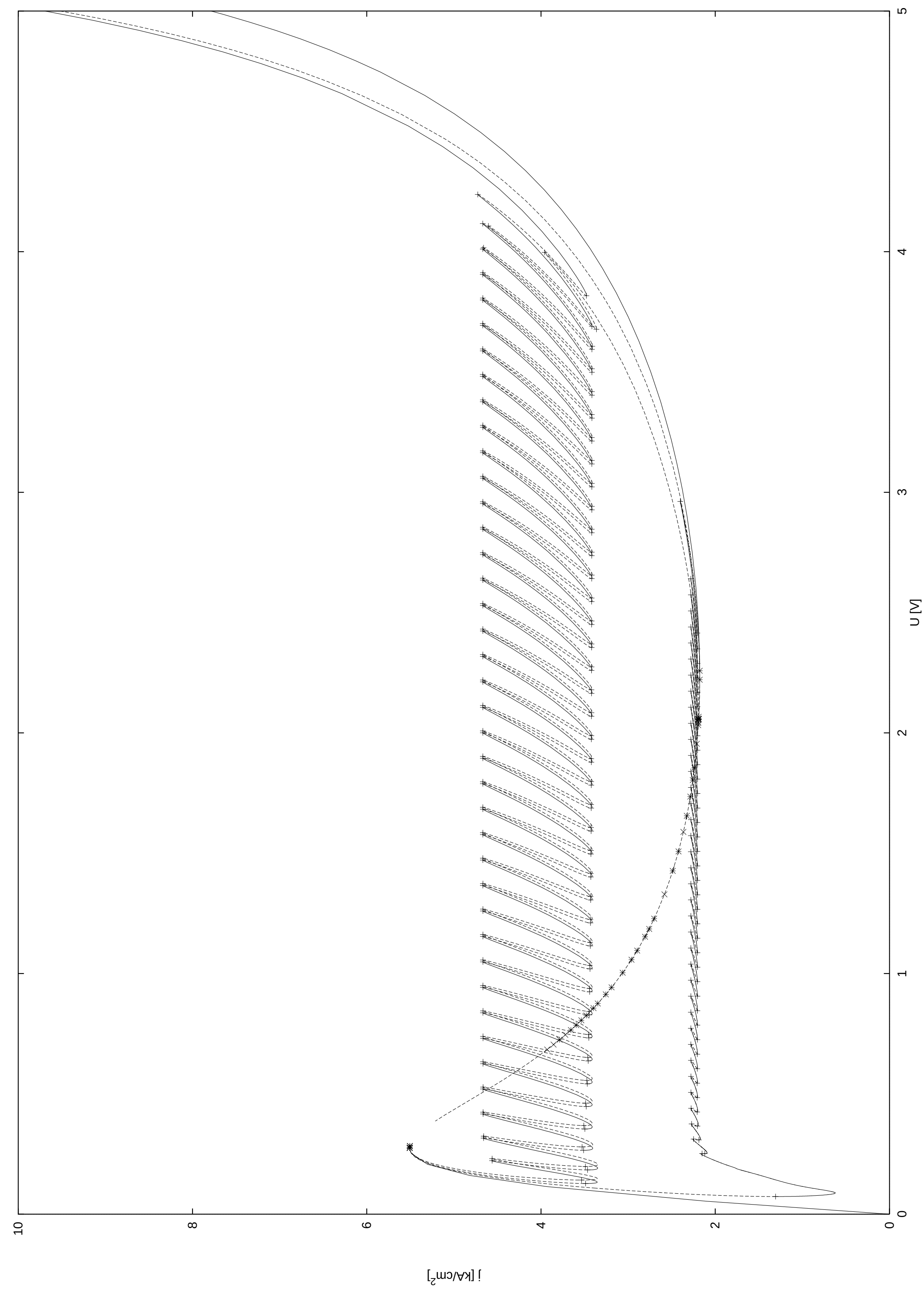

Figure 7.8: Current-voltage characteristic for heavy doping. Only a few of all branches have been calculated as can be seen by branches ending without bifurcation points or from missing branches at many transcritical bifurcation points.

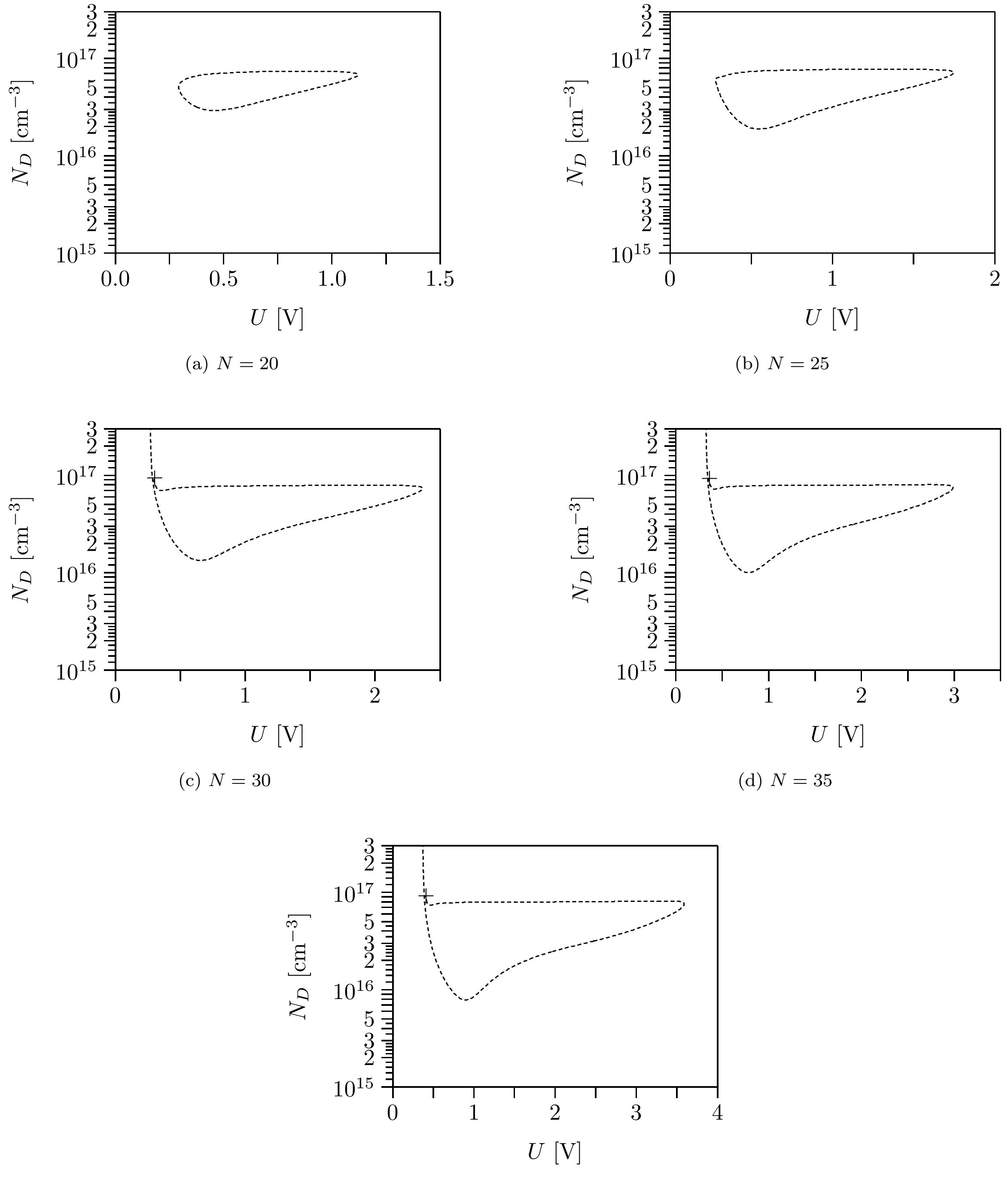

(a) $N = 20$

(b) $N = 25$

(c) $N = 30$

(d) $N = 35$

(e) $N = 40$

Figure 7.9: Location of bifurcation points ("phase diagram") for superlattices that consist of a different number of quantum wells. As it is not sensible to consider the large number of bifurcation branches connected with the formation of current branches, only the Hopf bifurcation points are depicted. If the superlattices are long enough, the curves of Hopf bifurcation points end in Takens-Bogdanov points, of which one lies above the depicted region.

7.5 Perturbed Superlattices

From the results presented so far it is clear that a small perturbation of the superlattice will change its behaviour quite substantially. From a bifurcation theoretic point of view, this is the case regardless of the value of the doping density: Even for a very small perturbation the homogeneous branch is no longer stationary (and thus does not even exist). As a consequence, the transcritical bifurcation points disappear.[7] In a simulation, the effects are much smaller as the "wrong domain" states still exist and are still stable.

The effects on oscillations are much stronger. The shape of the oscillation is determined by the homoclinic orbit starting at the homogeneous state. The homoclinic orbit is structurally unstable and is thus destroyed by even very small perturbations. As has already been demonstrated in Fig. 7.6, even very small deviations have very large effects. Thus with the destruction of the homoclinic orbit, the limit cycle is "freed", the shape of the oscillations become sinusoidal and the frequency increases.

7.6 Conclusions

When choosing boundary conditions for use in the main part of this thesis, the most important consideration was to choose some "generic" boundary conditions. Among the many boundary conditions investigated, almost all have shown to lead to similar results. The boundary conditions examined in this chapter are something "special".

The current-voltage characteristic, for heavy as well as for light doping, and the mechanism for oscillation are much more difficult than for other boundary conditions – without clear experimental results to back these more complex scenarios.[8] In addition, the system is highly degenerate. The main changes when perturbations are introduced come from the destruction of the degeneracy – especially the change of the shape of the oscillations.

When Neumann boundary conditions are used, it is possible to detect even the smallest perturbations of the superlattice by looking at the shape of the oscillations. For experimental problems this is not of much use. Due to effects not considered here, the experimental superlattice will never be degenerate so the effects from the destruction of the degeneracy will not be observed. Furthermore, it is possible to distinguish in a simulation very good between $\alpha = 0\,\%$ and $\alpha = 0.001\,\%$. For the experimentally important question about the differences for $\alpha = 3\,\%$ and $\alpha = 6\,\%$, they offer no advantages to the boundary conditions considered discussed in the preceding chapters. However, even if the boundary conditions introduced in this chapter cannot offer new insight into experiments, they still are interesting from a dynamical point of view.

---

[7] Even if the homogeneous branch would still exist, one has to remember that all transcritical bifurcations are structurally unstable.

[8] "simplex sigillum veri"

Chapter 8

Conclusions

In this thesis, the dynamics of electrons in semiconductor superlattices has been analysed using methods from nonlinear dynamics. Earlier publications of other authors had demonstrated that the model used, which is based on simple microscopic rate equations, leads to the formation of field domains and undamped oscillations depending on the doping density. The multistability of such field domains results in a current-voltage characteristic consisting of individual branches.

These self-organised patterns and their creation were examined using method from bifurcation theory. By computing the unstable branches of the current-voltage characteristic, it was shown that the simulated or measured characteristic consists of a single connected curve of stationary points (chapter 4). The stable and the unstable parts of the current-voltage characteristics are separated by saddle-node bifurcation points, which are created in cusp points at a certain doping density. Furthermore, it was demonstrated that oscillations are caused by stable limit cycles bifurcating from the stationary solution in supercritical Hopf bifurcation points.

Of special importance is the investigation of superlattices with disorder, in which the doping densities in the individual quantum wells may differ slightly. It was derived both analytically and numerically in chapter 5 that the heights of the individual branches of the current-voltage characteristics give direct information about the doping densities in the individual wells. Thus, the relatively easy measurement of the global current-voltage characteristic allow to quantitatively determine the quality of a sample as was demonstrated in appendix A.

If the level of disorder is higher than a certain threshold, new phenomena are observed. As was described in chapter 6, this affects the branches in the current-voltage characteristic of heavily doped superlattices as well as the oscillations observed for medium doping. The observed phenomena are too complex to summarise them in just a few sentences.

Another important question, which is only answered partly in this thesis, is the selection of appropriate boundary conditions as it is generally known that they have a large effect on pattern formation. Especially Neumann boundary conditions lead to some interesting results that were examined with methods of nonlinear dynamics in chapter 7 and are able to explain the results of simulations presented in other publications.

The self-organised patterns found, namely multistable field domains and limit cycle oscillations, are rather simple for a system of such complexity and such high dimension. If additional patterns like the creation of tori or chaos are desired, there have to be changes made to the model. Forthcoming investigations in the area of nonlinear dynamics will have to address this problem.

This thesis, however, also gives results relevant to the experimental effects of doping fluctuations even though the present state of growth technology does not allow to verify them by growing specially designed samples. Nevertheless, these results can already help to determine the quality of a sample more precisely than it had been possible before.

The model used in this thesis certainly suffers from numerous deficiencies. When an improved model will have been developed, the computations presented in this paper dealing the with effects of disorder should be repeated. Then, experimental verifications might not be so important as they are for the present model.

Finally, I believe that the connection between the physics of semiconductors in the form of a non-trivial device and nonlinear dynamics has been a very successful one. Without the methods from nonlinear dynamics, many of the results of this thesis would not have been possible or – at least – much more difficult to obtain. Even though many questions are still open and are waiting to be answered, the results in this thesis still have lead to a better understanding of the investigated system.

Appendix A

Quantitative Analysis of the Amount of Disorder from Experimental Data

In chapter 5, we have analytically analysed how the current-voltage characteristic of a superlattice changes if the level of disorder is increased. The results derived there were later verified by numerically simulating characteristics in section 5.2 (Fig. 5.5 on page 56). It therefore makes sense to apply this also to experimentally grown superlattices.

The current-voltage characteristic of such a superlattice is depicted in Fig. A.1. It was demonstrated in [Sch95b] that the jump near 1 V is caused by a thicker barrier. This wider barrier is of no further interest as we are only interested in doping fluctuations. The results derived in section 5.2 implied that all branches end at approximately the same current (except for

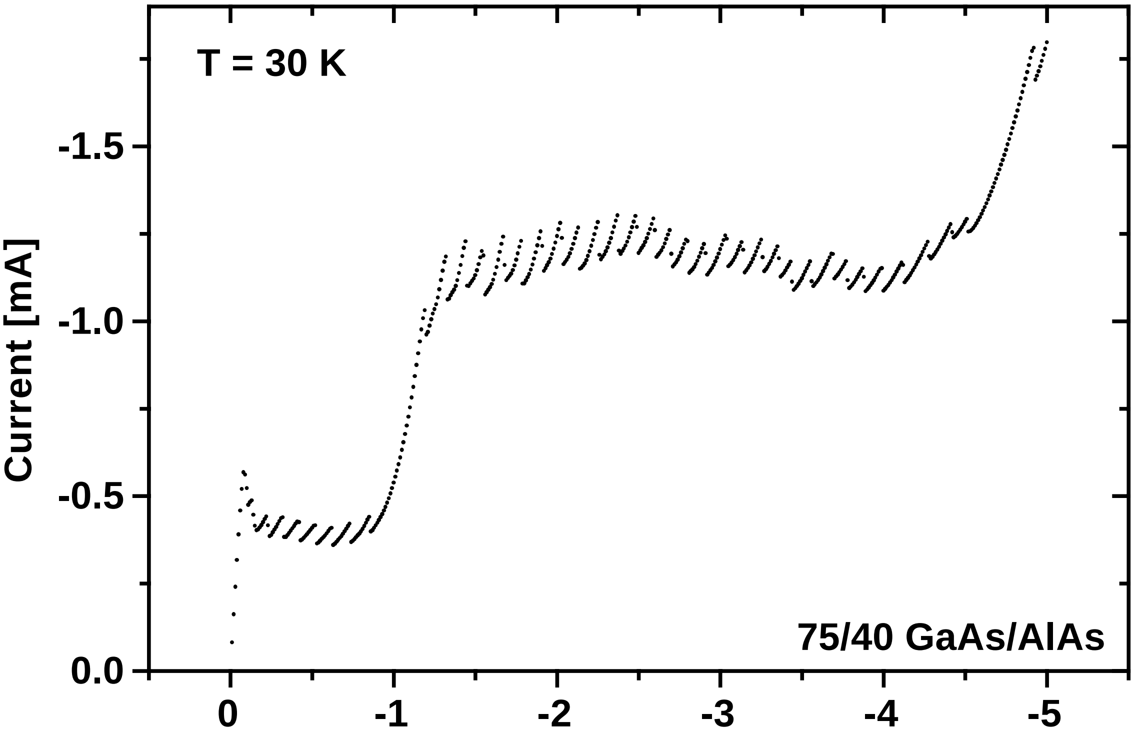

Figure A.1: Experimental current-voltage characteristic of a *GaAs*-*AlAs* semiconductor superlattice (from [Kas95a]). Only the "plateau" at approximately -1 V to -4 V will be considered in this chapter.

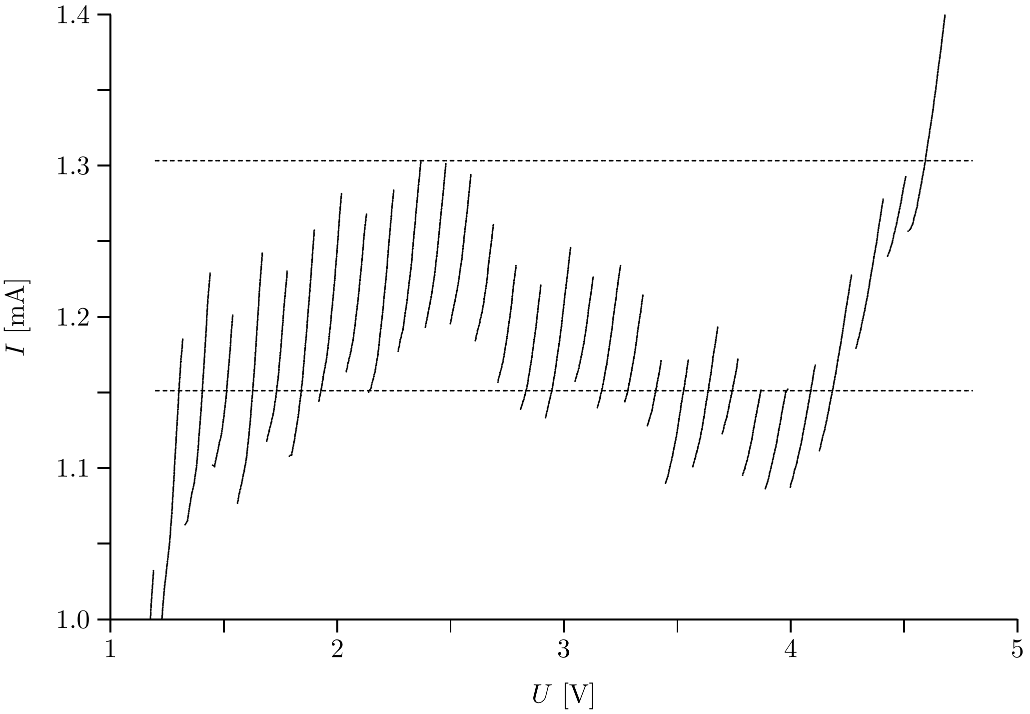

Figure A.2: Enlarged part of the experimentally determined current-voltage characteristic in Fig. A.1. The two dashed lines mark the minimum and the maximum value of the current at the upper end points of the stable branches.

1,22886	1,20109	1,24215	1,23007	1,25725
1,28140	1,26812	1,28382	1,30314	1,30133
1,29408	1,26087	1,22947	1,22101	1,24577
1,22645	1,23370	1,21437	1,17089	1,17150
1,19324	1,17210	1,15157	1,15217	1,16787
1,22766	1,27778			

Table A.1: Currents (in mA) at the upper end points of all branches in the considered interval.

boundary effects). Thus, we will concentrate on the "plateau" from approximately 1 V to 5 V.

Fig. A.2 depicts the relevant region.[1] We have to determine the minimum and the maximum value of the electric current at the *upper* end point of the branches. These values can be "read off" as $I_{max} = 1.303$ mA and $I_{min} = 1.151$ mA. The average current is thus $I = 1.227$ mA, the extrema deviate by $\Delta I = 0.076$ mA or 6.2 %. If we take into account that there are only 27 quantum wells in the region considered we have to multiply with 28/27 to get $\alpha = 6.4\,\%$.

This calculation actually used only two branches (the highest and the lowest). It can be improved by using the information from all branches. The currents at the upper end points of all branches are compiled in table A.1. The average of these values is $I = 1.23$ mA with an average deviation of 0.036 mA yielding a "full stroke" of $\Delta I = 0.073$ or 5.91 %. Multiplying once again with 28/27 gives as final result $\alpha = 6.1\,\%$.

Comparing both results, it might be sensible to give an estimation like $\alpha = 6 \pm 1\,\%$. This does not mean, however, that there is a physical argument to support this error margin. In [Sch95b] it has been shown from simulations that, if a single barrier is just a single atom layer thicker than the others, this will lead to characteristic changes in the current-voltage characteristic. This was later verified by intentionally growing a superlattice with one thicker barrier. To verify the results from this thesis in a simi-

---

[1] As can be seen from the enlarged characteristic, the deviations of the doping densities in the individual quantum wells are not independent of each other. This means that there are regions in the superlattice with heavier doping and regions with lighter doping. This makes sense as the composition of the source material might change slightly during the growth process. If the characteristic time scales for these processes are longer that the time needed to grow one superlattice period, one has to expect this kind of behaviour.

lar way, one would have to grow a superlattice with intentional (and well defined) variations of the doping density. For the relevant region $\alpha < 10\,\%$, this is, however, not possible (at least in the foreseeable future).

Thus, the value of α "calculated" in this chapter should be considered as "educated guess". On the other hand, remember that all prepositions from section 5.1 are sensible and are most probably fulfilled in "experimental" superlattices: weakly coupled wells, only doping fluctuations, no (important) fluctuations in the growth plane and no (important) dependence on the distribution of electrons among the subbands. If one believes these prepositions to be fulfilled, there is no reason not to believe the values of α calculated (or "guessed") here.

Appendix B

Laser Illumination

In order for pattern formation to be possible, there must be the possibility for electrons to accumulate in certain quantum wells. These electrons are supplied by doping the superlattice. However, there are other methods of supplying the necessary electrons, the most common being laser illumination. Laser illumination may be used with undoped superlattices or with doped superlattices if the doping density is not high enough for a specific phenomena to be observable [Kas95b].

The rate equations from sections 3.2 have to be supplemented by terms describing the dynamics of the holes, $p^{(i)}$ being their density in the i-th quantum well:

$$\begin{aligned}\dot{n}_1^{(i)} &= \cdots + \tau_1^a - \tau_1^e p^{(i)} n_1^{(i)} \\ \dot{n}_2^{(i)} &= \cdots + \tau_2^a - \tau_2^e p^{(i)} n_2^{(i)} \\ \dot{p}^{(i)} &= \tau_1^a + \tau_2^a - \tau_1^e p^{(i)} n_1^{(i)} - \tau_2^e p^{(i)} n_2^{(i)}\end{aligned}$$

These equations are easy to understand: Electrons are excited with a constant rate τ_k^a and thus lifted from the valence band to the k-th subband resulting in an electron in that subband and a hole in the valence band. In order for a recombination process to take place, there has to be an electron in one of the subbands as well as a hole in the valence band. The corresponding term is thus proportional to the product of the two densities. In addition to the rate equations, the Poisson equation has to be modified to include the positive charge of the holes.

Let us consider an undoped superlattice with just a single energy level. Furthermore, let us assume that there is a homogeneous field distribution, so there has to be $p^{(i)} = n_1^{(i)}$. The stationary value for the hole concentration can then be calculated as $l_0 = \sqrt{\tau_1^a/\tau_1^e}$. The characteristic time scale until the stationary state is reached is $l_0/\tau_1^a = 1/\sqrt{\tau_1^a \tau_1^e}$. Please note that this time scale is not relevant to the transport of electrons between different wells and is thus not relevant to oscillation frequencies.

As there is no (usable) experimental data for τ_k^a and τ_k^e (τ_k^a depends on the strength of the laser illumination) we will choose these values so as to get the desired behaviour. We know from the preceding chapters how high the doping density N_D has to be for a certain phenomenon (branches or oscillations) to be observable. If we set l_0 equal to this value of N_D, this yields the ratio τ_1^a/τ_1^e for which similar effects may be expected under laser illumination. If we choose characteristic time scales in the range between 1 ns and 10 ns, we get initial values for τ_1^a and τ_1^e. By varying these values we can optimise the results, for example, maximise the amplitude of oscillations.

For the simulations presented in this chapter, it was assumed that laser excitation is only possible into the first energy level. Simulations without this constraint yield similar results. Fig. B.1(a) depicts the current during an oscillation, Fig. B.1(b) the corresponding field profile. The parameters were chosen to be $\tau_1^e = 2 \cdot 10^{-6}\ \mathrm{cm}^6\,\mathrm{s}^{-1}$ and $\tau_1^a = 2.4 \cdot 10^{25}\ \mathrm{cm}^{-3}\,\mathrm{s}^{-1}$.[1] This value maximises the oscillation amplitude for the voltage $U = 0.5$ V. The hole density is approximately $3.5 \cdot 10^{16}\ \mathrm{cm}^{-3}$, which is similar to the value of N_D at which similar oscillations can be observed without illumination. In addition, the field profiles are similar which implies a similar mechanism for the oscillations.

In a similar manner, it is possible to simulate the branch structure known from heavily doped superlattices. Fig. B.2(a) depicts such

---

[1] The following boundary conditions were used: The electron density in each “virtual” quantum well is equal to the electron density in the last “real” quantum well plus $10^{16}\ \mathrm{cm}^{-3}$. This way, the electron densities in the virtual wells will be “sensible” even if we do not know in advance how large the electron densities will be. The offset $10^{16}\ \mathrm{cm}^{-3}$ destroys any unwanted effects from Neumann boundary conditions.

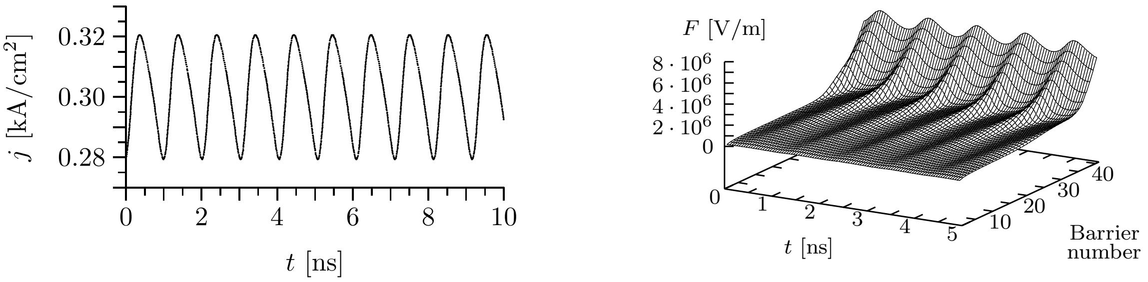

(a) Current oscillation

(b) Field distribution

Figure B.1: Oscillation in an undoped superlattice under laser illumination. There is almost no difference to the oscillations found in doped superlattices without illumination.

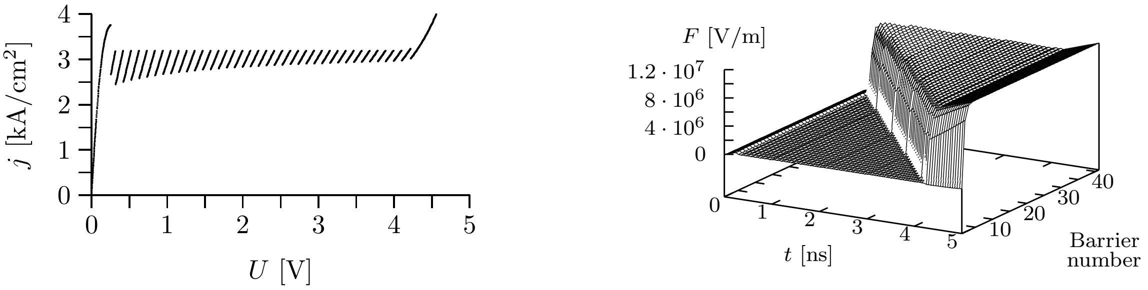

(a) Current-voltage characteristic

(b) Field distribution

Figure B.2: Current-voltage characteristic under laser illumination. For parameters see text.

a current-voltage characteristic, Fig. B.2(b) the corresponding field profile ($\tau_1^e = 5\cdot10^{-8}$ $\mathrm{cm}^6\,\mathrm{s}^{-1}$ and $\tau_1^a = 9\cdot10^{27}$ $\mathrm{cm}^{-3}\,\mathrm{s}^{-1}$). Both figures are similar to those for doped superlattice.

Doping a superlattice and illuminating it can be combined. As both result in similar effects, one may not expect new phenomena. This is also the result of numerous simulations. If there were any new effects, these should be observable for parameters like the ones used in Fig. B.1 because the time scales for laser excitement and transport between different quantum wells are then of equal magnitude. The final result is – this knowledge has been used by experimentalists for a long time – that doping and laser illumination can be interchanged. Additional constraints like wanted or unwanted scattering at donor atoms determine which method is used.

Appendix C

Very Heavily Doped Superlattices

So far in this thesis, superlattices with doping densities between $N_D = 10^{15}$ cm^{-3} and $N_D = 10^{18}$ cm^{-3} have been investigated. There is no sense in decreasing the doping density below $N_D = 10^{15}$ cm^{-3} as the current-voltage characteristic for this doping density does not differ any more from the homogeneous characteristic as given by the $v(F)$-characteristic. This section deals with the case of doping densities above the range considered so far; here $N_D = 10^{19}$ cm^{-3} has been chosen.

Fig. C.1 depicts the current-voltage characteristic as determined by a numerical simulation. The simulation has been no voltage sweep-up or sweep-down; rather, the voltage was for every point on the characteristic instantaneously increased from zero to the corresponding voltage. One gets a similar characteristic if a voltage sweep-up is simulated and the electron densities are slightly perturbed after each step to account for imperfections, thermal noise or noise of the voltage supply.

The simulated characteristic displays different behaviour for medium voltage than for higher or lower voltage. This can be explained if the field distribution as depicted in Fig. C.2 is taken into account: For medium voltage, there is a high-field domain but it is not located at one side of the superlattice. The sharp increase of the electric field near the end of the superlattice is due to boundary effects.[1] If the applied voltage is increased, this high-field domain grows until it fills the entire superlattice.

These facts can be understood if one remembers that there is a charge accumulation at the beginning of a high-field domain, and there is a charge depletion at the end. The (absolute) size of the accumulation or depletion does not depend on the doping density and is thus relatively smaller for higher doping density. At a doping density of $N_D = 10^{19}$ cm^{-3}, the additional charge in the accumulation layer is just about 2 % of the doping density.

A charge depletion leads to a drop in the elec-

---

[1] The boundary conditions in this chapter were chosen to be $c_1 = 0$ and $c_2 = 1.1$. This way, the charge accumulation in the boundary layers is approximately equal to that in the previous chapters.

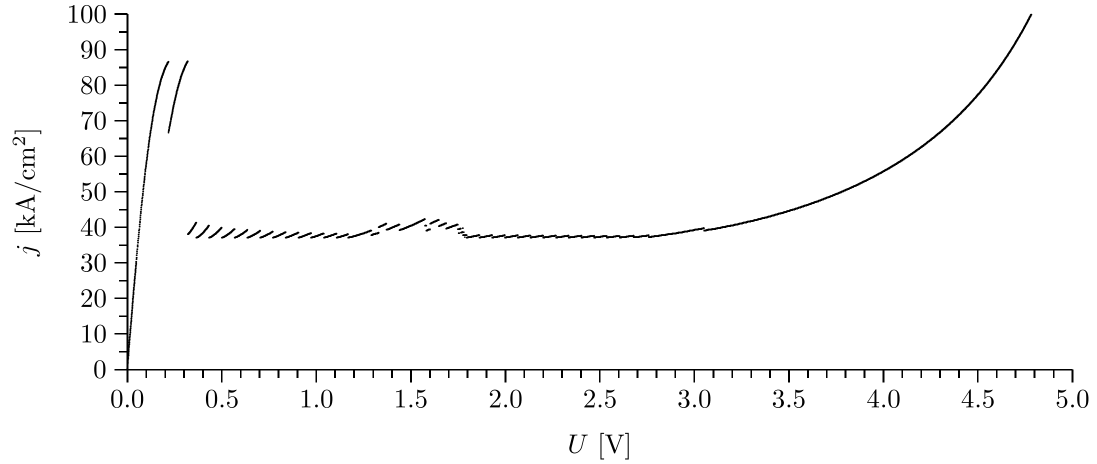

Figure C.1: Simulated current-voltage characteristic.

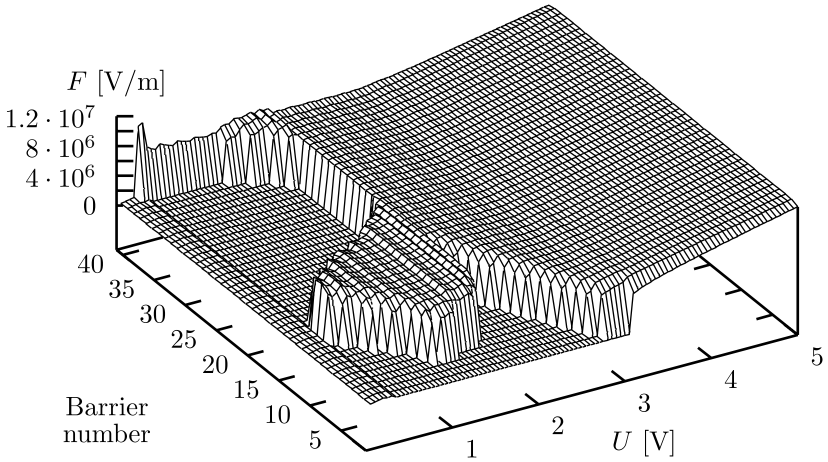

Figure C.2: Field distribution for the current-voltage characteristic in Fig. C.1.

tric current as the current is proportional to the number of available electrons. For higher doping density, this "disadvantage" becomes smaller. Thus, even boundary conditions modelling a carrier reservoir may lead to charge depletion layers in the superlattice.

The question, whether there may be charge depletion layers, is also of experimental relevance. If we assume that a high-field domain will always form at one side of the superlattice, this question is equivalent to whether the high-field domain will form at the anode or the cathode side. Heavy doping could thus explain the results from [Hel90].

The additional stable states corresponding to states with charge depletion belong to a curve which has no connection with the "standard" current-voltage characteristic. Apart from that, they are similar to the "standard" characteristic.

Appendix D

Scaling the Parameters and Variables

The dynamics of the system were given by an equation of the form $\dot{\mathbf{N}} = f(\mathbf{N}, U, N_D)$ where the electron densities in the individual quantum wells have been labelled with the capital letter $\mathbf{N}$ in this section. These "physical" variables are difficult to handle as if a bifurcation analysis is intended.

In order to use continuation techniques or any other methods depending on arc length parametrisation, all variables and parameters have to be of equal magnitude.[1] The voltage U is just a few volts whereas the doping density N_D and thus the electron densities $\mathbf{N}$ may have values up to $10^{18}\,\mathrm{cm}^{-3}$.

Furthermore, it does not make sense to use the doping density directly: The interval relevant to oscillations ranges from about $10^{16}\,\mathrm{cm}^{-3}$ to $10^{17}\,\mathrm{cm}^{-3}$, i. e. just 10 % of the entire doping interval.[2] The only solution is to use a logarithmically scaled control parameter.

Finally, we also have to be careful about calculating the partial derivates of f, i. e., of $A := \frac{\partial \dot{\mathbf{N}}}{\partial \mathbf{N}}$. Many algorithms use products of the form $\prod_i A_{i\sigma(i)}$. If the elements of A are (on average) too large, the algorithm may overflow.[3] As new variables for the electron concentrations should depend linearly on them, this problem has to be solved by choosing a suitable unit to replace the "physical" time T.

Thus, we will use the following new variables, which are denoted by small letters:

$$\begin{aligned} n_D &= \log_{10}\left(\frac{N_D}{N_0}\right) \\ \mathbf{N} &= N_D \cdot \mathbf{n} \\ t &= \lambda \cdot T \end{aligned} \tag{D.1}$$

Rescaling the voltage U is not necessary as it already lies between 0 and 5 (in volts). Choosing $N_0 = 10^{15}$, n_D will be in the range from 0 and 3. The new values of the electron concentration will be between 0 and approximately 1 with a strong difference between the two subbands; this could be solved by an additional scaling operation.[4] Time is scaled by setting $\lambda = 10^{-10}$.

(D.1) yields directly

$$\dot{\mathbf{n}} = \frac{1}{N_D \cdot \lambda} \dot{\mathbf{N}},$$

where $\dot{\mathbf{n}}$ means $\frac{d\mathbf{n}}{dt}$ and $\dot{\mathbf{N}}$ means. $\frac{d\mathbf{N}}{dT}$. Next, we have to calculate the partial derivates of f:[5]

---

[1] This applies to quantities that are "plain" numbers. If we think of "physical" variables with "physical" units, we anyway have to divide them by some suitable quantity to render them dimensionless.

[2] We would then have to use a very high accuracy to find all bifurcation points – even for the 90 % where we do not need such a high accuracy as the doping density is higher.

[3] Standard workstations can represented numbers up to 10^{310}. Assuming 80 variables, this means that, on average, the elements of the matrix may be no higher than 10^4. If they are, on the other hand, smaller than 10^{-4}, the algorithm will underflow to yield the result 0.

[4] So far, λ was not considered as it has no effect on the arc length but only on the elements of the Jacobi-matrix. Its value can be determined from noting that typical elements of this matrix are of magnitude $10^{10}\,\mathrm{s}^{-1}$.

[5] Derivatives with respect to quantities that are not scaled by itself transform like the derivatives with respect to the applied voltage, U

$\frac{\partial \dot{\mathbf{n}}}{\partial \mathbf{n}} = \frac{1}{\lambda} \cdot \frac{\partial \dot{\mathbf{N}}}{\partial \mathbf{N}}$	$\frac{\partial j}{\partial \mathbf{n}} = N_D \cdot \frac{\partial \mathbf{j}}{\partial \mathbf{N}}$
$\frac{\partial \dot{\mathbf{n}}}{\partial U} = \frac{1}{N_D \cdot \lambda} \cdot \frac{\partial \dot{\mathbf{N}}}{\partial U}$	
$\frac{\partial \dot{\mathbf{n}}}{\partial n_D} = \frac{\ln 10}{\lambda} \cdot \left[-\frac{1}{N_D} \cdot \dot{\mathbf{N}} + \frac{\partial \dot{\mathbf{N}}}{\partial N_D} + \mathbf{n} \cdot \frac{\partial \dot{\mathbf{N}}}{\partial \mathbf{N}} \right]$	$\frac{\partial j}{\partial n_D} = \ln 10 \cdot N_D \cdot \left[\frac{\partial j}{\partial N_D} + \mathbf{n} \cdot \frac{\partial j}{\partial \mathbf{N}} \right]$

Table D.1: Summary of the transformation rules between "physical" variables (capital letters) and the variables used in the actual bifurcation analysis (small letters); refer to the text for more information.

$$\frac{\partial \dot{n}_i}{\partial n_j} = \frac{\partial \dot{n}_i}{\partial \dot{N}_i} \cdot \frac{\partial \dot{N}_i}{\partial N_j} \cdot \frac{\partial N_j}{\partial n_j} = \frac{1}{\lambda} \cdot \frac{\partial \dot{N}_i}{\partial N_j}$$
$$\frac{\partial \dot{n}_i}{\partial U} = \frac{\partial \dot{n}_i}{\partial \dot{N}_i} \cdot \frac{\partial \dot{N}_i}{\partial U} = \frac{1}{N_D \cdot \lambda} \cdot \frac{\partial \dot{N}_i}{\partial U}$$

When computing the partial derivates with respect to the "new" doping density, we have to keep in mind that there are two effects when n_D is changed: On the one hand, the "physical" doping density N_D changes directly; on the other hand, the electron densities $\mathbf{N}$ change for fixed $\mathbf{n}$ due to (D.1). Actually, this makes sense from a physical point of view: When the doping density is changed by some factor, the electron densities will – in first order – change by the same factor. This means that electrically neutral regions of the superlattice will stay neutral, and that the location of a domain boundary will not change. Thus, we get:

$$\begin{aligned}
\frac{\partial \dot{n}_i}{\partial n_D} &= \frac{\partial}{\partial n_D} \left[\frac{1}{N_D \cdot \lambda} \dot{N}_i \right] \\
&= \frac{1}{\lambda} \frac{\partial}{\partial n_D} \left[\frac{1}{N_D} \right] \cdot \dot{N}_i + \frac{1}{N_D \cdot \lambda} \cdot \frac{\partial \dot{N}_i}{\partial n_D} \\
&= -\frac{\ln 10}{N_D \cdot \lambda} \cdot \dot{N}_i + \frac{1}{N_D \cdot \lambda} \cdot \left[\frac{\partial \dot{N}_i}{\partial N_D} \cdot \frac{\partial N_D}{\partial n_D} + \sum_j \frac{\partial \dot{N}_i}{\partial N_j} \cdot \frac{\partial N_j}{\partial n_D} \right] \\
&= \frac{\ln 10}{\lambda} \cdot \left[-\frac{1}{N_D} \cdot \dot{N}_i + \frac{\partial \dot{N}_i}{\partial N_D} + \sum_j n_j \cdot \frac{\partial \dot{N}_i}{\partial N_j} \right]
\end{aligned}$$

Sometimes, it might be necessary to calculate the derivates of other quantities. These derivates are, here formulated for the current density $j = j(\mathbf{N}, N_D, U)$:

$$\begin{aligned}
\frac{\partial j}{\partial n_i} &= \frac{\partial j}{\partial N_i} \cdot \frac{\partial N_i}{\partial n_i} = N_D \cdot \frac{\partial j}{\partial N_i} \\
\frac{\partial j}{\partial n_D} &= \frac{\partial j}{\partial N_D} \cdot \frac{\partial N_D}{\partial n_D} + \sum_i \frac{\partial j}{\partial N_i} \cdot \frac{\partial N_i}{\partial n_D} \\
&= \ln 10 \cdot N_D \cdot \left[\frac{\partial j}{\partial N_D} + \sum_i n_i \cdot \frac{\partial j}{\partial N_i} \right]
\end{aligned}$$

Appendix E

Number of Necessary Subbands

The model used in this thesis considers exactly two subbands. This leads to the question whether already *one* subband yields the desired results, and whether taking additional subbands into account will improve on the results presented in this thesis. The latter question has already been answered in [Sch95b, appendix D] and will not be dealt with here. The question whether already one subband is sufficient is of importance as other models like, e. g., [Bon94] use only a single subband.

Of course, there is more than just one bound state in a "real" quantum well; the exact number depends mainly on the depth of the well. Every theory considering just a single subband does not actually use only the electron concentration in the first subband but rather uses the total electron concentration in the quantum well, ρ. Thus, the transport equations for this "single" subband contain not only effects due to the first "real" subband but also allow for the effects of higher subbands due to their small but finite electron occupation. The main problem in "designing" such single-subband equations is that one has to know in advance, at least approximately, how the total electron concentration is distributed among the individual subbands.

Let us assume that we have a model with just a single "subband", and that we know the total electron density, ρ. We can then use the transport equations presented in chapter 3 if we are able to compute how the total electron density is distributed among n_1 and n_2. Of course, this is not possible for all states so will restrict this discussion to *stationary* states, that is, we will only discuss current-voltage characteristics.

Thus, we go to the equations for the transition rates from section 3.2 and restrict ourselves to $\dot{n}_1$ at the moment. We will use the following labelling scheme in the section: The quantities in the well which we are discussing right now have no index, the quantities in the well right to it are labelled with the index $+$, and the ones in the well left to it have a $-$. Furthermore, we assume that the field distribution is "sensible", that is, all electric fields are equal to or greater than zero.[1] The equation for the transition rates then reads:

$$\dot{n}_1 = \frac{n_2}{\tau} + n_1^- R_1(F^-) - n_1 \big[R_1(F^+) + X(-F^-) + X(F^+)\big] + n_2^- Y(-F^-) + n_2^+ Y(F^+) \qquad \text{(E.1)}$$

We know the total electron density $\rho = n_1 + n_2$ for each quantum well; thus, we also know the field profile (for known applied voltage). This means that all the coefficients in (E.1) like, e. g., R_1 can be computed even if only ρ is known. In the next step, we will use $n_1 = \rho - n_2$ to eliminate n_1:

$$\begin{aligned} \dot{n}_1 &= \frac{n_2}{\tau} + (\rho^- - n_2^-) R_1(F^-) - (\rho - n_2)\left[R_1(F^+) + X(-F^-) + X(F^+)\right] \\ &\quad + n_2^- Y(-F^-) + n_2^+ Y(F^+) \\ &= n_2 \left[\frac{1}{\tau} + R_1(F^+) + X(-F^-) + X(F^+)\right] \end{aligned}$$

---

[1] The most fundamental results do not depend on this assumption. As will be the result later on, the distribution of ρ among n_1 and n_2 is uniquely defined except for same special cases – without the assumption made in the text, it is just more difficult to tell what these special cases actually are.

$$\begin{aligned}&+n_2^-\left[-R_1(F^-)+Y(-F^-)\right]\\ &+n_2^+Y(F^+)\\ &+\rho^-R_1(F^-)-\rho\left[R_1(F^+)+X(-F^-)+X(F^+)\right]\end{aligned} \tag{E.2}$$

Remember that we had the problem of determining n_2 (and thus also n_1) for known, fixed ρ and thus known transport coefficients. Solving the equation $\dot{n}_1 = 0$ is then simply a matter of solving a system of linear equations for the three unknowns n_2^-, n_2 and n_2^+:

$$0 = a \cdot n_2^- + b \cdot n_2 + c \cdot n_2^+ - d \tag{E.3}$$

Comparing with (E.2) we see that the constant a may be zero whereas the constants b and c have to be positive. We will come back to this later on.

Equation (E.3) is not valid for the quantum wells located at the boundary of the superlattice. For these, either n_2^+ or n_2^- are "virtual" electron densities in "virtual" quantum wells. The electron densities in the "virtual" wells are fixed at a constant value,[2], so the respective terms is constant and can be included into d. Thus, the complete system of equations reads

$$\begin{aligned}d_1 &= b_1 \cdot n_2^{(1)} + c_1 \cdot n_2^{(2)}\\ d_i &= a_i \cdot n_2^{(i-1)} + b_i \cdot n_2^{(i)} + c_i \cdot n_2^{(i+1)} \qquad \text{for } 2 \le i \le N-1\\ d_N &= a_N \cdot n_2^{(N-1)} + b_N \cdot n_2^{(N)}\end{aligned}$$

or written as a matrix

$$\begin{pmatrix} b_1 & c_1 & & & & & \\ (a_2) & b_2 & c_2 & & & & \\ & (a_3) & b_3 & c_3 & & & \\ & & \ddots & \ddots & \ddots & & \\ & & & (a_{N-2}) & b_{N-2} & c_{N-2} & \\ & & & & (a_{N-1}) & b_{N-1} & c_{N-1} \\ & & & & & (a_N) & b_N \end{pmatrix} \cdot \begin{pmatrix} n_2^{(1)} \\ n_2^{(2)} \\ n_2^{(3)} \\ \vdots \\ n_2^{(N-2)} \\ n_2^{(N-1)} \\ n_2^{(N)} \end{pmatrix} = \begin{pmatrix} d_1 \\ d_2 \\ d_3 \\ \vdots \\ d_{N-2} \\ d_{N-1} \\ d_N \end{pmatrix} \tag{E.4}$$

The brackets around the a_i indicate that these elements may be zero as mentioned above. The other elements of this matrix are always nonzero.

The system of linear equations, (E.4), has a uniquely defined solution iff the determinant of the coefficient matrix is nonzero. Even if this determinant were to be zero, we have to remember that we have so far only used half of all transport equations (equation (E.1) only used the information about $\dot{n}_1$). This way, we get an additional matrix with "new" transport coefficients (R_2 and X). Only if both matrices are singular, there is no uniquely defined solution – this is thus a very, very special case.

So, let us assume that we have such a special case – how does the set of all solutions look like? The individual solutions differ by a solution of the homogeneous system corresponding to (E.4). Thus, the solutions fill an – at least one-dimensional – space; especially, it is not possible to have some "discrete" solutions. At least one $n_2^{(i)}$ can be changed to any desired value.[3]

So, let us go to the i-th line of system (E.4):

$$d_i = a_i \cdot n_2^{(i-1)} + b_i \cdot n_2^{(i)} + c_i \cdot n_2^{(i+1)} \tag{E.5}$$

Since $n_2^{(i)}$ is allowed to take on any value, b_i is nonzero, and (E.5) has still to be valid, either $n_2^{(i-1)}$ or $n_2^{(i+1)}$ or both have to change when $n_2^{(i)}$ is varied. We can get more information by considering the line above:

$$d_{i-1} = a_{i-1} \cdot n_2^{(i-2)} + b_{i-1} \cdot n_2^{(i-1)} + c_{i-1} \cdot n_2^{(i)} \tag{E.6}$$

Since c_{i-1} is nonzero, too, $n_2^{(i-1)}$ or $n_2^{(i-2)}$ (or both) are also changing during this process. Let

---

[2] If we choose Neumann boundary conditions, the equations can be simplified, too. Since $n_2^+ = n_2$ and $n_2^- = n_2$, we can simply add the coefficients c respectively a to b so that the electron density in the virtual wells "disappears". The only problem is that the combined coefficient could become zero; however, this would make the equations even more simple.

[3] This means that in this case even senseless solutions like states with negative electron density are allowed; all the solutions computed here are stationary states of the "full" modell – even states corresponding to such "special" cases.

$j = i - 1$ for the first case, and $j = i - 2$ otherwise. Then we have:

$$d_{j-1} = a_{j-1} \cdot n_2^{(j-2)} + b_{j-1} \cdot n_2^{(j-1)} + c_{j-1} \cdot n_2^{(j)} \tag{E.7}$$

Similar to the argument given for (E.6), at least one of the two $n_2^{(\cdot)}$ from (E.7) also have to change.

Thus, when a particular $n_2^{(i)}$ is varied, at least every other $n_2^{(\cdot)}$ also has to change for decreasing indices. Usually, they will also change for increasing indices but there are special cases where they will not.

Finally, we will consider the boundary of the superlattice:

$$d_1 = b_1 \cdot n_2^{(1)} + c_1 \cdot n_2^{(2)}$$

When one of the two electron densities $n_2^{(1)}$ or $n_2^{(2)}$ changes – and it does as we have just shown – the other has to change, too. Thus, if there is no unique solution, at least $n_2^{(1)}$ and $n_2^{(2)}$ have to change.[4]

Concluding, it is sufficient – apart from some very special cases – to consider only *one* subband as long as only stationary states are of interest. The "special" cases are nonphysical as the distribution of the electron densities in a large number of the quantum wells is then allowed to be continuously varied. However, it is very unlikely that the conditions for these special cases will be ever fulfilled. Unfortunately, the transport coefficients from appendix G are much too complicated to give definite results.

---

[4] This includes the case that $i = 1$ or $i = 2$ in equation (E.5).

Appendix F

Numerical Aspects and Used Programs

In this thesis, the behaviour of semiconductor superlattices was examined using methods from nonlinear dynamics. Main part was the investigation of local bifurcations. However, these techniques are usually applied to “simple” systems[1], in which the dynamics of a small number of state variables is given by relatively simple rate equations. Both assumptions are not fulfilled for the model investigated in this thesis.

F.1 Precision

Already the dynamical equations are relatively complex, which does not only result in an increase in the cost per evaluation but also gives rise to some numerical problems. These are caused by the fact that the change of the electron density in a particular quantum well is given by the difference between the number of electrons flowing into that well and the number leaving it. First, for resonant tunnelling, the transport coefficients for transport in and against field direction do not differ much. Second, most electrons entering a particular quantum well will just flow through it without changing the electron density in it. As result, $\dot{n}_k^{(i)}$ is much smaller than the individual transition rates. This is especially easy to understand for the stationary case, in which the electron densities do not change any more but a current flows nevertheless.[2]

The transition rates for two exemplary situations are given next. The notation is the one introduced in Fig. 3.4 (page 18). Please note that, e. g., $A^{(i)}$ does not refer only to the transport coefficient but also to the transition rate. The first situation considered is an oscillation ($N_D = 2 \cdot 10^{16}$ cm^{-3}). The transition rates are then:

$$\begin{aligned}
A^{(i)} &= 7.61178 \cdot 10^{26}\ \mathrm{cm}^{-3}\,\mathrm{s}^{-1}\\
R_1^{(i)} &= 1.10215 \cdot 10^{27}\ \mathrm{cm}^{-3}\,\mathrm{s}^{-1}\\
R_1^{(i+1)} &= 1.10158 \cdot 10^{27}\ \mathrm{cm}^{-3}\,\mathrm{s}^{-1}\\
X_l^{(i)} &= 3.80998 \cdot 10^{26}\ \mathrm{cm}^{-3}\,\mathrm{s}^{-1}\\
X_r^{(i+1)} &= 4.01135 \cdot 10^{26}\ \mathrm{cm}^{-3}\,\mathrm{s}^{-1}\\
Y_r^{(i)} &= 9.89034 \cdot 10^{24}\ \mathrm{cm}^{-3}\,\mathrm{s}^{-1}\\
Y_l^{(i+1)} &= 1.11042 \cdot 10^{25}\ \mathrm{cm}^{-3}\,\mathrm{s}^{-1}\\
\dot{n}_1^{(i)} &= 6.04420 \cdot 10^{23}\ \mathrm{cm}^{-3}\,\mathrm{s}^{-1}
\end{aligned}$$

The resulting rate of change $\dot{n}_1^{(i)}$ is smaller by about a factor of 100 than the individual transition rates. Thus, we loose a precision of two digits just by making the final subtraction. If field domain states are examined, this becomes even more of a problem. The transition rates are then ($N_D = 6.7 \cdot 10^{17}$ cm^{-3}):

$$\begin{aligned}
A^{(i)} &= 2.36163 \cdot 10^{28}\ \mathrm{cm}^{-3}\,\mathrm{s}^{-1}\\
R_1^{(i)} &= 2.17750 \cdot 10^{28}\ \mathrm{cm}^{-3}\,\mathrm{s}^{-1}\\
R_1^{(i+1)} &= 2.17750 \cdot 10^{28}\ \mathrm{cm}^{-3}\,\mathrm{s}^{-1}\\
X_l^{(i)} &= 1.20082 \cdot 10^{28}\ \mathrm{cm}^{-3}\,\mathrm{s}^{-1}\\
X_r^{(i+1)} &= 1.22569 \cdot 10^{28}\ \mathrm{cm}^{-3}\,\mathrm{s}^{-1}
\end{aligned}$$

---

[1] For many aspects, this is sufficient as even very simple systems may exhibit very complex behaviour.

[2] A semiconductor with an applied bias is a dynamical system far from equilibrium Thus, one may not expect detailed balance.

$$
\begin{aligned}
Y_r^{(i)} &= 1.20082 \cdot 10^{28}\ \mathrm{cm}^{-3}\,\mathrm{s}^{-1} \\
Y_l^{(i+1)} &= 4.38733 \cdot 10^{26}\ \mathrm{cm}^{-3}\,\mathrm{s}^{-1}
\end{aligned}
$$

$\dot{n}_1^{(i)}$ should be 0 as this state is (supposed to be) stationary. Of course, when doing numerical computations, it is necessary to give a threshold for the $\dot{n}_1^{(i)}$ under which a state is considered to be stationary. This bound was chosen to be $10^{17}\ \mathrm{cm}^{-3}\,\mathrm{s}^{-1}$ (that is, the characteristic time scale would then be one second). This means that the individual transition rates are up to 10^{10} higher than the bound given for the total rate of change of the electron densities. The final subtraction thus results in a loss of ten digits of precision – in addition to the rounding errors made during the already complicated calculation of the transport coefficients.

A floating point number stored in 8 bytes (“`double`”) has a precision of 15 to 16 digits. Thus, the precision of the final result might by less then five digits. For many computations, this is not enough. In this case, they were made on a IBM-compatible computer. Its numerical coprocessor always uses a precision of ten bytes internally. This excess precision just has to be used also when storing the data. Thus, we get another four digits of precision – this means that the precision of the final result is doubled – almost for free.

If even higher precision is needed – during the computations made for this thesis, this was only necessary for a few computations made in order to verify the correct function with “normal” precision – workstations (for example, SUNS running SunOS 5.4 or higher) with 16 byte floating point support have to be used. Unfortunately, this drastically reduces the speed of the computation. A Pentium is slower by about 40 % when compared to a reference workstation (see below) if all computations are done using 8 Byte doubles. If the additional precision of the coprocessor is used, the speed sinks by about 20 %.[3] A Sun-10 using “`long double`”s is slower by about a factor of 1000 than the same workstation when using “`doubles`” (using “`doubles`”, a Sun-10 is about as fast as a Pentium). Thus, it is possible to use the extra precision on a PC even for long computations while this is not possible on workstations like a SUN.

F.2 Number of Variables

For most problems in linear algebra, there is a choice between a large number of different algorithms. One important consideration in the selection of a particular algorithm is the dimension of the vectors and matrices involved. For example, the direct computation of a determinant by calculating all permutations of the row indices may be a suitable algorithm when the number of variables is very small. For 80-dimensional problems, resulting from 40 quantum wells, this will be of no use as the rounding errors accumulate to yield “quasi-random” results; furthermore, the algorithm might need a few years just to compute a single result. Unfortunately, the algorithms suitable for larger problems are usually more complex; thus, they are not just in most programs.

Similar, the computation of the zeros of the dynamical system might be a problem. For low-dimensional problems, the radius of convergence in a Newton-Raphson algorithms is limited by the condition that the linear approximation of the function in question has to be close enough to the “real” function. However, if the number of variables is increased, rounding errors become more important. Very often, convergence is not limited by the validness of the linearisation but by these rounding errors. Thus, a simple algorithm like the one in [Pre92] will usually not converge at all.

However, there is no clear distinction between this section and the preceding one. Even for good algorithms, the available precision is very important. When using floating point numbers of length 8 bytes, they need a better initial guess and more iteration steps than when using 10 byte long floats.

F.3 Programs

For simulating the system, I developed programs myself based on the integration routine from [Hei92]. The allowed error in the integration process – used for adjusting the time step

---

[3] The exact factor depends on whether the extra precision is used by the algorithms. This may mean that more iteration steps may be necessary to fully utilize the extra precision. On the other hand, the extra precision may lead to faster convergence or even a larger radius of convergence. Thus, for certain problems, a Pentium is up to five times faster than the reference workstation if the larger radius of convergence is used by the algorithm.

– depends on what kind of state is investigated. For example, if a stable limit cycle oscillation is simulated, small deviations of the simulated trajectory from the limit cycle are not important as the system will nevertheless stay very near the attractor. Furthermore, the precise shape of transient effects is not that critical. Important is that the “right” attractor is reached when there is multistability.

If stationary states are of interest, the precision of the integration algorithm is much more critical. The position of the stationary state has to be reached so good that the transition rates at that point are smaller then a given bound. If the accuracy of the integration is not good enough, the system would make quasi-random steps around the fixed point without being able to reach it. As has been shown in section F.1, the values of $\dot{n}_1^{(i)}$ are higher by about a factor 10^6 during a oscillation when compared with the bound for detecting of stationary states. Thus, it makes no sense to use the same error bound for the integration algorithm in both cases.

This problem has been solved by adjusting the allowed error in dependence on the rate $\dot{n}_k^{(i)}$. This way, the speed of the algorithm can be increased by about a factor of ten when compared to a fixed error bound.

Most computations in this thesis were done using continuation techniques. With a few exceptions, the program CANDYS/QA [Feu92, Can95] was used. From the computed data it constructs a graph with the stationary states (or codimension-n bifurcations) forming the arcs and the bifurcation points (or codimension-(n+1) bifurcations) the nodes. The program had to be adapted to the high-dimensional problems investigated in this thesis by loosening some criteria in the Newton-Raphson algorithm used for root-finding. Additionally, the routine for the calculation of the eigenvalues was replaced with the one from [Pre92]. The phase portraits as well as the unstable manifolds were computed using the program DsTool [Guc95]. This involves no complicated numerical procedures so that only the root-finding algorithm had to be replaced. (The routine from CANDYS/QA was used for this purpose).

For one computation (Fig. 4.14), the program LOCBIF, which is integrated into DsTool, was used. LOCBIF is able to continue a larger number of bifurcation types than CANDYS/QA, among them a few points which are not really bifurcation points. Among these additional types are points at which two eigenvalues are equal. However, this program is not designed for high-dimensional problems at all. A large portion of the algorithms dealing with linear algebra had to be replaced. Among these there were algorithms whose dependence on the number of elements is a high as $\mathcal{O}(N^5)$. Apart from the time needed by this algorithms, the large number of internal steps done by them leads to an accumulation of rounding errors. In most cases there was no correlation between the input data and the computed results when using the original algorithms.

Similar has to be said about the bifurcation functions employed by LOCBIF. These functions - being the heart of a program for continuation - had to be rewritten completely. As this thesis deals with the investigation of semiconductor superlattices and not with the development of continuation algorithms, I did not optimise the bifurcation functions. In addition, LOCBIF determines the derivates of the bifurcation functions numerically and not analytically.[4] As a result, CANDYS/QA is faster by about a factor 100 when continuing bifurcation points; DSTOOL was therefore only used when a bifurcation type was not implemented into CANDYS/QA.

F.4 Computing Time

The computing times given in this section are relative to a reference workstation, namely a IBM RS-6000/370. The speed of a Sun-10/40 is approximately the same, a Cray X-MP is faster by about 150 %.

It takes about one to two hours to simulate a current-voltage characteristic - of course, it depends on the size of the steps in which the voltage is increased. On the other hand, if a current-voltage characteristic is determined by continuation techniques, the time needed depends mainly on the number and the length of the unstable branches; in other words, it depends on the arc length of the characteristic. For heavy doping, simulation and continuation need approximately the same time but the simu-

---

[4] Such an algorithm will need at least one evaluation of the bifurcation function per variable. The most expensive part of this function evaluation is computing the transport coefficients which has to be done once regardless of whether just the function is evaluated or the entire Jacobi matrix is computed.

lation computes much less data. For small doping, continuation is faster by more than a factor of 10.

The most time-consuming problem is the computation of oscillations as the system of ODEs has to be integrated long enough for all transient effects to disappear. Especially for Neumann boundary conditions, this time may become very large. Just the data presented in Fig. 7.4 took about 1500 hours to compute. The other possibility to investigate oscillations is to also use continuation techniques which allow to investigate unstable limit cycles as well. However, the Jacobi matrix has to be integrated then.[5] A single step usually takes about one hour but may take as long as 10 hours for Neumann boundary conditions.

I will not give a “total” number of hours used for “producing” this thesis due to two reasons: First, on most machines the computing time used by individual users is not accounted for. Second, a large part of “overall” time was used for just a few computations - one may doubt whether the effort was justified in every case. However, it is very time-consuming to “find” interesting phenomena in parameter- and phase space. If no such phenomena are found, the time invested may be a “write-off” but the search had to be done nonetheless as one can not know the result in advance. For example, the figures presented in section 6.1 took just a few hours to compute but finding the relevant values of the parameters a few hundred hours.

---

[5] More precisely, the Jacobi matrix is the exponent of a power function. This is similar to computing the Floquet-exponents which are just the eigenvalues of the matrix computed this way.

Appendix G

Transport Coefficients

The exact expressions for transport coefficients introduced in chapter 3 are given in this appendix. They have been taken from [Pre94a].

The coefficients $R_1(F)$ and $R_2(F)$ for miniband conduction read:

$$R_k(F) = \frac{2\lambda_k}{\hbar}\sqrt{\frac{\tau_m}{\tau_e}}\frac{F/\tilde{F}}{1+\left(F/\tilde{F}\right)^2}$$

$\tilde{F} = \frac{\hbar}{\epsilon_0 d \tau_m \tau_e}$ is the critical electric field and λ_k the overlap integral of the wavefunctions for the k-th energy level in two adjacent quantum wells. The exact values for the latter are:

$$\begin{aligned}
\lambda_1 &= 2c_1^2 V_0 \frac{e^{-\kappa_1(d+L/2)}}{k_1^2+\kappa_1^2}\left[k_1 \cosh\left(\frac{\kappa_1 L}{2}\right)\tan\left(\frac{k_1 L}{2}\right) + \kappa_1 \sinh\left(\frac{\kappa_1 L}{2}\right)\right] \\
\lambda_2 &= 2c_2^2 V_0 \frac{e^{-\kappa_2(d+L/2)}}{k_2^2+\kappa_2^2}\left[\kappa_2 \cosh\left(\frac{\kappa_2 L}{2}\right) - k_2 \sinh\left(\frac{\kappa_2 L}{2}\right)\cot\left(\frac{k_2 L}{2}\right)\right]
\end{aligned}$$

The coefficients for resonant tunnelling are:

$$\begin{aligned}
X &= \left[\frac{S(b_- + b_+) + 2b_- b_+}{b_- - b_+}\right]^2 \cdot \frac{E_+ - E_-}{2\pi\hbar} \\
Y &= \left[\frac{S(b_- + b_+) + 2}{b_- - b_+}\right]^2 \cdot \frac{E_+ - E_-}{2\pi\hbar}
\end{aligned}$$

Here, the abbreviations mean:

$$\begin{aligned}
b_\pm &= -\frac{P}{2} \mp \sqrt{\frac{P^2}{4} + Q} \\
P &= \frac{(E_1 - E_2 + \delta)\left(1 - S^2\right) + \left(V_1^{12'} - V_2^{12'}\right)S + V_2^{11} - V_1^{2'2'}}{V_1^{12'} - V_1^{2'2'}S} \\
Q &= \frac{V_2^{12'} - V_2^{11}S}{V_1^{12'} - V_1^{2'2'}S} \\
E_\pm &= \frac{(E_1 + \delta/2) + (E_2 - \delta/2)\, b_\pm S + b_\pm V_1^{12'} + V_2^{11}}{1 + b_\pm S}
\end{aligned}$$

The values of the overlap integrals are:

$$\begin{aligned}
V_1^{12'} &= \left(-V_0 + \frac{edF}{2}\right)\alpha_L \\
V_2^{12'} &= \left(-V_0 - \frac{edF}{2}\right)\alpha_R
\end{aligned}$$

$$
\begin{aligned}
V_2^{11} &= \left(-V_0 - \frac{edF}{2}\right)\gamma_1 \\
V_2^{2'2'} &= \left(-V_0 + \frac{edF}{2}\right)\gamma_2 \\
S &= \alpha_L + \alpha_M + \alpha_R
\end{aligned}
$$

with the abbreviations

$$
\begin{aligned}
\gamma_1 &= c_1^2 \frac{e^{(-2d+L)\kappa_1}}{2\kappa_1} \\
\gamma_2 &= c_2^2 \frac{e^{(-2d+L)\kappa_2}}{2\kappa_2} \\
\alpha_L &= 2c_1c_2 \frac{e^{-(\kappa_2 d+\kappa_1 L/2)}}{\kappa_1^2+\kappa_2^2}\left[k_1 \cosh\left(\frac{\kappa_2 L}{2}\right)\tan\left(\frac{k_1 L}{2}\right) + \kappa_2 \sinh\left(\frac{\kappa_2 L}{2}\right)\right] \\
\alpha_R &= 2c_1c_2 \frac{e^{-(\kappa_1 d+\kappa_2 L/2)}}{\kappa_1^2+\kappa_2^2}\left[k_1 \cosh\left(\frac{\kappa_1 L}{2}\right) - \kappa_2 \sinh\left(\frac{\kappa_1 L}{2}\right)\cot\left(\frac{\kappa_2 L}{2}\right)\right] \\
\alpha_M &= c_1c_2 \frac{e^{kappa_1 L+\kappa_2 d} - e^{\kappa_2 L+\kappa_1 d}}{\kappa_2-\kappa_1} e^{-(\kappa_1+\kappa_2)(d+L/2)} \\
c_1 &= \left[e^{-\kappa_1 L}\left(\frac{1}{\kappa_1} + \frac{L}{2\cos^2(k_1L/2)} + \frac{1}{k_1}\tan(k_1L/2)\right)\right]^{-1/2} \\
c_2 &= \left[e^{-\kappa_2 L}\left(\frac{1}{\kappa_2} + \frac{L}{2\sin^2(k_2L/2)} + \frac{1}{k_2}\cot(k_2L/2)\right)\right]^{-1/2}
\end{aligned}
$$

In the expressions above, the width of the quantum wells has been named L in contrast to the other chapters of this thesis. d is the superlattice period, that is, the sum of the width of one barrier and one quantum well. $\delta = edF$ is the shift of the energy levels due to the local electric field F.

In addition, the wave vectors $k_j = \frac{1}{\hbar}\sqrt{2m_jE_j}$ (in the quantum wells) and the constant $\kappa_j = \frac{1}{\hbar}\sqrt{2m_j(V_0-E_j)}$ (in the adjacent barrier) of both bound solutions of the Schrödinger equation have to be inserted. These solutions have to be determined numerically by computing the energies E_j for which the condition

$$\kappa_j = \frac{m_2}{m_1}\tan(kL/2)$$

is fulfilled [Pre94a]. This conditions differs from the one used normally by the ratio of the effective masses.

Appendix H

Parameters of All Calculations

Fig.	U	N_D	n_D	α	real.
3.6	0.0-5.0		1.5		
3.7	0.0-5.0		2.8		
4.1(a)			0.5	0 %	
4.1(b)			1.0	0 %	
4.1(c)			1.5	0 %	
4.1(d)			2.0	0 %	
4.1(e)			2.35	0 %	
4.2			2.9	0 %	
4.3			2.9	0 %	
4.4			2.9	0 %	
4.5	3.8		2.9	0 %	
4.6			2.9	0 %	
4.7	1.0	$5 \cdot 10^{16}$		0 %	
4.8	0.75		1.5	0 %	
4.9		$5 \cdot 10^{16}$		0 %	
4.10				0 %	
4.11				0 %	
4.12(a)	3.5	$2 \cdot 10^{16}$		0 %	
4.12(b)	1.5	$3 \cdot 10^{16}$		0 %	
4.12(c)	1.5	$5 \cdot 10^{16}$		0 %	
4.14				0 %	
4.15				0 %	
4.16		$1 \cdot 10^{16}$		0 %	
4.17	3.8		1.5	0 %	
4.18				0 %	
4.19	1.0			0 %	
4.20				0 %	
4.21	1.0			0 %	
4.22				0 %	
4.23				0 %	
4.24			2.9	0 %	
4.25	2.348		2.9	0 %	
4.26			2.9	0 %	
4.27			2.9	0 %	
4.28			2.9	0 %	
4.29			2.9	0 %	
4.30			3.0	0 %	
5.2	2.34182 - 2.35349		2.9		1
5.3			2.9		2
5.4(a)	0.915022518		2.9	0 %	2

Fig.	U	N_D	n_D	α	real.
5.4(b)	0.9148		2.9	10 %	2
5.4(c)	0.9148		2.9	10 %	2
5.5			2.8	8 %	1
5.6			2.9		1
5.7					1
5.10					1
5.8, left			2.9		1
5.8, centre			2.8		1
5.8, right			2.7		1
5.9, left			2.9		1
5.9, centre			2.8		1
5.9, right			2.7		1
5.11(a)				12 %	1
5.11(b)				12 %	4
5.11(c)				12 %	6
5.11(d)				12 %	7
6.1			2.9	10 %	1
6.2			2.9	10 %	1
6.3			2.9		1
6.4			2.9	10 %	1
6.5			2.9	0 %	1
6.6			2.9	0 %	1
6.7			2.9		1
6.8			2.9		1
6.9(a)			2.9		1
6.9(b)			2.9	0 %	1
6.9(c)			2.9		1
6.9(d)			2.9	0 %	1
6.10			2.9		1
6.11(a)			2.9		1
6.11(b)			2.9	9 %	1
6.14(a)			2.9	9.04245 %	1
6.14(b)			2.9	9.042462 %	1
6.14(c)			2.9	9.04247 %	1
6.15	2.0944318		2.9	9.042462 %	1
6.16			2.9	9.042462 %	1
6.17			2.9		1
6.18			2.9	14 %	1
6.19			2.9	14 %	1
6.20			2.9	14 %	1
6.21					1
6.22					1
6.23			2.3868		1
6.24			2.3868		1
6.26			2.33	17.5 %	1
6.27			2.33	17.5 %	1
6.28	2.002		2.33	17.5 %	1
7.1		$2 \cdot 10^{16}$		0 %	
7.2		$2 \cdot 10^{16}$		0 %	
7.3	1.0			0 %	
7.4		$2 \cdot 10^{16}$		0 %	
7.5		$2 \cdot 10^{16}$		0 %	
7.6	1.0		1.5	0 %	
7.7		$2 \cdot 10^{16}$		0 %	
7.8			2.8	0 %	
7.9				0 %	
B.1	0.5	0		0 %	
B.2		0		0 %	

Fig.	U	N_D	n_D	α	real.
C.1		4.0		0 %	
C.2		4.0		0 %	

Table H.1: Precise values of all parameters for each figure in this thesis. "real." is the number of the realisation of frozen-in fluctuations, n_D is defined on page 113.

	+1	+2	+3	+4	+5
0	+0.936142	−0.866539	−0.0434378	+0.819069	−0.296615
5	+0.865067	+0.308872	−0.95786	+0.0244097	−0.595962
10	+0.879954	−0.591835	−0.242342	+0.586228	−0.423598
15	−0.465687	−0.286355	−0.743253	+0.406596	+0.474827
20	+0.605042	+0.830462	+0.0227633	+0.524115	−0.0872372
25	−0.057876	−0.400899	+0.225119	−0.853238	−0.00362927
30	−0.560825	−0.917096	+0.129832	+0.395737	+0.901973
35	+0.833217	+0.260804	+0.210844	+0.875357	−0.714786

Table H.2: Frozen-in fluctuations for realisation 1 ("standard realisation").

	+1	+2	+3	+4	+5
0	0.0	0.0	0.0	0.0	0.0
5	0.0	0.0	0.0	0.0	0.0
10	0.0	0.0	0.0	0.0	0.0
15	0.0	0.0	0.0	0.0	1.0
20	0.0	0.0	0.0	0.0	0.0
25	0.0	0.0	0.0	0.0	0.0
30	0.0	0.0	0.0	0.0	0.0
35	0.0	0.0	0.0	0.0	0.0

Table H.3: Frozen-in fluctuations for realisation 2.

	+1	+2	+3	+4	+5
0	−0.7068	−0.473982	−0.0704654	+0.764672	−0.62663
5	+0.865073	+0.728941	+0.101892	−0.131348	−0.626173
10	−0.747873	−0.55129	+0.566449	+0.170055	−0.173973
15	+0.710723	+0.293483	+0.991452	+0.272798	−0.0282634
20	−0.358087	−0.118153	+0.457988	−0.481902	+0.372265
25	−0.470352	+0.446735	−0.762089	−0.360843	+0.337826
30	+0.394595	−0.228634	−0.548835	−0.0942771	−0.684055
35	+0.34623	+0.307642	−0.838937	+0.406451	−0.396039

Table H.4: Frozen-in fluctuations for realisation 4.

	+1	+2	+3	+4	+5
0	+0.0246972	−0.738236	+0.417337	+0.634606	−0.71217
5	−0.278348	+0.561903	+0.744417	−0.613879	+0.936042
10	−0.147552	+0.362828	−0.157157	−0.720546	+0.710416
15	+0.619223	−0.6383	−0.122326	−0.880627	+0.862695
20	+0.685764	+0.770533	−0.881519	+0.725448	+0.258207
25	−0.648086	+0.0290125	+0.18607	+0.830846	−0.833702
30	+0.54049	+0.00892775	−0.568183	+0.742135	+0.799399
35	−0.506282	−0.364789	+0.700417	+0.176976	−0.159355

Table H.5: Frozen-in fluctuations for realisation 6.

	+1	+2	+3	+4	+5
0	+0.764478	+0.606861	+0.00778312	−0.983954	+0.222996
5	+0.870308	+0.808331	+0.501767	−0.411232	+0.400809
10	−0.859965	−0.306265	−0.936468	+0.0382501	−0.466728
15	−0.0722249	−0.348991	−0.923974	−0.48468	−0.771004
20	+0.0934742	−0.863781	−0.994303	−0.0725615	−0.0226838
25	−0.654556	−0.000787315	−0.26547	−0.971405	−0.734324
30	−0.461664	+0.0316007	+0.88491	−0.36467	−0.00716537
35	−0.320504	+0.161428	−0.466008	−0.801841	+0.0297467

Table H.6: Frozen-in fluctuations for realisation 7.

Acknowledgements

I wrote this thesis while being a member of the group of Prof. E. Schöll. I want to acknowledge the support I received from him and all the other group members. Especially, this refers to F. Prengel and G. Schwarz, without whose earlier results on the subject of semiconductor superlattices this thesis would not have been possible. Furthermore, I want to thank S. Bose for his help in solving all kinds of computer problems, D. Merbach for valuable discussion on nonlinear dynamics, and Dr. A. Wacker for his guidance at the start of my thesis.

Bibliography

[Abr83] R. H. Abraham and Ch. D. Shaw. *Dynamics: The Geometry of Behavior.* Aerial, Santa Cruz, 1983.

[All90] E. L. Allgower and K. Georg. *Numerical Continuation Methods*, volume 13 of *Springer Series in Computational Mathematics*. Springer-Verlag, Berlin, 1990.

[Bon94] L. L. Bonilla, J. Galán, J. A. Cuesta, F. C. Martínez, and J. M. Molera. Dynamics of electric field domains and oscillations of the photocurrent in a simple superlattice model. *Phys. Rev. B*, 50:8644, 1994.

[Bon95] L. L. Bonilla. Dynamics of electric field domains in superlattices. In F. J. Niedernostheide, editor, *Nonlinear Dynamics and Pattern Formation in Semiconductors*, chapter 1, pages 1–20. Springer, Berlin, 1995.

[Can95] *CANDYS/QA User's Manual.* Potsdam, 1995.

[Cho87] K. K. Choi, B. F. Levine, R. J. Malik, J. Walker, and C. G. Bethea. Periodic negative conductance by sequential resonant tunneling through an expanding high-field superlattice domain. *Phys. Rev. B*, 35(8):4172, 1987.

[Dev86] B. Deveaud, A. Regreny, J-Y. Emery, and A. Chomette. Photoluminescence study of interface defects in high-quality GaAs-GaAlAs superlattices. *J. Appl. Phys.*, 59:1633, 1986.

[Die90] B. De Dier, D. Roose, and P. van Rompay. Interaction between fold and Hopf curves leads to new bifurcation phenomena. In H. D. Mittelmann and D. Roose, editors, *Continuation Techniques and Bifurcation Problems*, volume 92 of *International Series of Numerical Mathematics*, pages 171–186. Birkhäuser Verlag, Basel, 1990.

[Dra92] P.G. Drazin. *Nonlinear Systems.* Cambridge texts in applied mathematics 10. Cambridge University Press, Cambridge, U.K., 1992.

[Dum92] F. Dumortier, R. Roussarie, and J. Sotomayor. *Generic 3-parameter families of planar vector fields, unfolding of saddle, focus and elliptic singularities with nilpotent linear parts.* Lecture Notes in Mathematics 1480. Springer-Verlag, Berlin, 1992.

[Esa70] L. Esaki and R. Tsu. Superlattice and negative differential conductivity in semiconductors. *IBM J. Res. Develop.*, 14:61, 1970.

[Esa74] L. Esaki and L. L. Chang. New transport phenomenon in a semiconductor superlattice. *Phys. Rev. Lett.*, 33(8):495, 1974.

[Ete93] G. Etemadi and J. F. Palmier. Effect of interface roughness on non-linear vertical transport in GaAs/AlAs superlattices. *Sol. Stat. Comm.*, 86(11):739, 1993.

[Feu92] U. Feudel and W. Jansen. CANDYS/QA - A software system for qualitative analysis of nonlinear dynamical systems. *International Journal of Bifurcation and Chaos*, 2:773–794, 1992.

[Gol85] M. Golubitsky and D. G. Schaeffer. *Singularities and Groups in Bifurcation Theory*, volume I of *Applied mathematical sciences 51.* Springer-Verlag, Berlin, 1985.

[Gra92] H. T. Grahn. Vertikaler Transport in GaAs-AlAs "Ubergitterstrukturen. Habilitationsschrift, 1992.

[Gra95a] H. T. Grahn. Electric field domains. In H. T. Grahn, editor, *Semiconductor Superlattices, Growth and Electronic Properties*, chapter 5. World Scientific, Singapore, 1995.

[Gra95b] H. T. Grahn, J. Kastrup, K. Ploog, L. L. Bonilla, J. Galán, M. Kindelan, and M. Moscoso. Self-oscillations of the current in doped semiconductor superlattices. *Jpn. J. Appl. Phys.*, 34:4526, 1995.

[Guc83] J. Guckenheimer and P. Holmes. *Nonlinear Oscillations, Dynamical Systems, and Bifurcations of Vector Fields.* Applied mathematical sciences 42. Springer-Verlag, Berlin, 1983.

[Guc86] J. Guckenheimer. Multiple bifurcation problems for chemical reactors. *Physica D*, 20:1–20, 1986.

[Guc95] J. Guckenheimer, M. R. Myers, F. J. Wicklin, and P. A. Worfolk. *DsTool User's Manual.* Ithaca NY 14853, 1995.

[Hei92] G. Heinzel. Beliebig genau - Moderne Runge-Kutta-Verfahren zur Lösung von Differentialgleichungen. *c't Magazin für Computertechnik*, 8:172—185, Aug 1992.

[Hel90] P. Helgesen and T. G. Finstad. Sequential resonant and non-resonant tunneling in GaAs/AlGaAs multiple quantum well structures: High field domain formation. In O. Hansen, editor, *Proceedings of the* 14^{th} *Nordic Semiconductor Meeting*, page 323. University of Århus, Århus, 1990.

[Ign91] A. A. Ignatov, E. P. Dodin, and V. I. Shashkin. Transient response theory of semiconductor superlattices: Connection with bloch oscillations. *Mod. Phys. Lett. B*, 5(16):1087, 1991.

[Ioo90] G. Iooss and D. D. Joseph. *Elementary Stability and Bifurcation Theory.* Undergraduate texts in mathematics. Springer-Verlag, Berlin, second edition, 1990.

[Kas94] J. Kastrup, H. T. Grahn, K. Ploog, F. Prengel, A. Wacker, and E. Schöll. Multistability of the current-voltage characteristics in doped GaAs-AlAs superlattices. *Appl. Phys. Lett.*, 65:1808, 1994.

[Kas95a] J. Kastrup. Private Mitteilung, veröffentlicht in [Sch95b], 1995.

[Kas95b] J. Kastrup, R. Klann, H. T. Grahn, K. Ploog, L. L. Bonilla, J. Galán, M. Kindelan, M. Moscoso, and R. Merlin. Self-oscillations of domains in doped GaAs-AlAs superlattices. *Phys. Rev. B*, 52:13761, 1995.

[Kas96] J. Kastrup, F. Prengel, H. T. Grahn, K. Ploog, and E. Schöll. Formation times of electric field domains in doped GaAs-AlAs superlattices. *Phys. Rev. B*, 53:1502, 1996.

[Kaw86] Y. Kawamura, K. Wakita, H. Asahi, and K. Kurumada. Observation of room temperature current oscillation in InGaAs/InAlAs MQW pin diodes. *Jpn. J. Appl. Phys.*, 25:L928, 1986.

[Kaz72] R. F. Kazarinov and R. A. Suris. Electric and electromagnetic properties of semiconductors with a superlattice. *Sov. Phys. Semicond.*, 6(1):120, 1972.

[Kea95] B. J. Keay, S. J. Allen Jr., J. P. Kaminski, K. L. Champman, A. C. Gossard, U. Bhattacharya, M. J. M. Rodwell, and J. Galán. Sequential resonant tunneling via photon virtual states in semiconductor superlattices. In D. J. Lockwood, editor, *Proc. 22nd Int. Conf. Phys. Semicond., Vancouver 1994*, volume 2, page 1055. World Scientific, Singapore, 1995.

[Khi90] A. I. Khibnik. LINLBF: A program for continuation and bifurcation analysis of equilibria up to codimension three. In D. Roose, B. De Dier, and A. Spence, editors, *Continuation and Bifurcations: Numerical Techniques and Applications*, volume 313 of *NATO ASI series C: Mathematical and physical sciences*, pages 283–296. Kluwer Academic Publishers Group, Dordrecht, The Netherlands, 1990.

[Khi92] A. I. Khibnik, Yu. A. Kuznetsov, V. V. Levitin, and E. V. Nikolaev. *Interactive LOCal BIFurcation Analyzer*, 1992.

[Kla95] R. Klann, S. H. Kwok, H. T. Grahn, and R. Hey. Time-resolved photoluminescence investigations of electric-field domain formation in GaAs/AlAs superlattices. *Phys. Rev. B*, 52:8680, 1995.

[Kor93] A. N. Korotkov, D. V. Averin, and K. K. Likharev. Single-electron quantization of electric field domains in slim semiconductor superlattices. *Appl. Phys. Lett.*, 62(25):3282, 1993.

[Kwo94] S. H. Kwok, R. Merlin, H. T. Grahn, and K. Ploog. Electric field domains in semiconductor superlattices: Resonant or non-resonant tunneling? *Phys. Rev. B*, 50:2007, 1994.

[Kwo95a] S. H. Kwok, H. T. Grahn, M. Ramsteiner, K. Ploog, F. Prengel, A. Wacker, E. Schöll, S. Murugkar, and R. Merlin. Non-resonant carrier transport through high-field domains in semiconductor superlattices. *Phys. Rev. B*, 51:9943, 1995.

[Kwo95b] S. H. Kwok, T. B. Norris, L. L. Bonilla, J. Galán, J. A. Cuesta, F. C. Martínez, H. T. Grahn, K. Ploog, and R. Merlin. Domain wall kinetics and tunneling-induced instabilities in superlattices. *Phys. Rev. B*, 51:10171, 1995.

[Lai93] B. Laikhtman and D. Miller. Theory of current-voltage instabilities in superlattices. *Phys. Rev. B*, 48(8):5395, 1993.

[Mer95] R. Merlin, S. H. Kwok, T. B. Norris, H. T. Grahn, K. Ploog, L. L. Bonilla, J. Galán, J. A. Cuesta, F. C. Martínez, and J. M. Molera. Dynamics of resonant tunneling domains in superlattices: Theory and experiment. In D. J. Lockwood, editor, *Proc. 22nd Int. Conf. Phys. Semicond., Vancouver 1994*, page 1039. World Scientific, Singapore, 1995.

[Mil94] D. Miller and B. Laikhtman. Theory of high-field-domain structures in superlattices. *Phys. Rev. B*, 50:18426, 1994.

[Par89] T. S. Parker and L. O. Chua. *Practical Numerical Algorithms for Chaotic Systems.* Springer-Verlag, Berlin, 1989.

[Pat95] M. Patra. Bifurkationsanalyse von Stromoszillationen in Halbleiterübergittern. Studienarbeit, Technische Universität Berlin, Berlin, 1995.

[Pei92] J. Peinke, J. Parisi, O. E. Rössler, and R. Stoop. *Encounter with Chaos.* Springer-Verlag, Berlin, 1992.

[Pre92] W. H. Press, S. A. Teukolsky, W. T. Vetterling, and B. P. Flannery. *Numerical Recipes in C: The art of scientific computing.* Cambridge University Press, Cambridge, U.K., 1992.

[Pre94a] F. Prengel. Nichtlinearer Transport in Halbleiter-Übergittern. Diplomarbeit, Technische Universität Berlin, 1994.

[Pre94b] F. Prengel, A. Wacker, and E. Schöll. Simple model for multistability and domain formation in semiconductor superlattices. *Physical Review B*, 50:1705–1712, 1994.

[Pre95] F. Prengel, A. Wacker, G. Schwarz, E. Schöll, J. Kastrup, and H. T. Grahn. Dynamics of domain formation in semiconductor superlattices. In *Proc. 9th Symposium on Ultrafast Phenomena in Semiconductors*, volume 35, pages 404–407, Vilnius, 1995. Lithuanian Journal of Physics.

[Roo87] D. Roose. Numerical computation of origins for Hopf bifurcation in a two-parameter problem. In T. Küpper, R. Seydel, and H. Troger, editors, *Bifurcation: Analysis, Algorithms, Applications*, volume 79 of *International Series of Numerical Mathematics*, pages 268–276. Birkhäuser Verlag, Basel, 1987.

[Sch87] E. Schöll. *Nonequilibrium Phase Transitions in Semiconductors.* Springer, Berlin, 1987.

[Sch94] G. Schwarz. Vertikaler Transport in Übergittern mit Dickenfluktuationen. Studienarbeit, Technische Universität Berlin, September 1994.

[Sch95a] E. Schöll and A. Wacker. Oscillatory transport instabilities and complex spatio-temporal dynamics in semiconductors. In F. J. Niedernostheide, editor, *Nonlinear Dynamics and Pattern Formation in Semiconductors and Devices*, pages 21–45. Springer, Berlin, 1995.

[Sch95b] G. Schwarz. Felddomänen in imperfekten Übergitterstrukturen. Diplomarbeit, Technische Universität Berlin, 1995.

[Sch96a] E. Schöll, G. Schwarz, M. Patra, F. Prengel, and A. Wacker. Oscillatory instabilities and field domain formation in imperfect superlattices. In K. Hess, J. P. Leburton, and U. Ravaioli, editors, *Proc. 9th Int. Conf. on Hot Carriers in Semiconductors, Chicago 1995*, New York, 1996. Plenum Press. in print.

[Sch96b] G. Schwarz and E. Schöll. Field domains in semiconductor superlattices. *phys. status solidi (b)*, 194(1):351–369, 1996.

[Sch96c] G. Schwarz, A. Wacker, F. Prengel, E. Schöll, J. Kastrup, H. T. Grahn, and K. Ploog. Influence of imperfections and weak disorder on domain formation in superlattices. *Semicond. Sci. Technol.*, 11(4):475–482, 1996.

[Sha92] M. P. Shaw, V. V. Mitin, E. Schöll, and H. L. Grubin. *The Physics of Instabilities in Solid State Electron Devices.* Plenum Press, New York, 1992.

[Wac] A. Wacker, M. Moscoso, M. Kindelan, and L. L. Bonilla. Current-voltage characteristic and stability in resonant-tunneling n-doped semiconductor superlattices. submitted to Phys. Rev. B.

[Wac93] A. Wacker and E. Schöll. Spatio-temporal oscillations in the heterostructure hot-electron diode. In *Proc. 8th Vilnius Symposium on Ultrafast Phenomena in Semicond.*, page 37, Vilnius, 1993. Academia.

[Wac95a] A. Wacker, F. Prengel, and E. Schöll. Theory of multistability and domain formation in semiconductor superlattices. In D. J. Lockwood, editor, *Proc. 22nd Int. Conf. Phys. Semicond., Vancouver 1994*, volume 2, page 1075. World Scientific, Singapore, 1995.

[Wac95b] A. Wacker, G. Schwarz, F. Prengel, E. Schöll, J. Kastrup, and H. T. Grahn. Probing growth-related disorder by high-field transport in semiconductor superlattices. *Phys. Rev. B*, 52:13788, 1995.

[Wer91] B. Werner and V. Janovsky. Computation of Hopf branches bifurcating from Takens-Bodganov-points for problems with symmetries. In R. Seydel, F. W. Schneider, T. Küpper, and H. Troger, editors, *Bifurcation and Chaos: Analysis, Algorithms, Applications*, volume 97 of *International Series of Numerical Mathematics*, pages 377–388. Birkhäuser Verlag, Basel, 1991.

[Zha94] Y. Zhang, X. Yang, W. Liu, P. Zhang, and D. Jiang. New formation mechanism of electric field domain due to $\gamma - x$ sequential tunneling in GaAs/AlAs superlattices. *Appl. Phys. Lett.*, 65:1148, 1994.

Index

Legend

Symbols in the Figures

One variable parameter (bifurcation diagram)	
Stable fixed point	———
Unstable fixed point	-----------
Oscillation (limit cycle)	-·-·-·-·-
Saddle-node bifurcation	◇
Hopf bifurcation	+
Transcritical bifurcation	□

Two variable parameters (“phase diagram”)	
Saddle-node bifurcation	———
Hopf bifurcation	-----------
Cusp point	△
Takens-Bogdanov point	+

Important Quantities

U	Applied external voltage	(page 19)
N_D	Doping density	(page 19, for most figures: $7.9 \cdot 10^{17}$ cm^{-3})
α	Level of disorder	(page 53)
$F^{(i)}$	Electric field in the i-th barrier	(page 17)
$n_k^{(i)}$	Electron densities in the i-th quantum well	(page 17)

Applying methods from nonlinear dynamics, vertical transport in semiconductor superlattices has been analysed using a simple microscopic model. The relevant bifurcations are examined, and the spatio-temporal pattern formation (multistable field domains and limit cycle oscillations) is explained. Furthermore, spatial inhomogenities of the doping density are included, and their effects on the current-voltage characteristic and on the oscillations are investigated.